CRANFIELD UNIVERSITY

SCHOOL OF APPLIED SCIENCES

PhD THESIS

# Investigation into the Propagation and Inspection of Stress Corrosion Cracks under Compressive Loading.

Mahmood Dollah

# CRANFIELD UNIVERSITY

## SCHOOL OF APPLIED SCIENCES

## PhD THESIS

Academic Year 2003 – 2007

**Mahmood Dollah**

# Investigation into the Propagation and Inspection of Stress Corrosion Cracks under Compressive Loading.

**Supervisor : Dr. M.J. Robinson**

**July 2007**

# ABSTRACT

Eddy current testing has become a widely used nondestructive technique for material testing and evaluation. This technique depends on the interaction between the impedance of the test coil and the material as the probe scans the surface of a material under investigation. By measuring the change in impedance of the test coil, the size of an imperfection in the material can be determined. In this project, the first aim of the research was to investigate and develop the use of the eddy current technique to detect stress corrosion cracks (SCC) in the bore of fastener holes. Specimens were scanned with the probe moving in and out the hole to produce a signal of the eddy current response. In addition, due to the skin depth effect, the operating frequency was also taken into consideration as an important parameter. A calibration standard test piece was prepared to represent SCC around a fastener hole, with the cracks lying in a plane parallel to the surface. Data from eddy current tests on real stress corrosion cracks has been used to develop an eddy current calibration curve for predicting stress corrosion crack lengths in larger components.

The second aim of the project was to use the eddy current technique to study SCC crack growth in high strength aluminium alloy 7075-W under both tensile and compressive loading conditions. The importance of parameters such as heat treatment, grain shape, grain aspect ratio, component of stress, threshold stress intensity and microstructure were all taken into consideration. The SCC development was found to follow an intergranular path, which strongly depended on the microstructure of the material. Tests were carried out using double cantilever beam specimens to measure the threshold stress intensity, $K_{ISCC}$, below which SCC would not occur. The specimens showed evidence of exfoliation corrosion at the surface and corrosion product wedging within the stress corrosion cracks, which caused further crack growth at the low applied stresses.

Stress corrosion cracks were found to grow in 7075-W under high compressive loading, whereas control tests without compressive test stress produced only exfoliation corrosion and no crack growth. The mechanism of SCC in both tensile and compressive loading was thought to be anodic dissolution of metal at the crack tip, with protective films being disrupted by dislocation movement with the formation of active slip-steps.

# ACKNOWLEDGEMENTS

I am grateful thanks to Dr. Mike Robinson for his guidance, patience and support during the supervision of this research project. His expertise and understanding approach was very much appreciated.

Special thanks to my lovely wife, Fadzilah Mamat, for unconditional support and my younger sister, Fatimah Dollah, for her no limitation help. I also would like to mention my little girl, Mahshitah Mahmood, and my little boy, Mahyuddin Mahmood, who was born during my doctoral studies. They have brought more happiness during my good and bad time. I dedicate this work to all of them.

I would like to extend my thanks to the following people for their help;-

In the School of Industrial and Manufacturing Science (SAS):

Andrew Dyer

Colin Matthews

Tony Parker

Ruhksana Ormesher

In the **Malaysian Nuclear Agency** (Nuclear Malaysia):

Dr Daud Mohamad

Dr Nahrul Khair Alang Md Rashid

Dr Abd Nassir Ibrahim

Dr Azali Mohamad

Dr Abd Razak Hamzah

And finally, thanks to **The Government Of Malaysia** for the scholarship during my studies.

Mahmood Dollah.

# LIST OF CONTENTS

# LIST OF FIGURES

# LIST OF TABLES

# 1.0 Introduction.

Non-destructive testing (NDT) is the testing of materials to detect surface and subsurface defects using methods that do not damage or destroy the material under investigation. There are five major NDT methods; Radiography (RT), ultrasonic testing (UT), magnetic particles testing (MT), liquid penetrant testing (PT) and eddy current testing (ET). These techniques can be used separately or combined as they complement each other. There are advantages and disadvantages associated with each technique and the selection of the most appropriate depends on the particular circumstances. Ultrasonic can detect smaller cracks than X-ray radiography, even with fasteners installed, but sensitivity and reliability are problems due to the poor surface finish of the holes or tight cracks. At present, eddy currents are the only practical method for reliably detecting small, tight cracks around the fastener holes [1].

Eddy current testing is a non-destructive test technique based on induced electrical currents in the material being inspected and on observing the interaction between those currents and the material. In practice, eddy currents are generated by electromagnetic coils in the test probe, and these currents change as the electrical impedance of the coil changes as it scans a surface of test specimen. Since it is an electromagnetic induction process, the sample has to be a conductor [2]. There are a few parameters affecting the eddy current measurement such as the type of probe, operating frequency and material properties. In the aircraft industry, this technique is used to inspect for heat treatment condition, conductivity, grain size and hardness in materials [3].

High strength aluminium alloys, such as 7XXX Al-Zn-Mg-Cu series, have been used for high strength applications in a wide range of industries for over half a century. They are used in transport applications, for manufacturing aircraft, as well as rail and road vehicles. They are also used in the process industries for making pressure vessels. In the aircraft industry, high strength aluminium alloys have been used for wing's skin construction. They are fastened together with rivets, which are quite highly stressed,

particularly during take-off and landing [4]. This region is exposed to high risk of corrosion attack. The corrosion problem occurs due to the susceptibility of the high performance alloys and the corrosion that develops around the fastener holes is in the form of end grain corrosion, sometimes accelerated by stress corrosion cracking, fretting or corrosion fatigue [5]. This susceptibility to these forms of corrosion could cause a reduce time of the working life of the component and result in failure. As mentioned above, one of the problems sometimes found in high strength aluminium alloys is stress corrosion cracking (SCC), which occurs at the grain boundaries. Stress corrosion cracking normally requires tensile loading. However, under special conditions, it has been shown to occur under compressive loading [6].

The first aim of this project was to investigate and develop the use of the eddy current technique to detect stress corrosion cracking within the bore of fastener holes. In this work, spark machine defects were introduced in a test piece to represent stress corrosion cracking, by electrochemically machining defects inside the bore of a hole in 7075-W aluminium alloy. The relationship between SCC length and amplitude of the eddy current signal was recorded and used to construct a SCC length against eddy current amplitude calibration curve. The work describes the test frequency of the eddy current probe used to study. The response of the eddy current probe from the simulated cracks have been compared to the real stress corrosion cracking.

The second aim of project was to investigate the nature of SCC in high strength aluminium alloy with emphasis on the effects of the W heat treatment condition. The parameters related with these materials such as microstructure, corrosion susceptibility and heat treatment have been studied.

The effect of different forms of stress on the SCC, particularly the difference between tensile and compressive loading, was also studied. The aim was to demonstrate in the laboratory whether compressive loading can produce a SCC in the specimen if both compressive loading and a corrosive environment were applied. The results were compared with those for specimens under tensile loading. From the results of these tests,

knowledge of the SCC growth mechanism in these high strength aluminium alloys was discussed, especially under compressive loading conditions.

# Literature Review

## 2.0 Eddy current testing.

Nondestructive testing is widely used throughout the chemical and metal industries performing various functions of crack detection, sorting materials and quality control. It is the use of methods for evaluating material quality without any destructive effect on the material under test or its continuing service.

This chapter will introduce the general principle of eddy current testing and will describe how it can be used as a non destructive testing technique for crack detection, especially for stress corrosion cracking. It will consider basic theory, practice of eddy current measurement and summarize its advantages over the other techniques. There will be a brief look at how the induced eddy currents are distributed and factors affecting their depth of penetration into a material. Some of the information in this section is taken from a number of documented physics text books [7-14].

### 2.1 General principles of eddy current non-destructive testing

In 1831, English scientist Michael Faraday [15] was credited with the discovery of electromagnetic induction. Eddy current testing is a non-destructive test based on electromagnetic induction by which a coil carrying an alternating current is placed near the conductor, as shown in Figure 1. When an alternating current is passed through a coil, an alternating magnetic field is generating in the plane of the coil [16]. The existence of this magnetic field induces alternating electric currents in the conductor flowing in the opposite direction to the direction of the current flow in the coil. In accordance with Lenz's law, Figure 2, the eddy currents induced in the metal generate a magnetic field which opposes the original magnetic field. A back emf is produced in the coil from the interaction of the two fields, which causes a change in impedance of the coil. This change in impedance can be measured in terms of a change in voltage drop across or current

flowing through the coil. This also used to give an indication of defects or differences in physical, chemical and metallurgical structure [17].

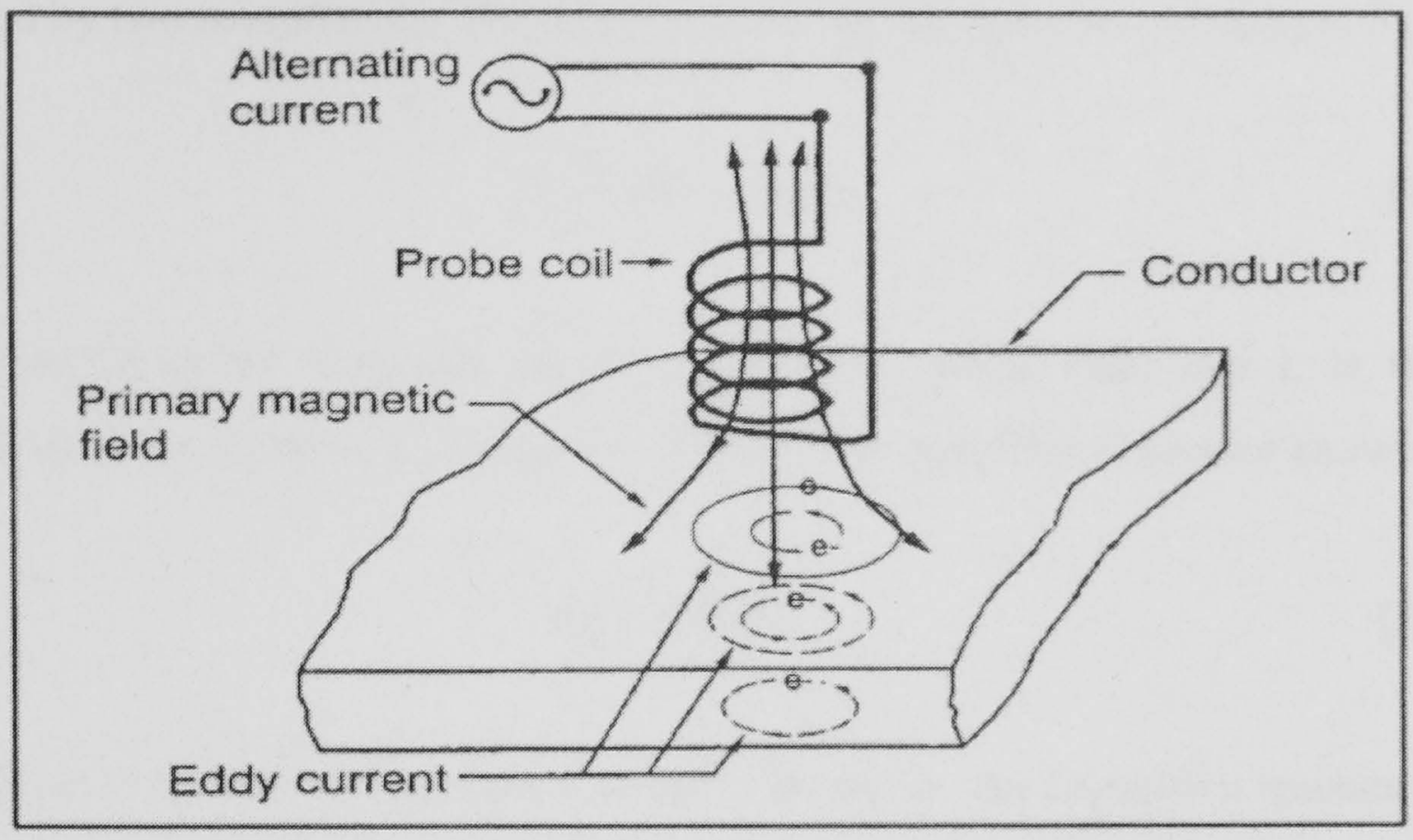


Figure 1 Generating an eddy current [18]

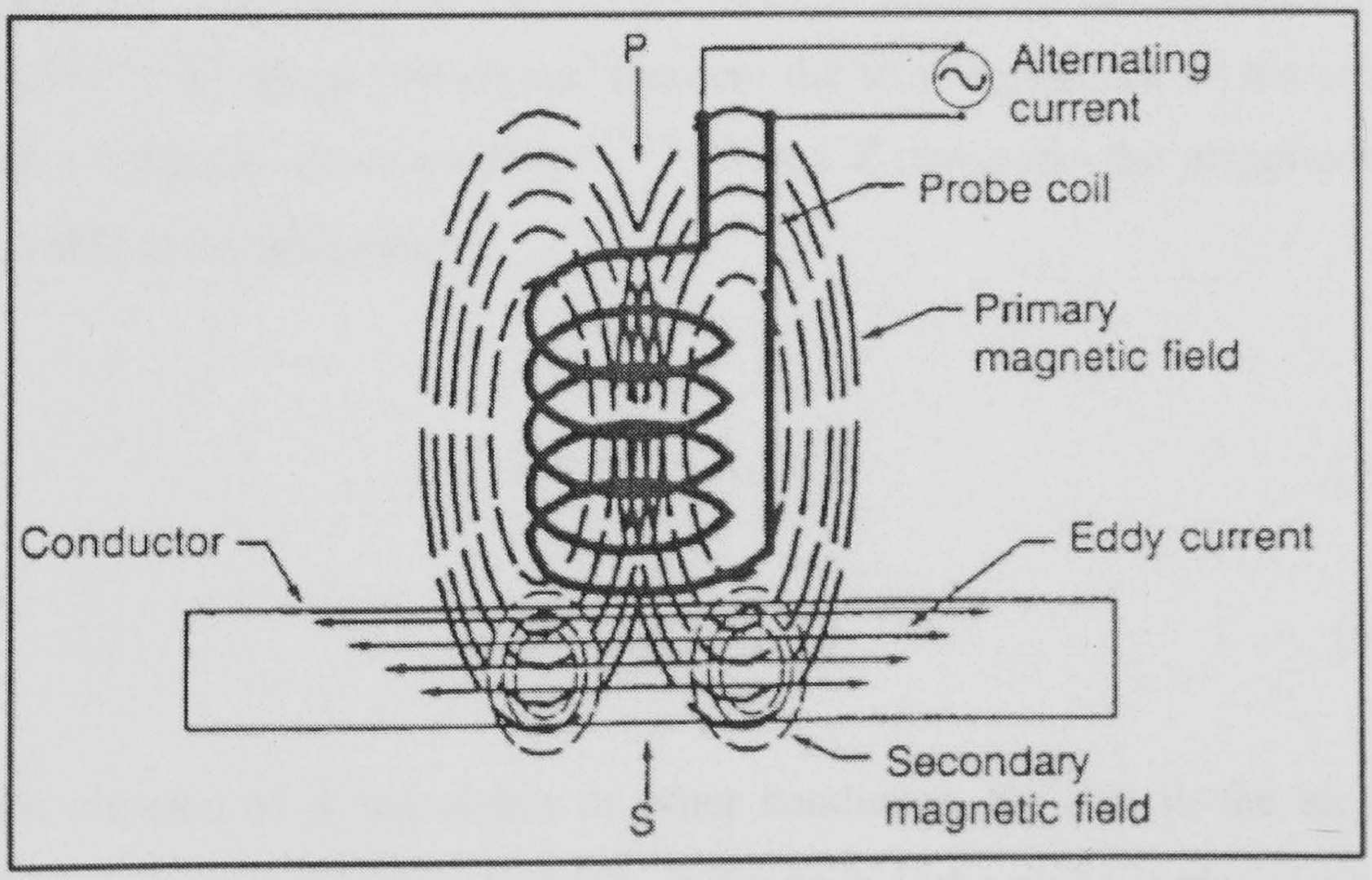


Figure 2 Generation of a secondary magnetic field in the metal [18]

## 2.2 Eddy current impedance plane diagram.

It is known that the electrical behaviour of an eddy current test coil can be represented by two components. The resistance, R, and the inductive reactance, $X_L$.

$$\mathbf{X_L = \omega L = 2\pi f L} \qquad [1]$$

Where $f$ is the frequency of the alternating current (Hz) and L is the self-inductance of the coil (Henry). The test coil also has a capacitive reactance known as $X_C$.

$$\mathbf{X_C = 1/2\pi f C} \qquad [2]$$

Where C is the coil capacitance (Farad). However, the capacitive reactance value is small compared to the inductive reactance. The capacitance of a long cable between the probe and the measuring instrument may be more significant. By convention, the signal of the resistance (R) component of the impedance is drawn on the horizontal X axis. On the other hand, the inductive reactance ($X_L = \omega L$) is drawn on the vertical Y axis as shown in figure 3. By using Pythagoras' theorem the total impedance of the coil (Z) is calculated as a complex vector quantity [15,19]. Where Z represents the magnitude of the impedance and ∅ is the phase angle.

$$\mathbf{Z = (R^2 + X_L^2)^{1/2}} \qquad [3]$$

$$\mathbf{\varnothing = \tan^{-1} (X_L/R)} \qquad [4]$$

In the absence of a test object or other conductor, the coil in the air has the impedance plane diagram shown as point $P_O$ in figure 3. If the probe is placed on the test object or moved close to a specimen, the eddy current changes the impedance Z and phase angle ∅ of the test coil circuit [7,9] such that the apparent impedance will move from $P_O$ to point $P_1$. It corresponds to new values of $X_L$ and R under the influence of the

test object. Eddy current testing is essentially the measurement of this change in impedance.

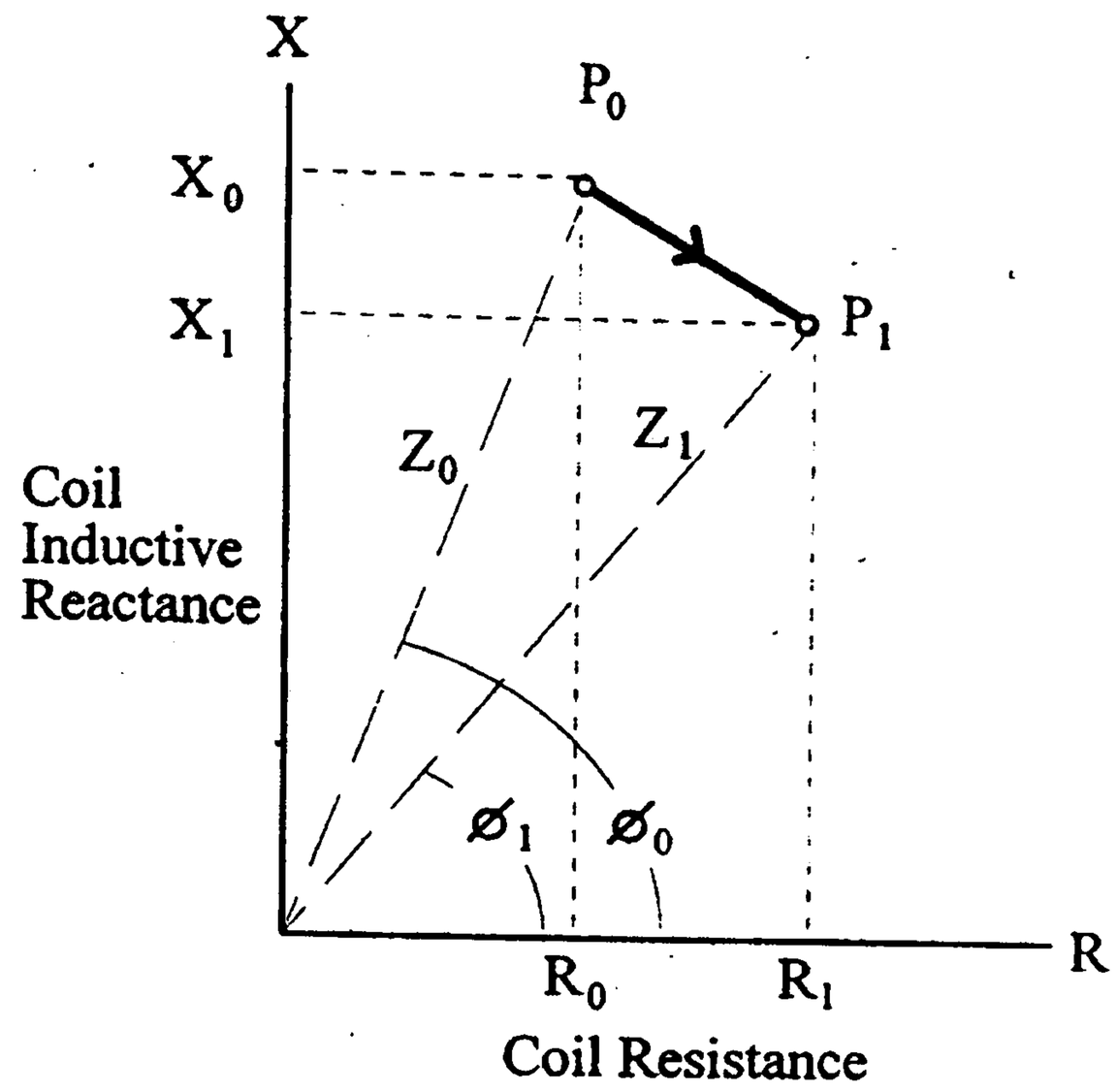


Figure 3 The test coil characteristics on the Impedance Plane Diagram [12].

The presence of flaws within the material plays an important part in eddy current testing as a result of the way the field and coil impedance is affected. Figure 4 shows the impedance vector $Z_O$, observed in air, and the way it moves to $Z_1$ when placed on a metal surface. When discontinuities or surface-breaking defects are present, the crack cuts into the eddy current field and the pattern is distorted, As a result, the spot for the impedance vector Z will be displaced and gives rise to a local increase in signal as the test coil is moved across the discontinuities [10]. The discontinuities that are perpendicular to the plane of the eddy current will have a much stronger effect than those in the plane of the eddy current flow.

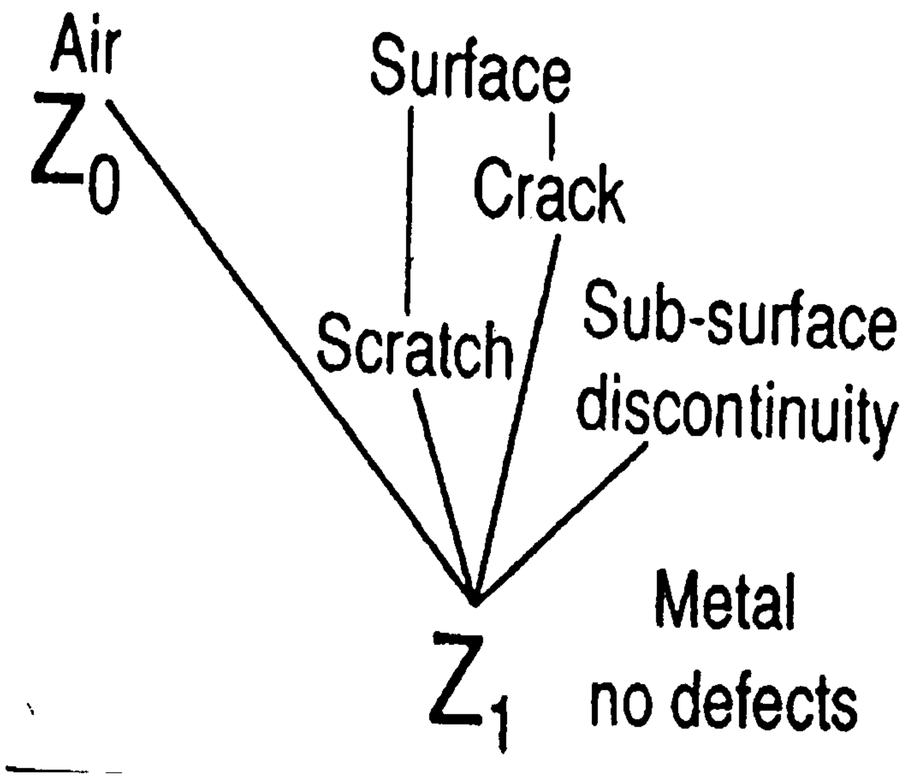


Figure 4 The response from discontinuities on the Impedance Plane Diagram [7].

### 2.3 Effect of magnetic properties of the metal.

The magnitude of eddy current flow is directly affected by the magnetic properties of the test material. These affect how easily the material can be magnetized and how far the magnetic field can penetrate into the material. The strength of the magnetic field is given by the equation below [20-22]

$$B = \mu H \qquad [5]$$

Where B is the magnetic flux density in the material (Webers/$m^2$), $\mu$ is the magnetic (Henrys/m) and H is the magnetizing force or magnetic field strength (Amperes/m). The value of magnetic permeability $\mu$ is directly related to the test medium. In general, for isotropic media, the permeability is given by:

$$\mu = \mu_0 \mu_{rel} \qquad [6]$$

Where $\mu_0$ is permeability of free space ($4\pi \times 10^{-7}$ Henry/meter) and $\mu_{rel}$ is the relative permeability of the medium [15].

For practical purposes, the relative permeability of the air and non-ferromagnetic (nonmagnetic) materials such as aluminium, copper and brass are approximately 1. On the other hand, ferromagnetic (magnetic) materials such as iron, cobalt and nickel have a high relative permeability of several hundred [23,24]. The particular value depends on the nature of the material and localized stress, heating effects, mechanical process etc. Figure 5 shows the impedance plane diagram response for materials of different permeability.

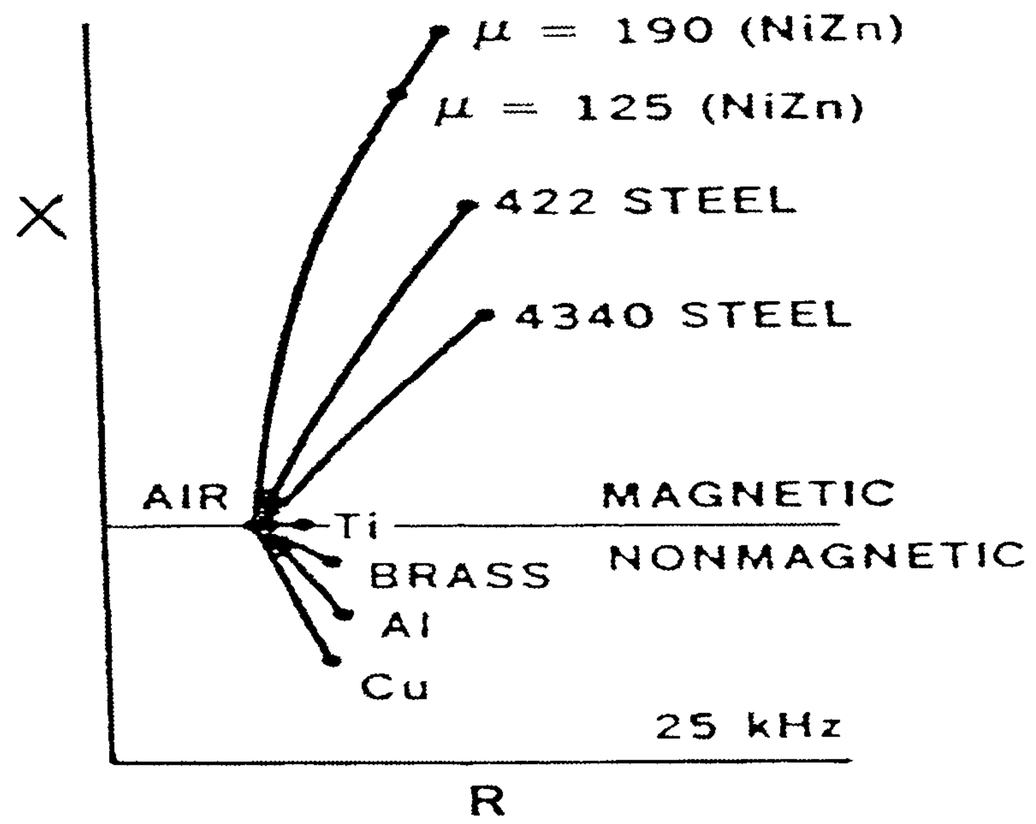


Figure 5 shows the impedance plane diagram response for materials of different permeability [20].

## 2.4 Effect of electrical conductivity of the metal.

The electrical conductivity of a material has a very direct effect on the eddy current flow. The higher the conductivity of a material the greater the flow of eddy current on the surface. The electrical conductivity is a measure of the ability of electrons to flow in a material and a high conductivity results in high eddy current density. Conductivity is frequently given as a percentage of the International Annealed Copper Standard (%IACS). In this system, conductivity of pure, annealed copper at $20^0$C is set to 100% and conductivity of other materials is given as a percentage of that for copper [23].

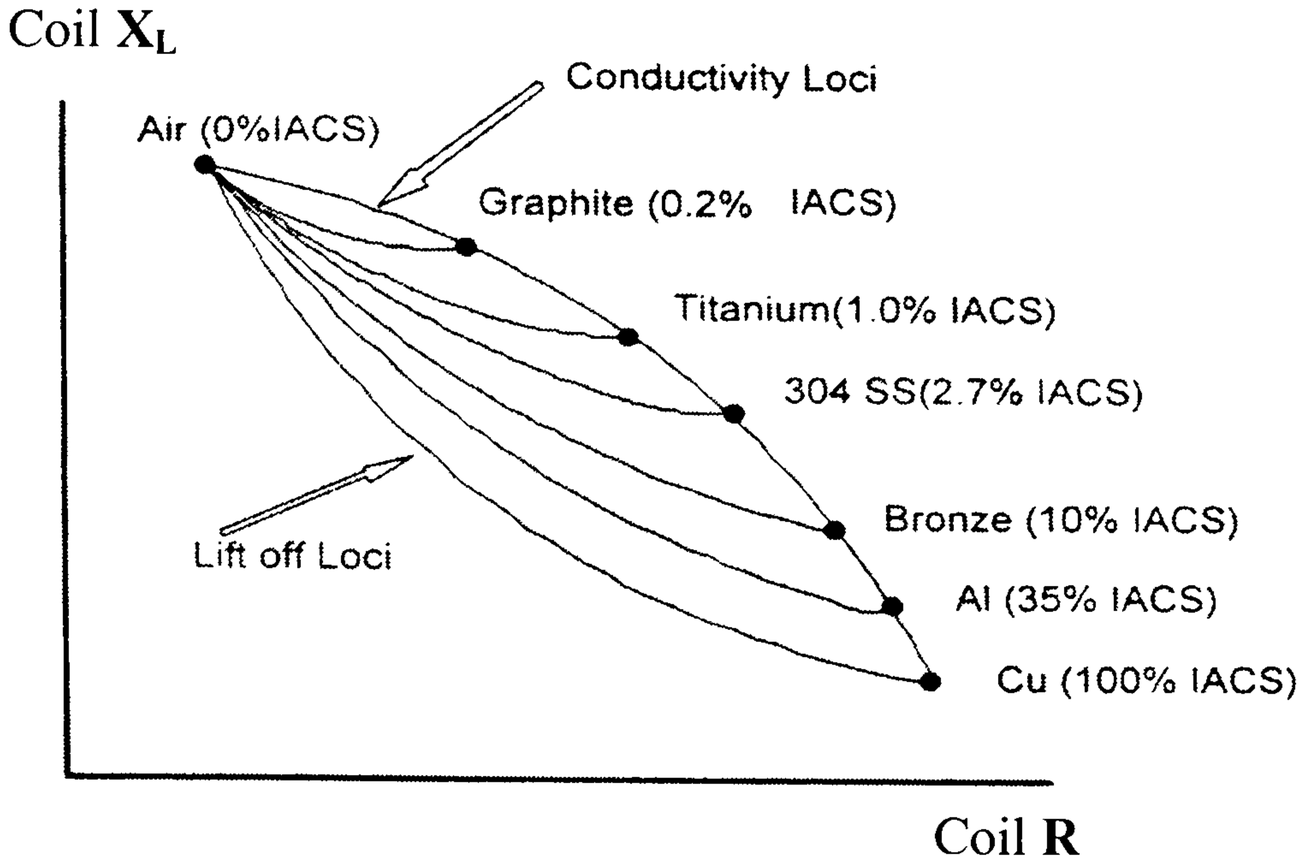


Figure 6 shows the impedance plane diagram response for materials of different conductivity (measured on thin sheet material) [23].

Figure 6 shows how the impedance plane diagram responds to the different conductivities of various materials with a single frequency and a fixed thickness (thin sheet) of specimen. For example, the Cu (100 % IACS) is a material with high electrical conductivity. This leads to strong eddy currents, high back EMF resulting in high coil resistance [13]. Conductivity of a material can be calculated from its resistivity as below;

$$\% \text{ IACS} = K/\rho \qquad [7]$$

Where ρ is resistivity of the material in microhm-centimeter and K is a constant, usually taken to be 172.4 [20,23]. The approximate value of the conductivity of pure (unalloyed) aluminium is then 67 % IACS. There are several different factors which can affect conductivity of the material such as composition, heat treatment, work- hardening and annealing. Table 1 shows the electrical conductivity for aluminium alloys 7XXX series [25].

| Electric conductivity (Percent IACS) | | |
|---|---|---|
| **Alloy and temper** | **Minimum** | **Maximum** |
| 7075-O | 44.0 | 48.0 |
| 7075-T6XX | 30.0 | 35.0 |
| 7075-T73X | 38.0 | 42.5 |
| 7075-T76X | 36.0 | 39.0 |
| 7079-O | 44.0 | 47.0 |
| 7079-T6XX | 30.0 | 35.0 |
| 7178-O | 43.0 | 47.0 |
| 7178-T6XX | 29.0 | 34.0 |
| 7178-T76 | 35.0 | 39.0 |

Table 1 Electrical conductivity ranges for aluminum alloys [15].

## 2.5 Effect of hardness.

The hardness value for high strength aluminium 7075 alloy is changed with heat treatment. Precipitation hardening is used to increase the hardness heat-treatable aluminium alloys. Figure 7 shows the relationship between hardness and heat treatment for high strength aluminium alloys. As can be seen, the hardness of the alloy increases as aging heat treatment increases. This phenomenon has been explained by the work of Hagemaier [3] who stated that small amounts of constituents are present in solid solution for annealed condition. As solution heat treatment (T4), on the other hand, the great amount of the second phase is taken into its microstructure and tends to increase the hardness. Overageing heat treatments, from T6 to T73, condition generally results in decreasing the overall hardness of the material.

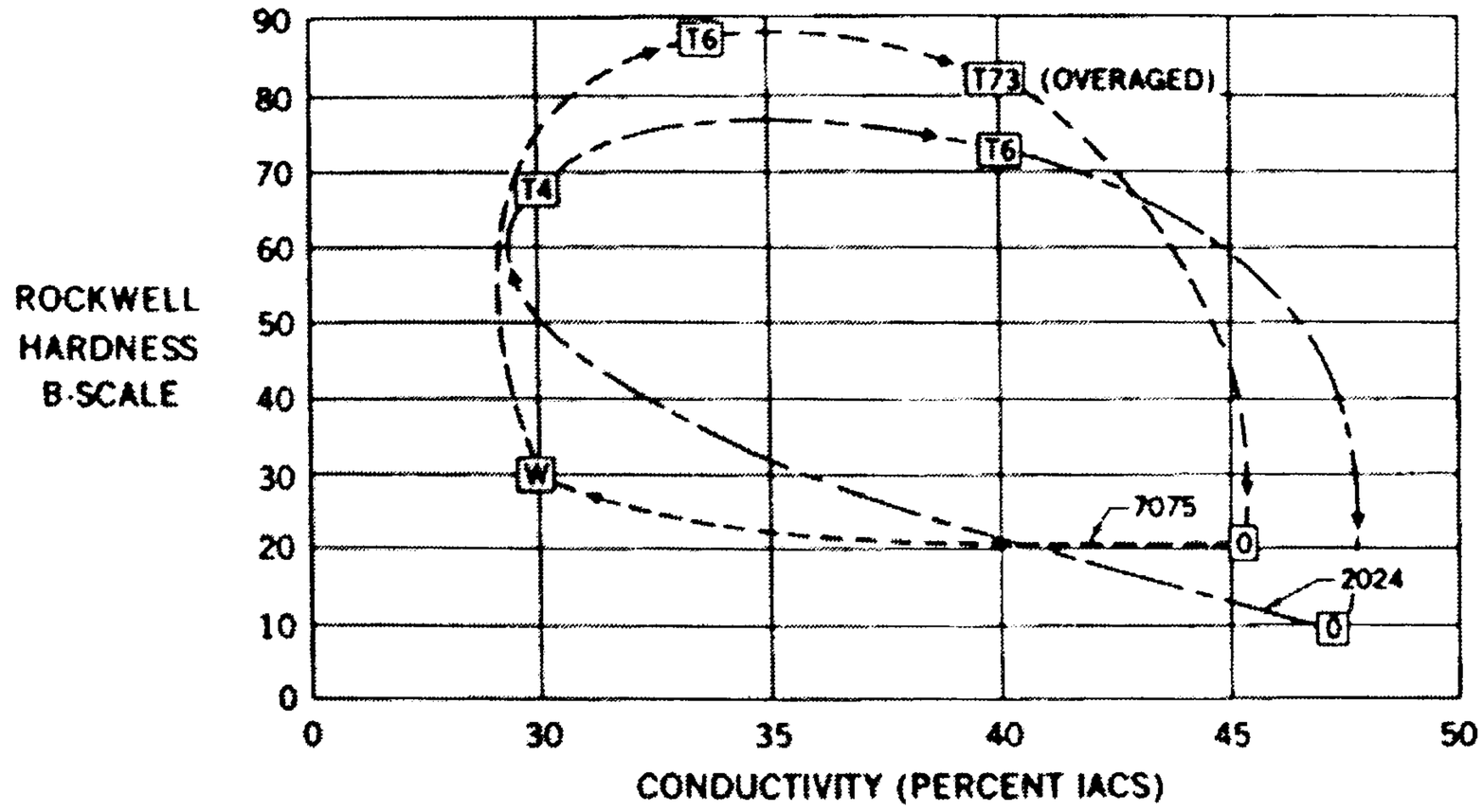


Figure 7 Hardness-heat treatment relationships for high strength aluminium alloys [3].

## 2.6 Effect of frequency selection.

The strength of the eddy currents contribute to the eddy current sensitivity [26]. The skin depth effect causes the eddy currents to attenuate with depth, depending on the material properties and the test frequency. The skin depth, δ, is given by the following equation:

$$\delta = 26/(f\sigma\mu)^{1/2} \qquad [8]$$

Where $f$ is the operating frequency, σ is the conductivity of the material and μ is the relative permeability [27]. The equation shows that skin depth is inversely proportional to the square root of frequency, electrical conductivity and magnetic permeability. The magnetic permeability is 1.0 for nonmagnetic materials, and the conductivity of a particular material is generally a known constant. Therefore, the skin depth is controlled by the operating frequency. These three variables are used to define the Standard Depth of Penetration (also termed skin depth). This is the depth at which the eddy current strength or intensity is reduced to 37 percent of its surface value. Table 2 shows how the current density decreases with each skin depth.

| No. of skin depths into material (δ) | Percentage (%) of surface value |
|---|---|
| 0 | 100.0 |
| 1 | 36.8 |
| 2 | 13.5 |
| 3 | 5.0 |
| 4 | 1.8 |
| 5 | 0.7 |

Table 2 shows change in eddy current density decreases with skin depth.

The sensitivity of crack size measurement depends on the eddy current density at that particular depth. Eddy current density at 3δ below the surface is only 5% of the surface density. This therefore represents the limitation of the detection. In practice it is usual to use eddy currents to detect cracks at a depth less than 3δ, for this reason [26]. Therefore, the standard depth, δ, formula is used as a guideline rather than a true measure of the depth. The standard depth of penetration value or operating frequency can be calculated by using the calibration graph in figure 8.

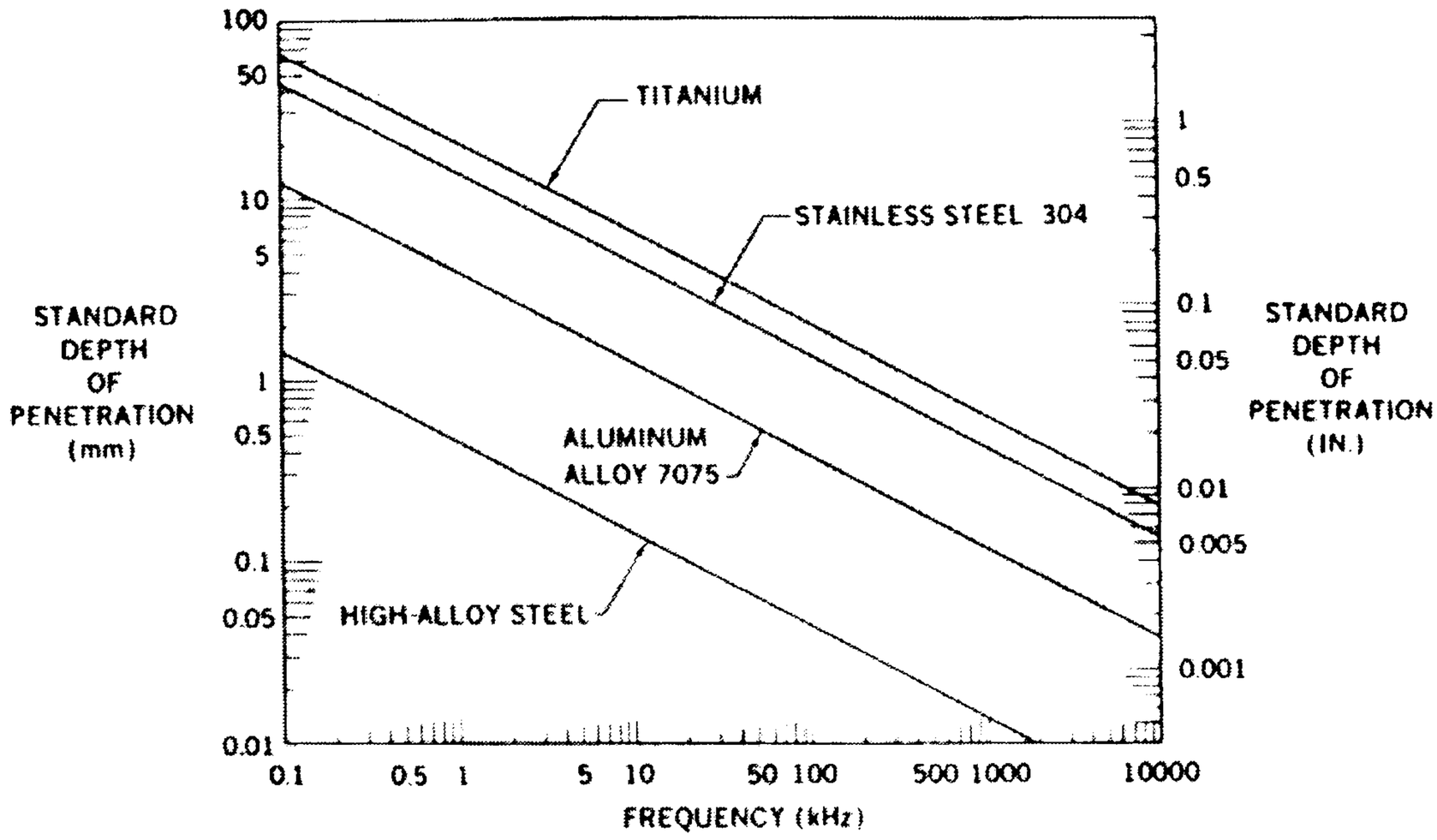


Figure 8 Eddy current standard depths of penetration for various conductivity materials at different frequencies [26].

The general practice in frequency selection is to obtain frequencies which have penetration to the expected defect depth. It should be chosen for good phase separation between defects and lift-off signals. Surface defects can be detected at higher frequencies than subsurface defects. Maximum penetration requires a low frequency, which still permits clear discrimination between lift-off and defect signals. Figure 9 shows the effect of test frequency on the conductivity and liftoff curves for nonmagnetic alloys. As can be seen, changes in frequency shift the point along the curve and also change the separation angle ($\theta$) between the liftoff and conductivity curves. At low frequencies the separation angle is quite small for some metals but by selecting a higher frequency, the separation angle is larger, which allows liftoff suppression and good sensitivity to conductivity variations [20,26,27].

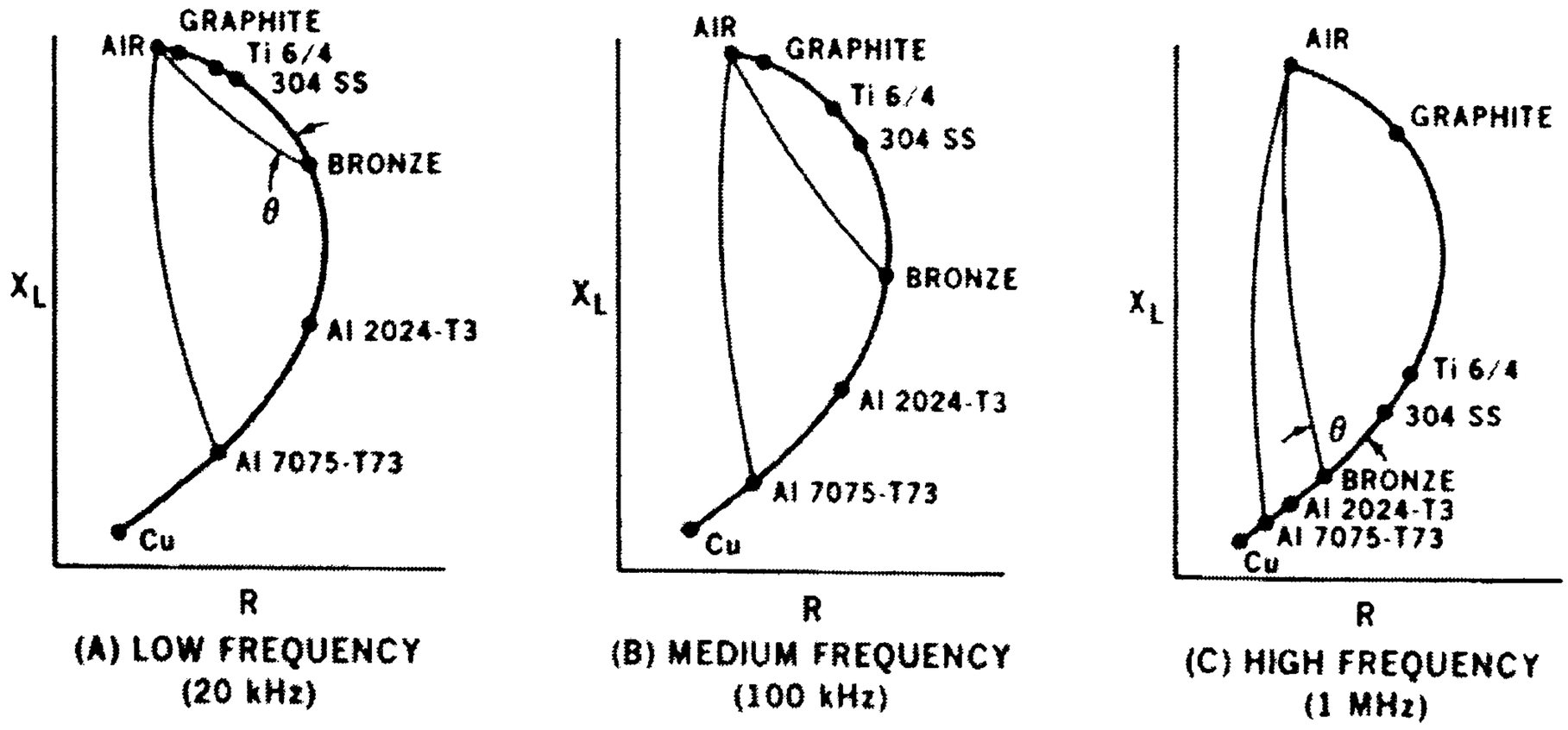


Figure 9 effect of frequency on impedance for different materials (measured on thick materials) [20].

It should be noted that aluminium alloys with their relatively high conductivities remain stable on the curve through a wide range of frequencies, and consequently the separation angles between the liftoff curve and conductivity curve remain similar. This means that good liftoff suppression can be achieved over a wide range of frequencies. These curves appear to be different to Figure 6 as these are for greater specimen thickness.

### 2.7 Phase lag.

Eddy current phase lag refers to a lag in phase between the eddy currents flowing at the surface with those below the surface. Phase lag increases with distance into the material and is given by the equation as below:

$$\beta = x/\delta \qquad [9]$$

Where **x** = Depth below surface and **δ** = skin depth.

At one skin depth, the eddy current flowing below the surface lags the surface currents by 57°. At two skin depth, they lag the surface currents by 114°. Since, the phase lag is a function of skin depth. It is also dependent on test frequency, conductivity and magnetic permeability.

## 2.8 Eddy current inspection for cracks around a hole.

When a structure is subjected to a large number of loading and unloading cycles that are well within its strength, sudden fractures are experienced, even though the stress never exceeds the material strength at any point and this type of failure is known as fatigue [28]. Fatigue begins with microscopic defects which grow in the presence of an intense stress or strain field. These concentrations usually occur in areas of sudden discontinuities, such as holes or notches, within a structure. Work carried out by Cooper et al [29] looked at the causes for cracks propagating from a fastener hole. They concluded that the structures suffered due to the effects of manufacturing holes and assembly as shown in figure 10.

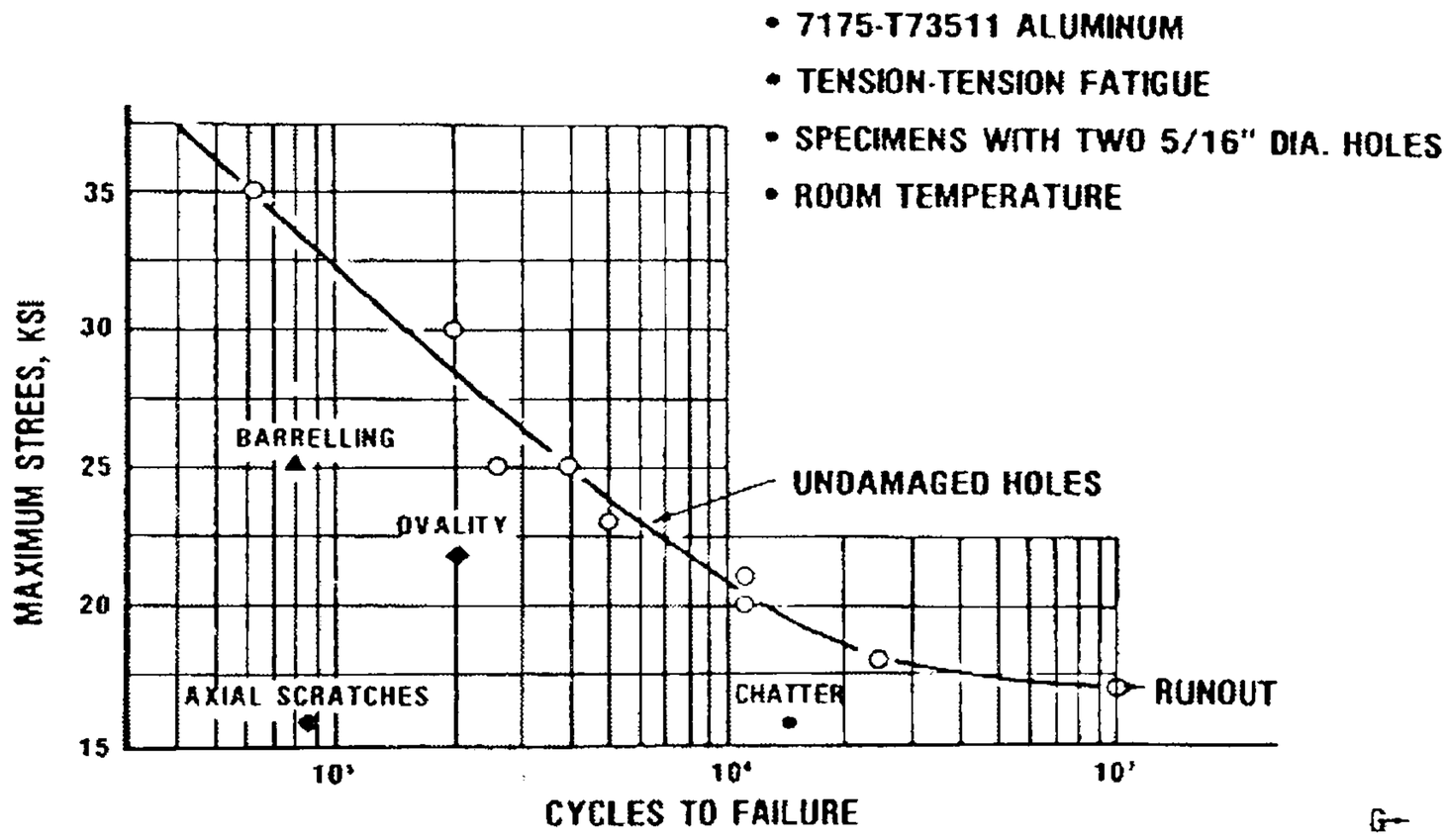


Figure 10 Hole quality affects fatigue life [29].

In contrast, stress corrosion cracking is caused by the simultaneous effects of both stress and a corrosive environment. The stress can be either an applied stress or one resulting from preloading the part during installation. High strength aluminium alloys such as 7075 are often highly susceptible to stress corrosion cracking when in the T6 condition, especially when a tensile stress is applied to the short transverse grain direction [15]. This intergranular corrosion is an attack on the grain boundaries of the material. This is because the stress is applied perpendicular to the grain boundaries and the grain centre can react with the grain boundary as anode and cathode. Rapid selective corrosion at the

grain boundary can occur with delamination [5]. This type of corrosion usually occurs in thick aluminium alloy plate around the fastener holes. Figure 11 shows the galvanic corrosion that can occur in the fastener hole.

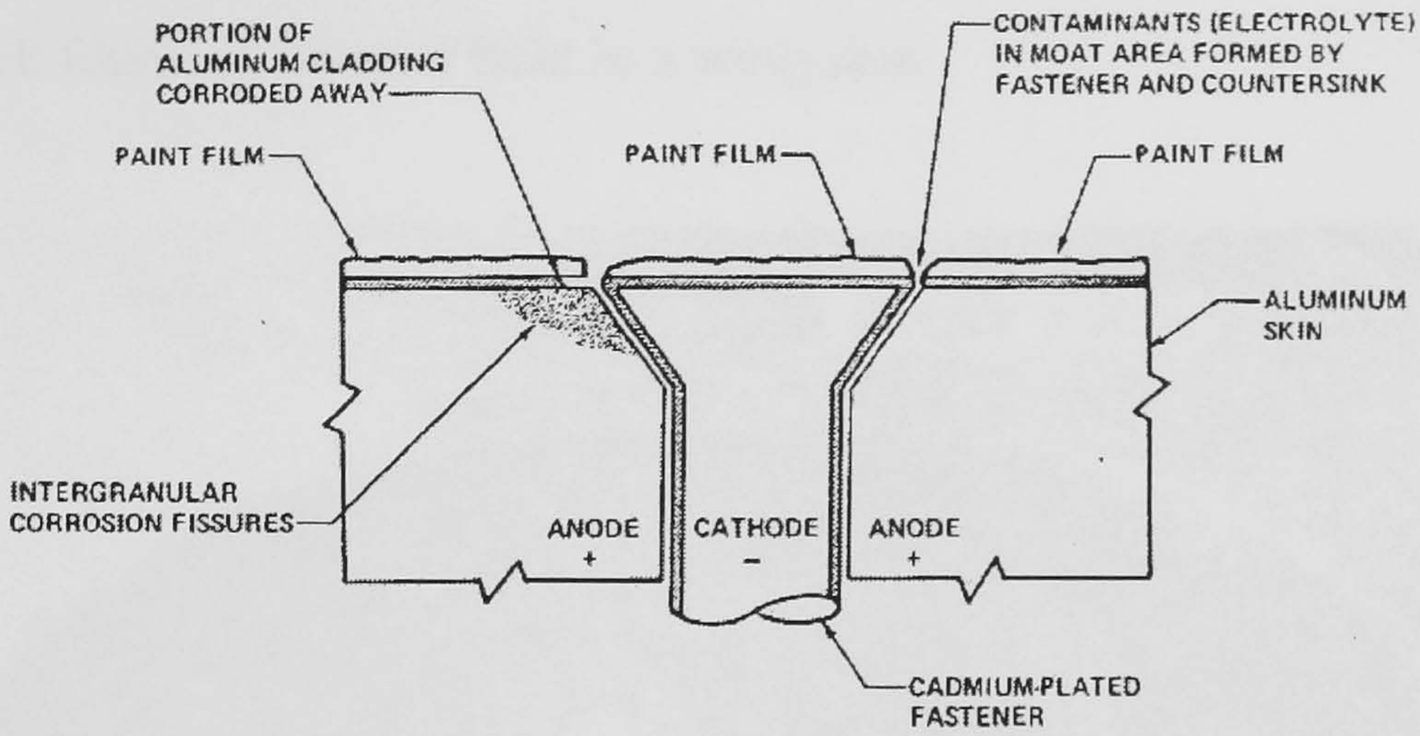


Figure 11 show schematic diagram to the galvanic corrosion occurring in a fastener hole [5].

Nondestructive testing techniques are widely used in many industrial applications, both during initial component manufacture and throughout service life. There are six main NDT techniques available. These techniques can be used separately or combined, as they compliment each other. There are advantages and disadvantages associated with each technique [7,10]. When relatively large cracks can be tolerated in a structure and where access problems exist, X-ray radiography can be used. Ultrasonic can detect smaller cracks than X-ray radiography, even with fasteners installed, but sensitivity and reliability are problems due to the poor surface finish of the holes or tight cracks. Penetrants perform poorly because of the tight cracks or smeared metal that sometimes covers cracks. At present, eddy currents are the only practical method for reliably detecting small, tight cracks around the holes [30]. In the aircraft industry, this technique is used to inspect for heat damage in materials by measuring changes in conductivity [3].

The aluminium alloy 7XXX series is a common material in the aircraft industry, especially in fuselage and wing skin areas. It is known that aluminium aircraft fuselage skins can develop small cracks after an extended period of service due to the numerous

pressurization [31] cycles during landing and take off. The fastener holes, being exposed to large forces, moisture and changing temperatures, can cause small cracks and corrosion. These situations may provide a high stress concentration for fatigue cracks and stress corrosion cracks generated along a particular row of fastener holes [31]. Figure 12 shows a typical fatigue crack found in fastener hole in a wing skin.

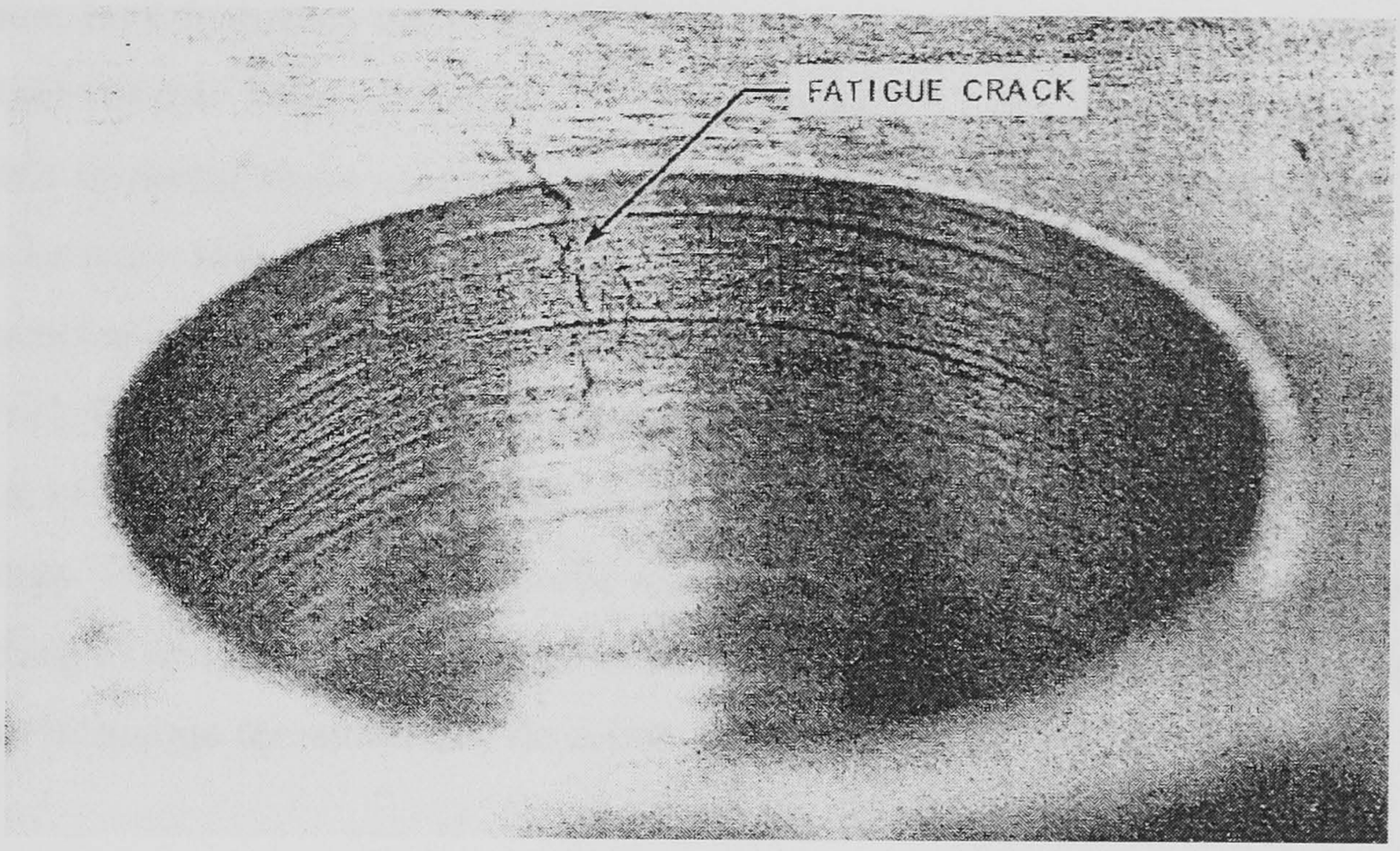


Figure 12 shows typical fatigue crack found in fastener hole of a wing skin [30].

The inner surface of the hole is one of the critical areas which can be effectively inspected by eddy current techniques. Many high frequency eddy current inspection techniques have been developed to detect surface cracks around the holes. Chapman et al [32] have used the frequency of 660 kHz eddy current to detect low cycle fatigue cracks occurring in stainless steel fastener bolt holes of aircraft engine components. They claimed that it was possible to indicate the presence of service-induced fatigue cracks as small as 0.05 mm deep in the bolt holes. Haywood [33] introduced a system which was designed to improve the reliability of bore-hole inspection. The system called the Rotoscan comprises a portable micro-computer interfaced to a test frequency of 500 kHz commercial eddy current test set. The inspection was performed on aluminium bar which has a smooth hole of the same diameter as the probe. The data display may be chosen as a

false colour contour plot or a cross-section through the data corresponding to a depth along the hole. The result can make a comparison between the magnitudes of the test signal to indicate the presence of a crack.

Although eddy current techniques are mostly used for the detection of surface defects, they have the capability of detecting some subsurface defects located close to the metal surface. Low frequency eddy current technique has been used to detect subsurface cracks around fastener holes. Hagemaier [34] and Steinberg [35] developed low frequency eddy currents to detect stress corrosion cracks in the forward section of the wing. The fatigue cracks were also detected in the window panels. The inspection was performed using frequencies of 100 Hz to 5 kHz with the probe placed over each fastener head. In the other work, Hagemaier et al [36,37] demonstrated the use of low frequency eddy current for detection of subsurface fatigue cracks, due to high stress concentration area, in copper alloy bushings. They used a bolt-hole probe with the frequency of 1 to 2 kHz to penetrate copper bushing in wing skin areas. Figure 13 shows the applications of the low frequency eddy current technique for subsurface detection.

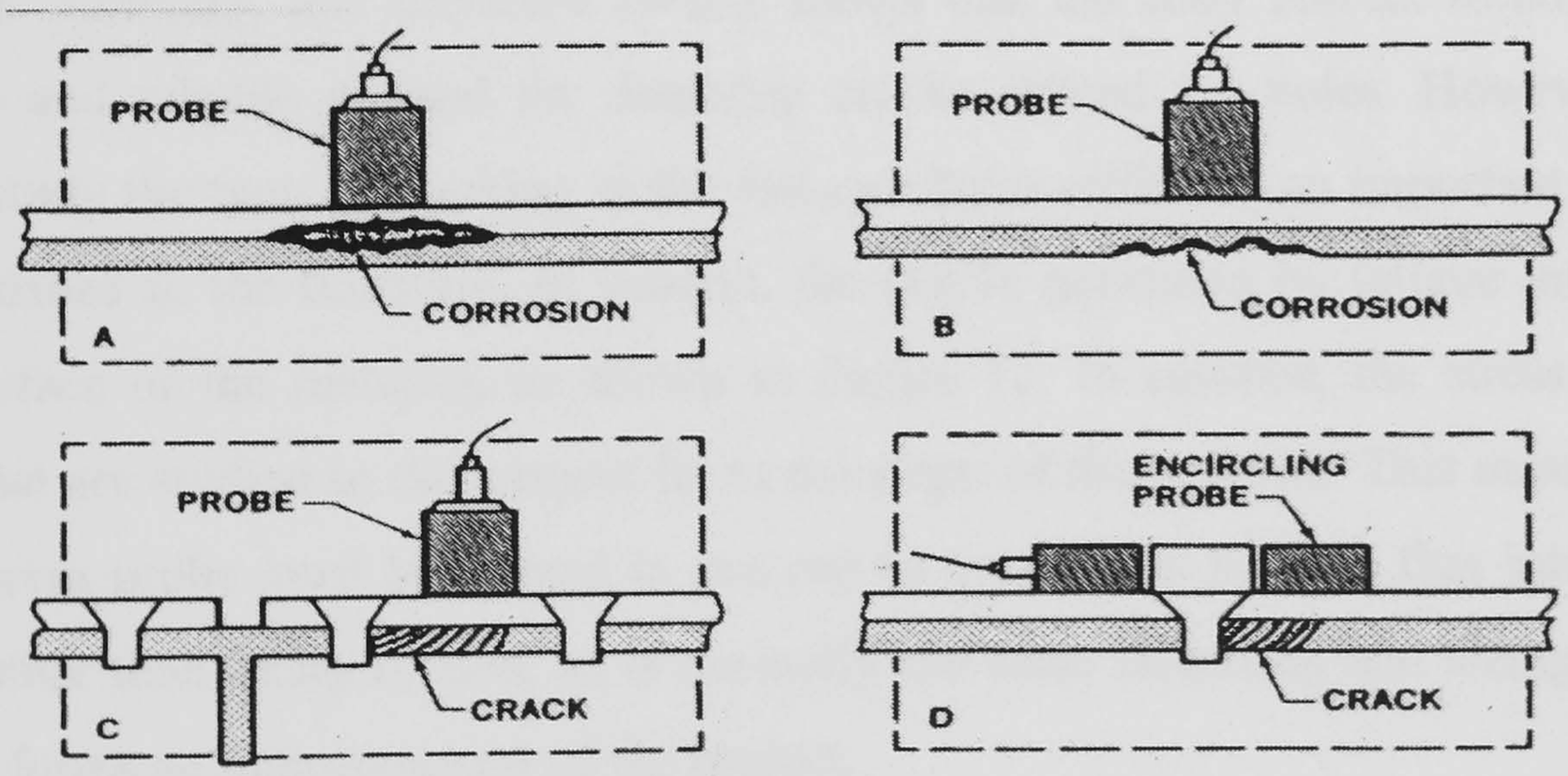


Figure 13 The low frequency eddy current technique for subsurface detection [35].

Hagemaier and Steinberg [35] at the Douglas Aircraft Company have shown that low frequency eddy current testing can detect subsurface cracks in aluminium aircraft structures. They demonstrated a 5 kHz low frequency eddy current technique for detection in skin cracks (second layer) initiated at fastener holes. Their experiments were

performed on aluminium fastener holes with different types of cracks, such as skin cracks, internal skin cracks and corner cracks. Figure 14 shows a typical example of a surface crack and its responses on the impedance plane, as obtained using an absolute probe.

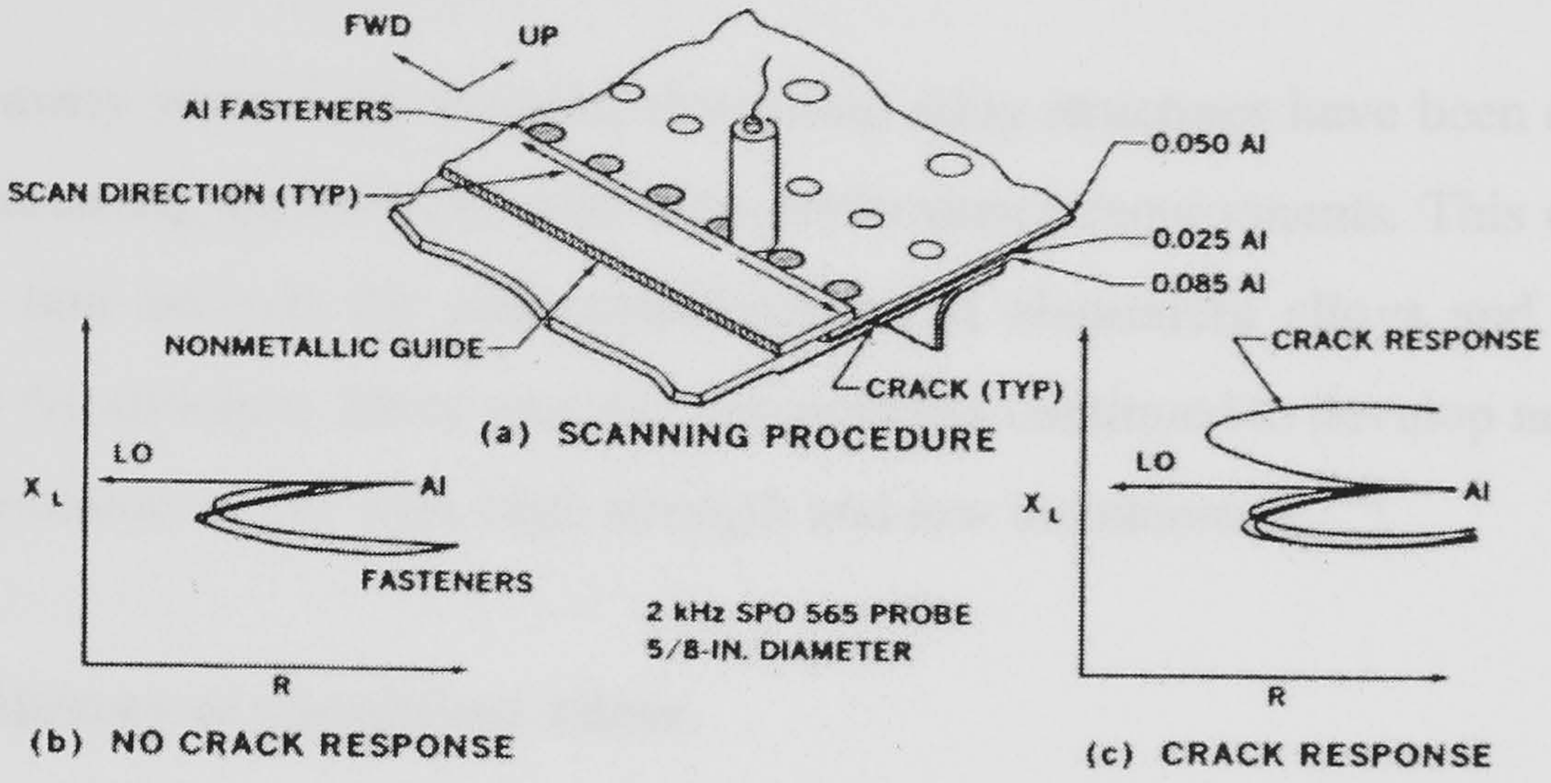


Figure 14 Detection of cracks in the second layer by scanning over aluminium fastener holes [27].

In summary, this literature clearly shows that the eddy current technique is an effective and reliable method for detecting cracks around the holes. However, in the present study the type of cracking in the fastener holes differs in an important way from that described in the literature. In general, the cracks generated by fatigue intersect the outer surface of the material, as shown in Figure 12. In contrast, the stress corrosion cracks that are studied in this project lie in the plane of the material. This means that the eddy current probe must be moved in and out of the hole so that the flux intersects the crack, rather than being rotated, as is normally the case. Detecting and sizing cracks in this way forms an important part of the project.

## 3.0 Aluminium Alloys.

Aluminium alloys have become the most widely used material in the transport, building and packing industries and the aluminium industry is now second in importance to the steel industry. This is due to the fact that aluminium alloys can have high strength,

hardened with alloying elements, the ability to be recycled, to be easily formed and to be very good for specific strength. These advantages of the aluminium alloys have made them popular to meet specific product requirements [38]. The most significant research and development programmes for aluminium alloys are to continue to improve their strength to weight ratio and corrosion resistance.

For many years, high strength aluminium alloy structures have been designed for general engineering applications with high performance requirements. This design work has to take into account the cost considerations of aluminium alloys and the damage tolerance of the structure. More recently, research has continued to develop new materials with a combination of low cost, high strength and low maintenance [39].

### 3.1 History of aluminium alloys.

In 1809, an oxide of aluminium was found in England by Sir Humphry Davy from a naturally occurring chemical compound called alum. In the same year, he named this new metal as aluminum. Ten years later, P. Berthier discovered a reddish and clay-like material, containing aluminium oxide, known as bauxite or aluminium oxide ore. Many scientists believed that pure aluminium could be isolated from bauxite and work began try to isolate it. Between 1821-1825, Hans Christian Oersted and Friedrich Wőhler obtained a small amount of aluminium metal and powder by the reduction of aluminum chloride with potassium amalgam. However, this was found to be a very expensive process. It was not until 1854 that aluminium was produced by Saint-Claire Deville but it proved to be more expensive than gold and platinum. A bar of aluminium was first exhibited to the public at the Paris Exhibition in 1855. During that time, there were increases in demands for aluminium in military applications [40].

Thirty years later, Hamilton Y. Cassner improved on Deville's process to develop a cheaper method to reduce the cost of aluminium production. Nevertheless, aluminium was still a very costly to produce. In 1886, two scientists named Charles Martin Hall and Paul L T Heroult, working separately, discovered the same basic process for producing

economic aluminium. Today, this process is known as the Hall-Heroult, process which remains as the basis for all aluminium production and is still used throughout the world. They discovered an electrolysis process in which aluminium oxide is dissolved in molten cryolite ($Na_3AlF_6$) and a high electric current is passed through the system. Later in 1888, Karl J. Bayer proposed a patent of aluminium production from bauxite, generally known as the Bayer process. Aluminium was produced in larger quantities, leading to lower aluminium prices. In the same year the price had fallen down between $US 1 and $US 2 per kilogram. The combined methods of the Hall-Heroult process and Bayer process have replaced the Deville/Cassner process and remain the basis of aluminium production today [40-42].

### 3.2 Aluminium alloys identification systems.

Aluminium alloys can be divided into two groups namely wrought alloys and cast alloys. Wrought alloys can be subdivided into two further groups; the first group can be hardened and strengthened by only mechanical working and the other by heat treatment [43]. Wrought alloys are normally designated into numbered series according to their main alloying elements. The system was developed by the Aluminium Association and it is called the International Alloy Designation System [44] (IADS). The first digit indicates the alloy group or major alloy addition. The second digit indicates modifications of the original alloy and the last two digits indicate the specific aluminium alloy, as shown in Table 3.

| Groups | Alloy series | Principle alloying elements |
|---|---|---|
| Non-heat treatable wrought alloys | 1XXX Series | 99.00 % pure aluminium |
| | 3XXX Series | 1.5 % Manganese |
| | 4XXX Series | 12 % Silicon |
| | 5XXX Series | 5 % Magnesium |
| | 9XXX Series | Limited use |
| Heat treatable wrought alloys | 2XXX Series | 5 % Copper |
| | 6XXX Series | 1 % Copper (Mg, Si added) |
| | 7XXX Series | 3-5 % Zinc, 1-3 % Mg, 0-2 % Cu |
| | 8XXX series | Other elements |

Table 3 Aluminium alloy designations for wrought alloys [44].

The cast aluminium alloys contain up to 13% silicon, with a melting point at $575^0$C. Magnesium, manganese and copper are added with a corresponding reduction in the silicon content. The addition of copper and magnesium reduces the corrosion resistance and allow the alloys to be heat treated to increase strength [45].

### 3.3 Temper Designation System.

The wrought aluminium alloys gain their optimum properties through a process of mechanical or thermal treatment. Generally, the temper designation consists of a capital letter indicating fabrication treatments. Table 4 shows the basic tempers for wrought aluminium alloys.

| Letter | Treatment |
|---|---|
| **F** | As fabricated - Applies to products of a shaping process with no special control over thermal or strain hardening conditions. |
| **O** | Annealed – Applies to products of a shaping process which have been heated to produce the lowest strength condition to increase ductility and toughness. |
| **H** | Strain hardened – Applies to products that are strengthened through cold-working (non-heat treatable). The strain hardening may be followed by supplementary thermal treatment to achieve stabilization in strength level. |
| **W** | Solution heat-treated – Applies only to alloys that age naturally and spontaneously at room temperature after solution heat-treatment. |
| **T** | Thermally treated - To produce stable tempers other than F, O, or H. Applies for heat-treated alloys. |

Table 4 The basic tempers for wrought aluminium alloys [46,47].

Further to the basic temper designation, there is a T temper subdivision for heat treated alloys. Subdivisions of the temper are indicated by one or more digits following the temper. The first digit after T always indicates the basic type of treatment. The other digits may be added to identify specific practices. The temper designation system applied to aluminium alloys is shown in Table 5.

| T temper | Heat treatment |
|---|---|
| **T1** | Naturally aged after cooling from an elevated temperature. |
| **T2** | Cold worked after cooling from an elevated temperature and then naturally aged. |
| **T3** | Solution heat-treated, cold worked and naturally aged. |
| **T4** | Solution heat treated and naturally aged. |
| **T5** | Artificially aged after cooling from an elevated temperature. |
| **T6** | Solution heat-treated and artificially aged. |
| **T7** | Solution heat-treated and stabilized (overaged). |
| **T8** | Solution heat-treated, cold worked and artificially aged. |
| **T9** | Solution heat treated, artificially aged and cold worked. |

Table 5 Subdivisions of the tempers for wrought aluminium alloys [46,47].

### 3.4 Development of 7XXX Series aluminium alloys.

The high strength aluminium alloys, such as 2XXX and 7XXX series, have been the most dominant alloys since the early sixties. These alloys are widely used in the military and aerospace industries [48]. This is due to the strength to weight ratio of the alloys. The strength of the heat treatable alloys is obtained from precipitation in the grain matrix and along the grain boundary. However, as a result of this precipitation strengthening the products from 7XXX series such as sheet, plate and extrusions are susceptible to stress corrosion cracking [49].

During World War II, the early aluminum alloys 7XXX series alloys were developed when scientists discovered the combination of Zn and Mg to aluminium alloys gave higher strength compared to 2XXX alloys. This idea leads German scientists to develop a new ternary Al-Zn-Mg alloy with exceptionally high strength properties. However, these alloys were found to have low resistance to corrosion. This problem was

solved in 1940 when the first commercial product of 7075 alloy was developed. After the war, the high strength 7178-T6 was developed for use in the commercial airplane Boeing 707. These alloys were made by adding higher percentage of zinc, magnesium and copper. These alloys have become widely used materials in both commercial and military aircraft [50]. The design approaches were mainly driven by the demand for improved strength rather than attention to corrosion. Unfortunately, the improved strength was accompanied by problems with durability and damage tolerance and 7178-T6 was not selected for the development of Boeing 747 aircraft. The same problem happened to 7079-T6 from Germany [51], and after long times in service, these alloys developed severe stress corrosion cracking. Aircraft designers also require high resistance to exfoliation corrosion. It was found that the conventional 7XXX alloys in T6 condition are highly susceptible to stress corrosion cracking and exfoliation corrosion, particularly in the short transverse direction. An effort was made over the years to control this problem.

As a result, the 7XXX alloys in the overaged condition, 7075 T73 and T76 were developed to solve the problem of stress corrosion cracking and exfoliation. This led to the successful development of Douglas DC10 and Lockheed L1011 aircraft. However, the scientists realized that the yield strength of 7XXX alloys in overaged, T73 and T76 condition, being reduced by 15% compared to the peak aged condition T6 [52]. As a result, the intermediate condition T74 has been developed to provide the strength of T6 condition. It is also resistant to corrosion. The fracture toughness of the aluminium alloys is also critical. In the late 1960s, designers needed aluminium alloys having the combination of strength and fracture toughness. It became mandatory for aircraft designers to deliver higher strength and for fatigue cracks to be detected before reaching the critical crack length. Although, the aluminium 7XXX series alloys were not completely successful, the aircraft designers still continued to use these alloys for aircraft structures[53].

The period 1960-70 saw the development of improvements in the short transverse ductility of 7079-T6 in thick section. There was also need for alloy with improvement in exfoliation corrosion resistance. Alloy 7075-T4 was developed to fill the need and also

several alloys such as 7049, 7050, 7175 and 7475. These alloys have been developed to give high strength in thick section material and a good resistance to stress corrosion cracking and exfoliation as well as good fracture toughness characteristics. In addition, the Cu content in alloy 7050 was increased and a slight modification in Zn/Mg ratio, which improved strength and corrosion resistance. It was about the same time, 7150-T77, which is a modification of 7075, was developed to provide corrosion resistance and obtain the strength equivalent to the peak strength, to save weight [51,53]. Today, aircraft manufacturer generally prefer 7XXX series aluminium alloys for the upper wing, body skin, floor and others. This is due to most of those structures being exposed to external air in compression [50]. The use of 7XXX series alloys, such as 7010, 7055, 7075 and 7150, in the airframes of Boeing 757, 767 and 777 aircraft is shown in Figure 15. All these 7XXX series alloys are in the overaged T7 temper condition, which provides the best resistance to stress corrosion cracking and exfoliation corrosion.

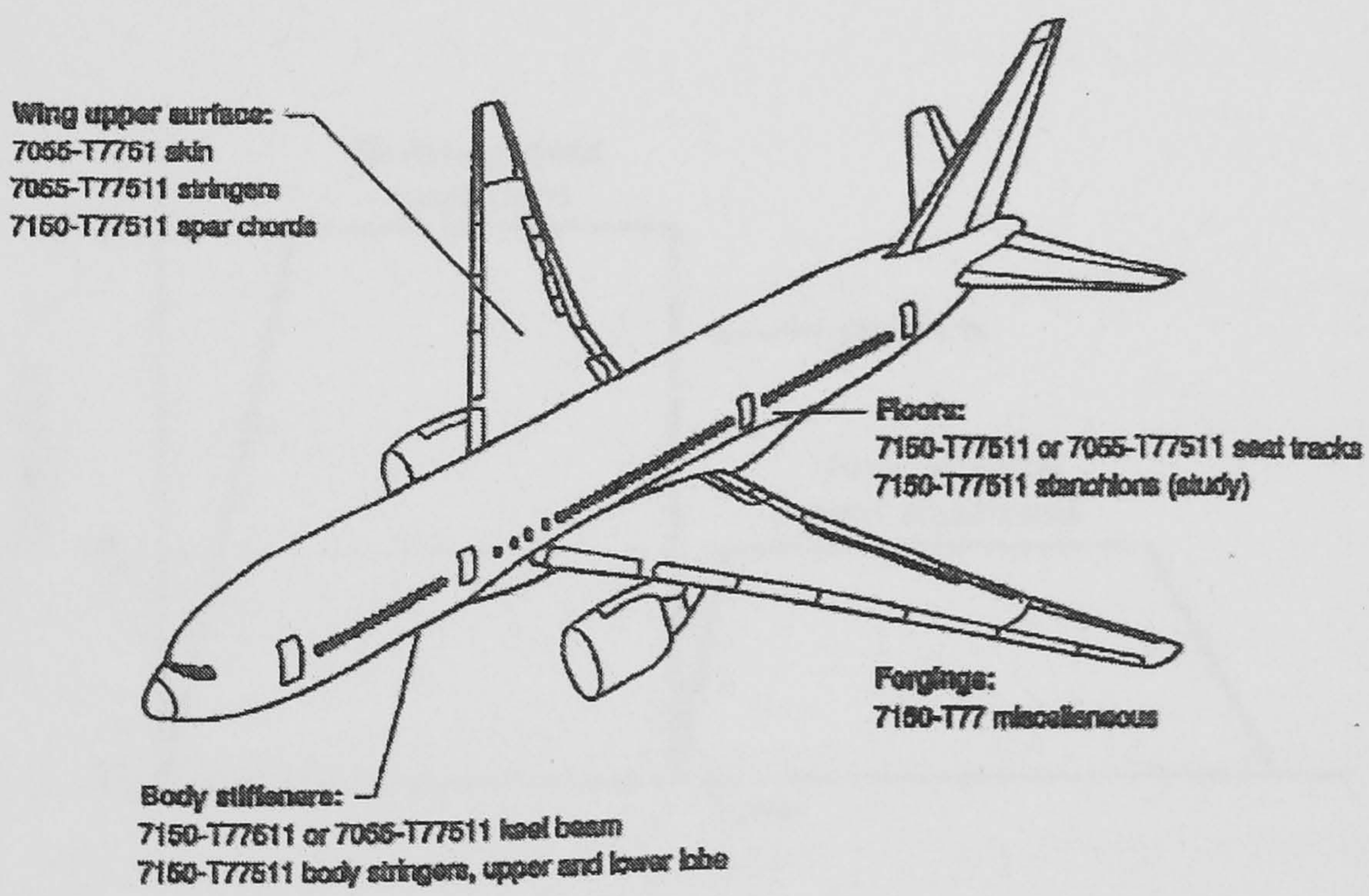


Figure 15 shows the 7XXX series aluminium alloys used in commercial transport aircraft airframes [51].

### 3.5 Microstructure of 7XXX Series alloys.

The 7XXX series alloys are based on the main alloying element of Zn with additional alloying elements of Mg and Cu together with small amounts of elements such as chromium, manganese, silicon and zirconium. The alloys from this group are heat treatable and form various precipitates within the matrix of the aluminium. This heat treatment is known as precipitation hardening or age hardening [46,52,54]. These alloys have improved mechanical properties, such as tensile strength and fracture toughness.

Precipitation hardening provides one of the most widely used mechanisms for strengthening of alloys. The first part is a solution heat treatment in which all the solute atoms, such as copper, magnesium, silicon or zinc are dissolved to form a single phase solid solution at a particular temperature, $T_0$; approximately 465 $^0$C [46], as shown in Figure 16.

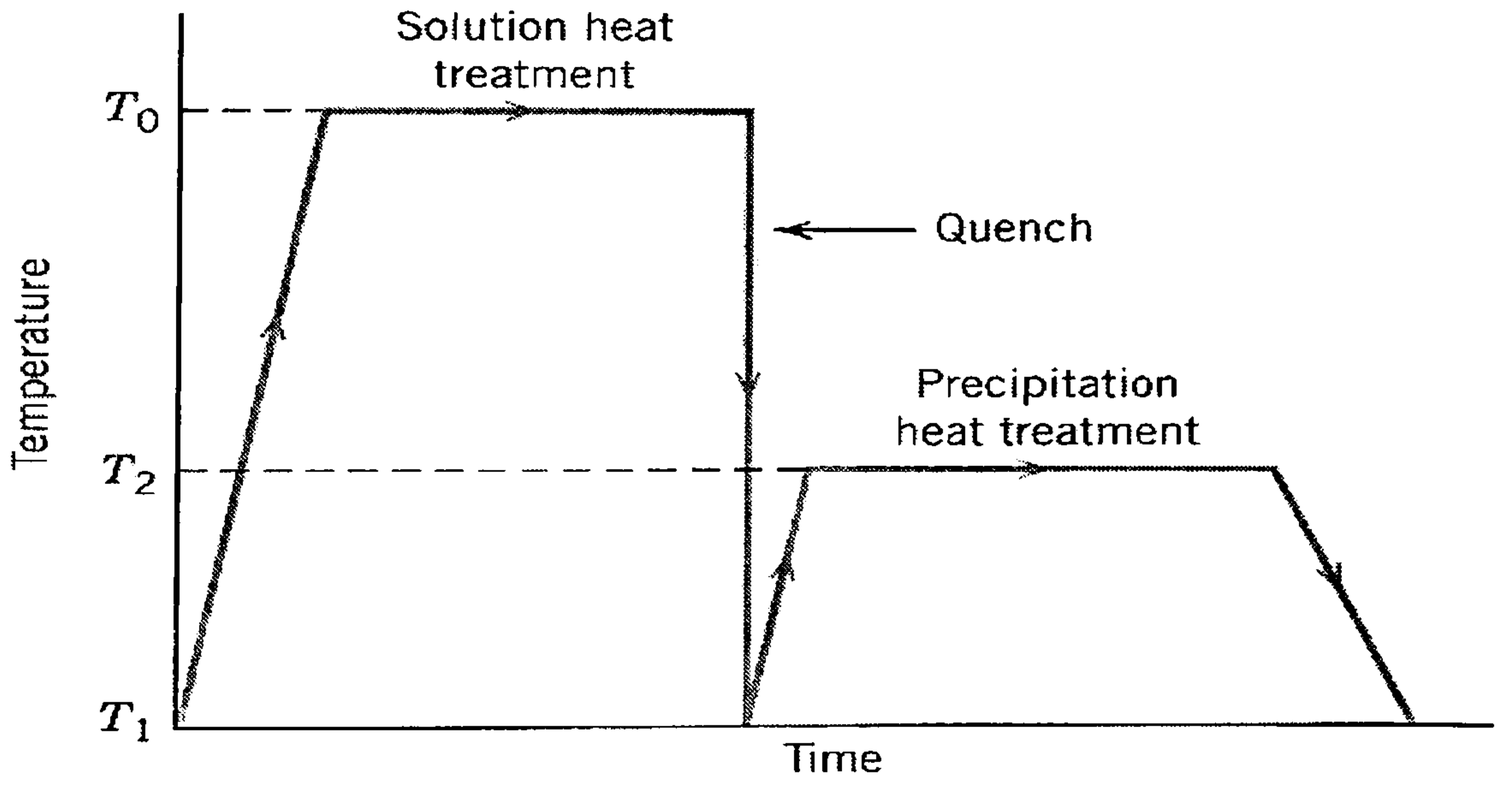


Figure 16 Schematic diagram of solution and precipitation heat treatment for aluminium alloys [55].

The next step is quenching the material. This is achieved by rapid cooling of the alloy to near room temperature. This process is to produce a supersaturated solid solution of the alloying elements in α (aluminium) phase. For the final step, the supersaturated

solid solution is heated to temperature, $T_2$, in between 120 and 135 $^0$C [46,56]. Upon ageing, the precipitates begin to form as finely dispersed particles and the material is then allowed to cool to room temperature. For Al-Cu, several transition aluminium phases are formed in specific sequence. The generally accepted sequence from a supersaturated solid solution (Al-Cu) is as follows, via Guinier Preston zones (GP zones) → Θ" → Θ' → Θ, $CuAl_2$, at the temperature below 190 $^0$C, [52,55,57] as shown in figure 17. Figure 17 shows the development of supersaturated solid solution to the equilibrium Θ phase. This is known as the precipitation heat treatment.

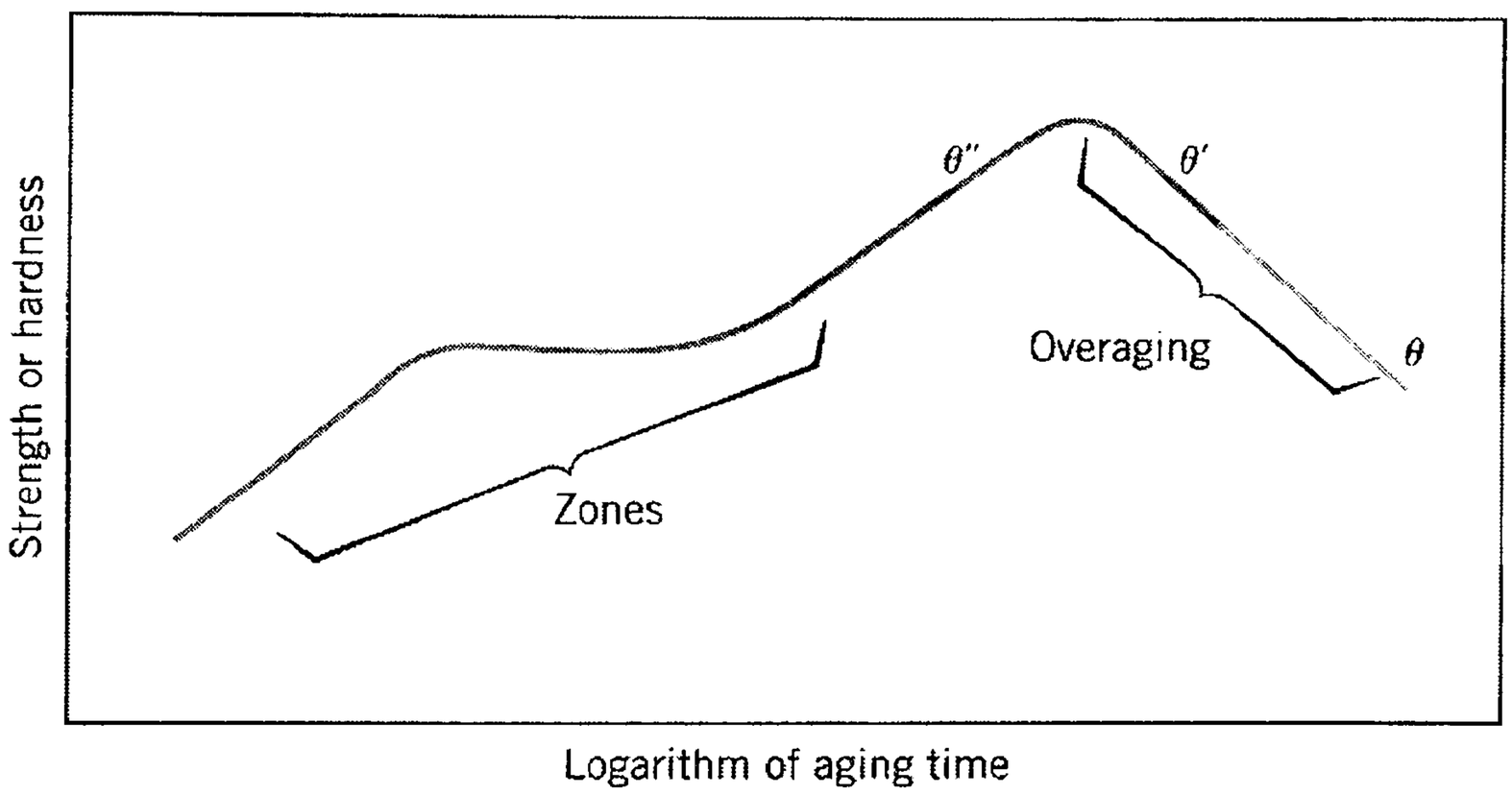


Figure 17 Schematic diagram of strength or hardness against ageing time [55].

### 3.6 The Al-Cu binary phase diagram.

Figure 18 shows the binary phase diagram for aluminium – copper with up to 55 wt % Cu. The α phase is a substitutional solid solution of Cu in Al and the intermetallic compound $CuAl_2$ is designated as the Θ phase [55].

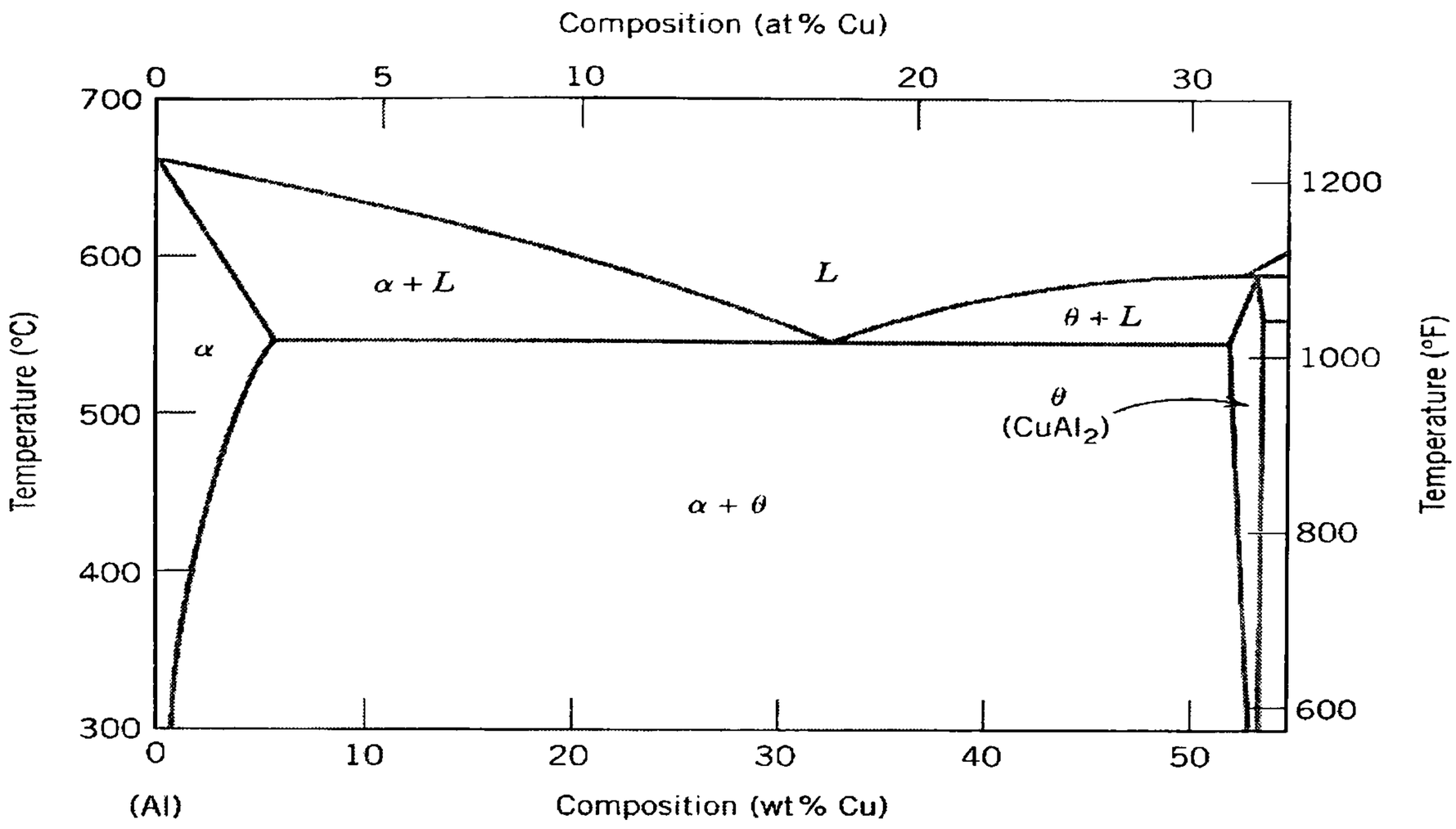


Figure 18 The aluminium-rich side of the aluminium-copper phase diagram [55].

When a metal is plastically deformed there is a movement of the dislocations through the metal lattice. Upon ageing, the copper atoms collect within the solid solution lattice to form Guinier Preston, GP, zone. Note that substitution of solute Cu atoms produces distortion or internal strain of the crystal lattice and these increase in size and volume as ageing time increases [40]. The precipitate particle then form an intermediate phase designated as Θ", as shown in figure 19. At this state, the dislocation motion is prevented by the distortion in the lattice, due to coherent interfaces, which increase the strength of the alloy. Further ageing or overageing results in particle growth. With even further ageing treatment, the precipitate growth process promotes the formation of the stable Θ' phase and Θ phase, $CuAl_2$. In this transition phase, due to lower lattice strain produced, the dislocations are allowed to move more easily. Therefore, strength progressively decreases with growth of equilibrium phase or stable phase [58].

The heat treatable alloys are specified with different in heat treatments. The letter T and followed by number is indicating what heat treatment has been given to the materials. The temper T6 results from ageing at 121 $^0$C producing a matrix of fine GP zones, Θ" particles and closely spaced grain boundaries. The temper T7, overaged condition, results in a matrix of Θ', Θ and increases the spacing between the particles [46].

On the other hand, Al-Zn-Mg-Cu alloys, such as those used in this research, do not show a stable W temper. Strength and corrosion resistance increase over a period of many years by the growth of GP zones [58].

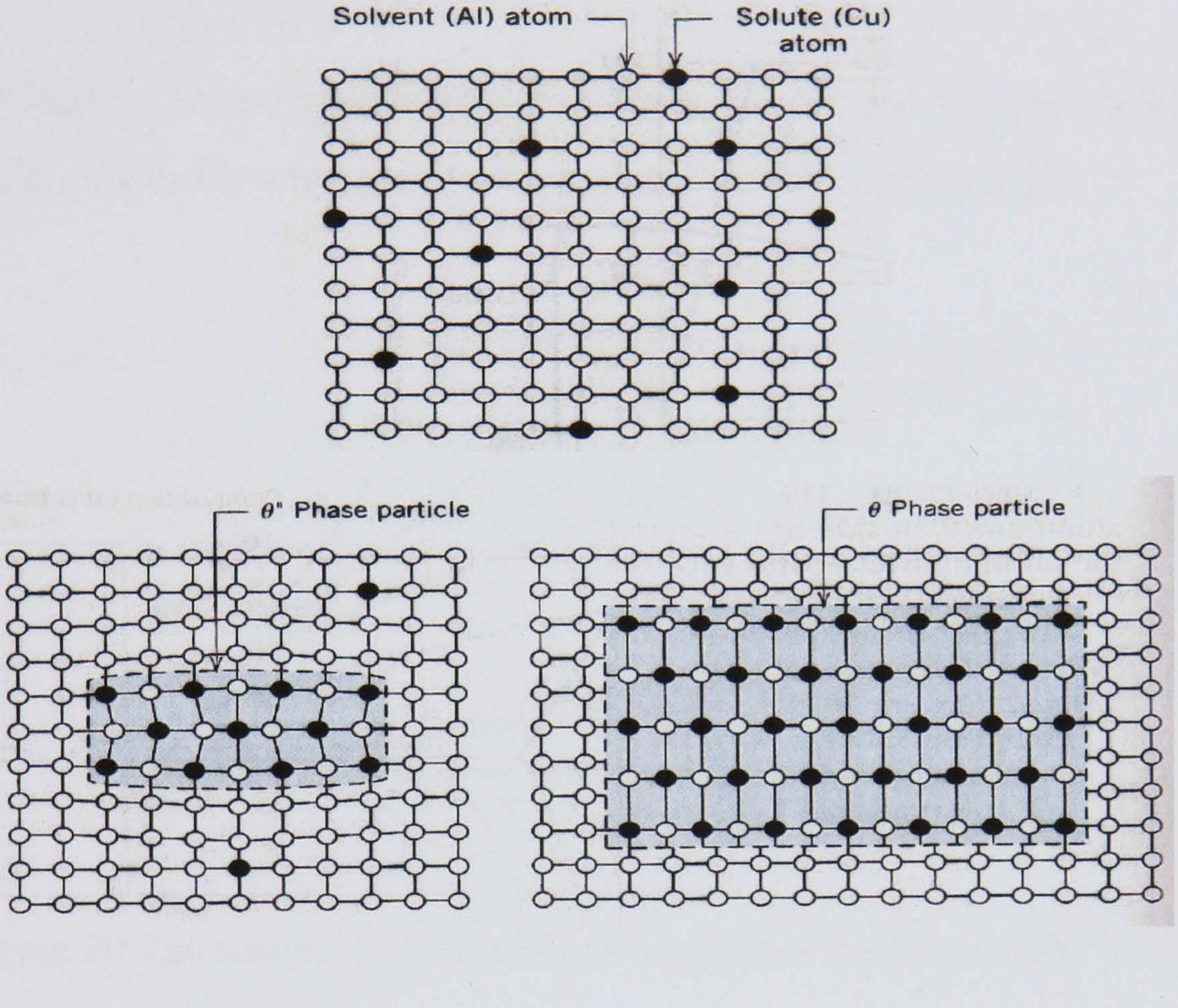


Figure 19 Schematic diagrams of several stages in the precipitates in aluminium-copper alloys [55].

### 3.7 Precipitation in Al-Zn-Mg alloys.

The Al-Zn-Mg ternary is the basis for precipitation hardening of high strength 7XXX series alloys. The precipitates of these alloys are mainly influenced by their zinc and magnesium content. The major precipitates are the Mg Zn Al phase and Mg Zn phase with the equilibrium phases of $Mg_3Zn_3Al_2$ and $MgZn_2$. However, the $MgZn_2$ phases are frequently present in the grain boundary [57]. The sequence of decomposition of the supersaturated solid solution is known to take place via the formation of several phases as follows:

Supersaturated solid solution → Spherical GP zones → ordered GP zones → **ή** $MgZn_2$ (semicoherent) → **η** ($MgZn_2$) + T ($Mg_3Zn_3Al_2$) [52,56,57,59].

In terms of stability: T > **η** > **ή** > ordered GP zones > Spherical GP zones [52].

The symbols of **ή** and **η** are sometimes known as M' and M respectively. The phase diagram for Al-Zn-Mg ternary system is shown at 200 $^0$C in Figure 20.

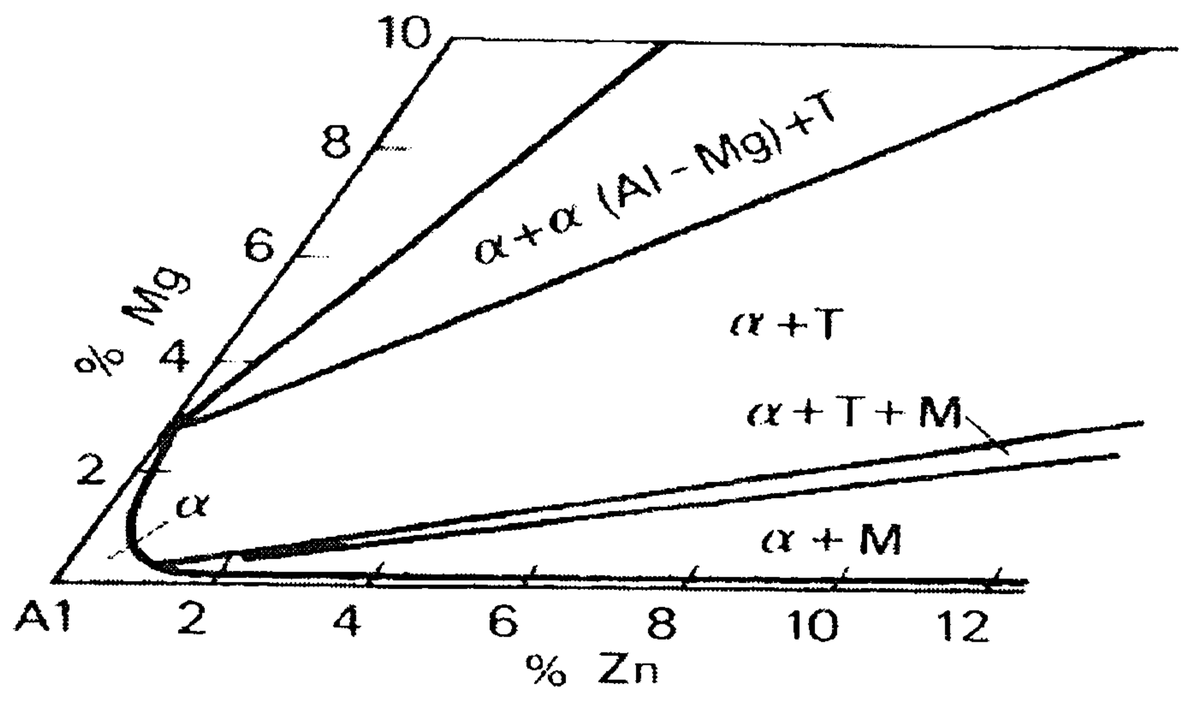


Figure 20 The section of Al-Zn-Mg ternary phase diagram at 200 $^0$C [40].

The addition of copper to Al-Zn-Mg alloys has a beneficial influence on the precipitation hardening with some contribution of copper atoms to the phase formation. In the Al-Zn-Mg-Cu quaternary system alloys, the M phase and T phase compositions are transformed to CuMgAl phase and $CuMg_4Al_6$ phase as well as $CuMgAl_2$ known as S phase. However, the $CuAl_2$ phase is present only if the copper content is greater than magnesium [47]. The phase diagram for Al-Zn-Mg-Cu quaternary containing 1.5% Cu is shown at 460 $^0$C in figure 21.

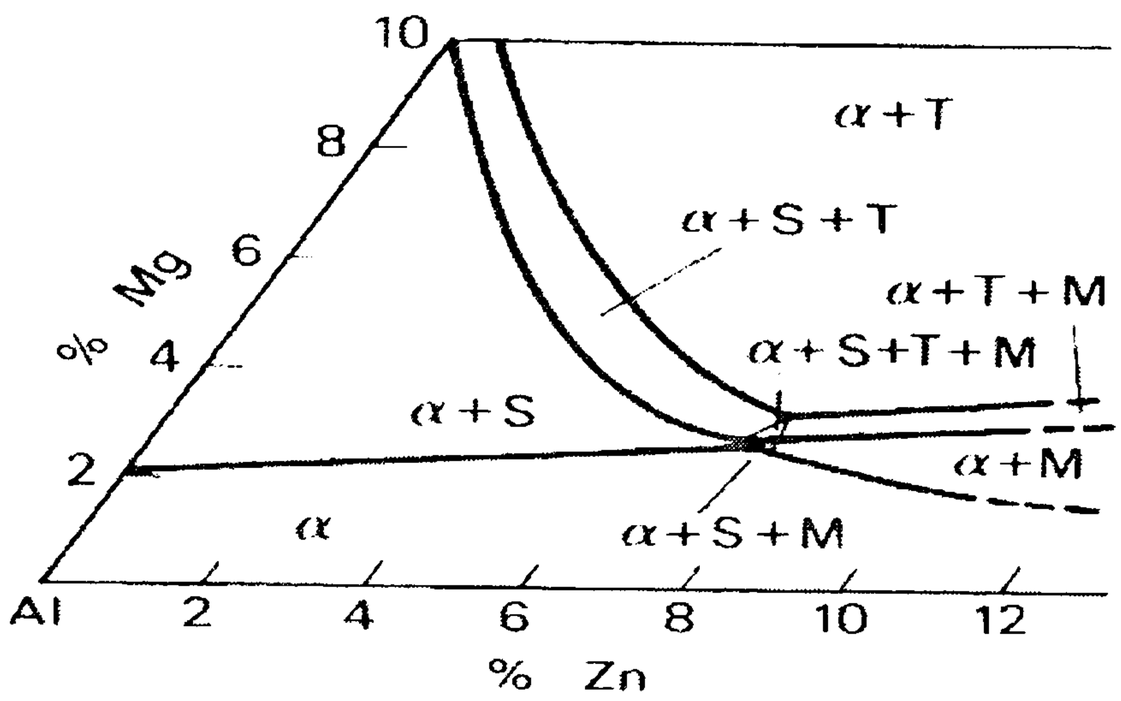


Figure 21 The section of Al-Zn-Mg-Cu quaternary phase diagram at 460 $^{0}$C [40].

### 3.8 Effect of alloying elements.

The metallurgical treatment determines the structure of the alloy, formation of second phase and the location of the second phase within its microstructure. The presence of second phase elements in aluminium alloys, whether via impurities or through alloying, generally decreases the corrosion resistance by all these factors. Table 6 summarizes the alloying elements used to produce the most commercial aluminium alloys [60].

| Major | Minor | Special | |
|---|---|---|---|
| Copper | Chromium | Antimony | Nickel |
| Magnesium | Copper | Beryllium | Phosphorous |
| Manganese | Iron | Bismuth | Sodium |
| Silicon | Manganese | Boron | Tin |
| Zinc | Silicon | Iron | Zirconium |
| | Titanium | Lead | |

Table 6 summary of the alloying elements used to produce most commercial aluminium alloys [60].

The addition of copper to 7XXX series alloys is to promote the development of ή from GP zones and also to stabilize metastable to stable phase, η [52,56]. Copper is added for strength but is found to be damaging to corrosion resistance. Manganese is added in a small quantity to accelerate the precipitation of ή from GP zones and to prevent a coarse grained recrystallised structure in the quenched alloy. Chromium, magnesium and nickel are added to increase alloy resistance to corrosion [40].

## 4.0 Corrosion of Aluminium and its Alloys.

Aluminium alloys are widely used in structures where a high strength to weight ratio is required, such as in the transport industry. Aluminium is an active metal having a strong reaction with its environment. The aluminium surface is easily attacked by most environments and converts it into a metallic compound, such as aluminium oxide. The amount of metal remaining is reduced. Aluminium oxide partially protects aluminium from further attack with its environment. The basic anodic aluminium reaction is given in equation 10.

$$Al \rightarrow Al^{3+} + 3e^{-} \qquad [10]$$

Aluminium alloys are susceptible to the severe localized corrosion including pitting, intergranular corrosion, exfoliation and stress corrosion cracking. Pitting corrosion is a form of extremely localized corrosion attack. It will continue to grow at a rate dependent on its environment and this can initiate other severe forms of corrosion, such as exfoliation and stress corrosion cracking. There are steps involved in localized corrosion attack [61].

1. The adsorption of the reaction anion on the aluminium oxide layer
2. A chemical reaction of the adsorbed anion with the aluminium ion in the aluminium oxide lattice or at the precipitate aluminium hydroxide.
3. The thinning of the aluminium oxide layer by dissolution or penetration of the oxide layer by the aggressive anion.

4. The direct attack of the fresh metal by the anion leading to pit formation. At certain sites pitting can occur simultaneously with thinning of the oxide layer at the other sites.

The importance of corrosion detection and monitoring is being recognized and after significant damage has occurred to the part it sometimes requires replacement. This has led to the development of a wide range of non-destructive testing (NDT) techniques for the examination of parts, in services. This chapter will describe the cause, process and factors in corrosion of aluminium alloys. Some of the information in this section was taken from a number of well documented corrosion text books [62-65].

### 4.1 Pitting corrosion.

It has been stated clearly that pitting corrosion is associated with breakdown of the oxide film, $Al_2O_3$, covering the aluminium metal [65]. A number of theories have been proposed for the mechanism of this breakdown. Current ideas support the views that the defects on the surface, such precipitates, grain boundaries, flaws or voids, are responsible for pitting corrosion to occur. It has been shown by the work of Foroulis et al [66], who investigated the role of chloride on the aluminium, pitting that local thinning of oxide layer was an autocatalytic process.

It is generally agreed that pitting corrosion is started with the absorption of the aggressive (pitting agents) species, such as $Cl^-$, $Br^-$and $I^-$, in the oxide aluminium layer. When the aluminium is exposed to water, with the presence of oxygen and chloride, then the pitting process will take place through the hydrolysis reaction as shown in equation 11 [67].

$$Al^{3+} + 3H_2O = Al(OH)_3 + 3H^{3+} \qquad [11]$$

Pitting is considered as the result of electrochemical action in the local cell on the aluminium surface. The aluminium metal is being pitted by chloride solution and

aluminium ions dissolved in the solution. The high concentration of aluminium ions formed within the pit area results in the migration of chloride ions into the pit to maintain electrochemical neutrality. As a result of the hydrolysis reaction in equation 11, there is increased acidity within the pit which gradually increases the dissolution (attack) of aluminium alloys [63]. This also has been confirmed by the work of Foley [61] who shows that the pH at the pit base being measured as 3.5 and the bulk solution having a pH about 7. Figure 22 shows the schematic diagram of the reactions occurring in the aluminium pit.

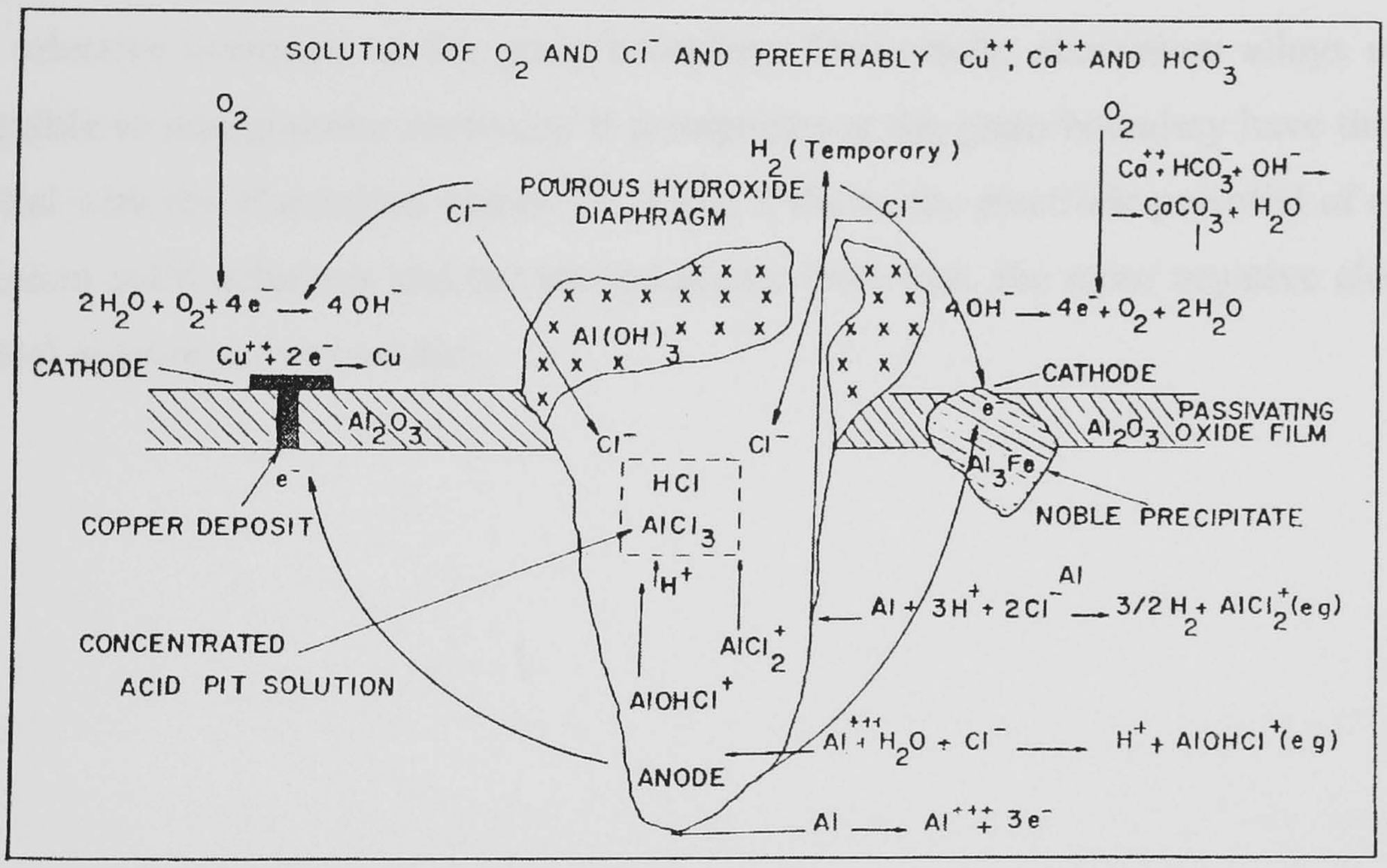


Figure 22 Schematic diagram of the reactions occurring in the aluminium pit [61].

## 4.2 Intergranular corrosion.

Intergranular corrosion is a special form of corrosion characterized by the preferential attack following a path along the grain boundary. This corrosion can occur if the grain boundary regions are having different composition from the bulk aluminium alloy. During heat treatment, precipitates and precipitate free zones are formed at the grain boundary and each has a different electrochemical potential. The electrochemical

potential difference is responsible for galvanic corrosion occurring at the grain boundary [63]. Consequently, there is severe reduction of mechanical properties of the aluminium with intergranular corrosion.

During their investigation into aluminium alloys, Hagemaier et al [37] stated that high strength aluminium alloys, such as 2XXX and 7XXX series, are susceptible to intergranular corrosion especially if the alloys have been improperly heat treated and exposed to a corrosive environment. They concluded that this is due to the grain boundary and the grain matrix is reacting as anode and cathode respectively and causing rapid selective corrosion at the grain boundary. Conversely, aluminium alloys are not susceptible to intergranular corrosion if precipitates at the grain boundary have the same potential with the aluminium matrix [40]. Table 7 shows the electrode potential of metals, aluminium solid solutions and the second phase. Note that, the more negative electrode potential is more active (anodic).

| Metal or alloy | Potential $V_{(SCE)}$ | Solid solution or second phase | Potential $V_{(SCE)}$ |
|---|---|---|---|
| Mg | - 1.73 | $Mg_5Al_8$ | - 1.24 |
| Zn | - 1.10 | Al-Zn-Mg SS (4% $MgZn_2$) | - 1.07 |
| Al 7075 | - 0.99 | $MgZn_2$ | - 1.05 |
| Al 5083 | - 0.87 | $Al_2CuMg$ | - 1.00 |
| Al (99.95%) | - 0.85 | Al-5% Mg SS | - 0.88 |
| Al 3004 | - 0.84 | $MnAl_6$ | - 0.85 |
| Al 2024 | - 0.83 | Aluminium (99.95%) | - 0.85 |
| Cadmium | - 0.82 | Al-Mg-Si SS (1% $Mg_2Si$) | - 0.83 |
| Mild steel | - 0.58 | Al-1% Si SS | - 0.81 |
| Lead | - 0.55 | Al-2% Cu SSS | - 0.75 |
| Tin | - 0.49 | Al-4% Cu SSS | - 0.69 |
| Copper | - 0.20 | $FeAl_3$ | - 0.56 |
| SS | - 0.09 | $CuAl_2$ | - 0.53 |
| Nickel | - 0.07 | $NiAl_3$ | - 0.52 |
| Chromium | - 0.49 | Si | - 0.26 |

Table 7 shows the electrode potential of metals, aluminium solid solutions and the second phase [40].

It is generally accepted that the first step of intergranular corrosion often involves pitting corrosion. The lower pH at the pit promotes attack at the grain boundary, as shown in figure 23. Figure 23 shows the acidic environment at the pit leads to grain boundary attack. The second step involves two mechanisms by which intergranular corrosion may occur. The precipitate can be anodic, such as $Mg_2Al_3$ in 5XXX series, which corrodes preferentially or it can be a cathode, such as $CuAl_2$ in 2XXX or 7XXX series, which forms adjacent to the grain boundary, causing it to corrode and form an acidic pit environment, as shown in figure 24 [37].

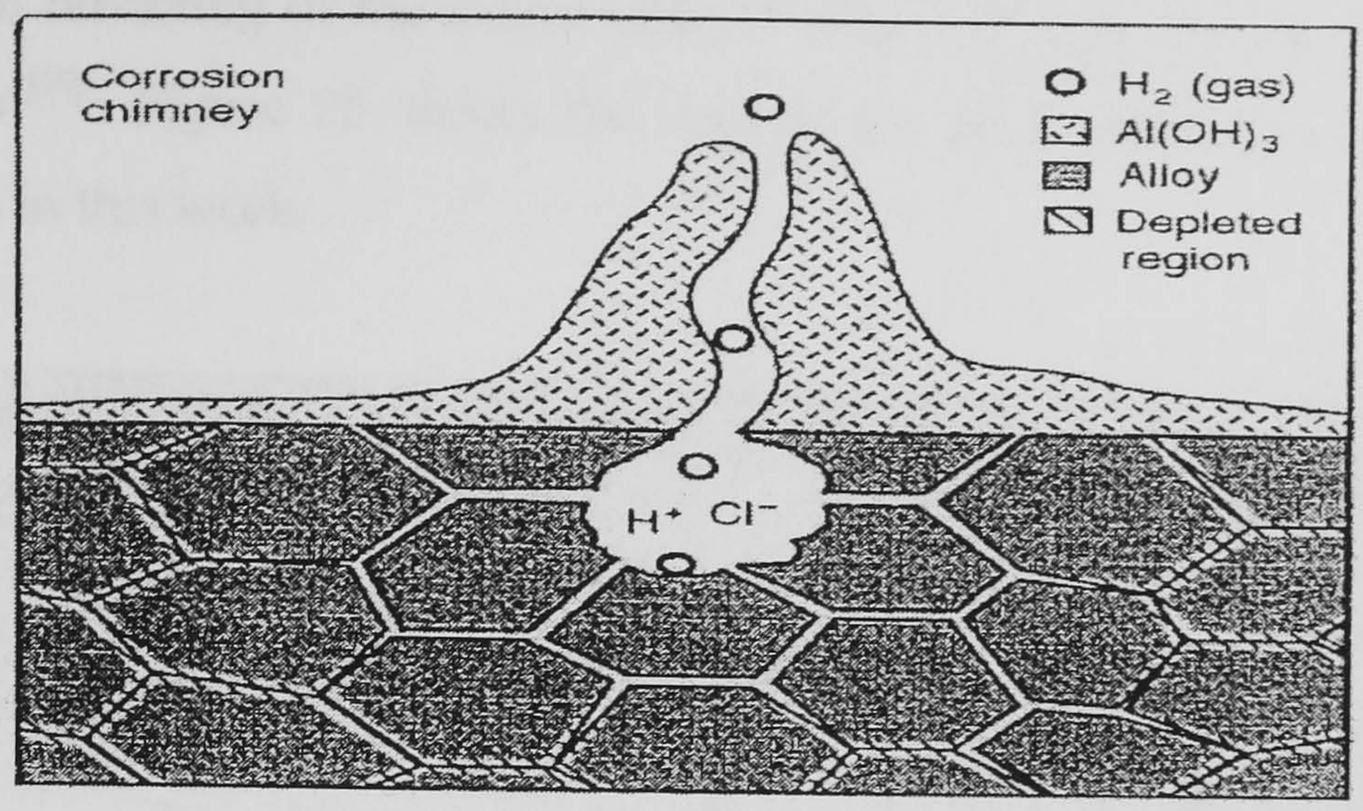


Figure 23 shows the acidic environment in the pit leads to grain boundary attack [37].

Figure 24 shows intergranular corrosion can occur by either the dissolution of grain boundary precipitates or the dissolution of the region adjacent to the grain boundary precipitate.

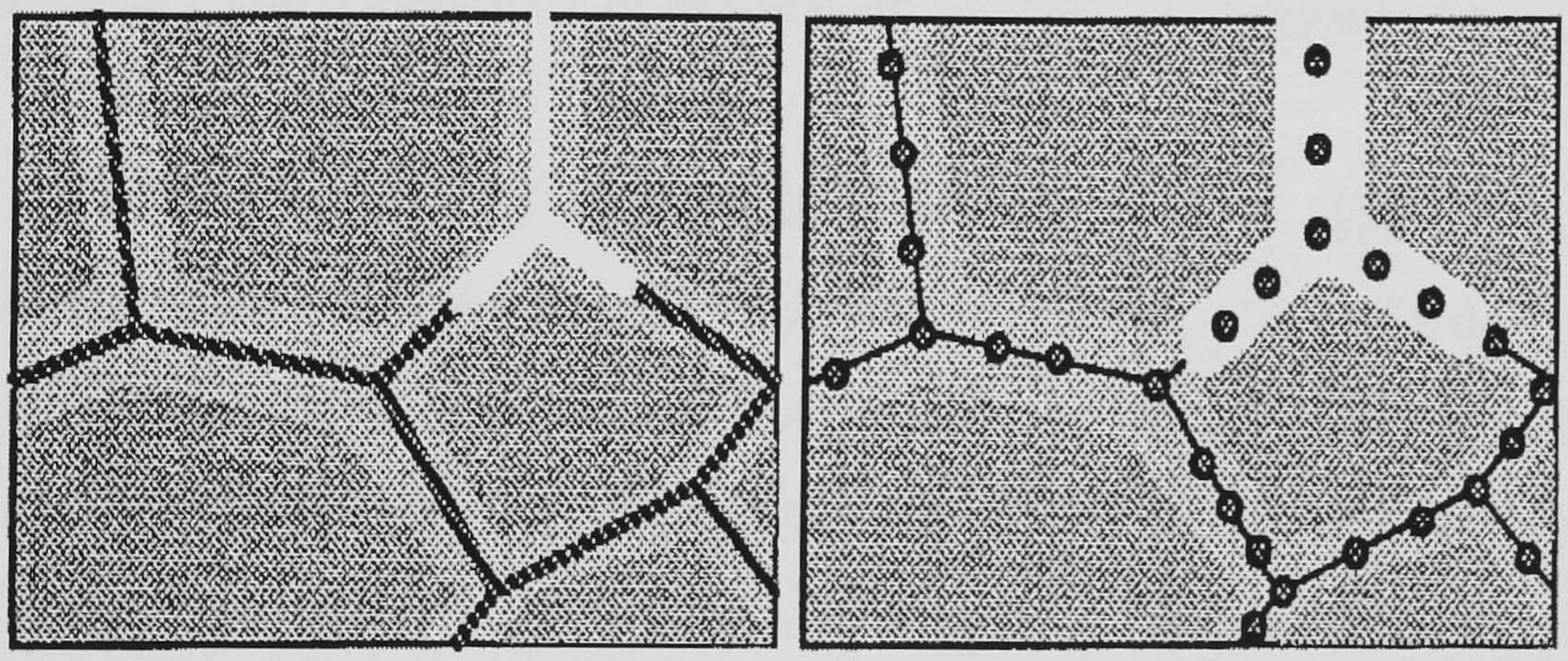

Figure 24 Diagram of corrosion along the grain boundary regions [37].

## 4.3 Exfoliation corrosion.

Exfoliation corrosion, also called layer or lamellar corrosion, occurs predominantly in 2XXX, 5XXX and 7XXX rolled sheet, plate and wrought alloys that have been age hardened [69]. This corrosion is a specific type of selective attack that occurs along multiple narrow paths parallel to the surface of the metal. This results in a

leafing action, with blistering of the surface due to flakes of metal being pushed up, by corrosion products [70]. Figure 25 shows the appearance of a section of exfoliation in 7075-W alloy used in this work.

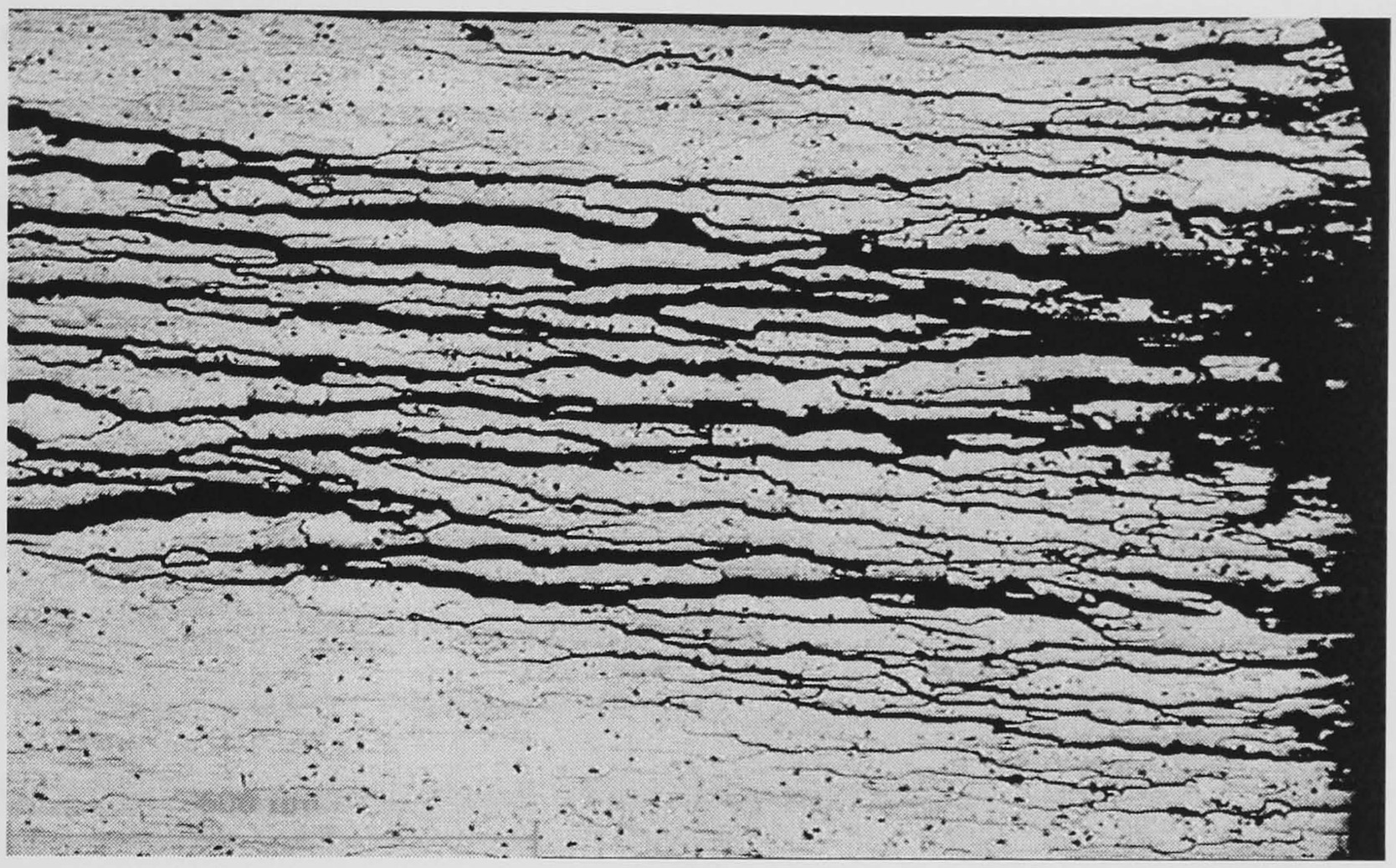

Figure 25 The appearance of exfoliation in 7075-W aluminium alloys.

This is an advanced form of intergranular corrosion which exhibits itself as a result of corrosion product wedging. During this process the corrosion product builds up internal stresses when it forms beneath the surface of the metal. The volume of the corrosion product is greater than the metal from which they formed three times the volume of the original alloy. In turn, this increased volume results in stresses within the material causing the metal to swell [68,71,72,73]. Initially, it starts with small amount of corrosion but once blistering has developed material degradation can be rapid. After long service times, it can lead to a reduction in the mechanical properties of the material by loss of metal cross section. Hagemaier et al [37] stated that the dominant danger of exfoliation is the potential loss in strength as a result of corroding away bearing surface and loss of effective cross section. The other point must be considered is the internal stresses produced by corrosion product wedging. This extra stress, if combined with other stress available, may be enough to exceed the threshold stress value for cracking to propagate in alloys which are susceptible to stress corrosion cracking.

The grain structure is thought to be one of the important factors in the susceptibility to exfoliation of high strength aluminium alloys. The difference between exfoliation and general intergranular corrosion is the fact that exfoliation corrosion only occurs in material with an elongated grain structure, where the grains have been flattened during the production, such as rolling of sheet material. The exfoliation corrosion attack is along the rolling direction [68,69]. In contrast, it has been reported that materials with partially or fully recrystallized grains are more resistant to exfoliation [74]. The statement can be supported by work done by Lifka et al [75] who demonstrated that different grain structures have an effect on exfoliation corrosion attack. They showed, after three years, aluminium with a fibrous grain structure was badly attacked by exfoliation corrosion in a marine environment. On the other hand, there was no exfoliation attack, only intergranular corrosion attack, on material with a recrystallized structure. Figure 26 shows the differences in corrosion attack with different grain structure.

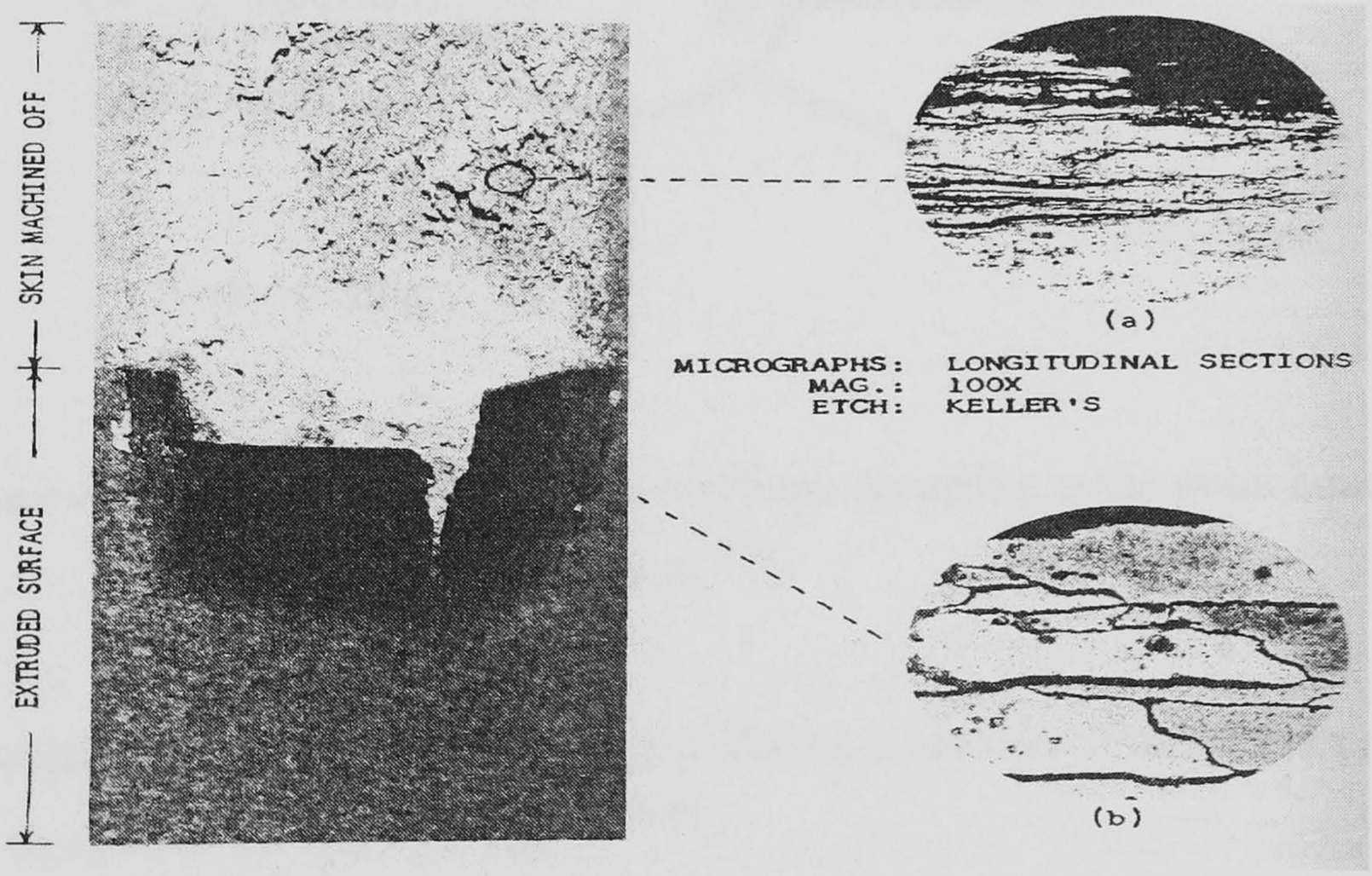


Figure 26 The microstructures of aluminium alloys seen by Lifka et al [76].

Similar to other forms of intergranular corrosion, exfoliation corrosion requires the presence of different electrochemical potential at the grain boundary. Note that electrochemical processes, in high strength aluminium alloys are usually associated with

the presence of second phase precipitates. The driving force for exfoliation corrosion depends on the microstructure of the alloys. If the precipitates are active (anodic) to the matrix they may be preferentially dissolved. If they are noble (cathodic) then attack occurs in the solute depleted zone (PFZ). Anwar [77] and Keddam et al [78] found that the level of magnesium and copper within the alloy affects susceptibility to exfoliation corrosion. The formation of precipitates such as $Al_2Cu$ or $Al_2MgCu$, made the PFZ Cu depleted. This caused the precipitates to become cathodic, with copper redeposition occurring on the depleted precipitate free zones. This phenomenon can be explained in figure 27.

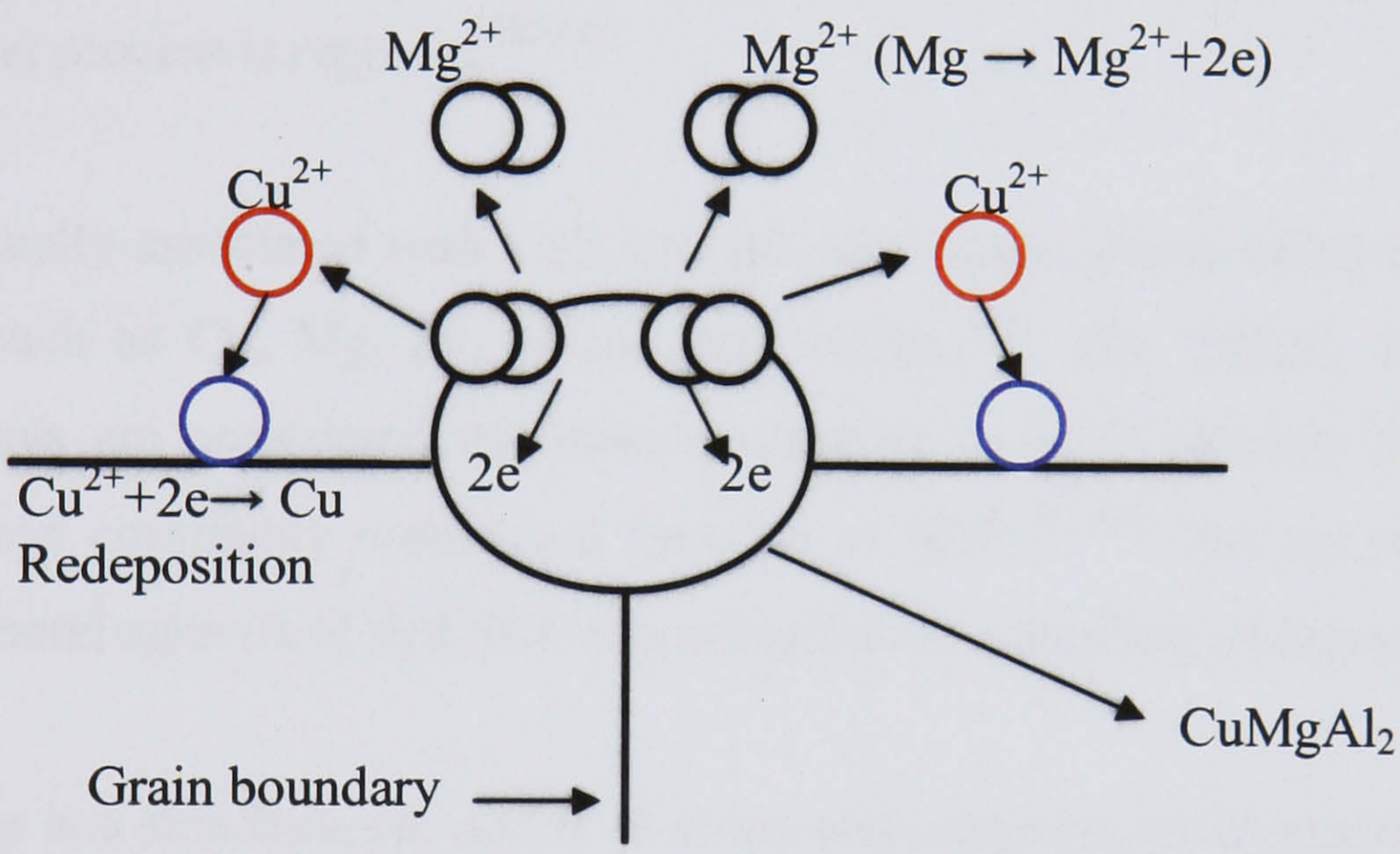


Figure 27 Schematic diagram of the reactions occurring at the grain boundary precipitates [77].

In summary, it has been showed that exfoliation corrosion of aluminium alloys is depending on three main factors to occur [71,79,80].

1. A highly directional grain structure with elongated grains which are relatively thin compared to their length.
2. A specific type of corrosive environment.
3. A preferential anodic corrosion path, which is usually at the grain boundary.

High resistance to exfoliation corrosion is usually obtained by over ageing to reduce the tendency to intergranular corrosion.

## 5.0 Stress Corrosion Cracking in Aluminium Alloys.

Stress corrosion cracking (SCC) of aluminium alloys is typically intergranular and this form of corrosion can be considered to be an extension of intergranular corrosion [60]. SCC is often a discontinuous process with electrochemical action producing surface fissures. In addition, there is high stress concentration at the crack tip and this causes cracking to occur. During that process, fresh metal is exposed to the specific environment and so the cracking process is repeated [62,63].

SCC is usually associated with high strength aluminium alloys which containing solute elements such as Cu, Mg, Zn, silicon and lithium [81]. The 2XXX, 5XXX and 7XXX series alloys are considered the most susceptible to SCC whereas 3XXX and 6XXX series alloys commonly considered immune to SCC [82,83]. For the aluminium alloys, there is general agreement that SCC can occur due to a numbers of factors [64].

1. There is a simultaneous action of stress and corrosive environment to cause progressive fracture [84].
2. The long induction period is necessary for pitting to produce crack initiation caused by electrochemical cells.
3. The conditions for cracking are dependent on specific alloys and environment.
4. There is a rapid crack growth at the crack tip and it is much less at the sides.
5. The mode of cracking can be intergranular or transgranular but it is predominantly one or the other. This is due to a function of grain structure.

The required stresses may be in the form of directly applied stresses, and it is usually thought that the stress must be tensile, or in the form of residual stress that has been left from the fabrication process. A threshold stress is needed for crack initiation and

growth may occur at stresses significantly below the yield stress [85]. Once SCC is developed, it is usually recognized after significant cracking has taken place and it then requires the replacement of the part [5].

### 5.1 Environments affecting SCC in aluminium alloys.

It is generally understood that moist environments are required to promote SCC as well as the presence of chloride [86]. The work of Speidel [82] showed that air humidity had a major influence on SCC growth in 7075 aluminium alloys. He found that the rate of crack propagation was directly proportional to the relative humidity of the air. Figure 28 shows effect of increasing humidity on crack velocity in SCC. In other work [87], he proposed several guidelines related to SCC in water vapour or gases as follow:

1. SCC neither initiates nor propagates in dry gases.
2. SCC initiates immediately from pre-cracks stressed when exposed to wet gases.
3. SCC fracture is intergranular with all type of gases or liquids.

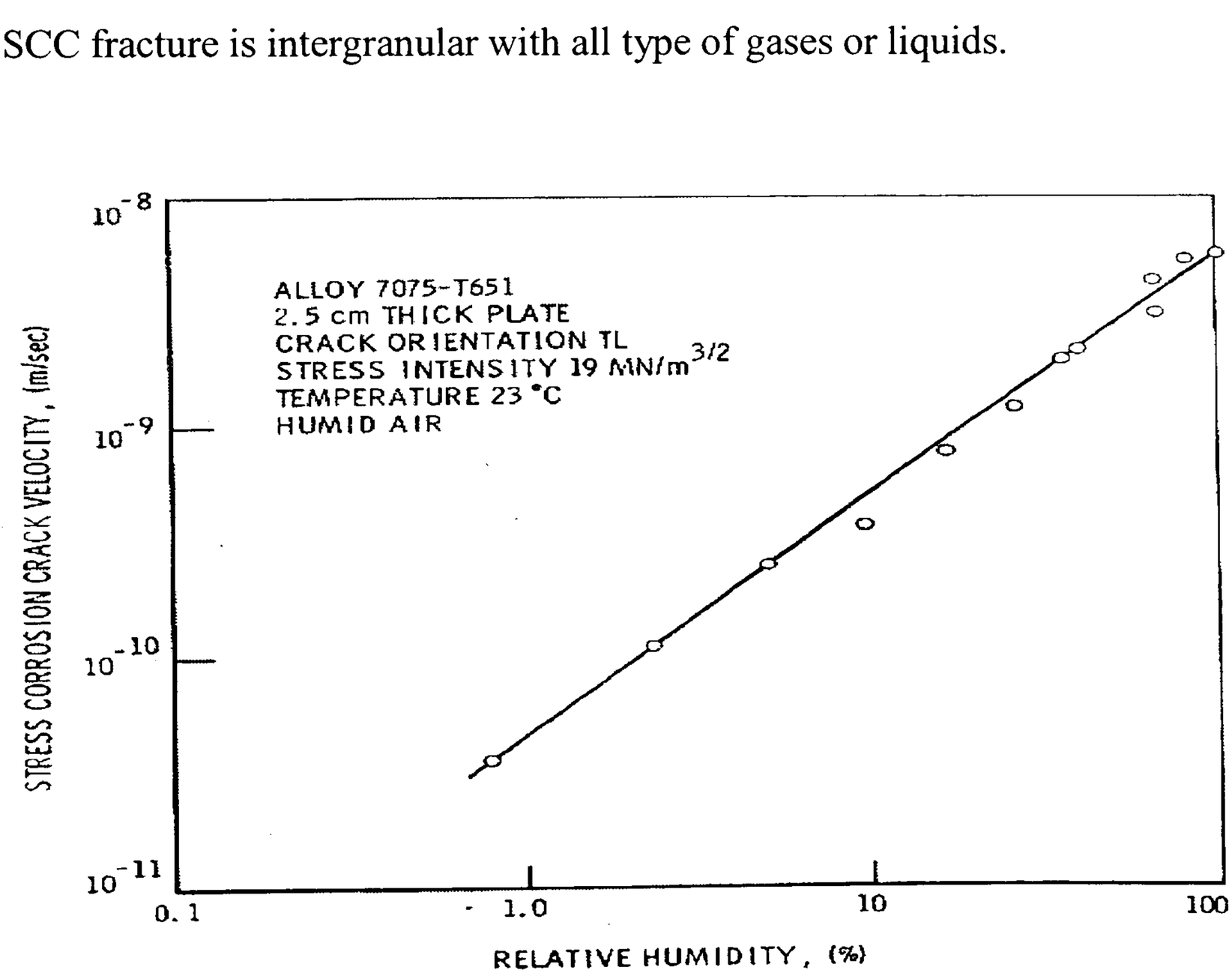


Figure 28 shows effect of increasing humidity on SCC velocity in SCC [82].

The acceleration of SCC growth is increased when the environment changed from moist gas to water. This is due to the presence of halides such as $Cl^-$, $Br^-$ and $I^-$ in the aqueous solutions. Speidel [87] and Speidel & Hyatt [57] demonstrated that chloride is the most aggressive ion, as shown in figure 29. They also found that SCC growth rates increased with increased halide ion concentration. This argument was supported with the works of De Jong [88] and Le et al [89] who showed that SCC increases with ion concentration, with the maximum crack growth rate for 7075 at 1M for NaCl solutions.

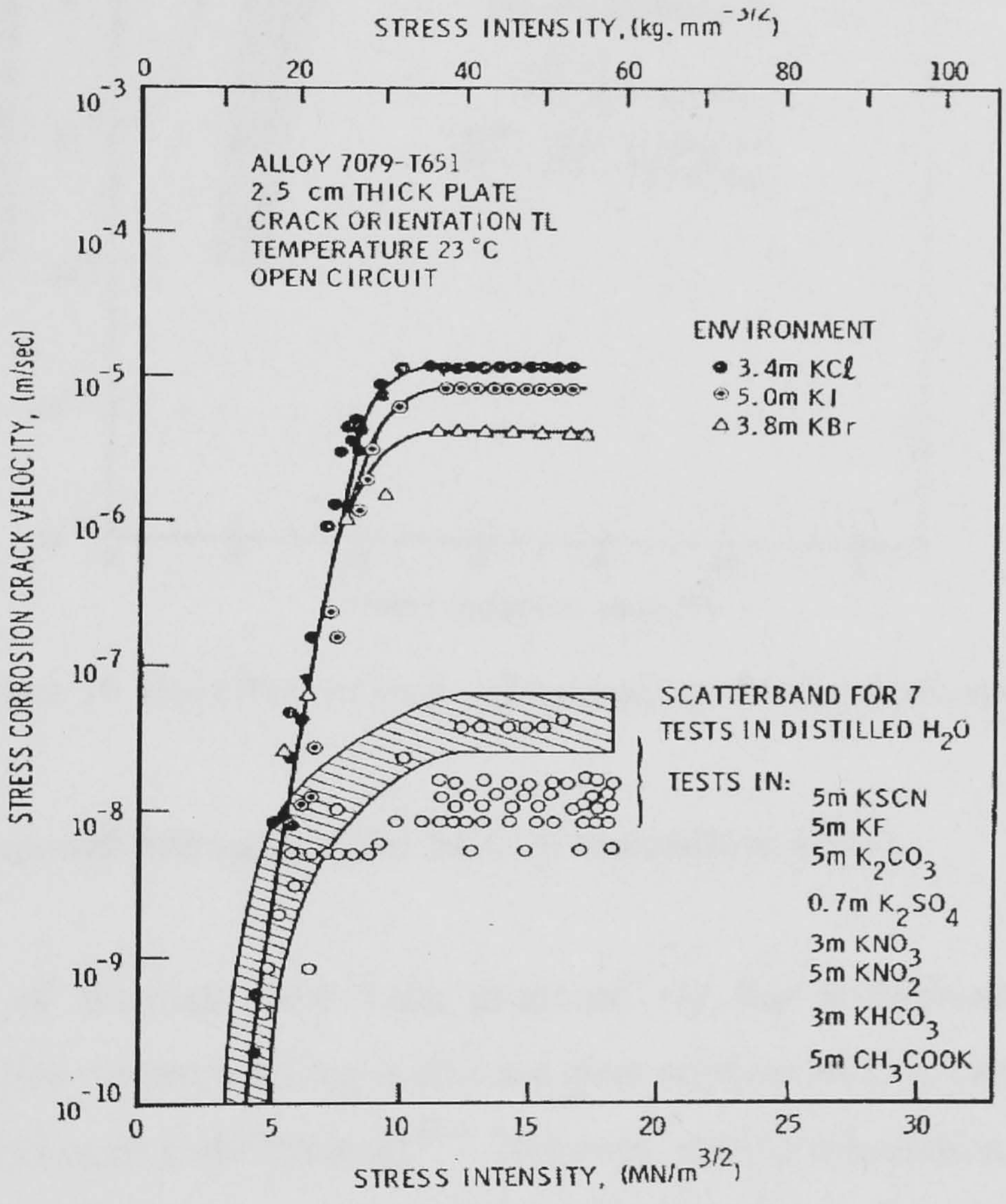


Figure 29 The effect of halide ions on SCC velocity in SCC [87].

The effect of pH of the bulk solution has been studied by the work of Holroyd [90] who showed that SCC resistance in aluminium alloys decreases with decreasing pH. Aluminium has been found to become more resistant to SCC in alkaline environment and less resistant as the environment becomes more acidic. Figure 30 shows effect of pH bulk solution ph on SCC growth rate [82,87].

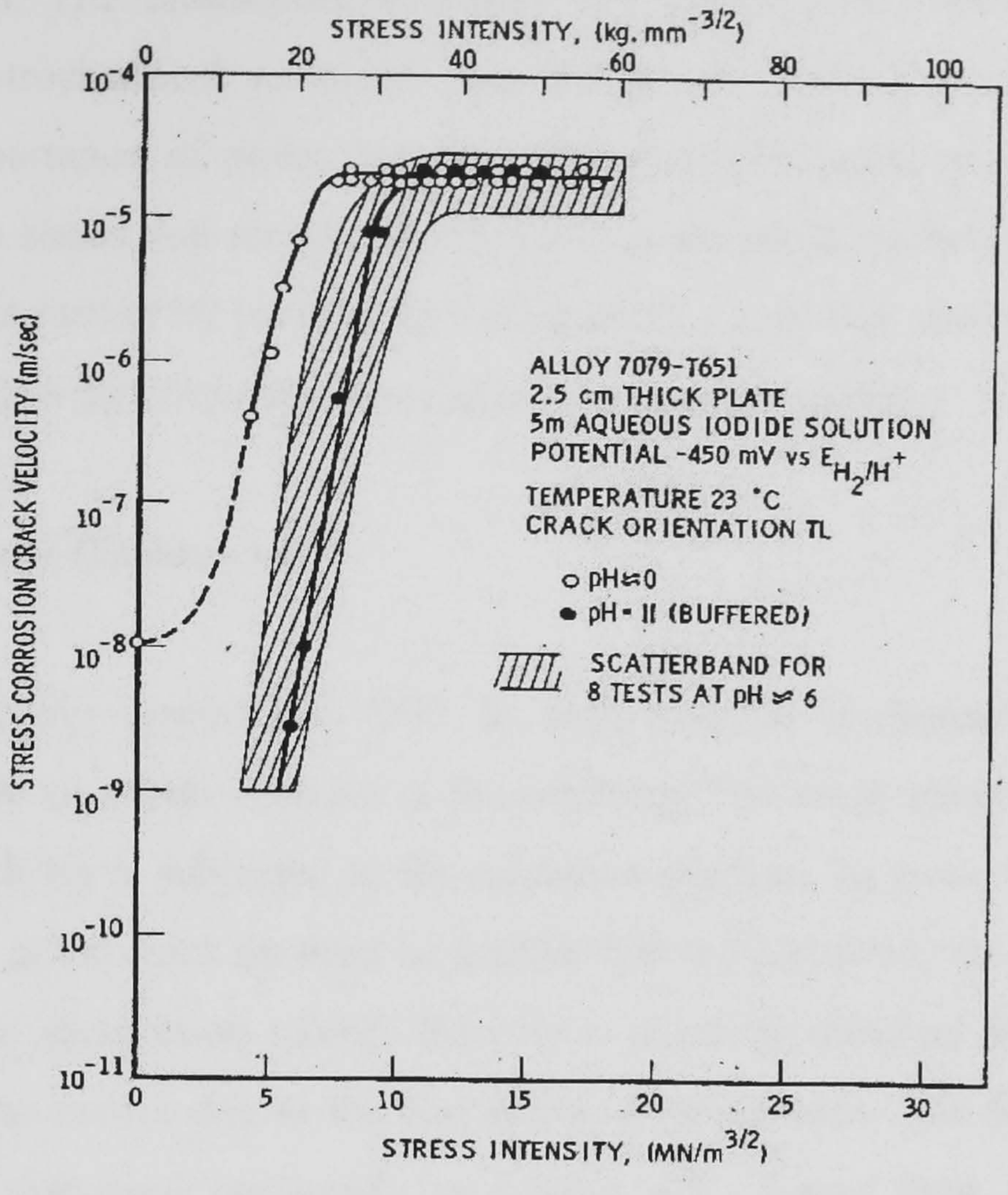


Figure 30 The effect of bulk solution pH on SCC growth rate [87].

## 5.2 The proposed mechanism for SCC in aluminium alloys.

A number of theories have been proposed for the mechanism of SCC in aluminium alloys. The current thinking is still not clear whether SCC is caused by anodic dissolution or by hydrogen embrittlement [91]. However, anodic dissolution has remained the main mechanism for SCC due to the preferential galvanic corrosion occurring along the grain boundary precipitates [92,93]. In contrast, it is thought that hydrogen is weakening the grain boundary due to the experimental evidence of hydrogen escaping from the metal as hydrogen bubbles [94-96].

Stress has always played a major role in the SCC of aluminium alloys. Stress is required for SCC to occur. Revie [59] has reviewed the theory of SCC in aluminium alloys from many authors work. He concluded that the component of tensile stress is $90^0$ degree

to the crack path in order to create a stress concentration at the base of the localized corrosion fissures. The interaction of tensile stress, corrosive environment and local chemical or electrochemical reactions was thought to make the crack grow. More recently, the importance of stress has been stated by the work of Speidel [57,87] and Bayoumi [81] who stated that stress concentration at the crack tip helped to open up the crack to propagate further by preventing formation of a new film and exposing the more anodic fresh metal to the corrosion attack along the grain boundary.

### 5.2.1 Anodic Dissolution.

It is generally agreed that SCC in high strength aluminium alloys is crack propagation due to an anodic reaction at the crack tip. The crack propagates because the region at the crack tip is subjected to the corrosion reaction. In order for SCC to occur, the corrosion rate at the crack tip must be greater than the corrosion rate at the crack walls [97]. In the anodic dissolution model, there is a potential different between the grain boundaries and the matrix due to the formation of precipitates. The formation of these precipitates was discussed previously in section 3.5. During their formation, which usually occurs along the grain boundaries, an adjacent depleted region is formed which can have a different electrochemical potential. Thus the corrosion process is produced cracking along the grain boundaries [94]. Here, it showed that a different in potential is required along the crack path. Figure 31 shows a schematic diagram of the microstructure of aluminium alloys.

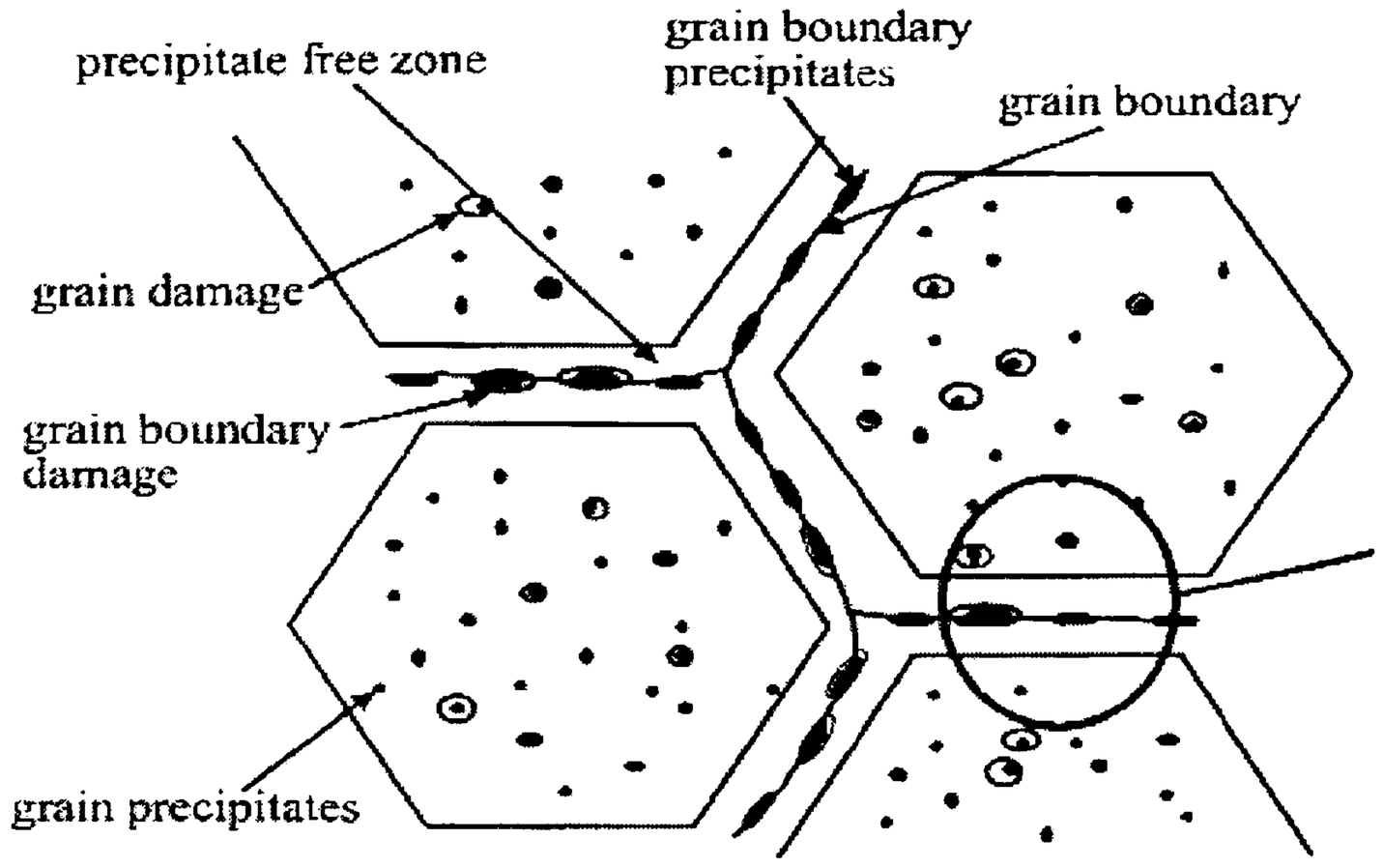


Figure 31 The schematic diagram of the microstructure of aluminium alloys [98].

During age hardening of 7XXX series aluminium alloys, it is observed that the concentration of the elements, such as Mg, Zn and Cu, at the grain boundary can influence SCC due to the effect of segregation. The oxide layer at the crack tip can be disrupted by the slip step to separate fresh metal at the matrix-grain boundary precipitate interfaces. Work by Shastry et al [99] and Deshais [92] indicated that segregation of solute elements to the grain boundaries could increase the corrosion potential and therefore increase the intergranular crack growth due to preferential anodic dissolution.

### 5.2.2 Hydrogen embrittlement.

Hydrogen embrittlement refers to the mechanical damage of the aluminium alloys caused by atomic hydrogen (H) entering and diffusing through the metal. When this hydrogen diffuses through the crystal lattice and concentrates at microstructural flaws it causes the material to fail in a brittle manner. The current thinking is that the atomic hydrogen can reduce the bond strength between metal atoms. This reduction in strength of the atomic bond can reduce ductility and tensile strength [55,63]. However, hydrogen embrittlement as the main mechanism of SCC still remains controversial.

A general mechanism of SCC in 7XXX series alloys in sea water was proposed by Holroyd et al [100]. They suggested that, for SCC to occur, the anodic dissolution played an important part in producing atomic hydrogen which diffused to the crack tip to support brittle fracture of the material. However, this seems to suggest that an increased rate of reduction of hydrogen ions is balanced by an increased rate anodic dissolution of the aluminium alloys. On the other hand, a hydrogen embrittlement delayed cracking mechanism was favored by Lee et al [93], for Al-Zn-Mg alloys exposed to an aqueous environment. They concluded that a gradual transition of SCC propagation mechanism occurs from anodic dissolution as applied stress increases. He claimed that the anodic dissolution is responsible for the stage I while hydrogen embrittlement is responsible for the stage II.

This seemed to suggest that there is no exact individual experiment evidence for this mechanism in aluminum alloys [97]. Overall, the view appears to be that SCC occurs in aluminium alloys as a result of combination anodic mechanism, followed by hydrogen embrittlement.

### 5.3 The effect of heat treatment and microstructure on SCC.

The influence of microstructure on stress corrosion cracking susceptibility of Al-Zn-Mg-Cu has been shown to strongly depend on their alloy additions and heat treatment. These affect the SCC resistance by changing the electrochemical nature of the alloy. It is known that heat treatment is used in the strengthening mechanism which gives high strength aluminium alloys their useful mechanical properties [101]. The ageing time can be controlled to give greatest strength at the peak-aged condition. However, it also has a strong effect on SCC, and gives a maximum susceptibility or minimum stress corrosion resistance usually just before the peak strength condition, which produces a poor resistance to environment cracking [102].

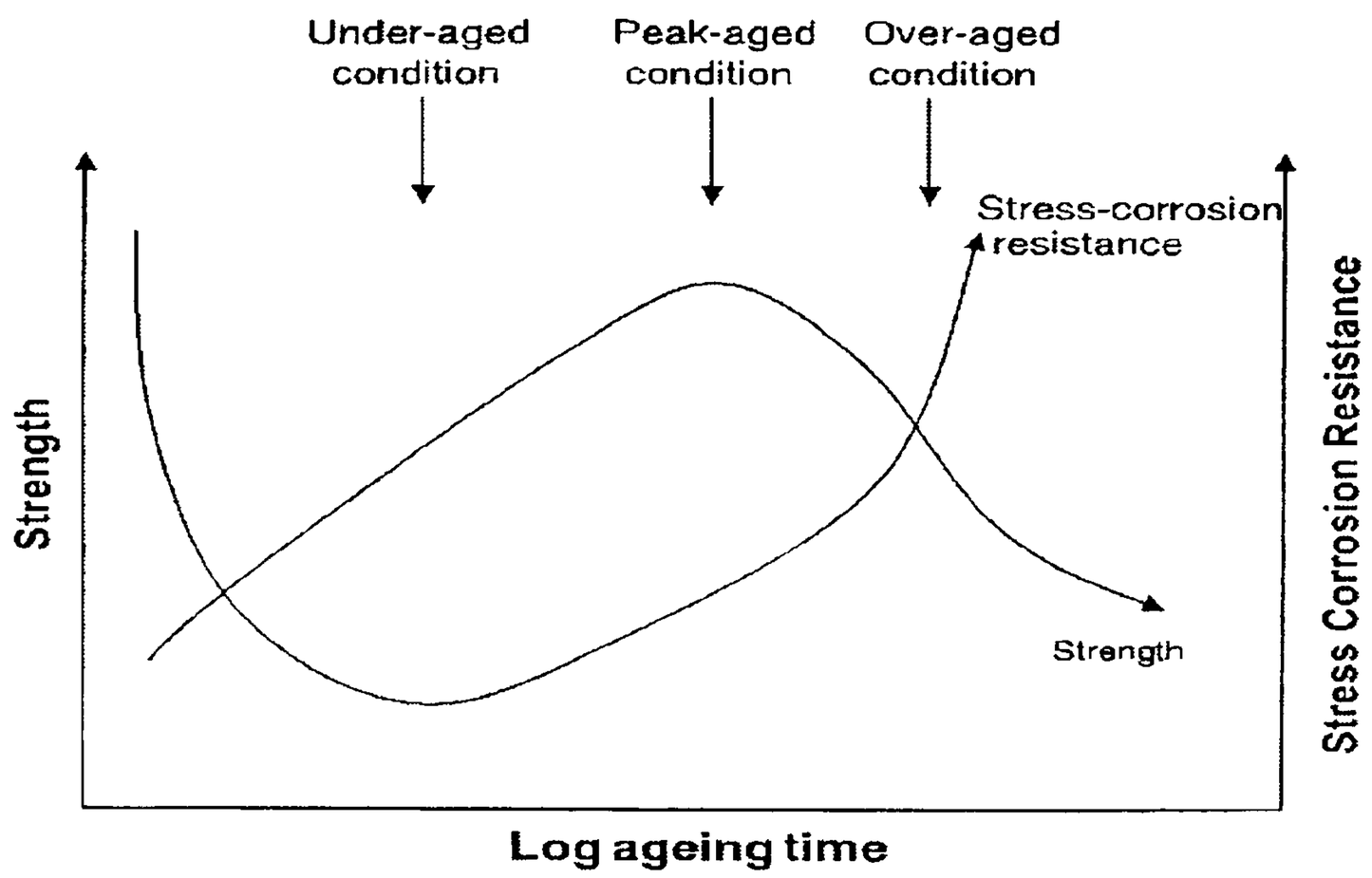


Figure 32 Diagram of the effect of ageing on SCC and strength [82].

Figure 32 shows the relationship between strength, stress corrosion crack susceptibility and heat treatment in high strength aluminium alloys. It can be seen that minimum resistance was found during the early stage of ageing for 7XXX series aluminium alloys and further ageing beyond peak strength (overageing) can significantly increase resistance to SCC. It is due to the precipitates becoming larger in size which increases the distance between them [82,87,103]. It is common to use these alloys in this overaged heat treatment condition. However, in the overaged condition, the strength of the material begins to decrease. This is thought to be due to the formation of larger incoherent or semicoherent precipitates, which are less effective at blocking dislocations. Preferential corrosion occurs at the grain boundaries and SCC follows an intergranular path.

Puiggali et al. [104] reported that continued ageing of an Al-Zn-Mg-Cu alloy may increase the volume of $MgZn_2$ precipitates and also the width of the precipitate-free zone. The change in volume and distribution of $MgZn_2$ phase precipitates that develop along the grain boundaries then affected both crack initiation and propagation of intergranular corrosion. The continued ageing of 7XXX series alloys results in a decrease in its susceptibility to SCC. This view was supported by Speidel [82,87] who has demonstrated

that there are reduced crack velocities in region II by the overageing process and this treatment results only a loss of strength. Work by Sarkar et al [105] explained that the reduction in crack velocity with overageing is due to a change of deformation mode from inhomogeneous in T6 condition to homogeneous in T7 condition and this also reduces the stress concentration at the grain boundaries. Figure 33 shows the effect of ageing on SCC velocity.

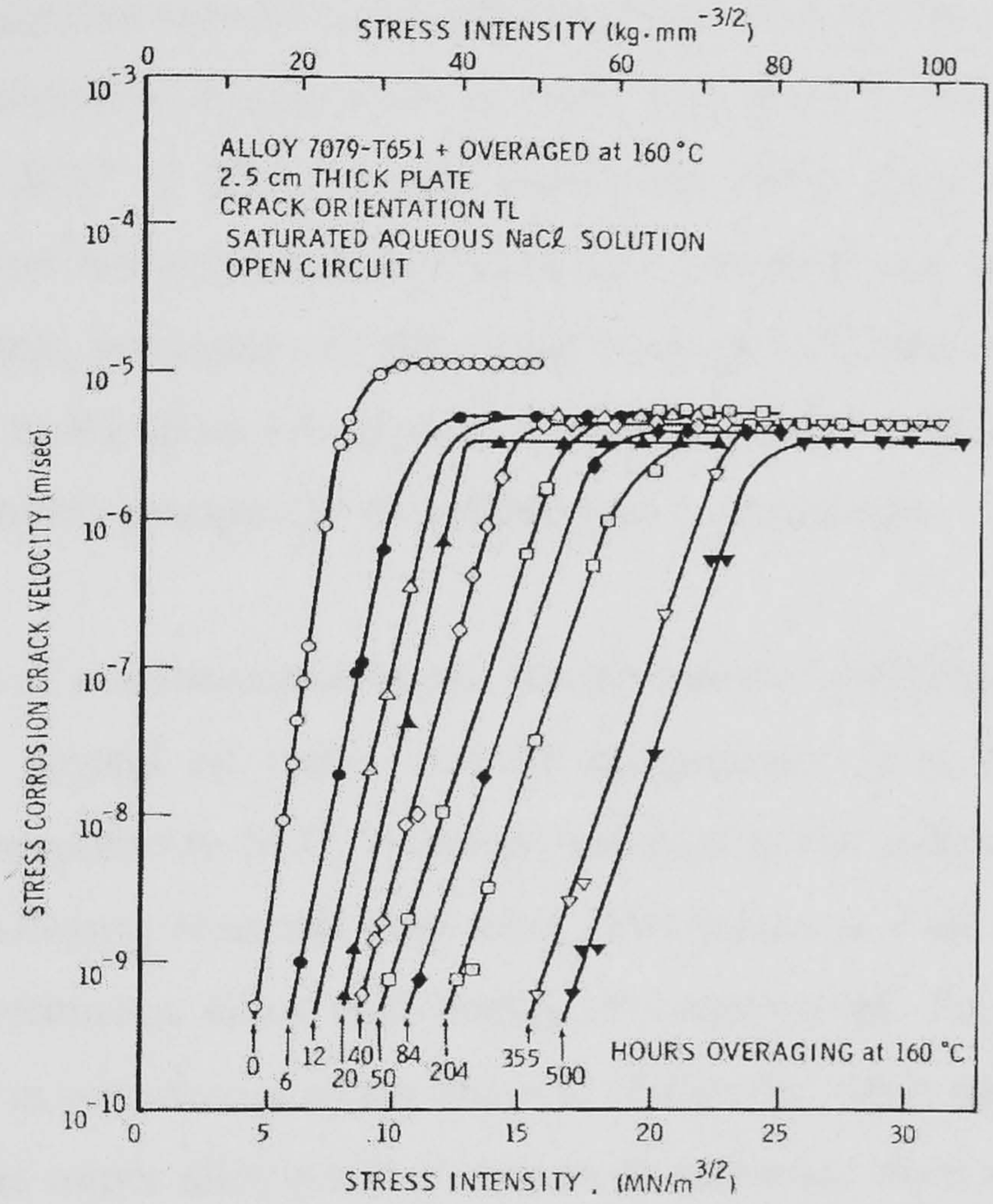


Figure 33 Diagram of the effect of ageing on SCC velocity [82,87].

A heat treatment known as retrogression and reageing (RRA) has been developed to avoid loss in strength. It can be applied to the high strength 7XXX series alloys (Al-Mg-Zn-Cu) to improve the combination of strength and SCC resistance. The treatment has been developed to give to near to the T6 peak strength and SCC resistance equivalent to the T7 temper. It is known that high dislocation densities at the grain boundaries are caused during the quench between solution treatment and ageing. Talianker et al [106] applied this RRA method to 7XXX series alloys, with test specimens subjected to various

stages of heat treatment and they discovered that matrix precipitates change in size and distribution, with coarsening of the grain boundary particles. The fine precipitates were thought to prevent plastic deformation and dislocation movement adjacent to the grain boundaries and accompanied by significant improvement in the resistance to SCC. T.C Tsai et al [102] showed that specimens of 7XXX series in the T6 condition that have undergone this treatment have shown an increased yield strength.

Speidel [57] suggested that SCC susceptibility was related to the size, spacing and coherency of the precipitates. In later work in 1997, Tsai et al [102] studied the effect of grain size upon the SCC of 7XXX series aluminium alloy. They found that grain refinement causes more homogeneous slip bands and a smaller size of grain boundary precipitates. As a result, homogeneous slip bands increase SCC resistance by reducing hydrogen movement to the grain boundaries. However, the SCC resistance can not be achieved if grain boundary precipitates are smaller than a critical size.

The influence of microstructure on the susceptibility of aluminium alloys to SCC has been shown to depend on their chemical composition. It is known that pure aluminium is not susceptible to SCC. However, changes in the composition affect the resistance to SCC. Alloying elements may form solid solutions with aluminium or be present as micro-constituents, either individually or compounded. Any or all of these conditions may exist in commercial alloys and will change the electrochemical nature of the alloys [103]. Certain minor alloy additions, in small quantities, such as Cr, Mn, Ti, V, Li, Ni, Zr added to high purity aluminium in 7XXX alloys form intermetallic phases with aluminium during solidification, which are insoluble during subsequent heat treatments. These particles pin down the high angle grain boundaries in the preferred orientation imparted during processing, and the result is beneficial to alloy systems and can reduce the SCC susceptibility of the alloy in the longitudinal or transverse directions [82,103].

The 7XXX and 2XXX series systems offer the highest strength aluminium alloys through age hardening. The addition of Cu has been studied in detail by many authors [82,87,105,107] because it is seen to show a drastic change on the nature of the alloys. Work

by Sarkar et al. [105] showed that increase in percentage of Cu content gave rise to higher $K_{ISCC}$ and lower plateau velocities in region II, as shown in Figure 34. They thought that this is due to the mode of deformation being changed from inhomogeneous to homogeneous by looped dislocations. Similarly, Hardwick et al. [107] concluded that an addition of copper to the 7XXX series alloys was beneficial to preventing hydrogen embrittlement. Results were compared from slow strain rate tests with between 2.0% and 0.01% copper content. Their comparison showed that the first alloy did not show hydrogen embrittlement for all ageing treatments, whereas the second alloy did show susceptibility to hydrogen embrittlement.

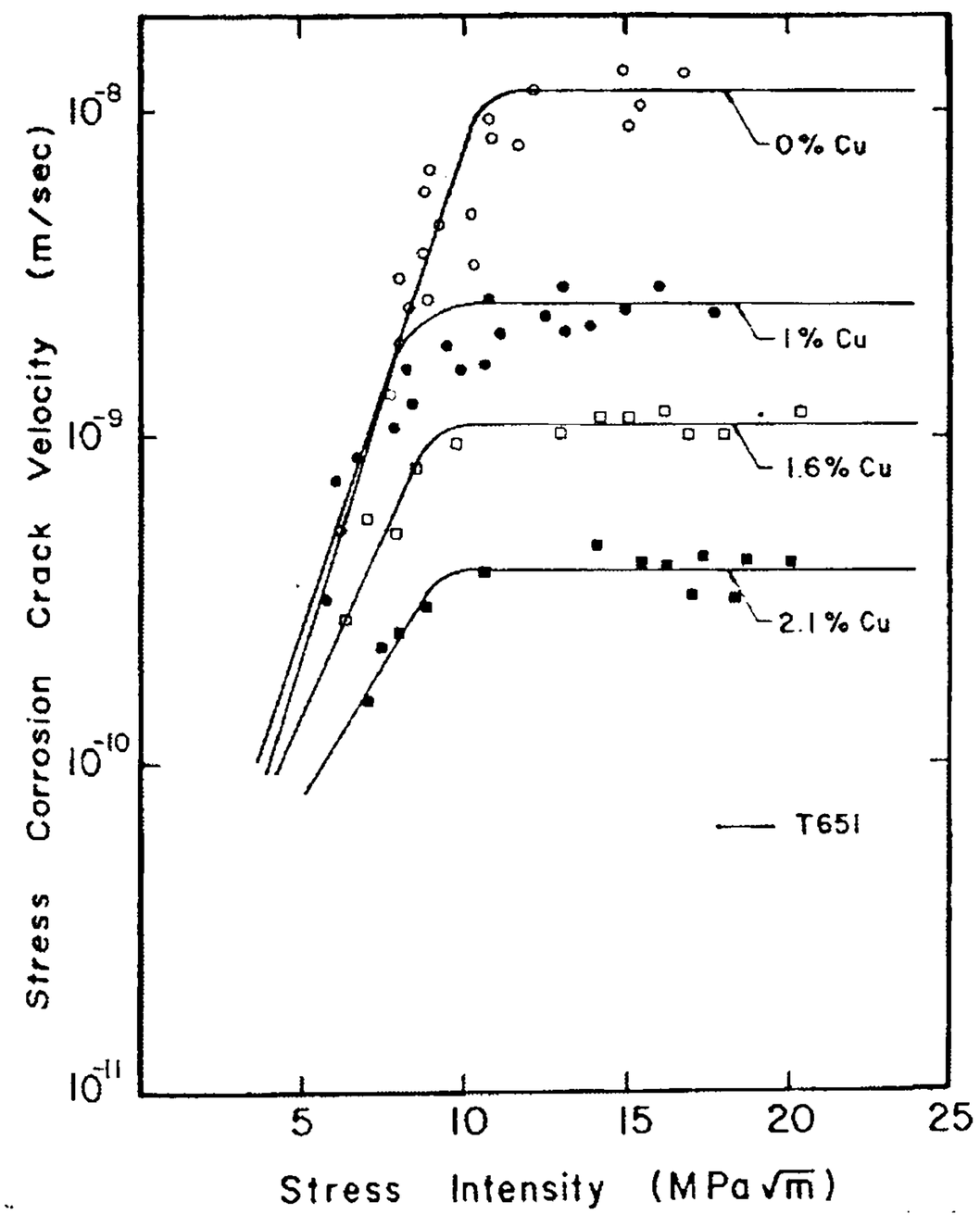


Figure 34 Effect of copper contents on SCC velocities in 3.5 % NaCl [105].

In summary, the improvement in the SCC resistance of these alloys has generally been attributed to changes in one or more of the following microstructure parameters [90,99].

1. Deformation characteristics of the matrix.

2. Nature and width of the precipitate free zone
3. Dispersion of precipitates at the grain boundaries.
4. Solute segregation to grain boundaries.

## 5.4 Double cantilever beam specimen (DCB) specimen.

The double cantilever beam specimen (DCB) has been widely used in the past and has proved one of the most popular designs for measuring the growth rate of stress corrosion cracks in materials [108]. These specimens were designed to calculate the effect on crack growth rate of the applied stress intensity at the crack tip. A constant displacement is applied to provide a stress to the specimen. The stress intensity at the crack tip decreases during the test as the crack length increases. By using this technique, a minimum threshold value or critical stress intensity factor ($K_{ISCC}$) for this alloy can be determined [109]. Normally, the double cantilever beam specimens (DCB) are immersed in an aggressive environment such as sea water or 3.5% NaCl solution [81]. Figure 35 shows the orientation of specimens taken from rolled plate material.

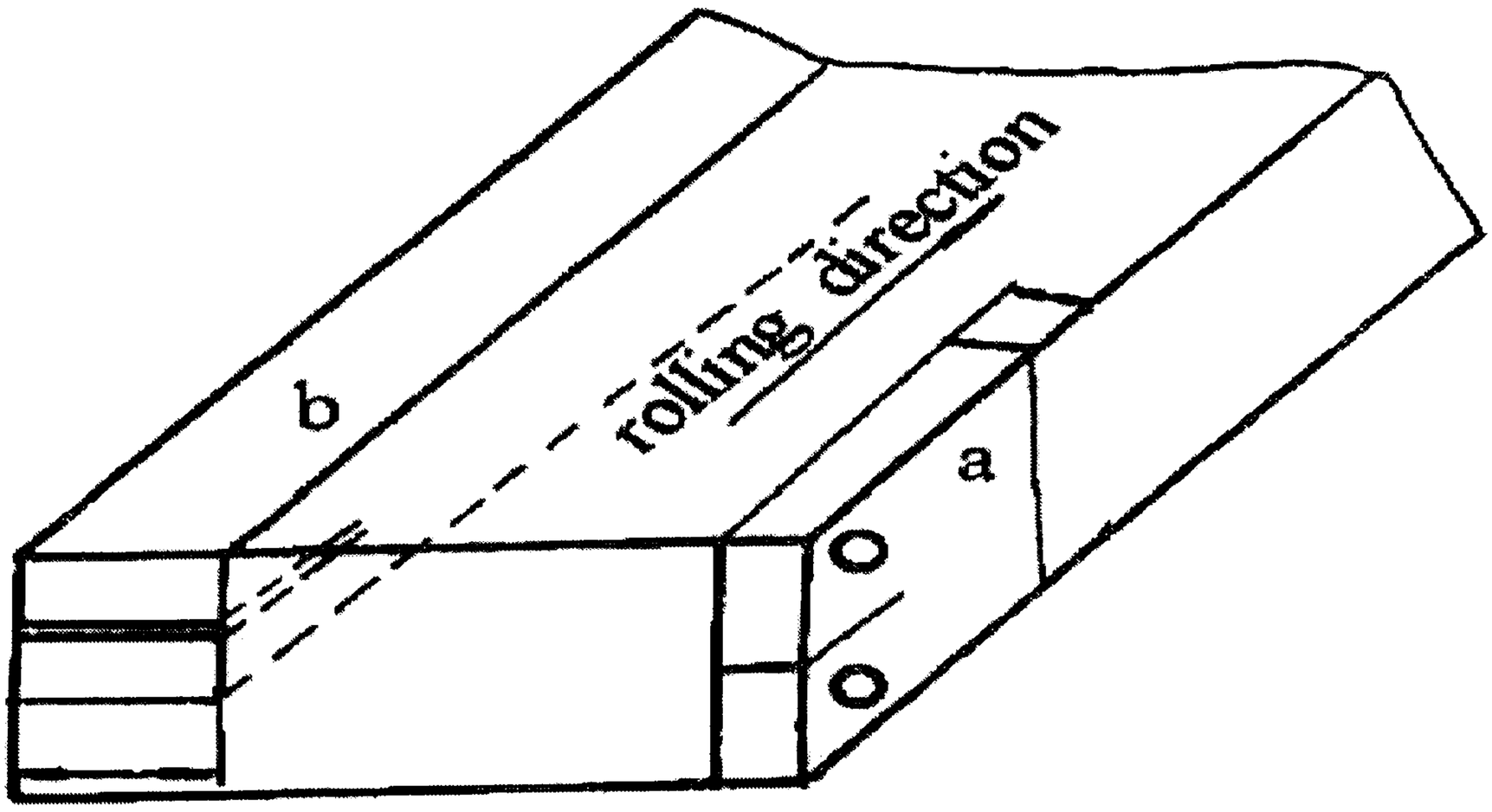


Figure 35 Orientation of the double cantilever beams (DCB) machined from the plate material [110].

## 5.5 The V-K Diagram

The data obtained from the DCB specimen can be described by a V-K diagram. Figure 36 shows the general relationship of the three regions of cracking in the V-K diagram [90].

1. Region I at low stress intensities where the crack velocity is stress dependent.
2. Region II at intermediate stress intensities where the crack velocity is stress independent.
3. Region III at high stress intensities where the crack velocity may be stress dependant.

The threshold value, $K_{ISCC}$, where the alloy is considered immune from SCC in that environment is obtained from Region I. Below the $K_{ISCC}$ value, the crack growth by SCC is not expected but above this value the SCC growth rate increases with increasing K. In region II, the crack growth rate is independent of stress intensity, K, and depends instead on the corrosive environment and temperature. During region II growth, K continues to increase and this leads to the rapid acceleration of the crack in stage III and final fast fracture when K reaches $K_{IC}$ [111]. In summary, the higher the value of $K_{ISCC}$, under given conditions, then the great the SCC resistance.

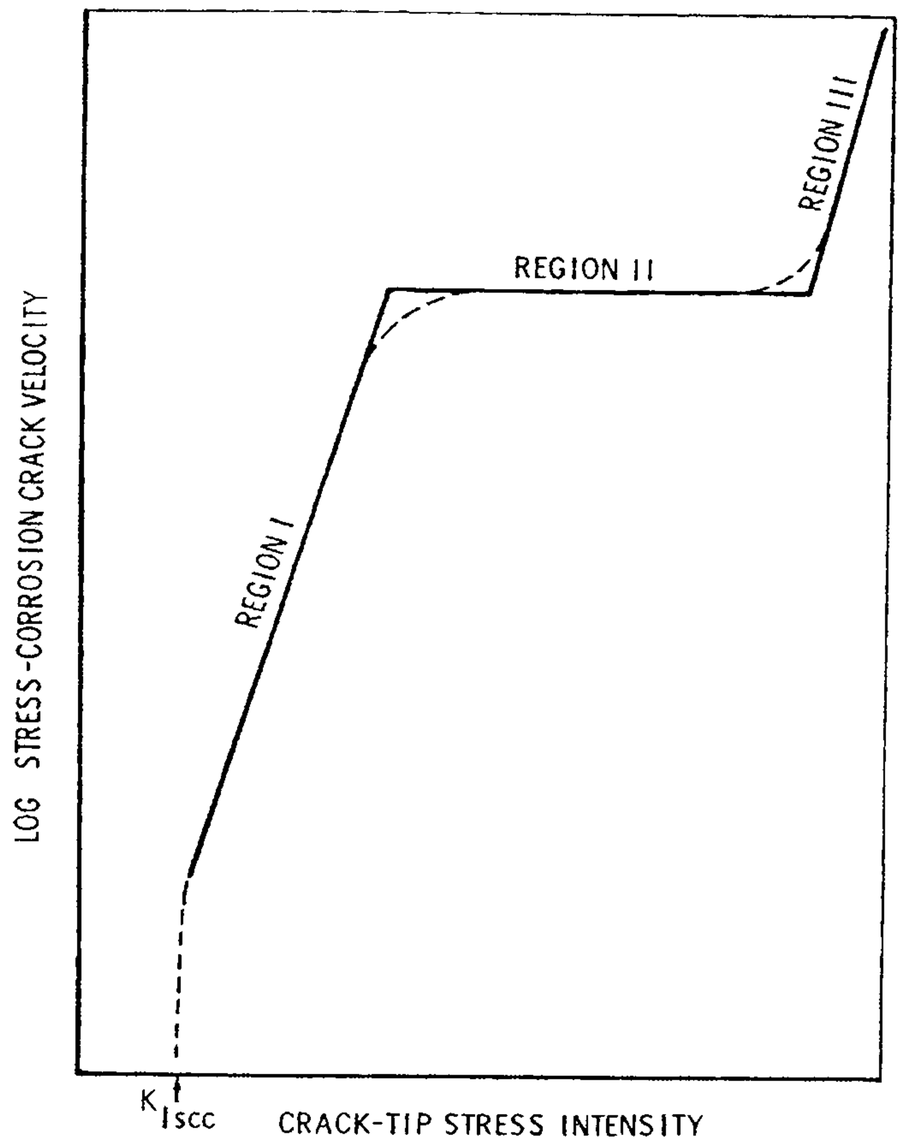


Figure 36 General relationship between the stress intensity factor, K, and stress corrosion crack velocity, V [82,87].

It has been demonstrated in the literature [112-114] that some results have shown an increase in crack growth rate, after $K_{ISCC}$ had reached, with decreasing stress intensity, on the left hand side of the V-K diagram. This effect is due to corrosion product wedging. Stress corrosion cracking of DCB specimens produced evidence of corrosion product wedging for aluminium alloys. This had the effect of increasing the stress intensity at the crack tip and resulted in an increase in crack velocity. The effect of wedging became apparent after very low stress intensity had been reached.

Figure 37 shows the effect of corrosion product wedging on the V-K diagram. It is important to note that in the corrosion product wedging region the stress intensity value is seen to decrease on V-K diagram. However, in contrast the stress intensity value is actually increasing. This explains the appearance of wedging after the $K_{ISCC}$ value had reached the lowest point.

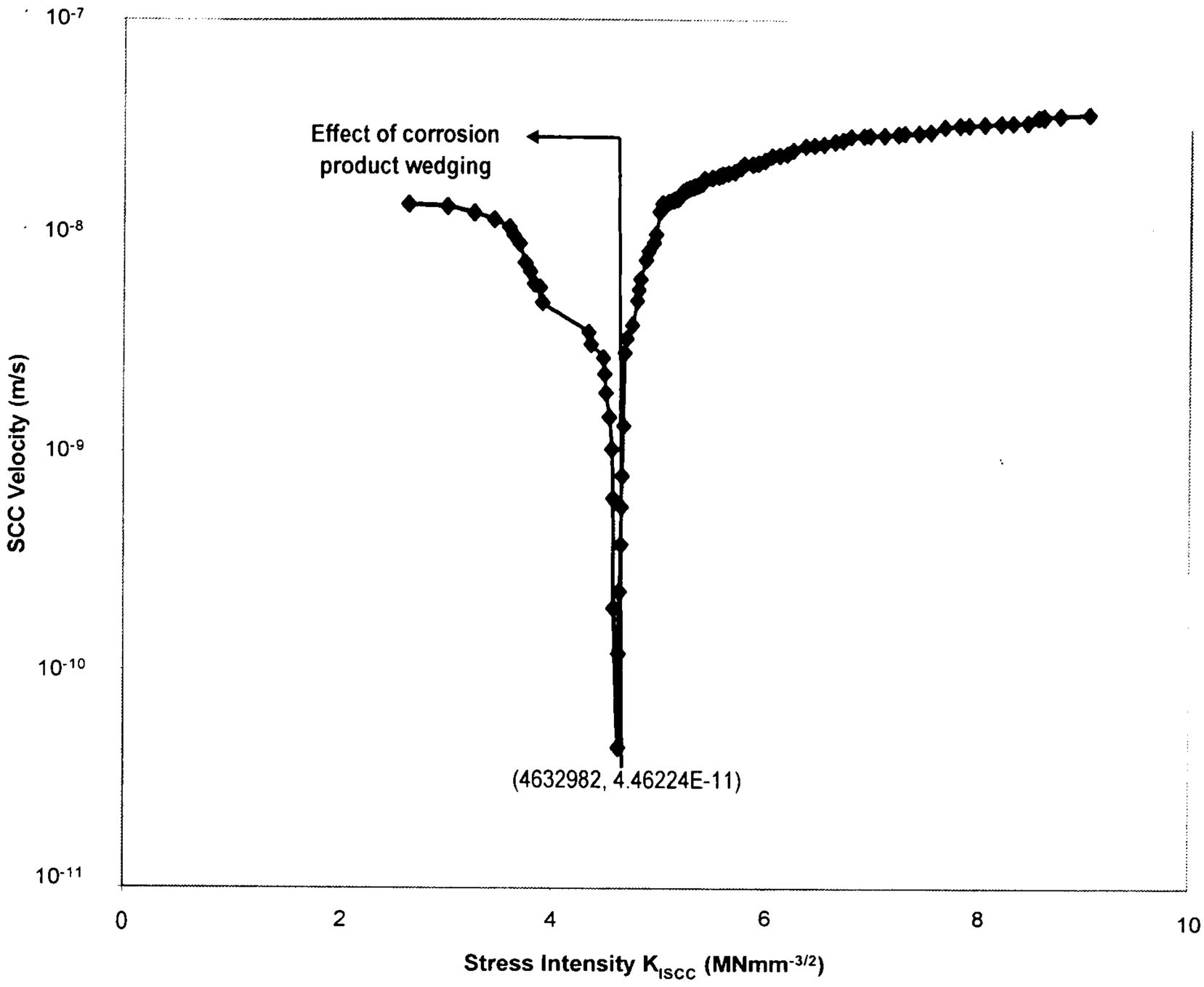


Figure 37 The effect of corrosion product wedging on the V-K diagram.

**5.6 SCC under compressive loading.**

It has been shown that stress corrosion cracking is one of the main problems found in high strength aluminium alloys, and that it occurs at the grain boundaries. Normally, tensile stress is a necessary condition for stress corrosion cracking to occur. However, under special conditions, it has been shown to occur under compressive loading [6].

In 1984, work done by W.Y. Chu et al [115] demonstrated that stress corrosion cracking of austenitic stainless steel occurred under compressive stress. This was achieved by using three different types of specimen, such as specimens with surface residual compressive stress, U-bend and modified WOL notched. All specimens were stressed with compressive stress. The SCC specimens were exposed to boiling 42% $MgCl_2$ solution. At the end of test they found that compressive stress produced stress

corrosion cracking in all specimens, perpendicular to the direction of compressive stress. The crack appeared to be intergranular. However, the SCC growth rate was lower than expected for the tensile loading. They concluded that the mechanism was anodic dissolution under compressive stress. They postulated that a compressive stress may also produce a slip step and cause film rupture at the notch tip and expose fresh metal to the environment.

A year later, W.Y. Chu et al [6] used the same idea to determine the threshold stress intensity ($K_{ISCC}$) value for compressive loading in high strength 7075 aluminium alloy. The modified WOL specimens were tested in a 3.5% NaCl as corrosive environment. They performed experiments to show the difference in stress. Each specimen was stressed with either tensile stress or compressive stress. For each case, they found a threshold stress intensity ($K_{ISCC}$) value of 8.3 $MNm^{-3/2}$ for tensile loading and 27.6 $MNm^{-3/2}$ for compressive loading. They mentioned that a longer incubation time and larger stress, under compressive loading, is required to produce slip and film rupture for dissolution take place along the grain boundaries. In contrast, they also doubted the role of hydrogen embrittlement of SCC under compressive stress due to low hydrogen concentration expected at the crack tip as compressive loading would reduce the size of interstitial sites. Another important piece of work was done by them regarding compressive stress. The same trend was also observed by the same authors [116] when they conducted stress corrosion cracking of mild steel in a boiling 60% nitrate solution. Intergranular cracking was observed in this test.

In summary, from this information, it appears that the mechanism of SCC is the combination of anodic dissolution and the disruption of surface films at the crack tip due to the effect of the compressive stress.

# Experimental Methods

## 6.0 Materials characterization.

It is expected that material properties are important parameters to eddy current testing. These parameters can be correlated to the material's composition, hardness and grain aspect ratio. They can provide indirect measurement of the material properties [117]. For that reason, the experimental section is divided into two parts. The first part of this section covers the hardness measurement of high strength aluminum alloy. The second of the test focuses on material characterization. A set of data of these tests will be used directly in extreme value statistics to obtain the grain aspect ratio. The material characterization used to study this material was also described.

### 6.1 Materials composition.

Stress corrosion experiments were performed on the high strength aluminium alloy 7075 in the W heat treatment condition. The nominal composition, for 7075-W, is shown in table 8.

**Chemical composition (%)**

| Zn | Mg | Cu | Zr+Ti | Fe | Si | Mn | Ti | Cr |
|---|---|---|---|---|---|---|---|---|
| 5.1-6.1 | 2.1-2.9 | 1.2 - 2.0 | 0.25 | 0.50 | 0.40 (max) | 0.30 (max) | 0.20 | 0.18-0.28 |

Table 8 shown composition of aluminium alloy 7075-W [118,119].

The W heat treatment refers to material that was solution treated, quenched and then naturally aged at room temperature. This has given a microstructure that is

particularly prone to stress corrosion cracks, making it ideally suited for these experiments.

### 6.2 Hardness measurements.

There are many factors can affect to the eddy current signal such as alloy microstructure, temperature and hardness changes. All these conditions will also influence eddy current flow in the material [3,15]. Therefore, it is considered an important part of the work to carry out the hardness measurement.

Hardness measurements were taken on a Vickers diamond hardness tester for the 7075-W aluminium alloy rather than using conventional methods that are based on a destructive test. This was done by an indenter pressed into the material and the diagonals of the resulting indentation are measured. The hardness number is calculated from the load divided by the surface area [120]. A micro Vickers hardness machine was used with loads of 100 gf, 200 gf, 300 gf and 500 gf. In each case six measurements were taken to obtain an average value.

### 6.3 Grain aspect ratio determination.

Wrought aluminium products have highly directional grain structures. The grains are elongated in the rolling direction and there is usually a difference in size and shape of the grains between the surface, longitudinal and transverse orientations. As stress corrosion cracking follows an intergranular path it is expected to be strongly influenced by the grain shape and for this reason the aspect ratio of the grains has been determined for each orientation. The grain length and width for the 7075(W) aluminium alloy specimens used in this research are important to assist the study of velocity of the grain boundary attack. The grain shape of the plate material was characterized by optical metallography using a digital scanner microscope.

The plate aluminium alloys displayed the typical pancake shaped grains common to a wrought structure. Figure 38 shows a diagram defining the grain orientation and direction with respect to the rolling direction.

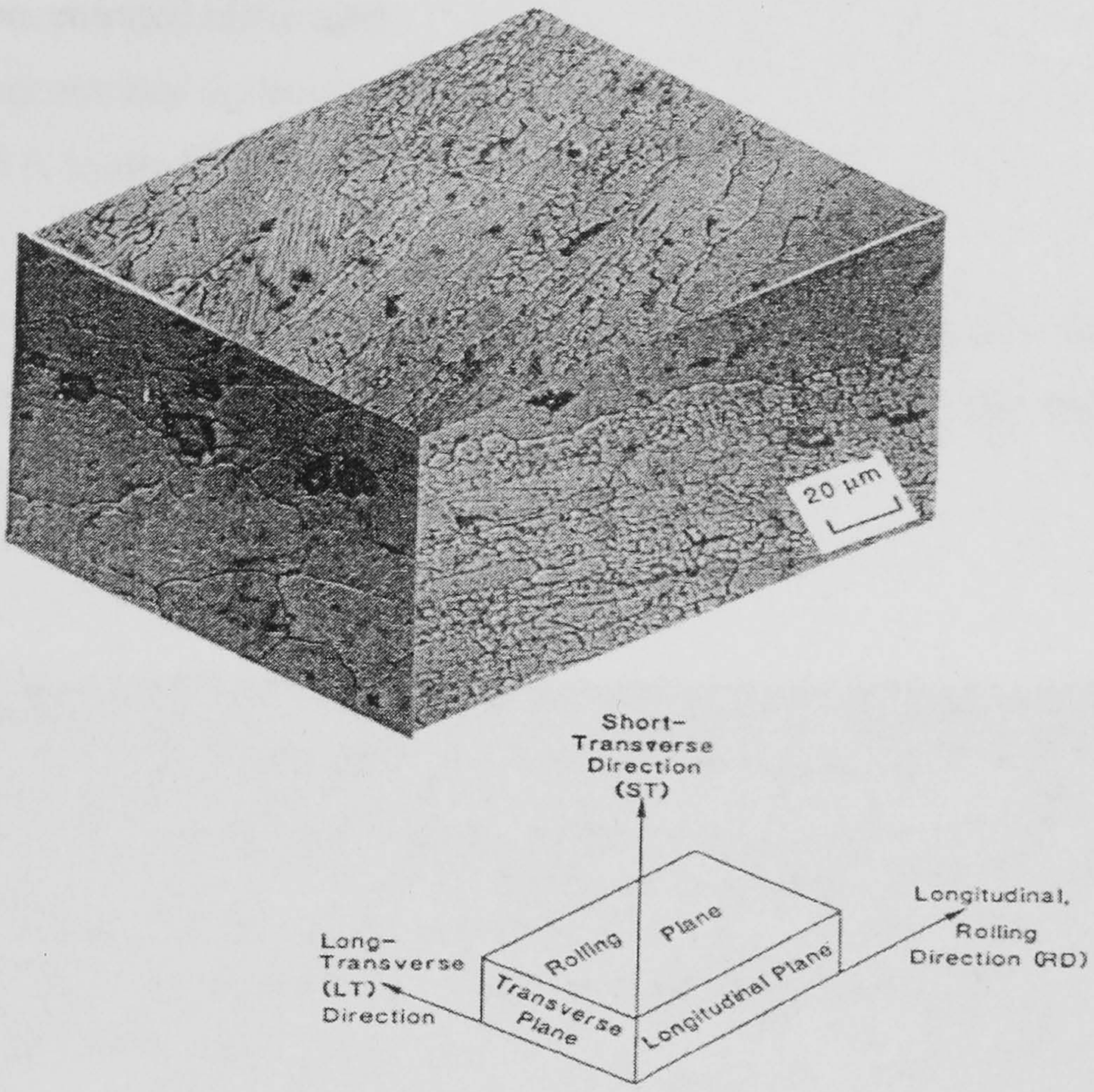


Figure 38 Composite micrograph showing 3 principle directions of the grain structure [25, 121].

### 6.3.1 Optical Metallography.

Specimens of 7075(W) aluminium alloy were taken from strategic points on the plate for material characterization. The grain structure measurements were carried out by optical metallography. Representative samples were machined from the longitudinal and transverse orientations. These specimens were mounted into Bakelite leaving exposed the surface to be inspected and polished down to a 1 µm finish on a cloth polishing wheel.

The grain structure of the alloys was then exposed by etching for 30 seconds with Keller's etch, the composition of which is as follows:

190 ml distilled water

5 ml concentrated nitric acid

3 ml concentrated hydrochloric acid

2 ml 40 % hydrofluoric acid.

The grain structure for each orientation can be seen in figure 39 – 40 respectively. Figure 39 shows the longitudinal grains and figure 40 shows the transverse, with reference to the explanation given in figure 38.

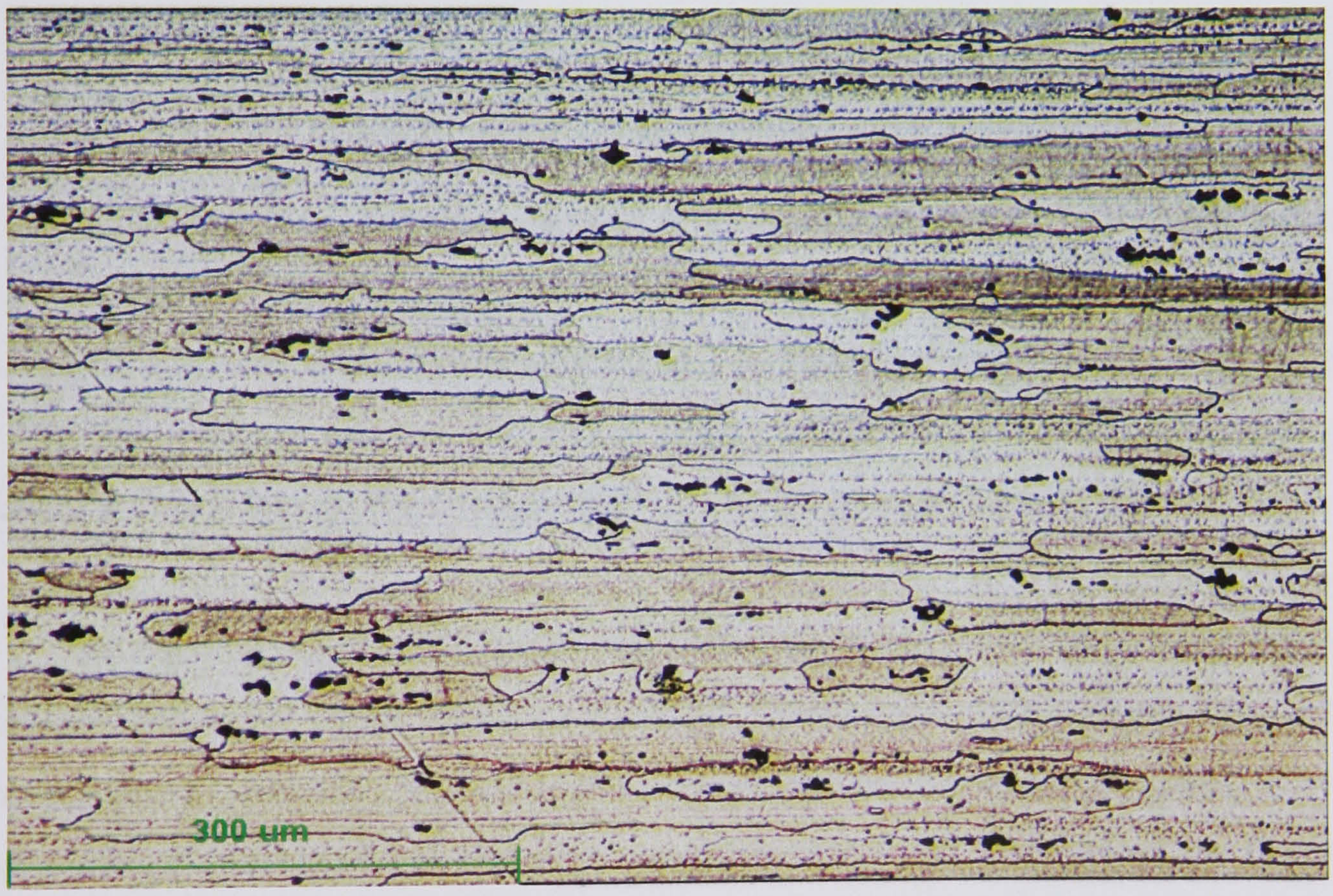


Figure 39 Longitudinal grain structure of aluminium 7075(W)

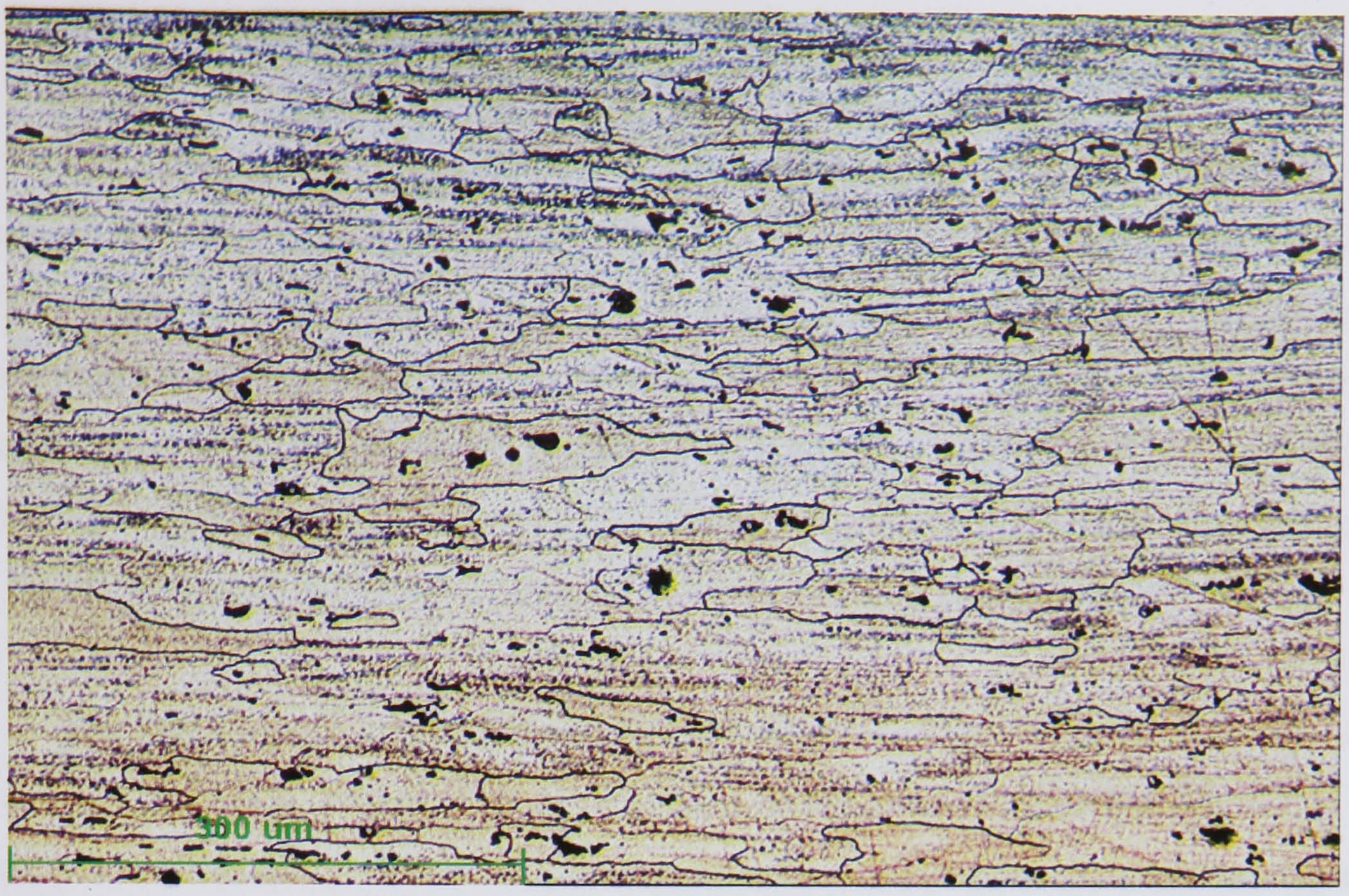


Figure 40 Transverse grain structure of aluminium 7075(W)

Aluminium 7075(W) plates tended to show an un-recrystallised grain structure. The microstructure of the longitudinal section in figure 39 shows that the general trend for material has more elongated grain structure, as pancake-shaped grains. It is expected that from the rolling process the centre grains would be the most elongated grain structure, which is typical for wrought aluminium alloys in the form of plate.

The microstructure of the transverse section in figure 40 shows that the transverse aspect ratio has lower values than the longitudinal aspect ratio. It is strongly believed that stress corrosion cracking (SCC) is much influenced by the grain structure. It would suggest that the longitudinal direction would be the most susceptible to the stress corrosion cracking (SCC) due to its grains having the highest aspect ratio [122].

### 6.3.2 Statistical procedure.

The lengths and widths of approximately 200 grains in each orientation were measured and the highest 10% of the values were used in an extreme value statistical model to calculate the most probable grain dimensions. From these values the grain aspect ratios were determined for each orientation [68,122]. It was assumed that all grains were the same shape and that they appeared to differ in size due to being sectioned at different points. The longest in length and width were therefore measured when the grain was sectioned across its diameter and this will represent the true grain size.

The grain aspect ratios for the aluminium alloys 7075(W) were determined by the use of extreme value statistics. If all the grains in the material were the same size and shape, a metallographic section would display not a single grain size but an apparent distribution of sizes. It is known that only a small proportion of grains would be sectioned through the center, revealing their true dimensions (grain length and width). Therefore the value of the length and width approximates to a normal distribution which gives a characteristic bell shaped curve and the true dimensions would be found at the upper end of the curve. The extreme value model [123] has accumulative distribution function given by:

$$F_{(I\,Max)} = ( X_e ; \mu_e ; \sigma_e) = -\exp\left[-\exp(-1/\sigma_e(X_e - \mu_e)\right] \qquad [12]$$

Where $X_e$ = an extreme value of grain size (length or width)

$\mu_e$ = location parameter

$\sigma_e$ = standard deviation

A plot of $X_e$ against –In (-In $F_{(I\,Max)}$) will give a straight line of gradient $1/\sigma_e$ and intercept $\mu_e/\sigma_e$, where $\mu_e$ gives the most probable extreme value. $F_{(I\,Max)}$ is the cumulative distribution function of the extreme values and is obtained by ranking the grain measurements in decreasing order and calculating R/(n+1) where R is the rank number

and n is the total number of extreme values. The extreme grain length/width is then calculated from the most probable extreme value, a function of the sample size and the standard deviation.

## 7.0 Eddy current calibration.

The main experiment of this work was to concentrate on the development of eddy current testing to detecting stress corrosion cracking in high strength 7075-W aluminium alloys. The important parameters, such as type of probe and frequency required, an also discussed in this section. The first part was the fabrication of a suitable calibration specimen, selection of operating frequency and the eddy current testing on the calibration specimen. The second part of the test was the effect of changes in surface finish to the frequency response. The experiment also defined the correct frequency to detect all depths of defects in the calibration specimen. The eddy current techniques used to study this material were also described.

### 7.1 Eddy current experiment layout.

All eddy current testing conducted in this work involved equipment and a probe originally designed for eddy current testing inside the bore of fastened hole. The main equipment was the NORTEC NDT25 with a CRT impedance plane display and operating frequency range of 60Hz to 6 MHz. The parameters such as frequency, gain setting, sensitivity and phase angle can be programmed and stored for each scan. The NDT25 provides separate analogue voltages output to the horizontal and vertical components of the impedance plane display. The bore probe was specially designed to detect cracks inside 5.0mm diameter holes. The eddy current probe had a single coil to present an absolute signal and was designed to operate at a frequency up to 4 MHz. The probe was mounted into a motion driven table, which allows detection in the horizontal axis.

The driven table was had been made by the Cranfield University workshop. The table itself consisted of a specimen mount and probe holder. The specimen was mounted

on a Perspex locator, which gives a good support to allow accurate positioning. The specimen was held in a fixed in position vertical axis with steel screws. The eddy current probe was held in the probe holder on the trolley. The trolley was mounted on a tubular steel bar and moved by a toothed belt on the pulley. This allowed the eddy current probe to move in and out of the hole by a pulley system driven by a geared stepper motor. The driven table was electrically connected to stepping motor drive Type CD20 and manually controlled for the probe speed in forward and backward directions.

The data acquisition system used for this experiment consisted of an IBM computer, ADC card and HP VEE version 4.01 software which is compatible with Windows 95 program. The ADC card used was 12 bit, 8 channels converted from analogue to digital data. Two channels of ADC card was used to connect into the NORTEC NDT25 for the vertical and horizontal channels which allowed transferring eddy current data to the computer. During the scan, the output response was collected automatically on the computer and converted to a voltage versus time graph for each channel. When the scan was complete, the data was saved to the disc as an ASCII data file. An ASCII data file was opened as text document with a ".DAT" and data written in EXCEL format. During the analysis process, the data was tested to determine the maximum and minimum values for each channel which is finally used for auto-scaling to produce eddy current signal for future analysis. A schematic of the experiment set-up is shown in figure 41. The equipments were maintained in the power-on condition for the duration of the work.

Initially, a problem arose due to the motion of the probe during the test. Care was taken to ensure that the eddy current probe was positioned in the centre of the hole. This procedure was taken to avoid probe wear and minimized lift off caused by vibration of the probe [124]. This is because zero lift off is based on good physical contact between the eddy current coil and the surface of the specimen without vibration or excessive friction. In this case, it was impossible to achieve zero lift off as the eddy current probe moved inside the hole.

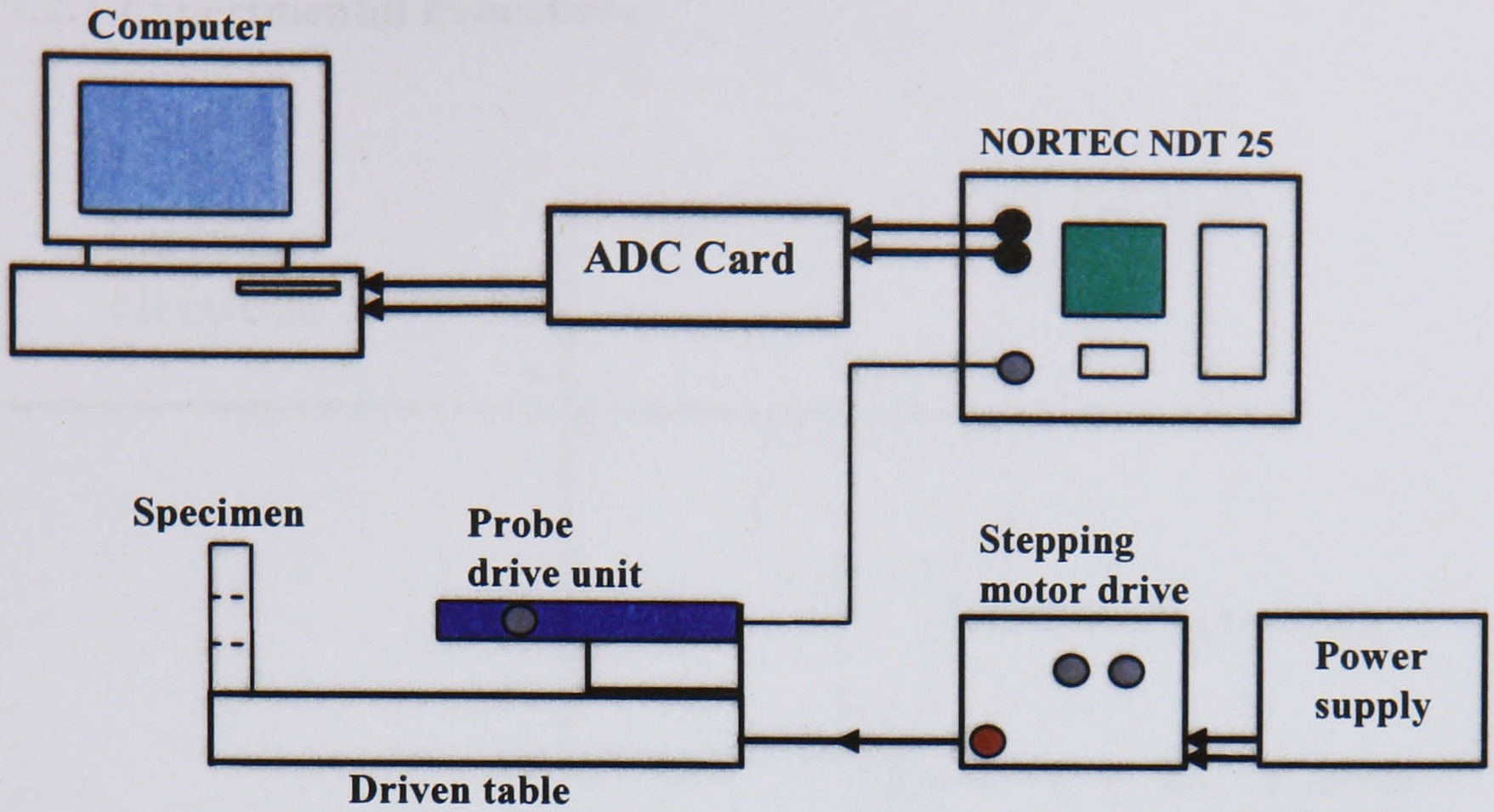


Figure 41 shows a schematic of the experiment set-up for eddy current testing.

### 7.2 Calibration specimen for eddy current testing.

Analysis of eddy current signal is a comparative method. A calibration Standard is necessary for comparing the signal amplitude of unknown defects to the amplitude of known calibration defect. The primary requirement for an eddy current test is to provide a valid calibration specimen that can be related to the minimum crack size to be detected [16]. It was considered important to calibrate the eddy current signals obtained from stress corrosion cracks in the compressive test specimens. For this reason, simulated cracks were produced in a specimen identical in material, heat treatment and thickness to be tested. The electrochemical machining method was selected to produce very narrow defect of known dimensions to simulate cracks in the calibration specimen. This procedure has been used by W.R. Randle et al [124] to produce a reference in alloy steel.

### 7.2.1 Experimental Procedure.

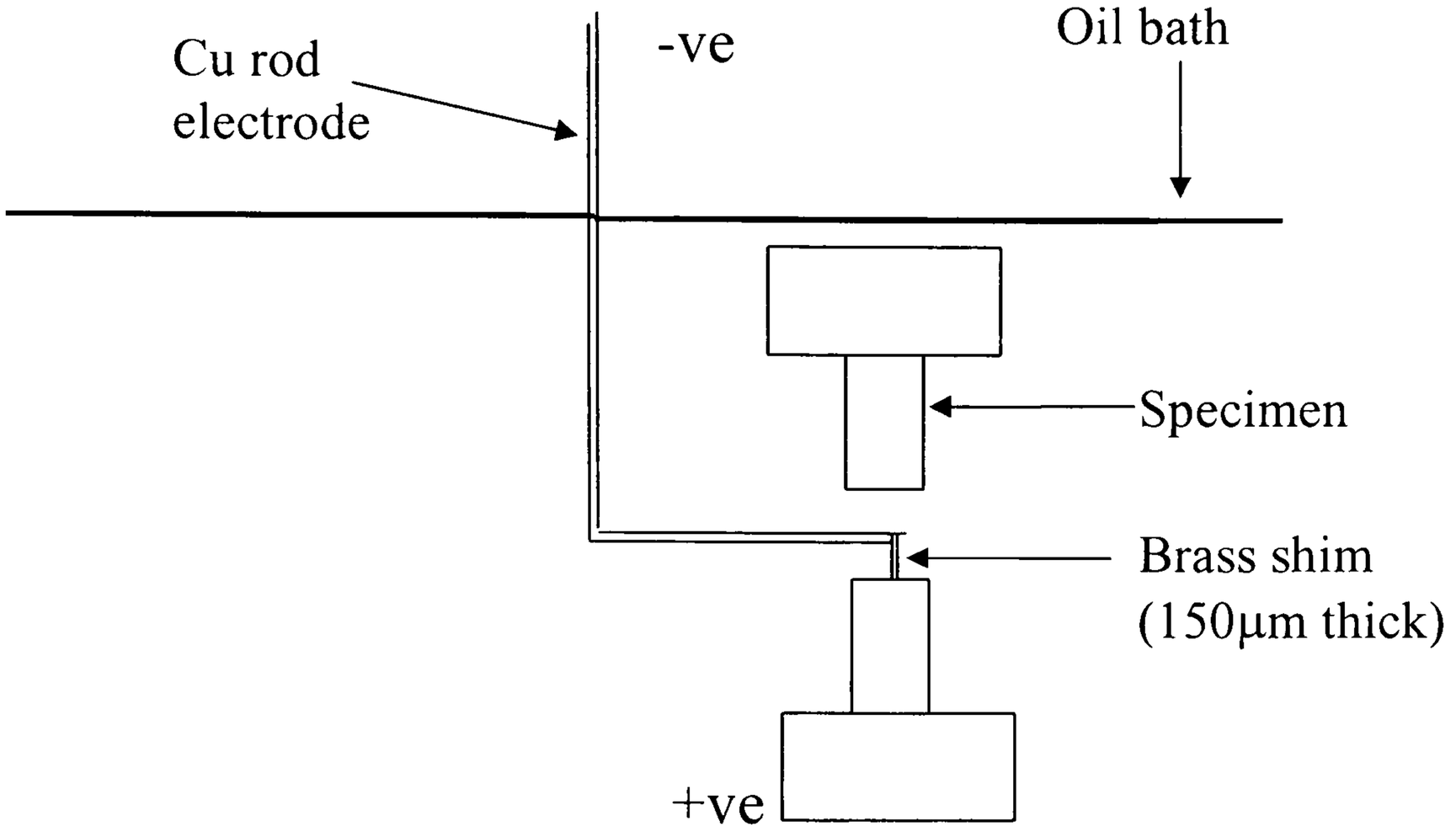


Figure 42 Diagram showing arrangement to produce spark machined defects inside 5mm diameter hole in the calibration specimen.

The experiment made use of an identical size of specimen to compressive test specimen. Figure 42 shows the general arrangement for spark machining defects of differing sizes to produce a calibration specimen. A purpose made electrode consisting of brass shim silver soldered onto a copper rod was used to introduce fine slots with a width of 150 μm to simulate stress corrosion cracks. This was technically difficult to achieve as the hole in the calibration specimen was only 5mm in diameter. Thus in table 9 points a, b, c and d correspond to the following depth of cracks in the calibration specimen.

| Defects | Depth of cracks (mm) |
|---|---|
| a | 0.5 |
| b | 0.6 |
| c | 1.0 |
| d | 1.5 |

Table 9 The depth of simulated cracks in calibration specimen.

Figure 43 shows the location and size of each defect inside the hole of the calibration specimen. It should be noted that the defects were in the plane of the specimen surface as this is the situation for stress corrosion cracking within the bore of fastener holes. The calibration specimen also used to establish the optimum instrument set-up, including frequency, phase rotation, lift-off and gain setting.

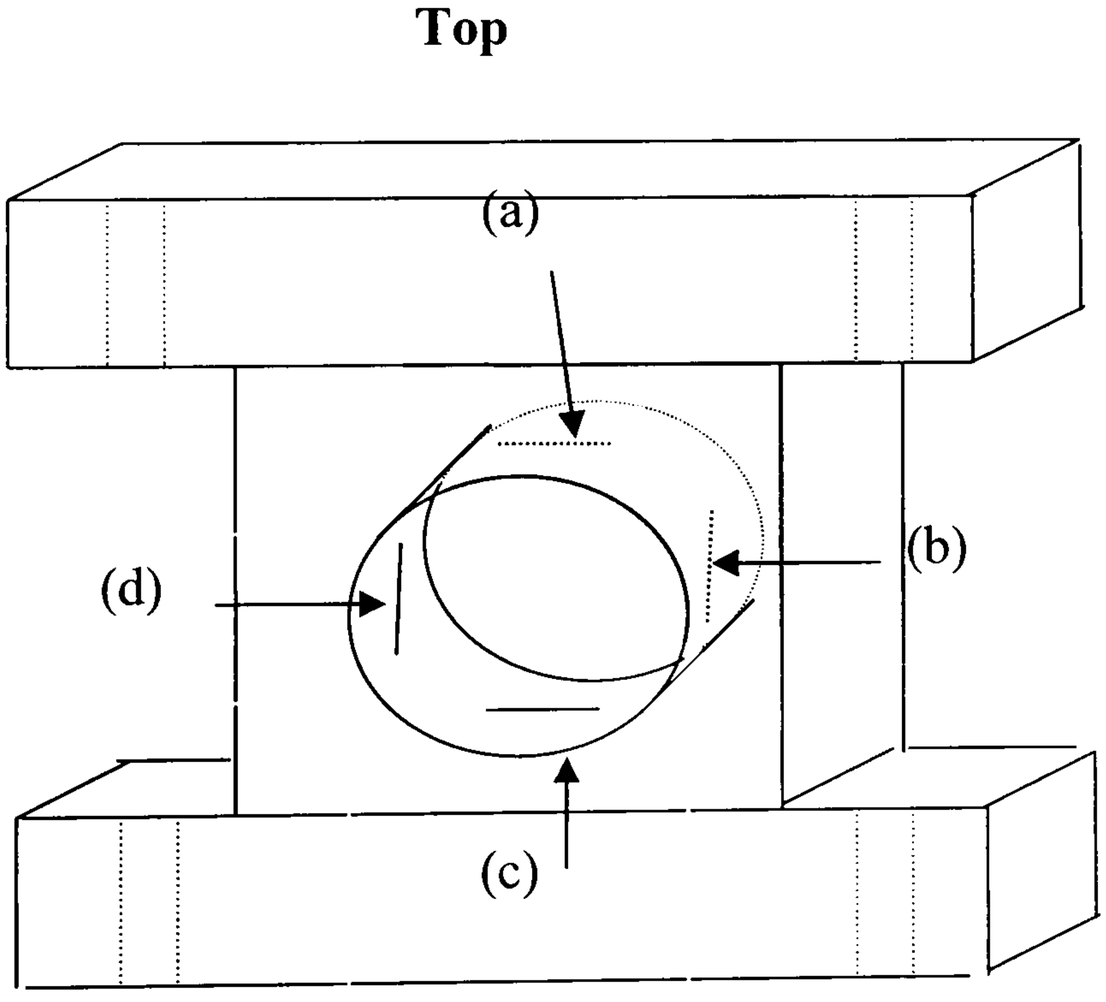


Figure 43 Diagram of calibration specimen with spark machined defects.

We now consider the method for choosing the operating frequency. In order to obtain the optimum frequency, the best method was to show response of the eddy current probe on the CRT instrument [125]. This was done by selecting frequencies of 100 kHz, 180 kHz, 218 kHz, 280 kHz, 450 kHz and 700 kHz and adjusting the gain setting to fit suitably sized eddy current responses on the CRT screen. Before the test, care was taken to ensure that the test probe was positioned inside the hole to avoid the test coil being affected by the edge of the test specimen. The calibration test started with the probe clear of the edge of the specimen. During the test, the specimen was held stationary while the stepper motor driven table moved the eddy current probe through the hole. The probe was moved forward until the simulated crack was detected. As is usually practice, the lift-off signal was rotated to give a horizontal line on the screen with crack signal being displayed as a vertical line on the eddy current CRT. In order to obtain all defects, the calibration specimen was rotated and the test probe was again moved through the hole. The horizontal and vertical positions were set at 20% to allow an image at the bottom of the screen as normally specified [126]. The crack signal for each defect was recorded on a Nortec 24 eddy current CRT instrument and saved on a disc as data files. The graphs were then plotted using EXCEL to provide a calibration allow the stress corrosion cracks that developed in the test machine can be determined.

## 7.3 The effect of changes in surface finish.

In general, in eddy current testing the probe plays two important roles. First, it induces currents in the test piece and second, it detects distortion of these currents caused by flaws in the material. Discontinuities and others variables in the materials can affect the signal presentation. For example, any change such as surface roughness or a corroded surface could be detected by the eddy current technique. An aim of this experiment was to see how the operating frequency responded to the corroded and smooth surface material. It was important to make sure that at every state of this experiment provided with the same setup. The different is only frequency which is under investigation.

### 7.3.1 Experimental procedure.

To test the effect of changes in surface finish on the eddy current signal, two operating frequencies were selected. This experiment used the frequency of 218 kHz and 430 kHz to analyze the signal presentation. Two different surface finishes; smooth surface and corroded surface, were used to scan the inside surface. The smooth surface had not been exposed to any chemical environment. Figure 44 shows a photomicrograph of the smooth surface. The specimen surface was given a light polish with 1200 grit silicon carbide paper inside the hole. It was then degreased by using propanol and rinsed with distilled water. However, the corroded surface was exposed to 3.5% NaCl solution under compressive loading for 60 days. Figure 45 shows a photomicrograph of the corroded surface inside the hole. The eddy current probe was inserted into the compression test specimen and the lift-off signal was rotated to give a horizontal line on the eddy current CRT. Care was taken to ensure that the test coil was positioned away from the edge of the test specimen. Then the eddy current signal was recorded onto the disc. To complete the test, this procedure was repeated with two different operating frequencies and the results were compared.

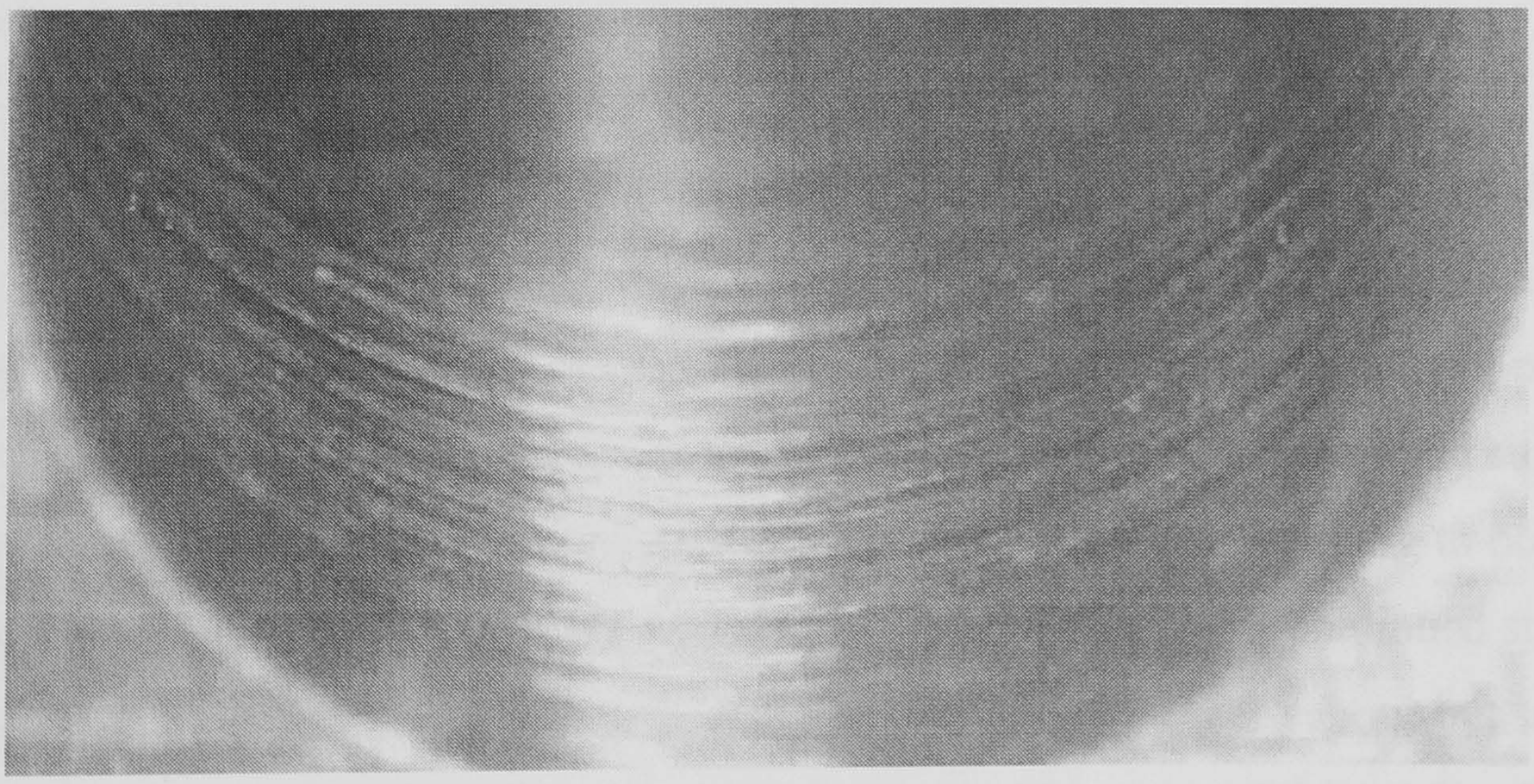

Figure 44 shows a photomicrograph of the smooth surface.

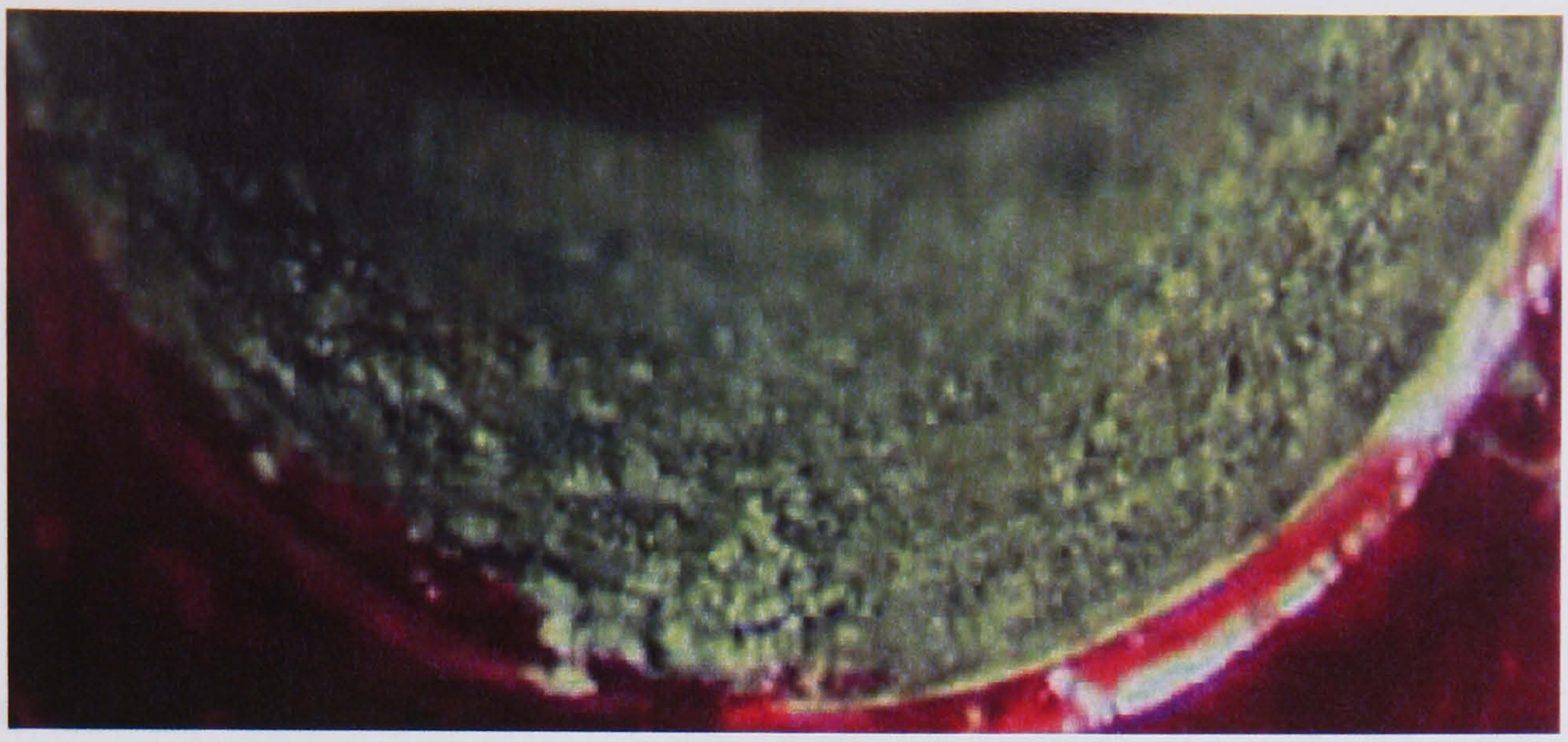

Figure 45 shows a photomicrograph of the corroded surface.

## 8.0 Stress corrosion cracking.

In this section, the experimental programme has been split into two parts. The first part of the experiment is focused on stress corrosion cracking under tensile loading and second, stress corrosion cracking under compressive loading.

### 8.1 Stress corrosion cracking under tensile loading.

Stress corrosion cracking (SCC) is a failure mechanism of a metal generated by the effects of both stress and corrosive environment that occur at the same time to cause progressive fracture [59,96,127]. The required stresses may be in the form of directly applied stresses or in the form of residual stresses and may be significantly below the yield stress. It is usually thought that the stress must be tensile. For stress corrosion cracking to occur, the part must be exposed to the corrosive environment and subjected to a continued stress for a period of time [5,128]. The corrosive environment may be only water vapour but salts, particularly chlorides, often lead to more severe cracking. This type of failure has been found in high strength aluminium alloys such as 7XXX series and occurs by cracking along grain boundaries [5,81].

### 8.1.1 The DCB specimen.

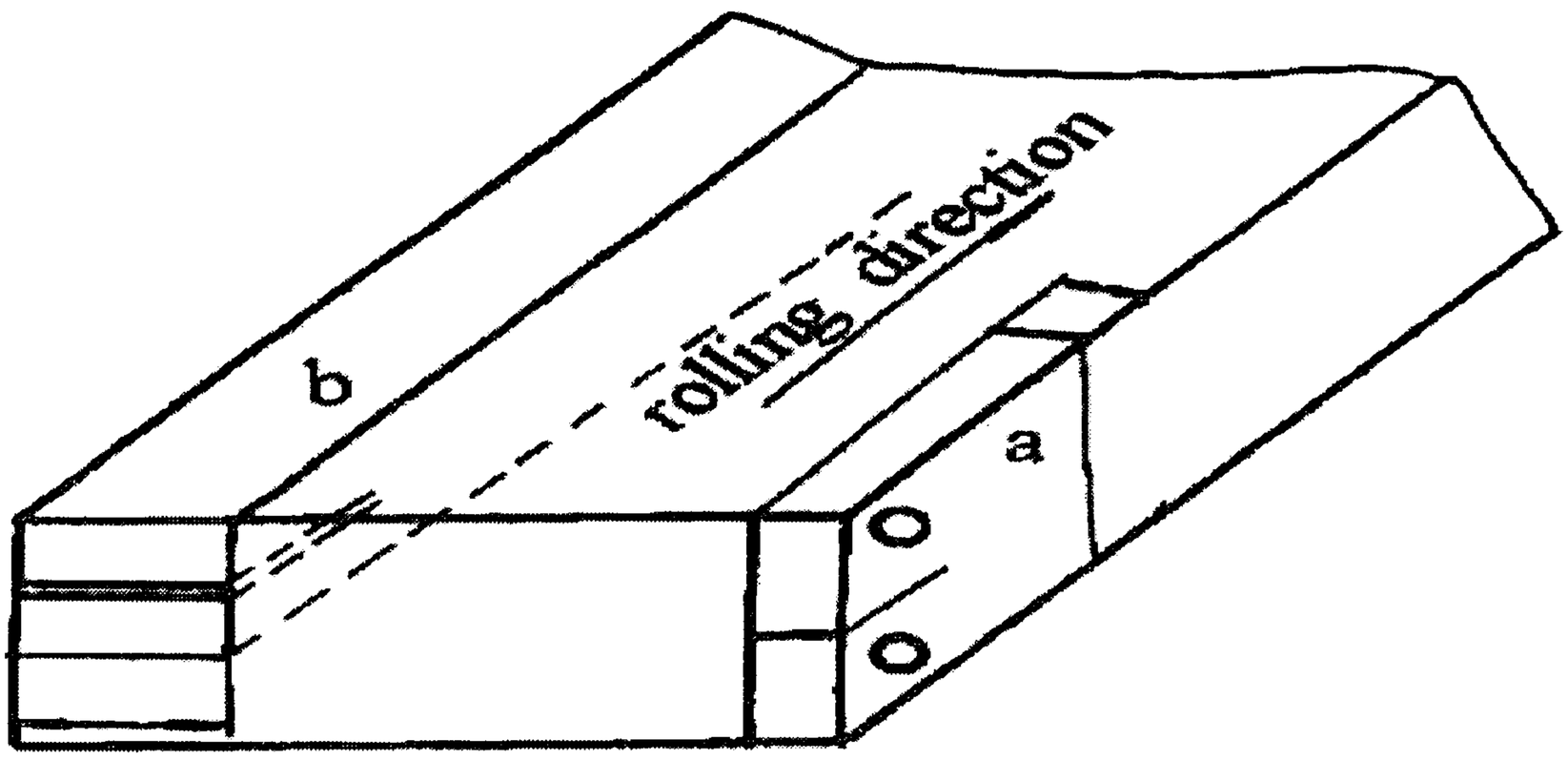


Figure 46 Orientation of the double cantilever beams (DCB) machined from the plate material [110].

The DCB specimens were used to test the stress corrosion cracking susceptibility of the plate material. Specimens were taken from aluminium alloy 7075 plate with the W temper. Figure 46 shows the orientation of specimens taken from rolled plate material. The DCB specimens were machined in the S-L orientation such that the plane of the crack was aligned along the rolling direction, parallel to the plate surface, which is the direction of maximum grain length. On the other hand, the specimens were loaded in the

short direction [87]. This is thought to be the most susceptible [59,109,129] orientation to stress corrosion cracking so that the crack would propagate along the length of the specimen.

Figure 47 gives the details of the dimensions of the test specimens. The DCB specimens were machined to give an angle at the slot of $60^{o}$. Both sides of the specimen were carefully machined in such a way that the length from the slot to the load line or centre of the hole drilled would be 20 mm and 15 mm from the load line to the top of the specimens. The load line was marked as a reference for crack length measurements using a travelling microscope. The specimens were threaded to fit screws of size M8 for applying the displacement across the beams.

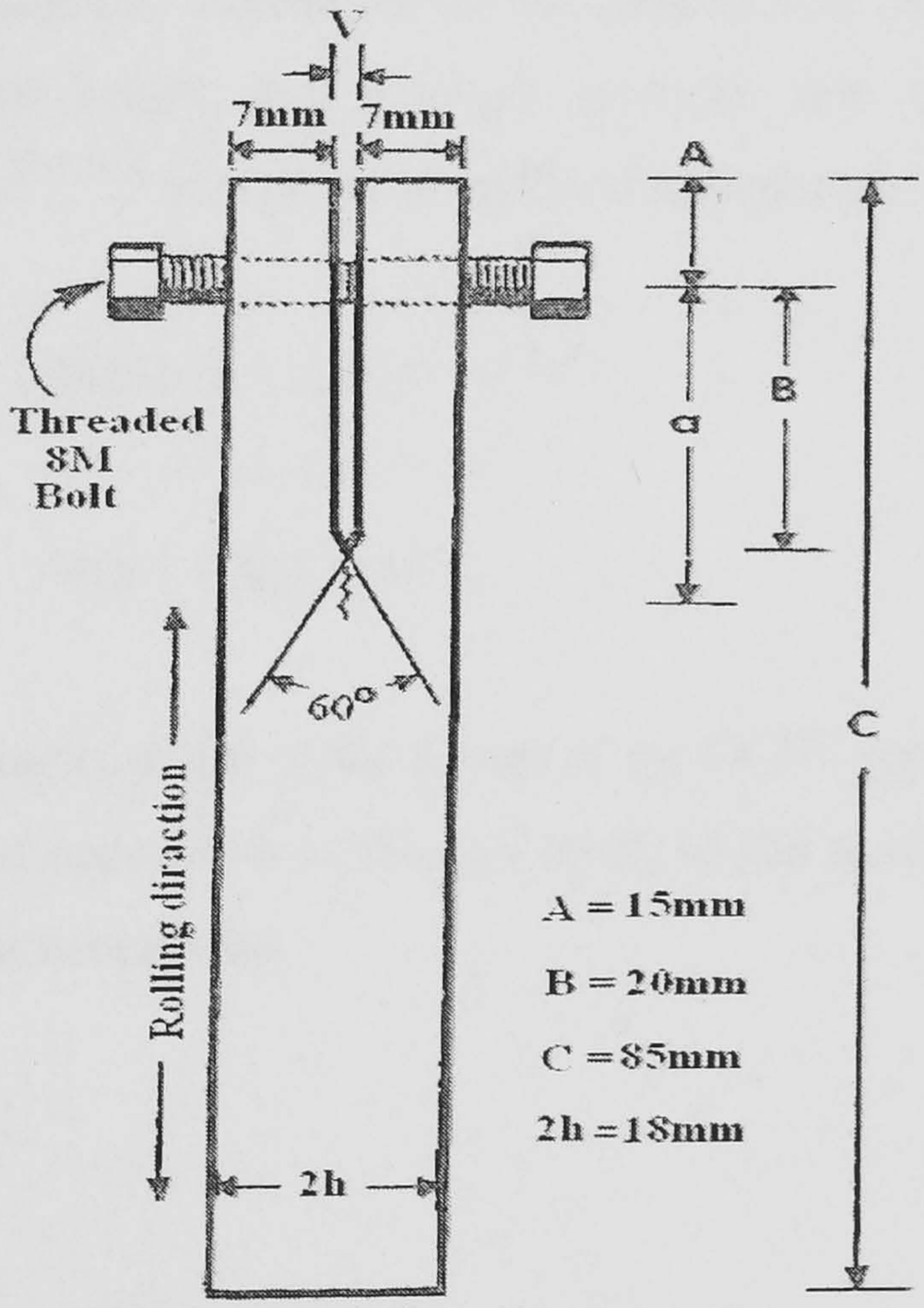


Figure 47 the double cantilever beam specimen.

### 8.1.2 Procedure for setting the initial load

The surfaces of specimens were polished using 1200 grit carbide paper and degreased with propanol. A load line was measured by using the traveling microscope as reference exactly at the centre of the drilled hole. A stress was placed on the end of the machined slot by the displacement of the DCB arms. A suitable displacement of the DCB arms was calculated to give an initial stress intensity at the crack tip. Two different initial values of 15 and 25 $MNm^{-3/2}$ were used [122]. It should be noted that these value was designed to be just below the fracture toughness value ($K_{IC}$). Otherwise, mechanical failure would have occurred when the stress intensity at the crack tip exceeded the above value [130]. The initial stress intensity was thought sufficient to produce region I and region II on the V-K diagram. Therefore, the calculation was made by substituting the beam dimensions, crack length, and Young's modulus into the fracture mechanics equation. This equation [131,132] was put onto an Excel spread sheet for ease of use:

$$K_I = \frac{vEh\{3h\,(a + 0.6h)^2 + h^3\}^{1/2}}{4\{(a + 0.6h)^3 + h^2 a\}} \qquad [13]$$

where v is the displacement of the beams of the DCB specimen at the load line, E is the elastic modulus of material, h is the half width of the specimen, and a is the total length from the load line to crack tip.

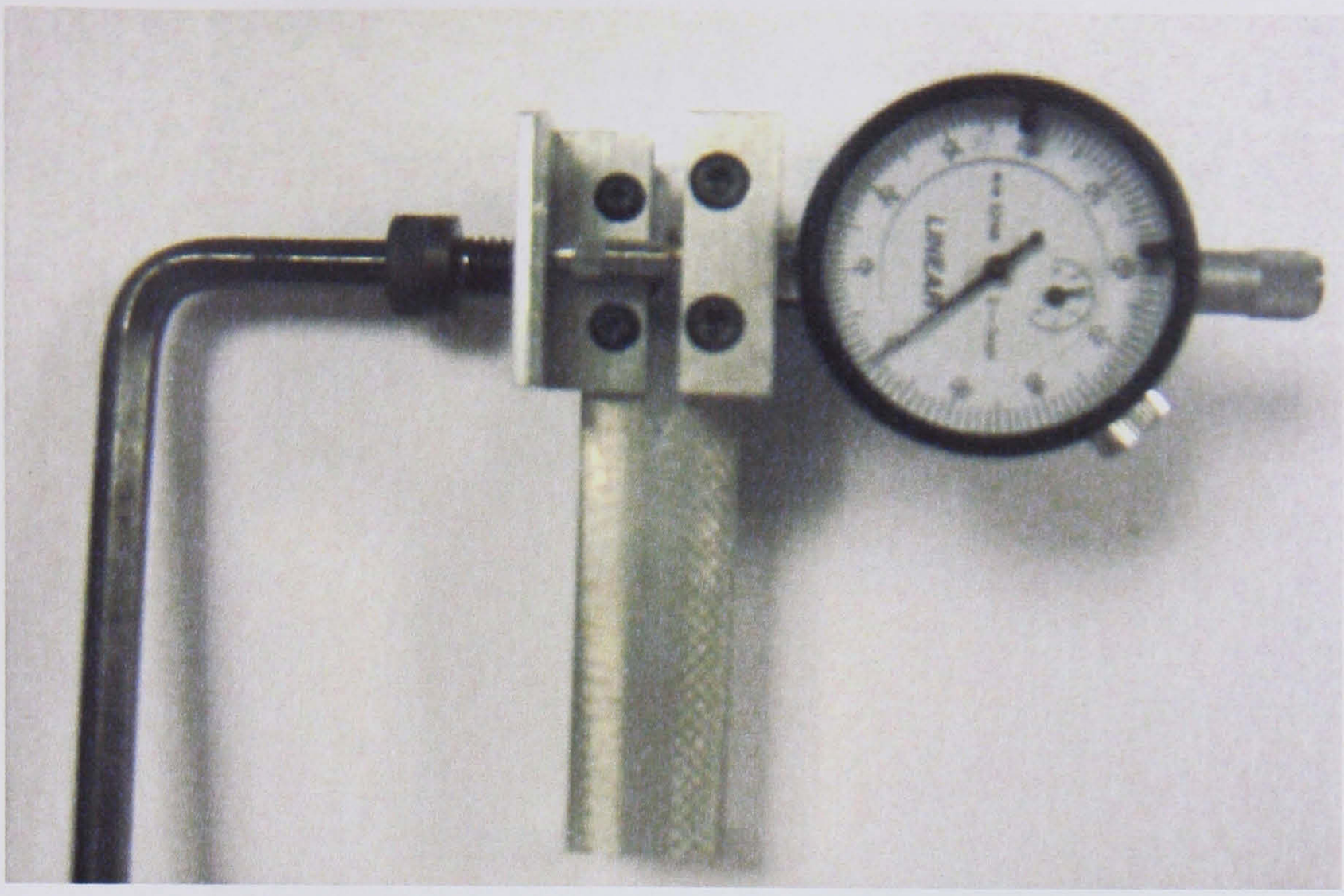

Figure 48 Photograph showing the arrangement for loading the DCB.

In order to measure displacement accurately, the required displacement was set using a dial indicator, which was attached to the DCB arms, as shown in figure 48. This was set by tightening one of the bolts against the other until the required displacement was achieved. The bolts and top portion of the DCB specimens were then covered by wax. This procedure was taken to prevent galvanic corrosion between the steel bolts and DCB specimen. It should be note that the level of the test solution was always kept below the bolts to avoid this problem. The specimen was supported by resting the bolts on the top of the beaker. Figure 49 shows a DCB specimen with bolts coated in wax under tensile loading. In the case of test for 15 $MNm^{-3/2}$, due to the low initial stress intensity, wetting and drying with EXCO of the notch tip was found to be necessary to promote cracking to occur before immersion.

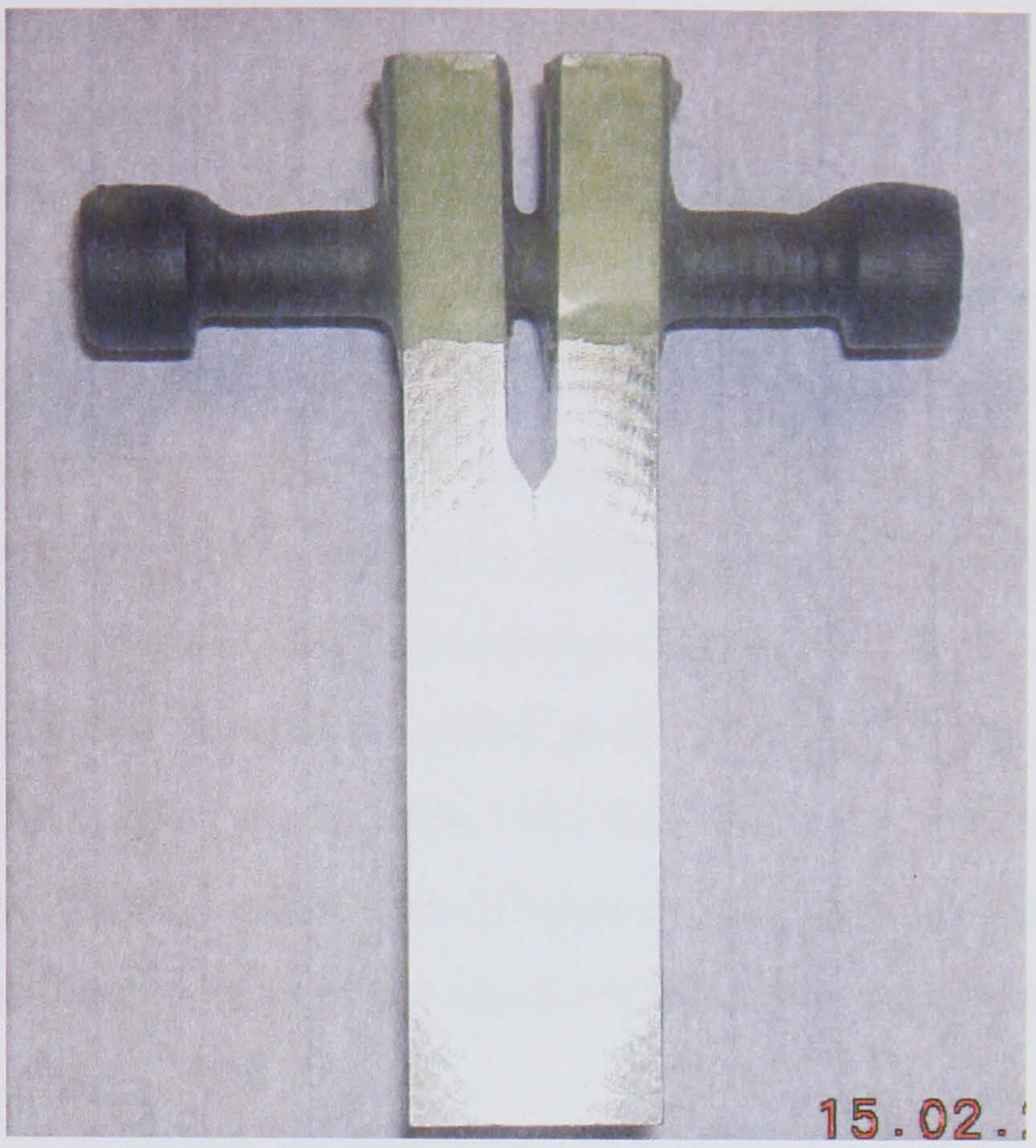


Figure 49 Photograph showing the DCB with the bolts coated with wax.

### 8.1.3 Experimental Procedure

Before exposure of the loaded DCB specimens a scalpel blade was used to remove the oxide film at the root of the slot to promote the initial corrosion attack. The crack tip was then subjected to wetting and drying using 3.5% NaCl conditions to initiate a stress corrosion cracking. After cracking had occurred, the new crack length was measured from the top of specimen to the new extension of the crack tip on both sides of the specimen. The specimens were then immersed to the level of the crack in 3.5% NaCl solution and this was taken to be start of the experiment. During the experiment, specimens were removed from solution for crack length measurements. The crack lengths were measured on both sides of the specimens using an optical travelling microscope and then by averaging both readings. The crack length was measured as a function of time. The measurements were taken from the top of the specimen to the extension of the crack tip. The measurements were carried out every hour, then every three hours for the first few days and then twice a day as the crack growth rate decreased.

Constant immersion over several days caused corrosion product build up around the surface of the specimens. Therefore, the DCB specimens were abraded with silicon carbide paper at 45° angle to the crack direction. This procedure was taken to highlight the crack path, particularly at the end of the crack tip for convenience of measurement. For every measurement of crack length, the time was recorded, so that the calculation of the crack velocities could be made. The measurement of the crack length was taken from an average of the readings from both sides of the specimen. Cracking was allowed to continue until the stress intensity at the crack tip reached a minimum value. At this point the bolts were unloaded to remove the stress at the load line. Then the specimens were again immersed to the level of the crack in 3.5% NaCl solution and the test was continued to measure the crack growth caused by corrosion product loading. At the end of the test the DCB was broken open to observe the crack surface of the specimen.

Graphs of crack length against time were then plotted for each of the DCB specimens. From the graphs, crack velocity was determined by taking gradients from the curves. Every crack length at which crack velocity was measured was used to calculate the stress intensity by using the fracture mechanics equation. From this data, a crack velocity was obtained for each stress intensity and this allowed a crack velocity (V) versus stress intensity at the crack tip (K) to be plotted. These curves allowed the determination of $K_{ISCC}$, the minimum value of threshold stress intensity below which stress corrosion cracking will not occur (safety limit).

### 8.2 The pH measurement of solution at the crack tip.

It has been reported that the pH of solution inside the crack is one of the important environmental factors in high strength aluminium alloys. The pH in a crack is known to be acidic due to the hydrolysis of $Al^{3+}$ ions and the pH is thought to be constant for a range of external conditions. For that reason, information about the pH of the solution within the crack tip of the stress corrosion cracking specimen in high strength aluminium 7075-W alloy has been observed.

### 8.2.1 Experimental procedure.

The double cantilever beam specimens used for crack growth measurements were used in this test. The solution at the crack tip was tested after the crack stopped growing. When the DCB specimen was taken out of the 3.5 % NaCl solution small droplets of solution were visible at the crack and these were tested with pH paper. The measurements were made without the DCB specimen broken apart. The pH measurements have a value of ± 1 unit. Measurements were made near the crack tip on the side of the specimen. The small droplets were tested by placing dry pH paper onto the side of crack. The pH paper was then left for a few minutes to allow access of the solution to react with pH paper. This was to make sure that the final colour had been achieved before observing the colour change. Finally, the readings of pH were carried out by comparing the colour from the pH paper with the calibration colours.

## 8.3 Eddy current measurement of SCC under tensile stress.

The DCB specimen has been used for measuring the stress corrosion crack velocity in high strength aluminium alloys. In previous measurements, the crack length was optically measured on the both sides of the specimen. These crack lengths were used to calculate stress corrosion crack growth rates as a function of the applied stress intensity at the crack tip. However, it appeared that crack bowing had occurred [132-136] at the centre of the DCB specimen as crack the developed. The advancement of the crack front with bowing at the centre during the stress corrosion test can cause errors in the crack length measurement. Figure 50 shows an example of the crack front bowed at the centre of the DCB specimen.

Since, the objective of this experiment was to establish the curve of amplitude of the eddy current crack response (mV) against crack length (mm), it was important to accept that the crack front was not a straight-line. Therefore, it was important to display and determine the extra crack length due to crack bowing during the stress corrosion crack test in DCB specimens. In order to do that an ultrasonic technique [132,134] was

considered as one of the methods for assessing the final crack length. In this test, an ultrasonic C-scan was used together with a travelling microscope to obtain the extra crack length. Then the extra crack length was added to the original crack length. Finally, all data from DCB specimens and stress corrosion crack specimens was then plotted to establish the curve of amplitude of the eddy current crack response (mV) against corrected crack length (mm).

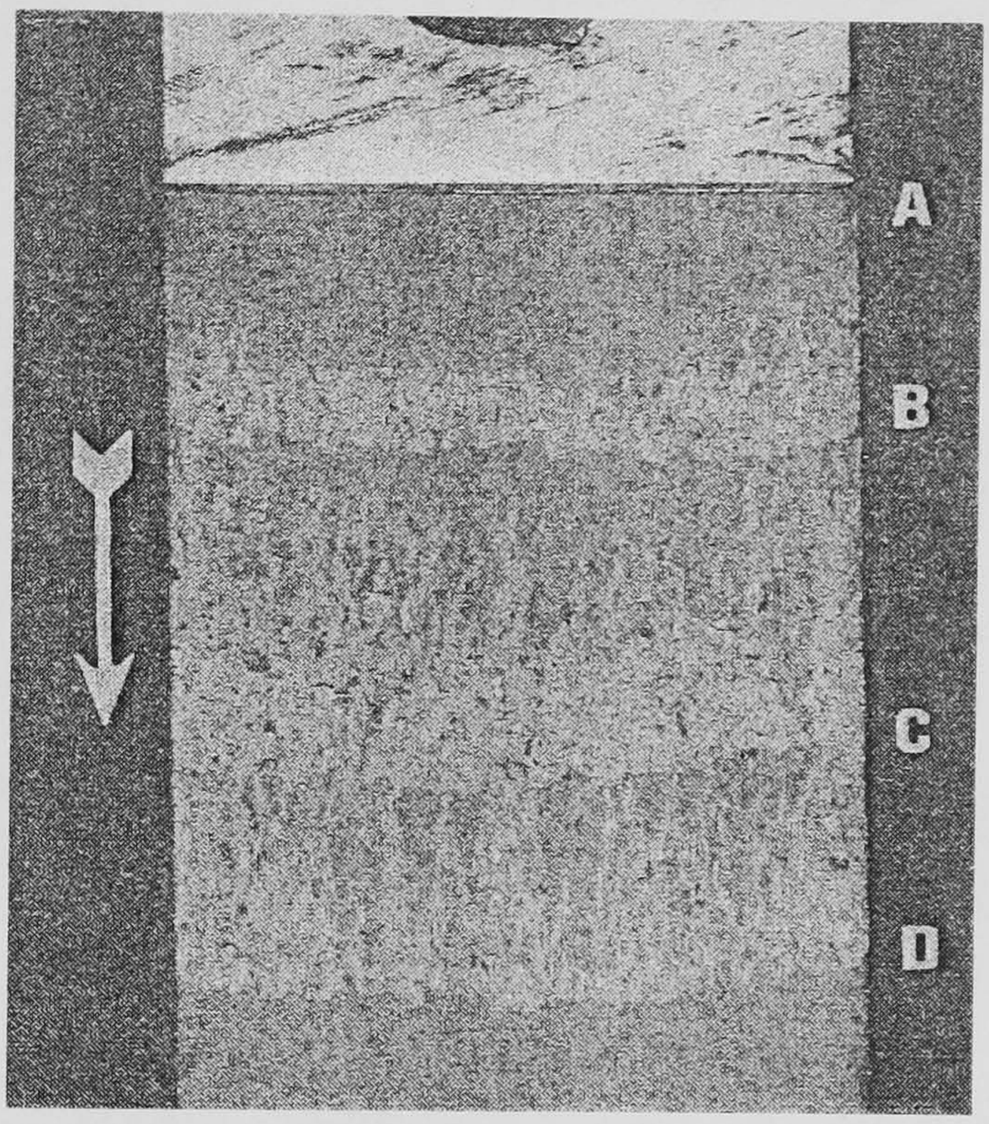


Figure 50 Example of the crack front bowed at the centre of the specimen [135].

### 8.3.1 Test Specimen.

In order to find the extra crack length due to bowing at the centre of specimen, a separate experiment was carried out to identify the position of the crack front. Each DCB specimens were drilled with one hole, 5mm. in diameter, right through the thickness, normal to the plane of crack and plate surface. During the drilling and reaming process, the DCB specimens were clamped on both sides to avoiding the crack advancing. A light cut was performed to avoid deformed metal blocking the crack. Since the bowed crack front was considered an important parameter, care was taken to ensure that the holes were

always symmetrically position as near to the centre as possible. Figure 51 shows schematically the location of the drilled hole in the DCB test specimens.

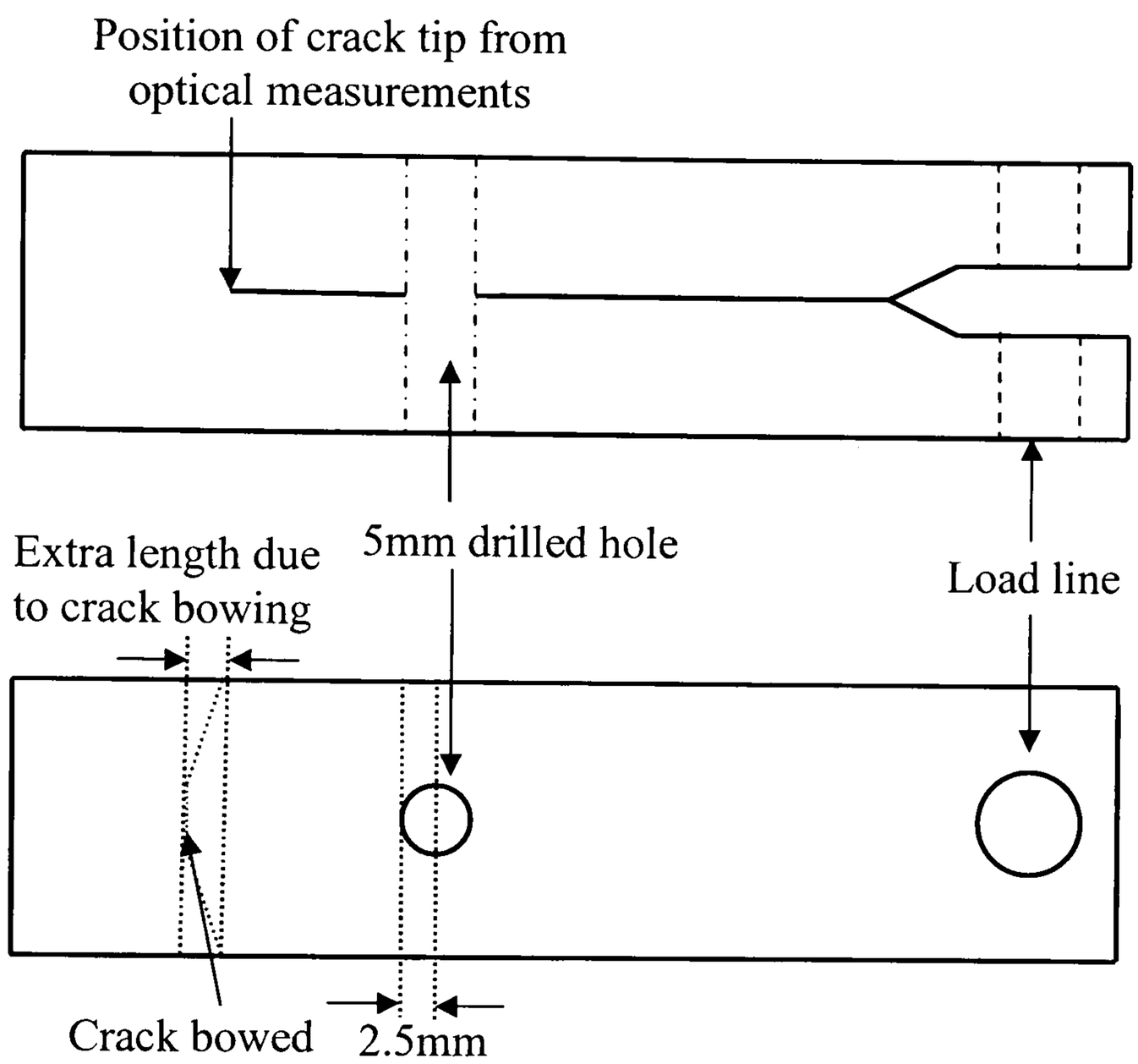


Figure 51 shows diagram of DCB dimensions for Eddy current testing.

### 8.3.2 Experimental Procedure

The crack lengths from the 5mm diameter drilled hole were measured on both sides of the specimen using an optical travelling microscope. The measurements were taken from the edge of the drilled hole to the crack tip. Three values were obtained during each measurement procedure. Two values were measured on an optical travelling microscope on both sides of the DCB specimen and the average from the both sides was calculated. Then the amplitude of the eddy current signal inside the drilled hole was measured. The probe inside the DCB specimen and required to pull in and out until the crack was detected. During the test, the eddy current coil must be facing the plane of crack at the centre of specimen. The liftoff response was rotated to give a horizontal line

on the oscilloscope with the crack response in the vertical direction. While the probe was moved along the hole, the horizontal and vertical coordinate output signals were saved to the disc. The crack signals were recorded as a permanent record for the future analysis. The crack depths were identified from the amplitude of the vertical coordinate signal. The amplitude of signal was measured from the base line lift off to the maximum peak for each scan. Measurements were carried out at regular intervals for a few weeks. Sometimes the crack stopped growing between the measurements, and the specimen was then immersed into water for a few minutes to provide the electrolyte required for further corrosion to occur. As a result, the crack grew for a few millimeters and by repeating the procedure extra data could be taken from the specimen.

In the middle of the test, the DCB specimen was scanned from the drilled hole to the end of specimen using the ultrasonic C-scan nondestructive technique. The scan images were recorded as a permanent record for analysis. This technique provided an image of the crack path and allowed crack length to be measured accurately from crack tip at the centre to the end of the specimen. The ultrasonic C-scan image provided the extra length of the bowed crack. In addition, this method made it very easy to identify the crack length at both sides of the specimen. With this technique, the DCB specimen and the ultrasonic transducer were immersed in water that provides as the coupling medium for the ultrasonic wave propagation.

### 8.4 Stress corrosion crack under compressive loading.

In this section, the experiment has been split into three parts; stress corrosion cracking under compressive loading with a 3.5% NaCl solution, stress corrosion cracking under compressive loading with EXCO solution and finally stress corrosion cracking under compressive loading with EXCO solution by immersion technique. The following section concentrates on the first part of the experiment.

### 8.4.1.1 SCC under compressive loading with 3.5% NaCl solution.

It is normally agreed that stress corrosion cracking can occur with the presence of loading and a corrosive environment. The last section, described stress corrosion crack under tensile loading. It has been reported that stress corrosion cracking may also occur under compressive loading [6]. It was therefore decided to try a new piece of work under compressive loading. The objective of this experiment was designed to discover whether compressive loading can produce a stress corrosion cracking in the specimen if both compressive loading and a corrosive environment were supplied.

### 8.4.1.2 Test specimen.

The specimen for the compressive loading experiments was designed as shown in figure 52. A specimen had one 5mm diameter hole drilled right into the center of the 10mm thick sample to simulate a rivet hole. The hole was arranged symmetrically as near to the centre of the specimen as possible. Mounting holes were machined at the top and bottom of the specimen to allow secure fixing to the compression rig. The hole was reamed after drilling to achieve a smooth surface. The specimen was given a light polish with 1200 grit silicon carbide paper inside the surface of the hole. This was necessary to remove all dirt from the surface. This was done to attempt to achieve a uniform finish. The specimen was degreased by using propanol and rinsed with distilled water. Then the surrounding surface was protected by coating using lacomit lacquer. This procedure was taken to make sure that the area of attack was limited to the rest of the centre of the specimen surface.

It is necessary to point out that the same dimension of specimen was used throughout this work. This test was intended to study the growth of stress corrosion cracks inside the hole when the specimen was loaded in compression. This loading was expected to cause a through thickness strain in the specimen in a direction parallel to the central hole.

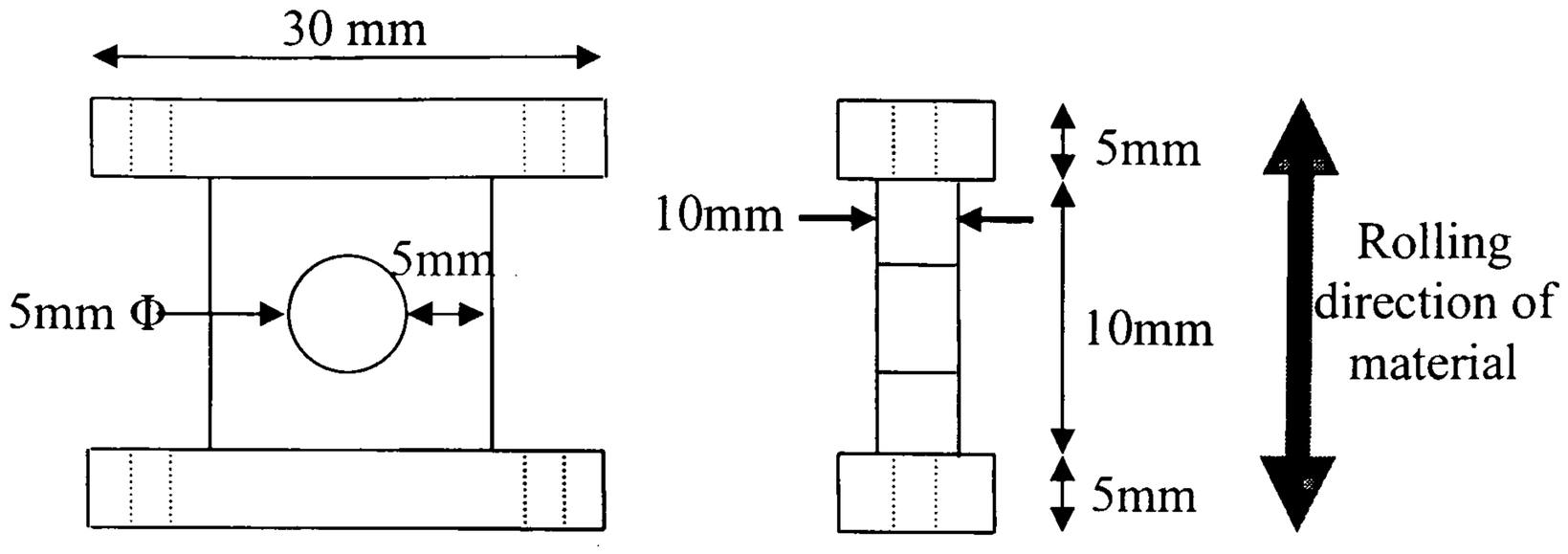


Figure 52 Diagram of 7075(W) compressive test specimens.

### 8.4.1.3 Experimental procedure.

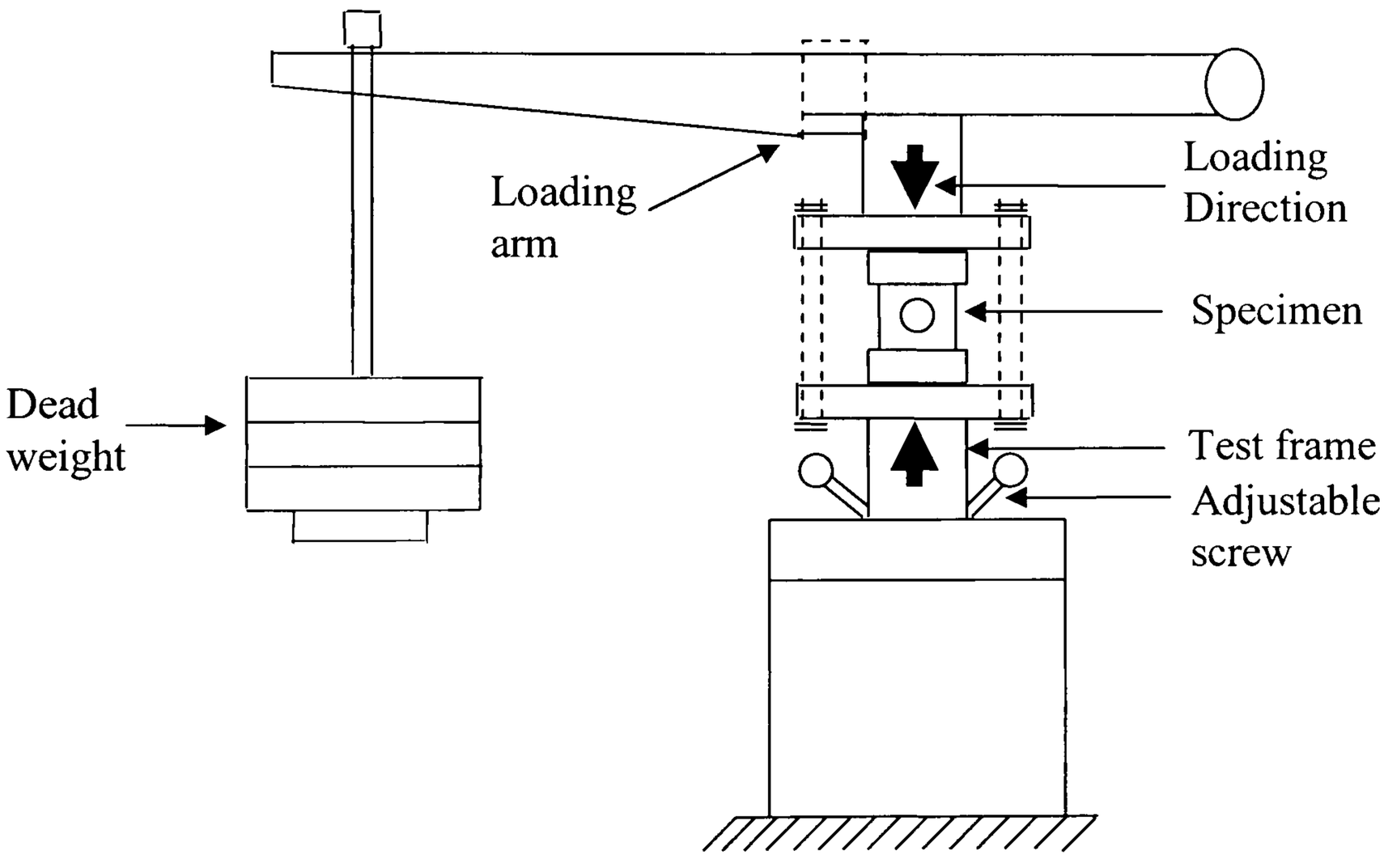


Figure 53 the experiment set up of stress corrosion cracking test specimen on compressive rig machine.

Figure 53 shows the experimental set up of the stress corrosion cracking test specimen placed on compressive rig machine which the hole facing out to allowed the corrosive solution access to the hole surface. Loads were added to the loading beam which stressed the specimen in compression through a 10:1 lever arm. The compressive

stress applied around the hole was 375 $Nmm^{-2}$. This is thought to be slightly above the yield stress of 7075(W), so some local yielding was expected. Finally, the hole in the specimen was wetted and dried in a 3.5 % NaCl solution at daily periods to induce stress corrosion cracking in the hole. The specimen was exposed and left to dry using this procedure in constant room temperature for two months.

At the end of the test, the specimen was removed from the compressive rig and washed in running water and dried thoroughly to prevent any further degradation. The lacomit lacquer around the edge of the hole area was removed before examination by eddy current testing.

In the case of eddy current testing, the probe had a single coil to give an absolute signal and was designed to operate at a frequency up to 4 MHz. In this case, the operating frequency of 218 kHz, Gain 98 dB and phase angle of $282^0$ was used to provide the same set up as with the calibration standard. The corrosion product build up at the surface inside the hole was removed by using a reamer. The eddy current test was started with the probe just inside the hole and clear of the edge effect. During the test, the specimens were held stationary while the stepping motor driven table moved the eddy current probe in and out of the hole. The probe was moved forward until the signal from a pit or crack was detected. The instrument was adjusted so that the lift off was displayed as a horizontal line, whereas the signal from a pit or crack was shown as a vertical line on the oscilloscope. After one area of the hole had been examined in this way, the probe was rotated to scan new area and the procedure was repeated. All the data collected was saved in a computer and later displayed using EXCEL software.

#### 8.4.2.1 SCC under compressive loading with EXCO solution.

According to results obtained from section 11.4.1 it was decided to use a more aggressive solution to try to develop stress corrosion cracking in the hole. EXCO solution with pH of 0.4 has been reported as very aggressive to aluminium alloys and suitable for promoting corrosion in the form of both exfoliation and stress corrosion cracking. In this

experiment EXCO solution was used but otherwise the conditions were as described in section 8.4.1.1. These results are reported in the following results section.

### 8.4.3.1 SCC under compressive loading with immersion technique.

Next we considered the case where the specimen was exposed to fresh EXCO solution all the time. The previous experiment had clearly shown some damage of material through the wetting and drying technique. It was therefore decided to test with a full immerse technique in the following experiment in order to have more fresh EXCO solution to react with surface.

### 8.4.3.2 Preparation of full immersion cell.

The surrounding area of the specimen should be protected from the EXCO solution which causes corrosion damage so that only the hole is exposed. In order to achieve that, two pieces of 20mm x 15mm were made from 7mm thick PTFE sheet. Each piece had one 3mm diameter hole drilled from the side right through the center of the specimen with a cylindrical section 6mm in diameter and 5mm long. The cylindrical section was used to allow EXCO solution to enter to the hole in the aluminium specimen. Figure 54 shows schematically the location of the hole. Care was taken to ensure the holes were aligned to fit onto the sides of the test piece to produce a leak free cell.

A toolmaker's clamp was necessary to hold the cell in position as shown in figure 55. Two pieces of 100mm x 20mm were made from 3mm thick commercial stainless steel sheet. Each piece had two 3mm diameter holes from the side right through the specimen. Each piece had clearance hole and threaded hole section with 3mm in diameter. The two holes were separated 40mm in length. A small force was applied by the toolmaker's clamp to the edges when the two stainless steel plates screwed together. This clamp was used to prevent movement whilst the EXCO solution was running through the hole of the specimen and prevent the possibility of solution leakage

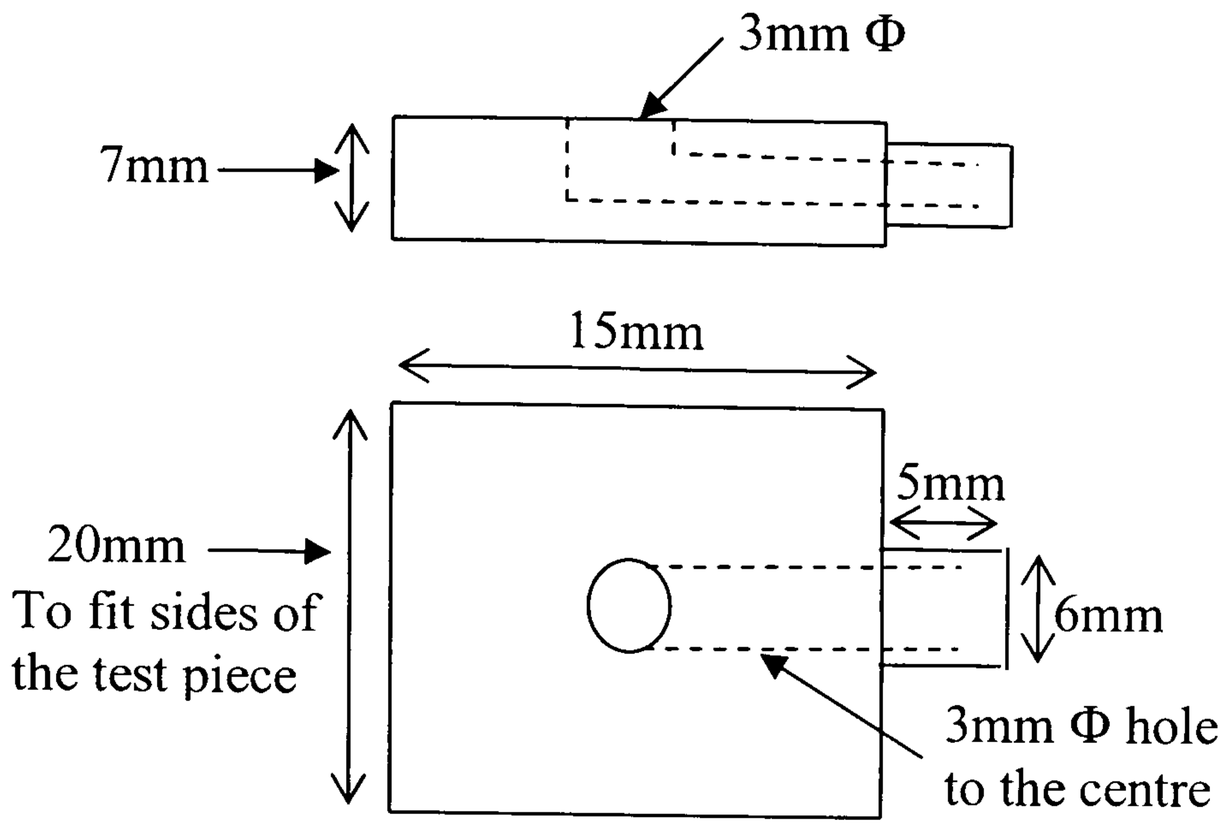


Figure 54 Schematic diagram for specimen used to produce a full immersion cell.

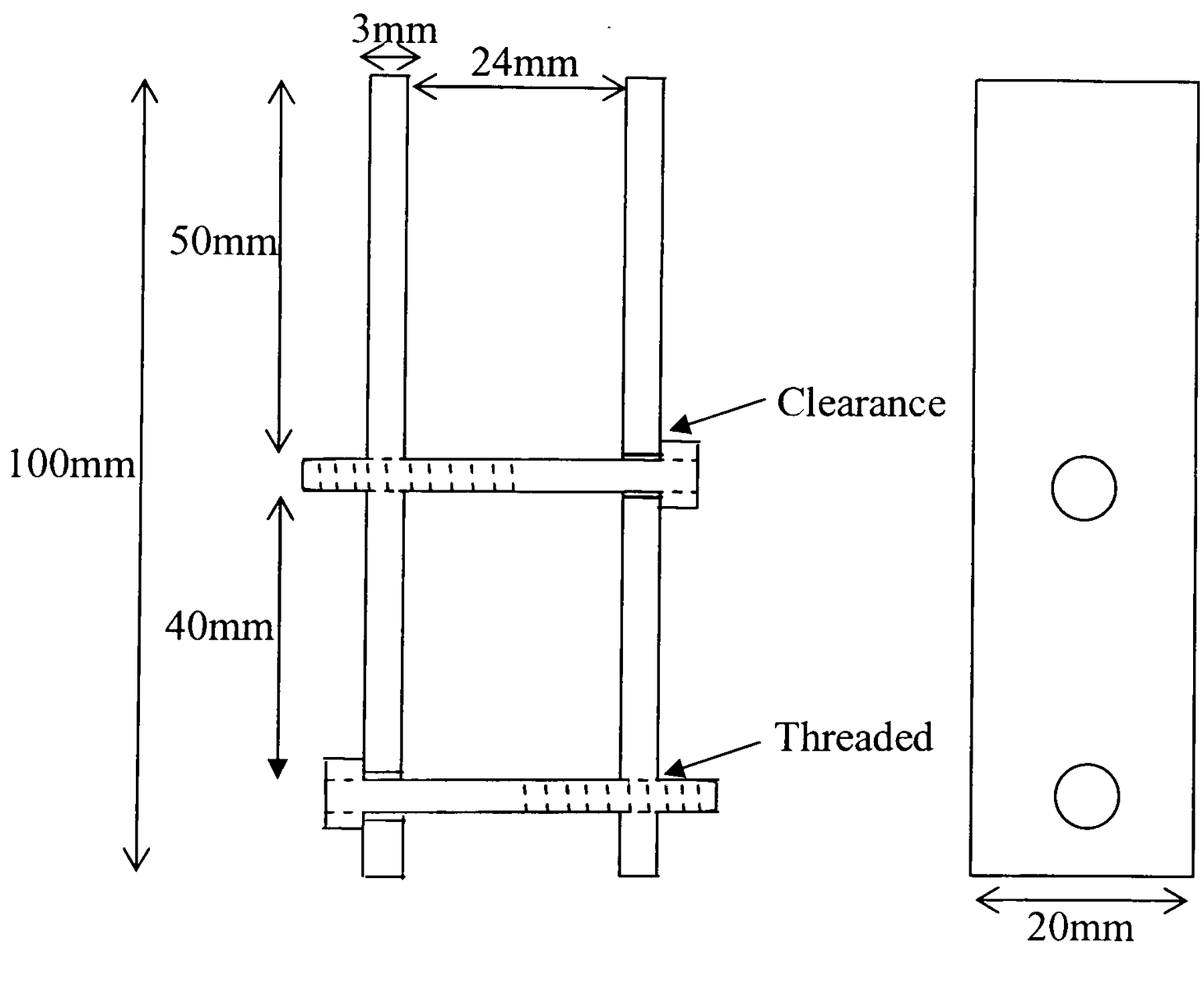


Figure 55 Schematic diagram for the toolmaker's clamp.

### 8.4.3.3 Experimental procedure.

Before every corrosion introduction, the specimen and cell were degreased by using propanol and rinsed with distilled water. A small amount of silicon sealant was applied to each side of the specimen before the cell was assembled in order to avoid leaks. The sealant has a high degree of flexibility and can be removed very easily with propanol allowing visual inspection of the hole. However, care should be taken to make sure that the sealant does not enter the hole and prevent corrosion of metal surface. The silicon sealant was removed as soon as the corrosion test was completed. This is thought to avoid an additional lift-off between specimen and corrosion product due to overlapping with silicon sealant.

Each piece of the cell was placed over the sides of the test specimen. Care was taken to ensure that the piece was positioned so that its centre was always in the centre of the specimen, according to the position of the hole. The cell was held by a toolmaker's clamp. An Allen key was used to turn the centre screw of the clamp so that a force was applied to the cell. The cylindrical sections were connected to a reservoir and tap by using PVC tube. Fresh EXCO solution was poured into the reservoir and by opening the tap some solution flowed into the cell and contacted the hole in the specimen. It should be pointed out here that EXCO solution was completely drained out from the system and replaced with another fresh EXCO solution in every 5 hours(during the day) and this procedure was continued for 2 weeks. This procedure can be shown in figure 56. In all, five sets of specimens were used in this experiment.

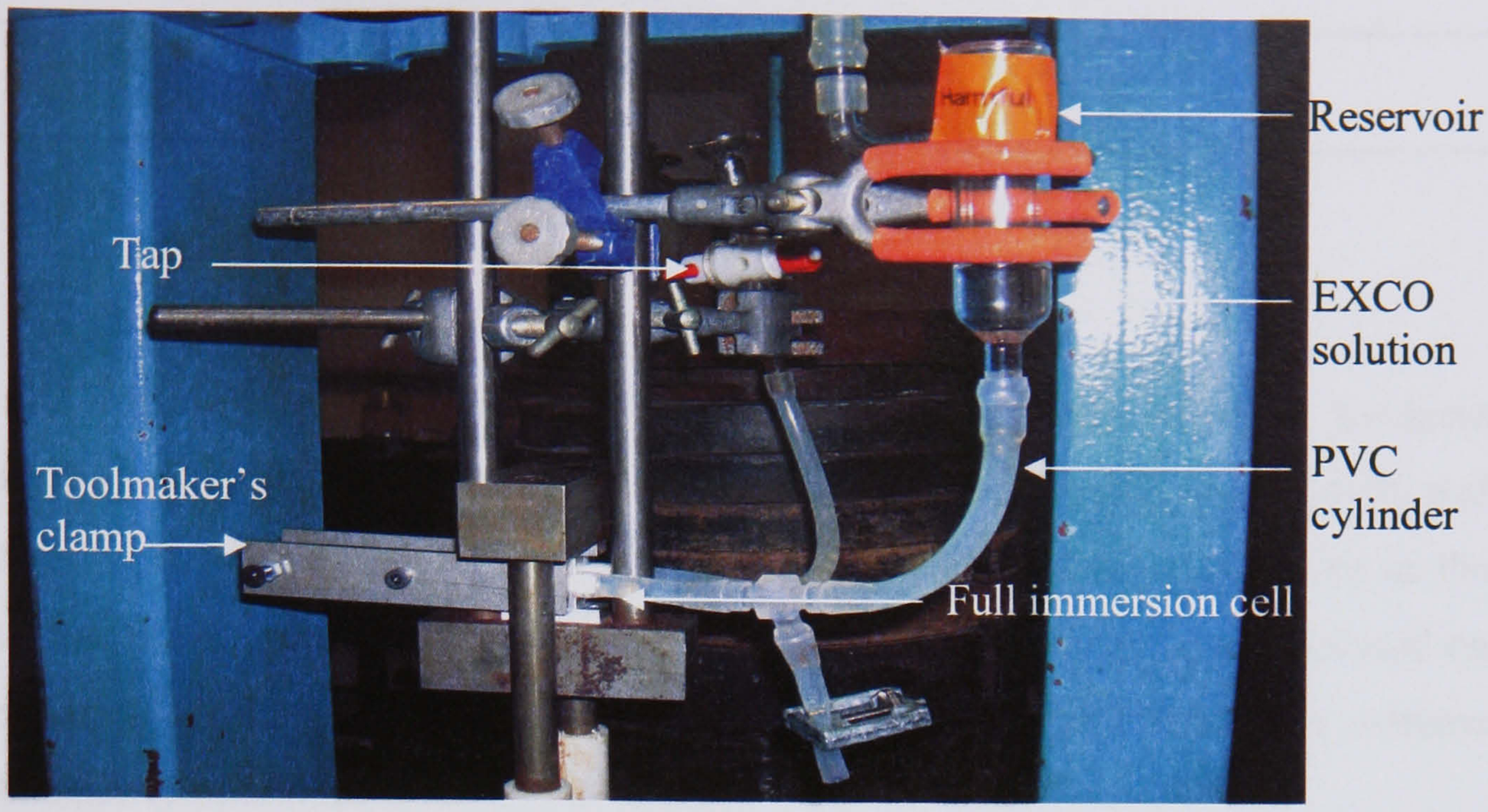


Figure 56 Apparatus for testing specimen under full immersion conditions with compressive.

### 8.4.4 Control tests without compressive loading.

In the last section, it was demonstrated that a stress corrosion crack had been produced in the presence of compressive loading and the surface of the hole immersed in the EXCO solution. An extension of this experiment was carried out to investigate whether crack would be produced without compressive loading. The experiment was repeated using same experimental procedure but in this case the compressive loading was removed from the system.

# Results

## 9.0 Material testing.

The results in this section have been divided into two parts including hardness measurement and grain aspect ratio. The correlation between hardness, conductivity and heat treatment has been stated in the literature. It was shown that any changes in the hardness will result in a change in conductivity. The second set of the results focused on material characterization. A set of data of these tests will be used directly in extreme value statistics to obtain the grain aspect ratio.

### 9.1 Hardness measurements.

Table 10 represents the result of hardness test. As can been seen, similar results has been obtained from the hardness measurement.

| Load (gf) | VHN1 | VHN2 | VHN3 | VHN4 | VHN5 | VHN6 |
|---|---|---|---|---|---|---|
| 100 | 192 | 188 | 189 | 182 | 182 | 179 |
| 200 | 183 | 191 | 192 | 189 | 184 | 191 |
| 300 | 187 | 192 | 184 | 186 | 186 | 178 |
| 500 | 184 | 183 | 184 | 176 | 189 | 178 |

Table 10 Summery of Vickers Hardness numbers.

The average Vickers hardness number of the aluminium 7075-W alloy is 185 ± 5. The conductivity affected by the hardness as stated in the literature.

## 9.2 Grain aspect ratio.

The measurement of the grain lengths and widths for both the longitudinal and transverse orientations were carried out by using a digital scanning microscope. A sample of 200 grains were taken for each section, and the top 10% of these values were taken to comply with the extreme value model [123] , with n + 1 having value of 21 for this case. The table 11 – 12 shows the measurement of lengths and widths for aluminium alloys 7075(W) in both orientations. This model involved plotting graphs of – In (-In $F_{(I\ Max)}$) against grain length and width respectively for aluminium 7075(W) in the longitudinal and transverse direction. $F_{(I\ Max)}$ represents the probability of any grain not exceeding the selected grain size. A line of best fit was drawn through the points on the graph from which the gradient and intercept were obtained.

Figure 57 – 60 show plots of –In (-In $F_{(I\ Max)}$) against $X_e$ (grain length and width) respectively for aluminium 7075(W) in the longitudinal and transverse directions. A microsoft excel program was used to calculate the line of best fit through the points on the graph, which gave the gradient, $\sigma_e$ and intercept, $\mu_e$ of the straight line. The most extreme value for grain length and width was calculated from the equation as below:

$$X_e = \mu_e + \sigma_e \ln (n) \qquad [10]$$

Where $X_e$ = most extreme value for grain length/width

$\mu_e$ = most probable grain length/width

$\sigma_e$ = standard deviation

n = population of sample

| Length(μm) | Width(μm) | Rank | $F_{(I\ Max)}$ | $-In(-InF_{(I\ Max)})$ |
|---|---|---|---|---|
| 928 | 67 | 20 | 0.952 | 3.012 |
| 809 | 59 | 19 | 0.904 | 2.293 |
| 794 | 55 | 18 | 0.857 | 1.868 |
| 741 | 51 | 17 | 0.809 | 1.551 |
| 727 | 47 | 16 | 0.761 | 1.298 |
| 676 | 47 | 15 | 0.710 | 1.072 |
| 673 | 45 | 14 | 0.666 | 0.900 |
| 595 | 43 | 13 | 0.619 | 0.735 |
| 555 | 39 | 12 | 0.571 | 0.580 |
| 514 | 38 | 11 | 0.524 | 0.436 |
| 506 | 34 | 10 | 0.476 | 0.298 |
| 489 | 33 | 9 | 0.428 | 0.166 |
| 471 | 30 | 8 | 0.381 | 0.035 |
| 442 | 29 | 7 | 0.333 | -0.095 |
| 436 | 27 | 6 | 0.286 | -0.225 |
| 413 | 26 | 5 | 0.238 | -0.361 |
| 399 | 25 | 4 | 0.190 | -0.506 |
| 383 | 23 | 3 | 0.143 | -0.666 |
| 375 | 23 | 2 | 0.095 | -0.855 |
| 354 | 22 | 1 | 0.048 | -1.113 |

Table 11 Grain lengths and widths for aluminium 7075-W in longitudinal direction.

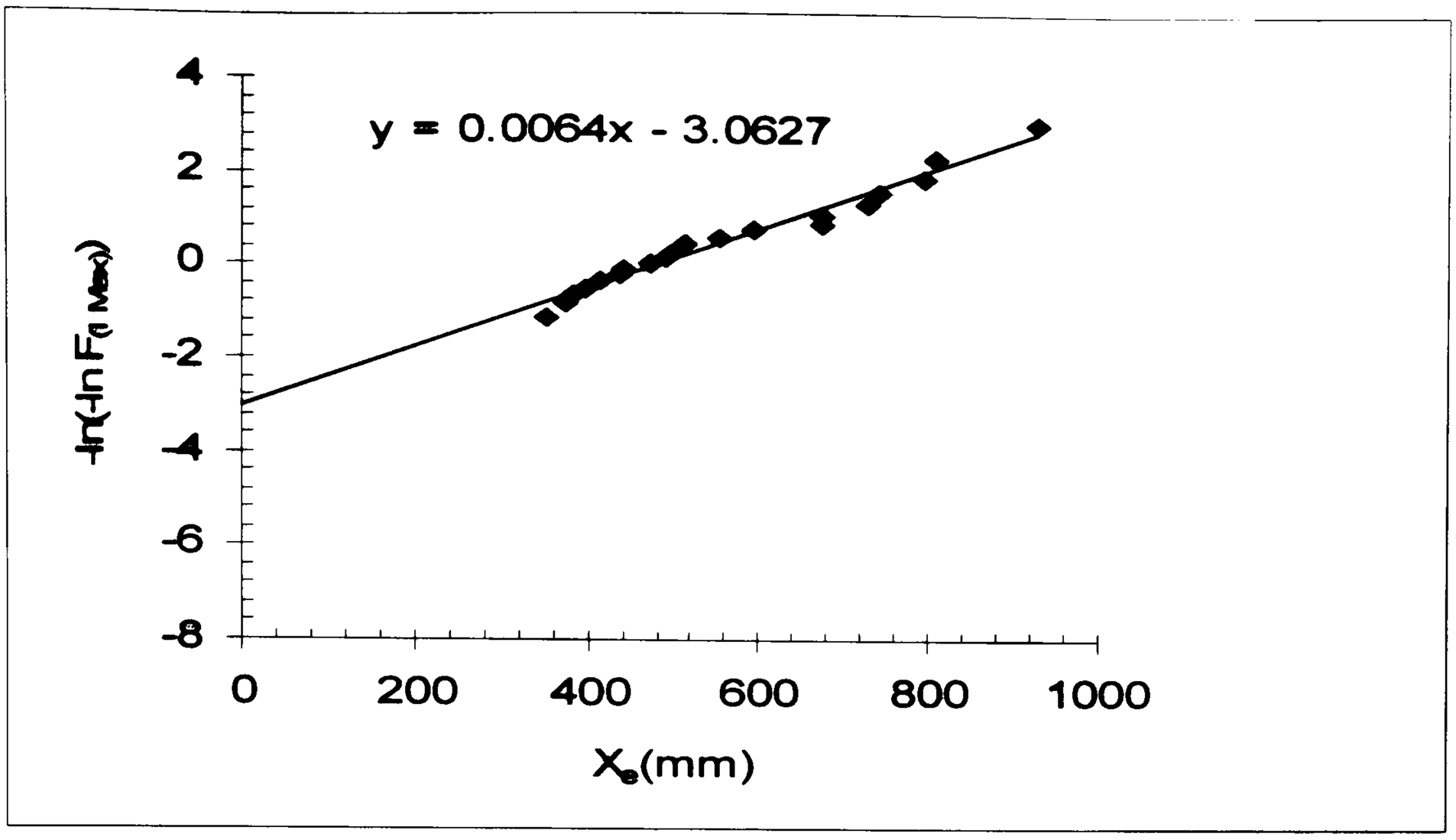


Figure 57 Graph used to obtain the most probable longitudinal grain length for aluminium 7075-W.

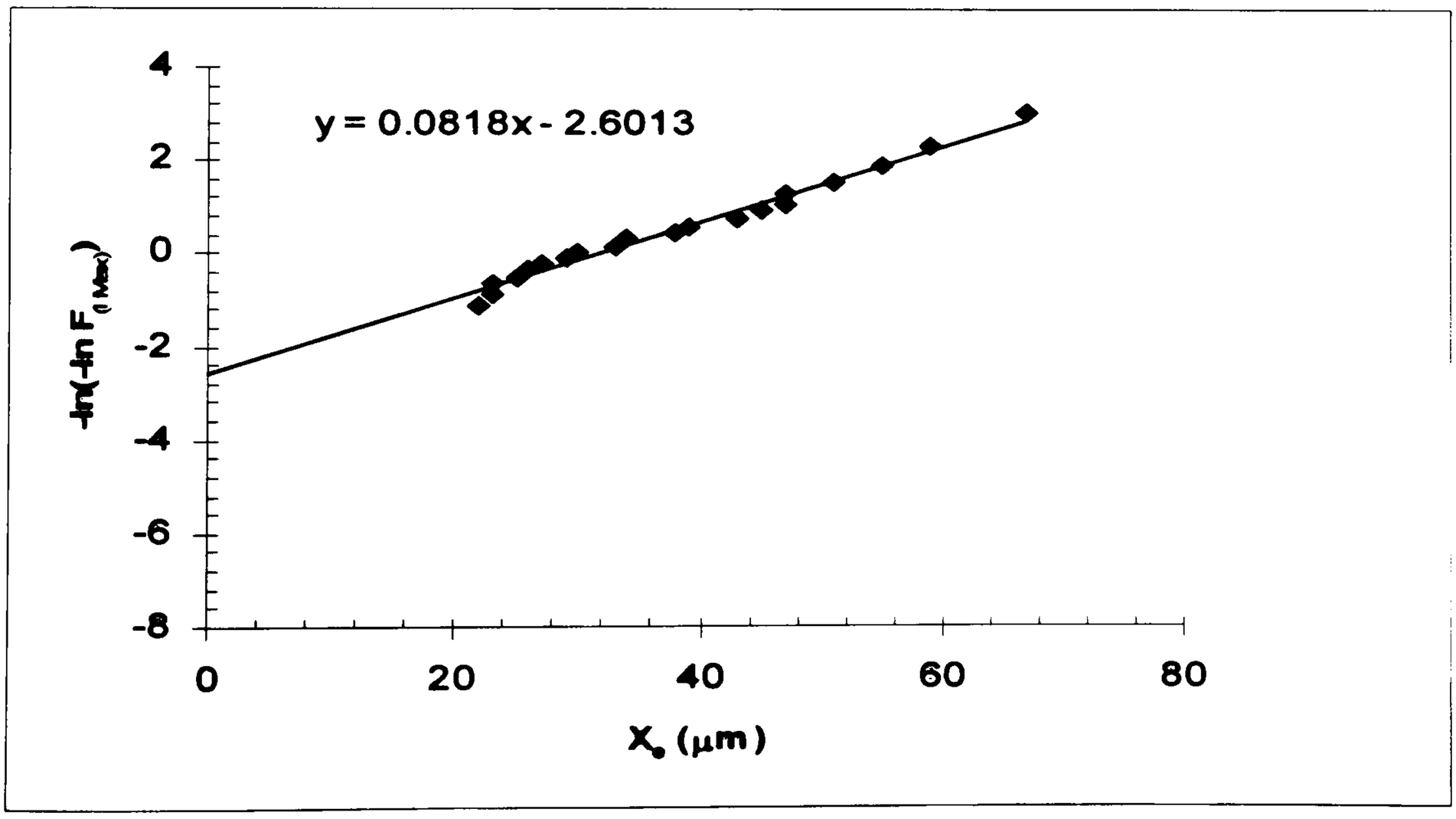


Figure 58 Graph used to obtain the most probable longitudinal grain width for aluminium 7075-W.

| Length(μm) | Width(μm) | Rank | $F_{(I\ Max)}$ | $-In(-InF_{(I\ Max)})$ |
|---|---|---|---|---|
| 346 | 51 | 20 | 0.952 | 3.012 |
| 305 | 51 | 19 | 0.904 | 2.293 |
| 297 | 47 | 18 | 0.857 | 1.868 |
| 293 | 43 | 17 | 0.809 | 1.551 |
| 285 | 43 | 16 | 0.761 | 1.298 |
| 280 | 43 | 15 | 0.710 | 1.072 |
| 276 | 39 | 14 | 0.666 | 0.900 |
| 268 | 39 | 13 | 0.619 | 0.735 |
| 260 | 39 | 12 | 0.571 | 0.580 |
| 243 | 38 | 11 | 0.524 | 0.436 |
| 252 | 36 | 10 | 0.476 | 0.298 |
| 236 | 35 | 9 | 0.428 | 0.166 |
| 223 | 35 | 8 | 0.381 | 0.035 |
| 219 | 34 | 7 | 0.333 | -0.095 |
| 211 | 34 | 6 | 0.286 | -0.225 |
| 211 | 31 | 5 | 0.238 | -0.361 |
| 202 | 30 | 4 | 0.190 | -0.506 |
| 187 | 28 | 3 | 0.143 | -0.666 |
| 180 | 26 | 2 | 0.095 | -0.855 |
| 178 | 26 | 1 | 0.048 | -1.113 |

Table 12 Grain lengths and widths for aluminium 7075(W) in transverse direction.

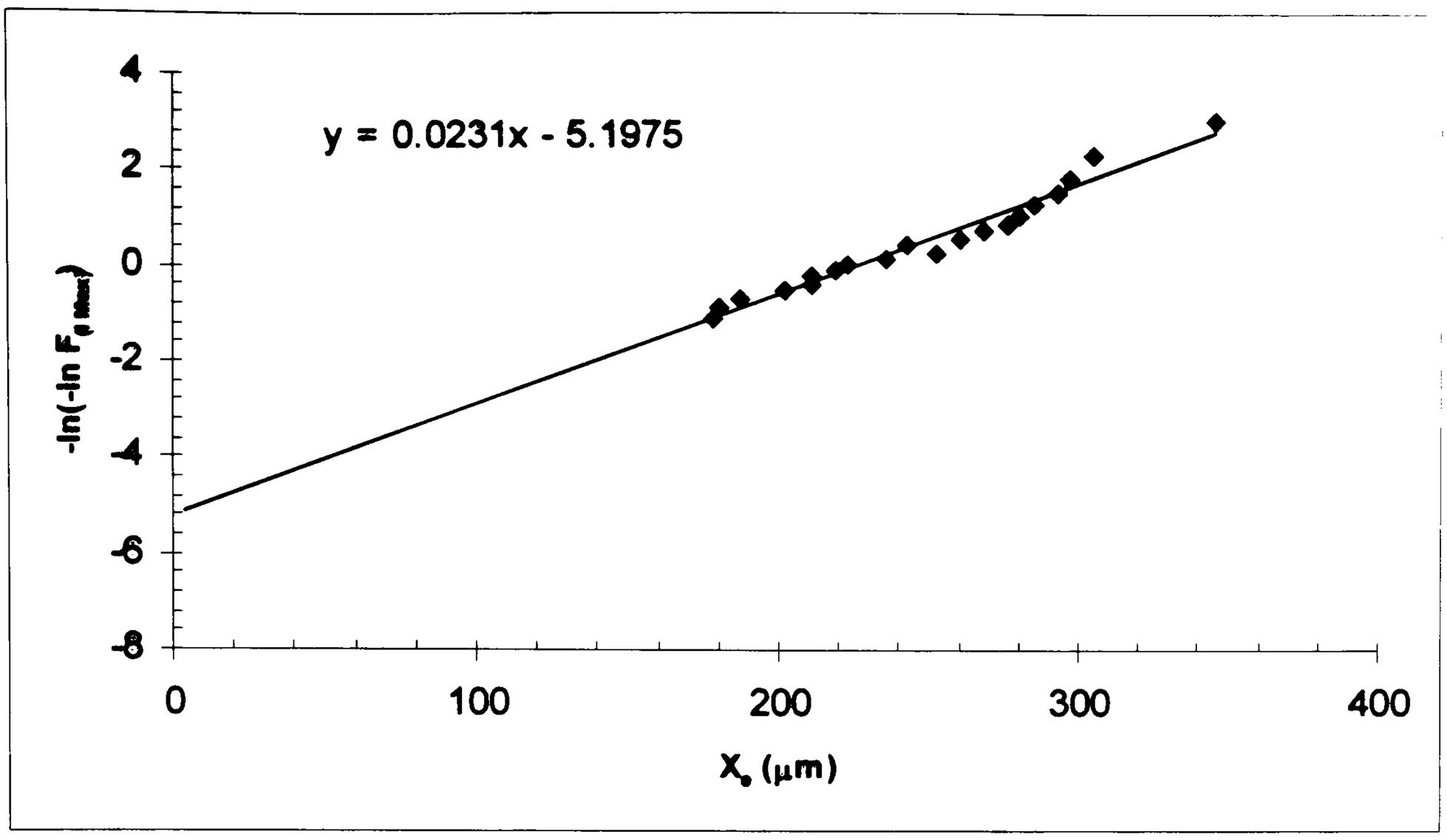


Figure 59 Graph used to obtain the most probable transverse grain length for aluminium 7075-W.

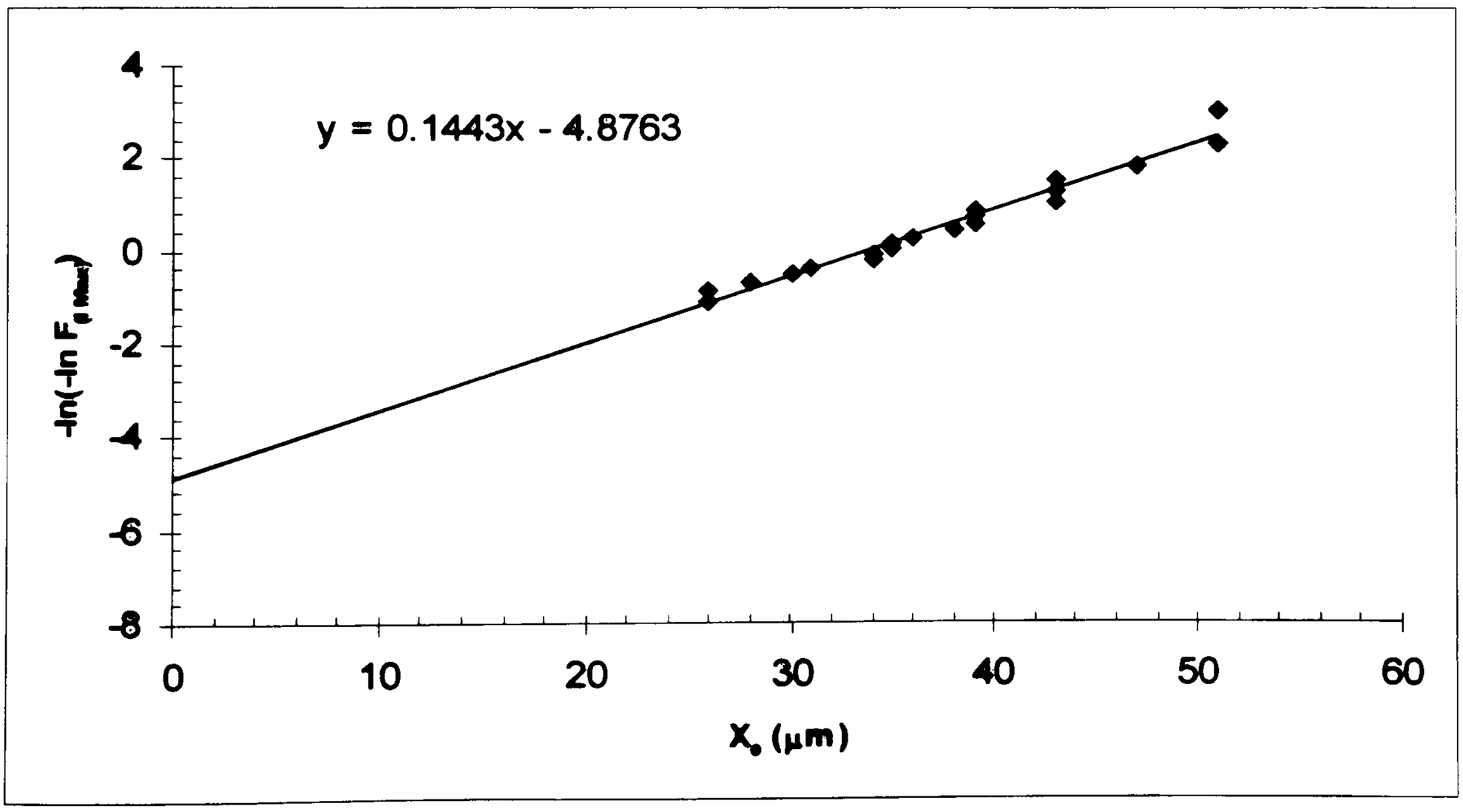


Figure 60 Graph used to obtain the most probable transverse grain width for aluminium 7075-W.

The grain aspect ratio was then determined by the ratio of grain length to grain width for longitudinal and transverse directions. The extreme value statistics results from the curve fitting can be seen in Table 13.

| **Material** | **Orientation** | **Length** (μm) | **Width** (μm) | **Grain aspect ratio** |
|---|---|---|---|---|
| Aluminium 7075(W) | Longitudinal | 946 ± 156 | 68 ± 12 | 14 ± 7 |
| | Transverse | 355 ± 43 | 55 ± 7 | 7 ± 4 |

Table 13 Grain aspect ratios from the extreme value statistics results.

As can be seen from Table 13, the longest grains were found in the longitudinal section as this represents the rolling direction of the plate. The longitudinal grain length was approximately twice as long as the transverse grain length. On the other hand, both the longitudinal and transverse section has shown very similar results in grain width, as would be expected. The use of extreme value statistics shows that aluminium 7075(W) has a high grain aspect ratio in the longitudinal direction, as twice as much as the transverse direction. The high grain aspect ratio of the aluminium 7075(W) would indicate that this material may be susceptible to stress corrosion cracking as this is an intergranular type of corrosion.

## 10.0 Eddy current calibration.

This section shows the results in detail regarding the eddy current calibration. The results in this section were used to make directly compared and defined the correct operating frequency for the material under investigation. The eddy current responses from calibration specimen, smooth surface and corroded surface were also discussed.

## 10.1 Calibration specimen for eddy current testing.

The testing frequency should be chosen to suit the size of cracks to be detected in the specimen. In this case, when all initial test parameters had been determined, the probe was inserted into the calibration specimen containing the simulated cracks and the material was scanned by moving the probe across the plane of the cracks. The testing frequency was chosen to give penetration to the depth of all the defects, while still allowing clear discrimination between lift-off signal and the defects. The eddy current responses to defects were compared at frequencies of 100, 180, 218, 280, 450 and 700 kHz. Figures 61 - 66 show the different eddy current response of the simulated cracks with changing the frequency. As can be seen, the frequency of 100 kHz and 180 kHz has shown overlapping of the eddy current responses obtained from the calibration specimen. For both frequencies, there was low sensitivity and a small angle between the crack and the lift off signals, as shown in figure 61 and figure 62. In both cases the gain setting needed to be increased to detect the signals. It also showed that all the signals from the calibration specimen move in the same direction and there is very small separation between defect signals. It was clear from these results that decreasing the frequency decreased the phase angle making interpretation of the calibration signals unsatisfactory.

At the frequency of 218 kHz, as shown in figure 63, there was better separation between defect signals particularly for the defect size of 0.5mm and 0.6mm. Figure 63 also shows a better angle between the crack and the lift-off signals. This shows that a better sensitivity can be obtained at this frequency. As can be seen, the interpretation becomes easier at this operating frequency. However, the defect signal of 1.0mm is still overlapping with the defect signal of 1.5mm. On the other hand, as frequency increased to 280 kHz, 450 kHz and 700 kHz the phase angle increased because of high frequency the gain setting needed to be set lower [20]. It can be noticed also that the edge of the signals started to turn upwards particularly as the frequency increased to 700 kHz. At these higher frequencies it was difficult to distinguish between the 1.0mm and 1.5mm cracks.

In this experiment the frequency of 218 kHz had the best detection capability with a good separation angle for all defects in calibration specimen. Therefore this frequency was used for the measurement of stress corrosion cracks in aluminum alloy 7075-W for the rest of the work.

Figure 63 shows the eddy current signal for each of the machined defects at an operating frequency of 218 kHz, gain setting 98 dB and phase angle $280^0$. The amplitude of the eddy current signals from simulated cracks can be obtained from this scan. The stress corrosion cracks from the compressive test specimen can be measured by comparing the amplitude of the test specimen with the amplitude of signals from the calibration specimen. Table 14 shows the amplitude of the eddy current signal obtained from the calibration specimen for the different defect depths. By providing the same setup as used in calibration, the amplitude of the eddy current signal in the vertical direction can be used to compare directly to the depth of the calibration specimen. This procedure was used to determine the depth of the stress corrosion cracks detected in the 7075-W material.

| Depth of crack (mm) | Magnitude of calibration signal (mV) |
|---|---|
| 0.5 | 270.0 |
| 0.6 | 538.1 |
| 1.0 | 619.2 |
| 1.5 | 831.4 |

Table 14 the amplitude of the eddy current signal obtained from the calibration defects.

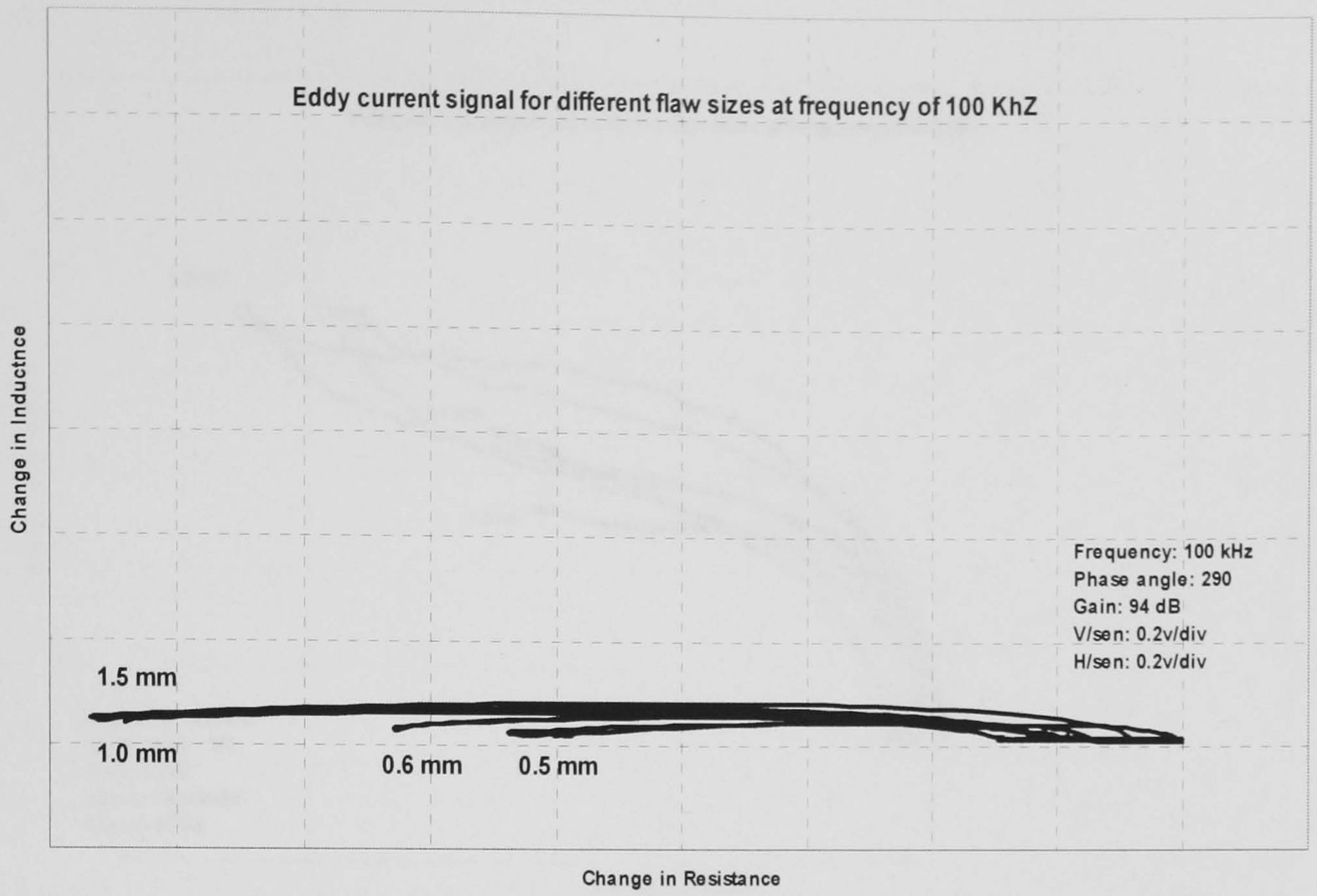


Figure 61 Eddy current signals for different flaw sizes at frequency of 100 kHz.

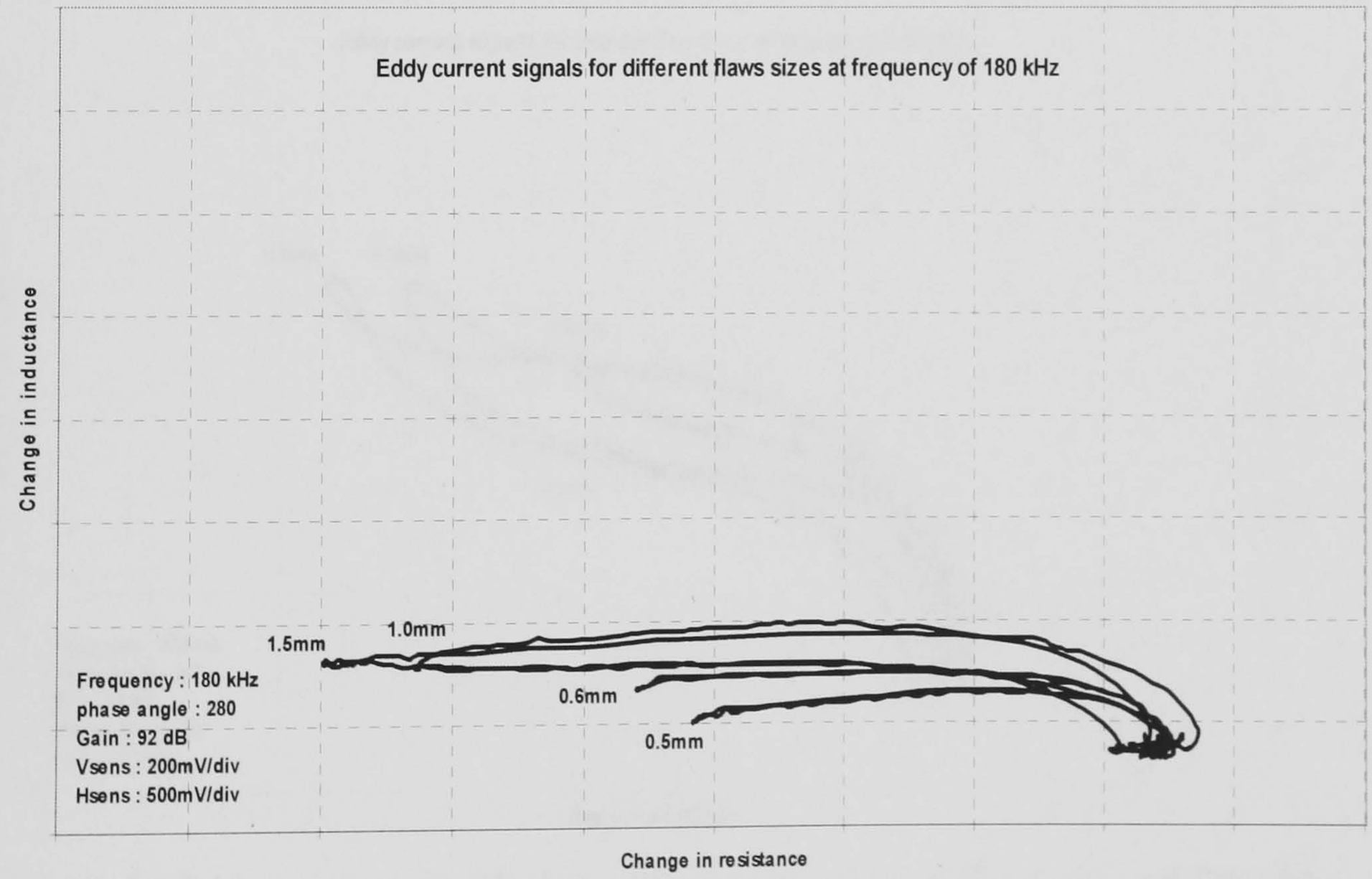


Figure 62 Eddy current signals for different flaw sizes at frequency of 180 kHz.

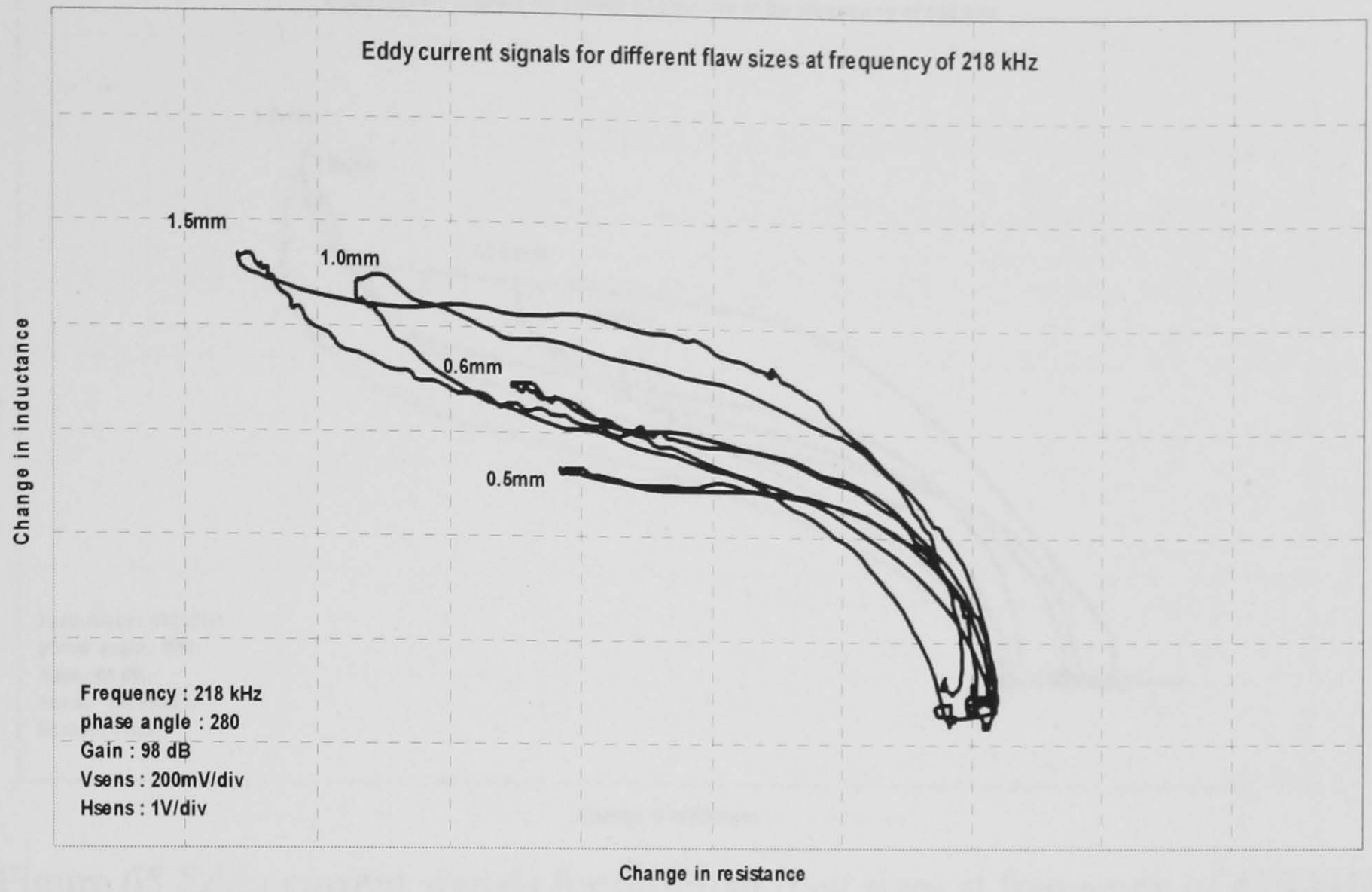


Figure 63 Eddy current signals for different flaw sizes at frequency of 218 kHz.

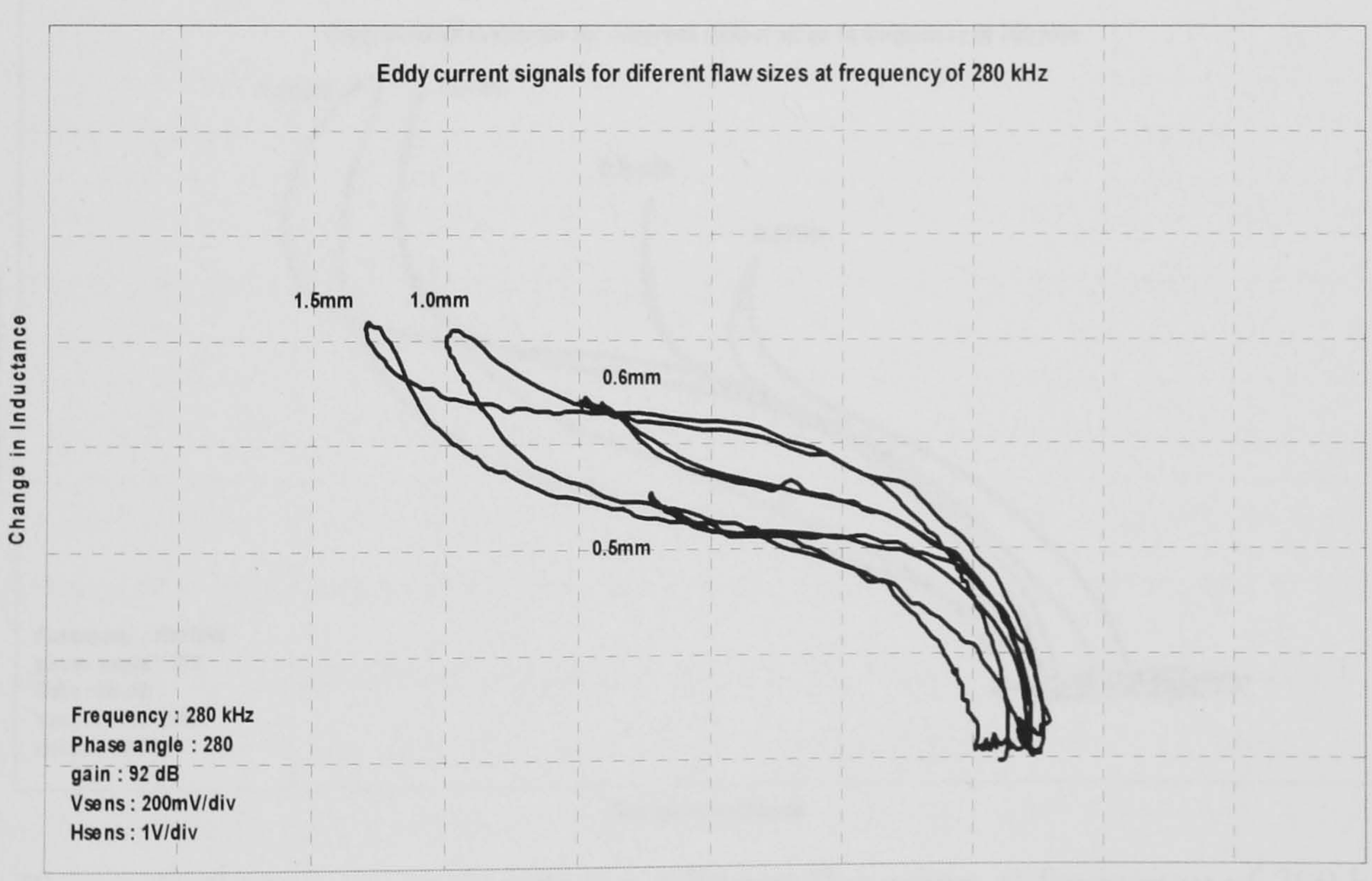


Figure 64 Eddy current signals for different flaw sizes at frequency of 280 kHz.

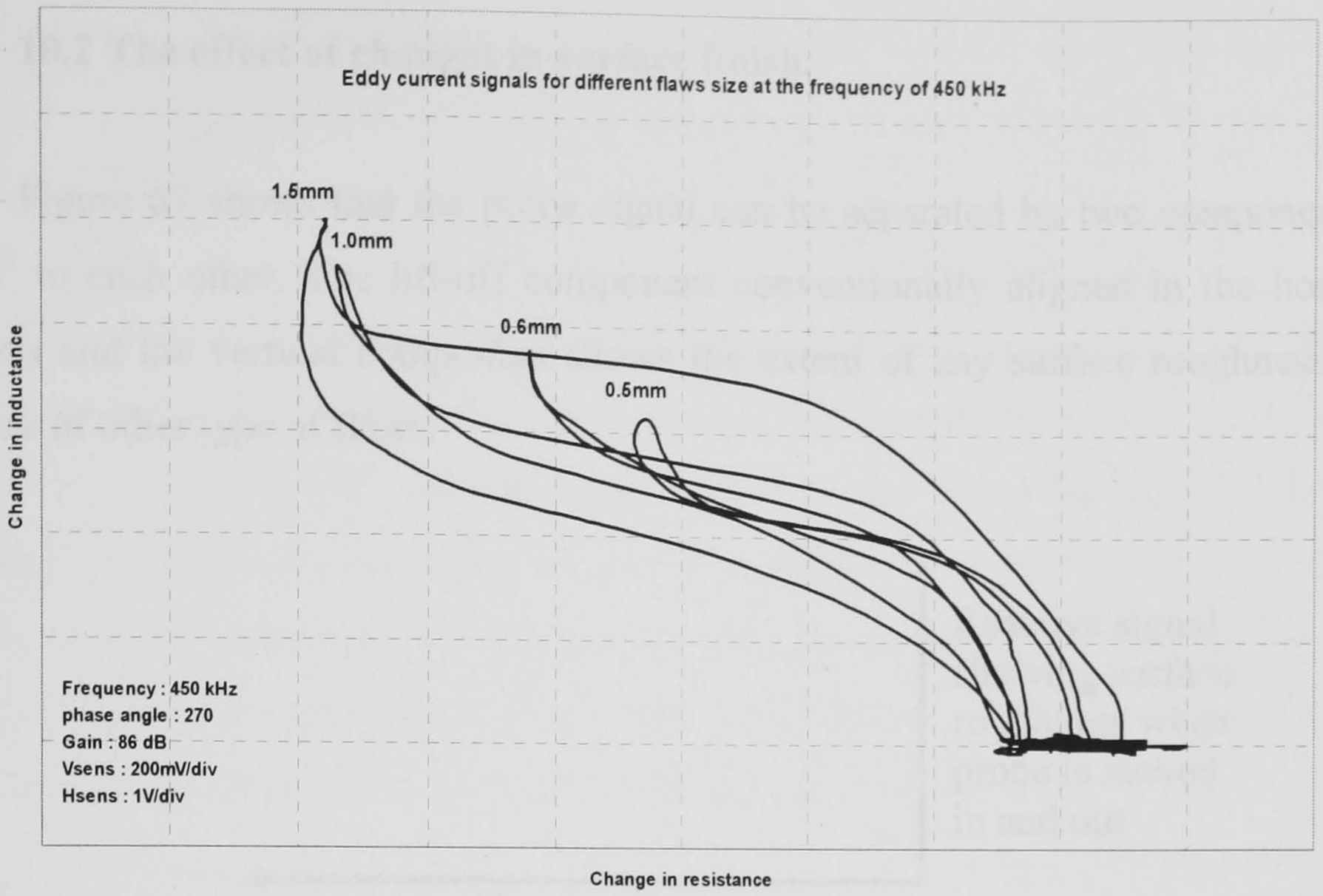


Figure 65 Eddy current signals for different flaw sizes at frequency of 450 kHz.

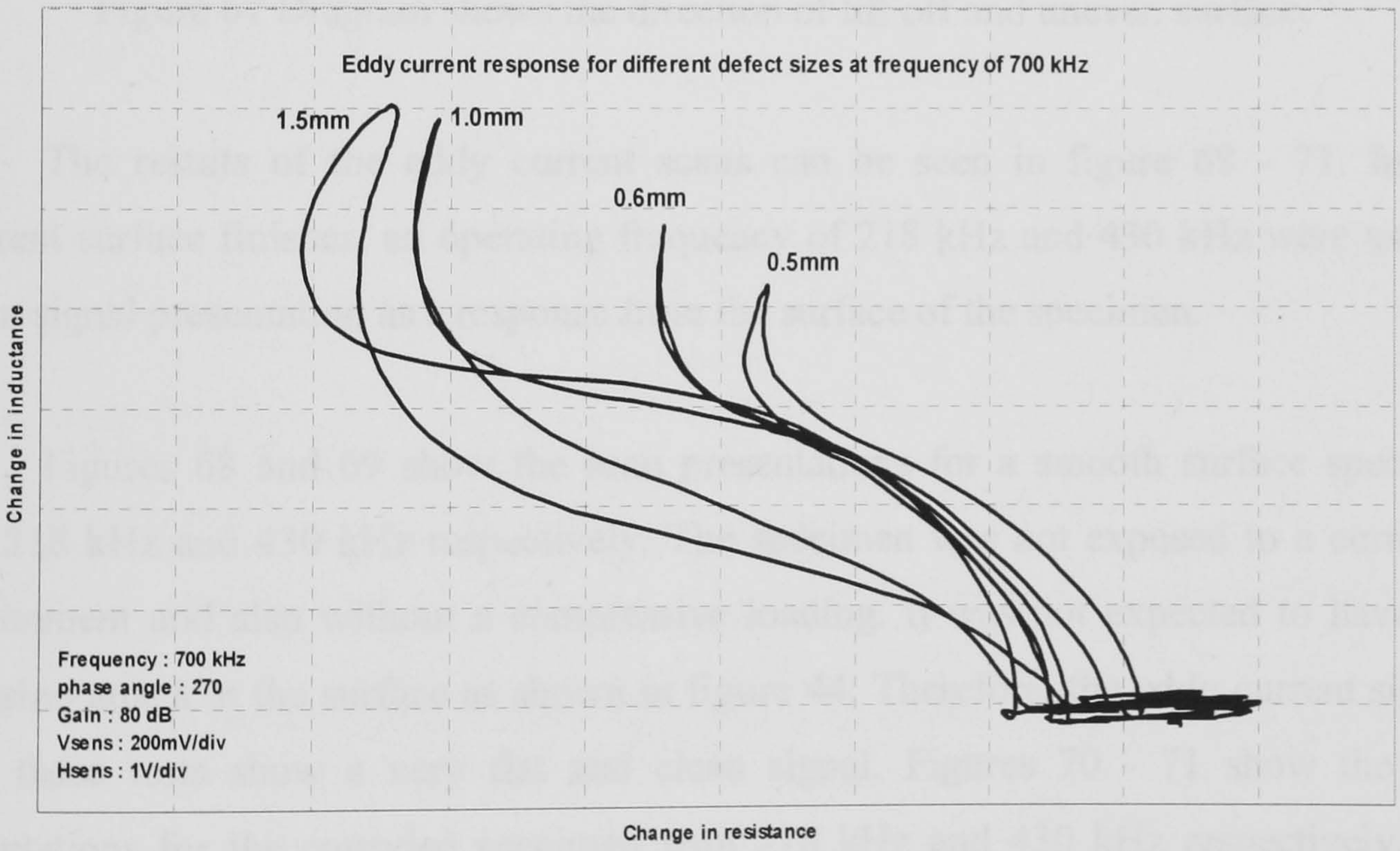


Figure 66 Eddy current signals for different flaw sizes at frequency of 700 kHz.

## 10.2 The effect of changes in surface finish.

Figure 67 shows that the probe signal can be separated by two components that are $90^0$ to each other. The lift-off component conventionally aligned in the horizontal direction and the vertical component shows the extent of any surface roughness or the presence of other type of flaws.

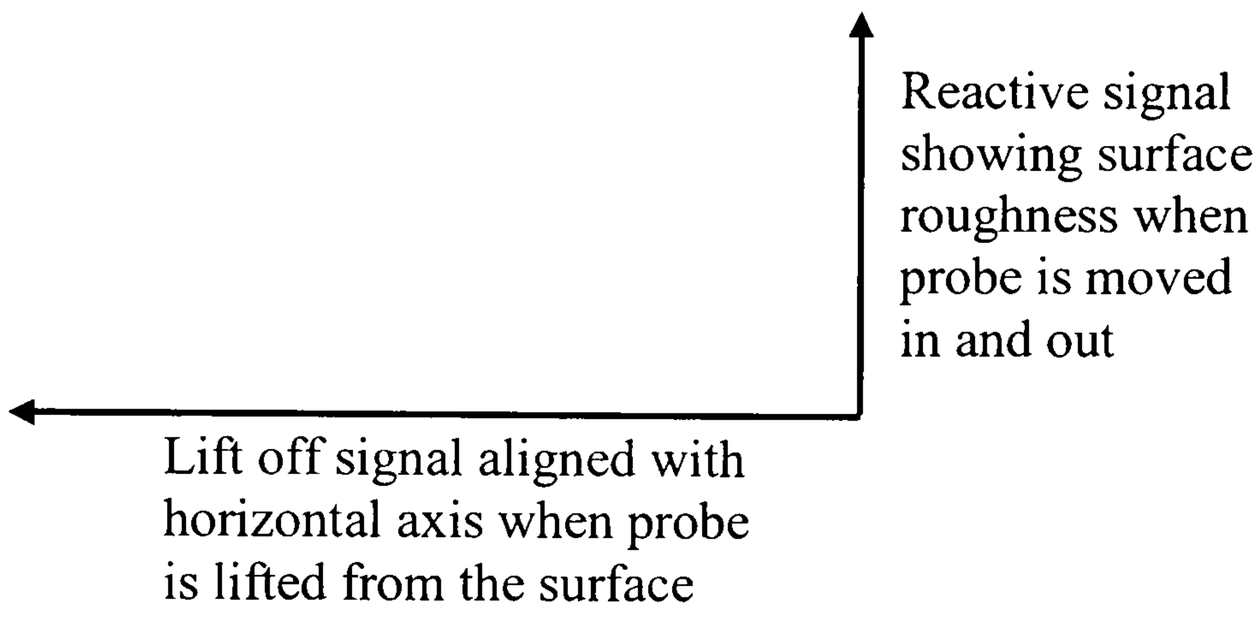


Figure 67 Diagram shows the direction of lift off and uneven surface.

The results of the eddy current scans can be seen in figure 68 - 71. In two different surface finishes, an operating frequency of 218 kHz and 430 kHz were used to obtain signal presentation as a response from the surface of the specimen.

Figures 68 and 69 show the scan presentations for a smooth surface specimen with 218 kHz and 430 kHz respectively. The specimen was not exposed to a corrosive environment and also without a compressive loading. It was not expected to have any corrosion attack at the surface as shown in figure 44. Therefore, the eddy current signals from these tests show a very flat and clean signal. Figures 70 - 71 show the scan presentations for the corroded specimen with 218 kHz and 430 kHz respectively. The specimen was exposed to a 3.5% NaCl solution under compressive loading. After 60 days, the superficial corrosion product build up at the surface of the hole was removed using a hand-held reamer. This procedure was required to remove voluminous corrosion products that would otherwise prevent the eddy current probe being inserted into the hole.

The scans show the eddy current signal was not very flat and clean like the scans on smooth surface. Instead, they had vertical components of approximately one division (for a setting of 1V/div).

For both cases, the frequency of 430 kHz presented a greater eddy current signal than the frequency of 218 kHz. In case of smooth surface, the large lift-off was produced by the frequency 430 kHz and the interpretation of the signal becomes easier at this frequency. The eddy current signal of 218 kHz appears not to be sensitive to the near surface. In terms of the corroded surface, the eddy current signal was greater than for the smooth surface. This experiment shows that the frequency of 430 kHz was obtained a better sensitivity than the frequency of 218 kHz for any surface finish.

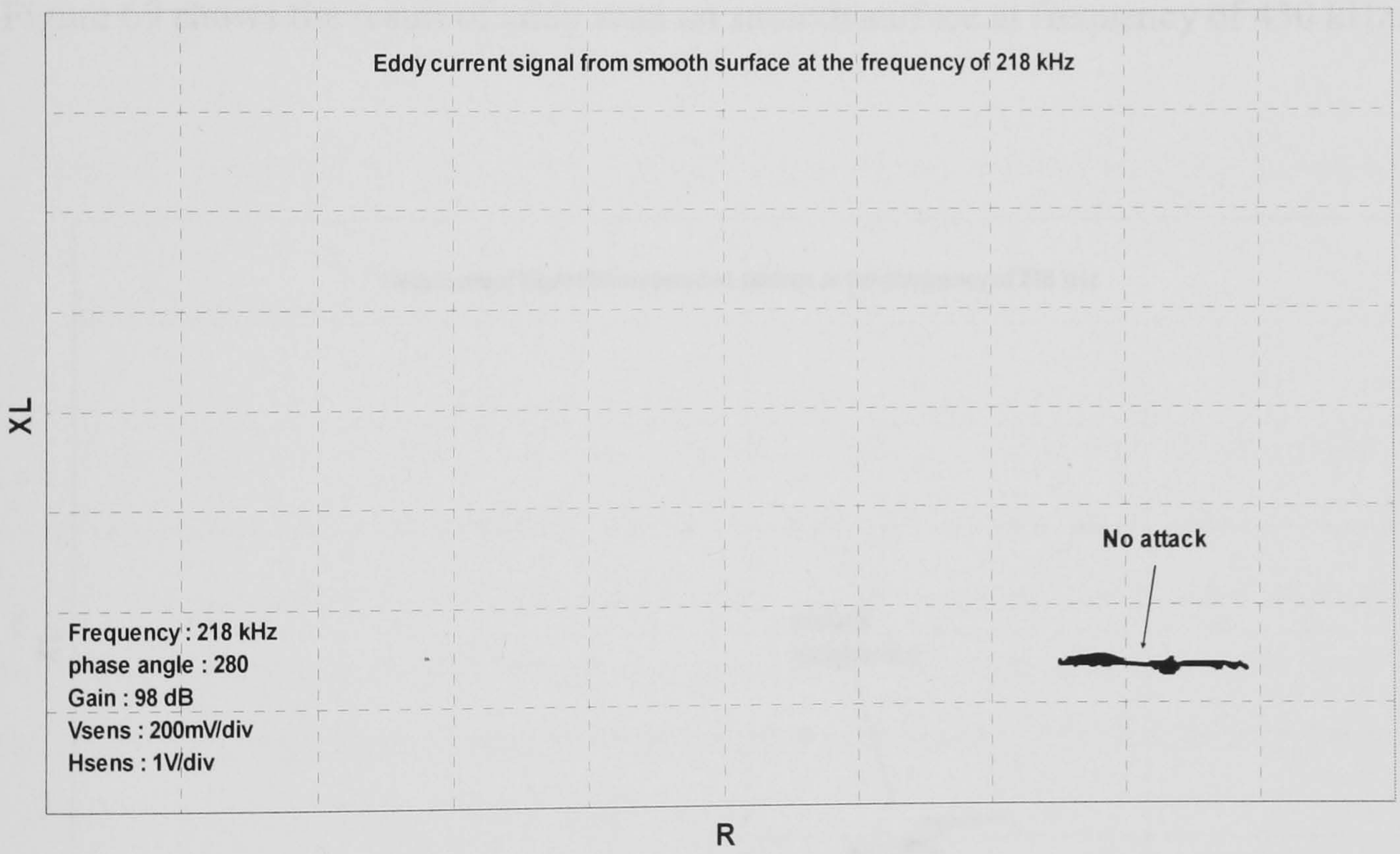


Figure 68 shows the result of eddy scan on smooth surface at frequency of 218 kHz.

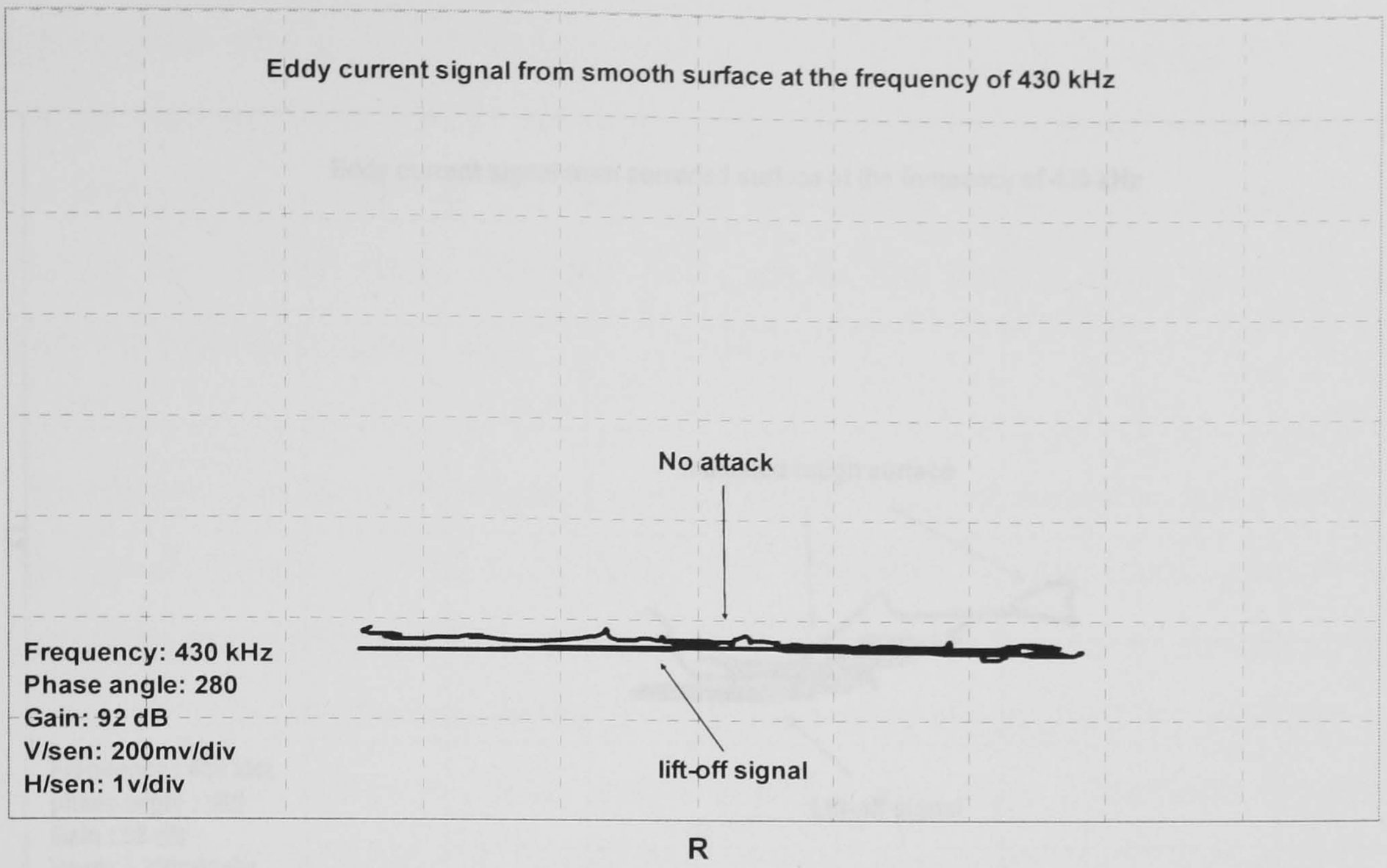


Figure 69 shows the result of eddy scan on smooth surface at frequency of 430 kHz.

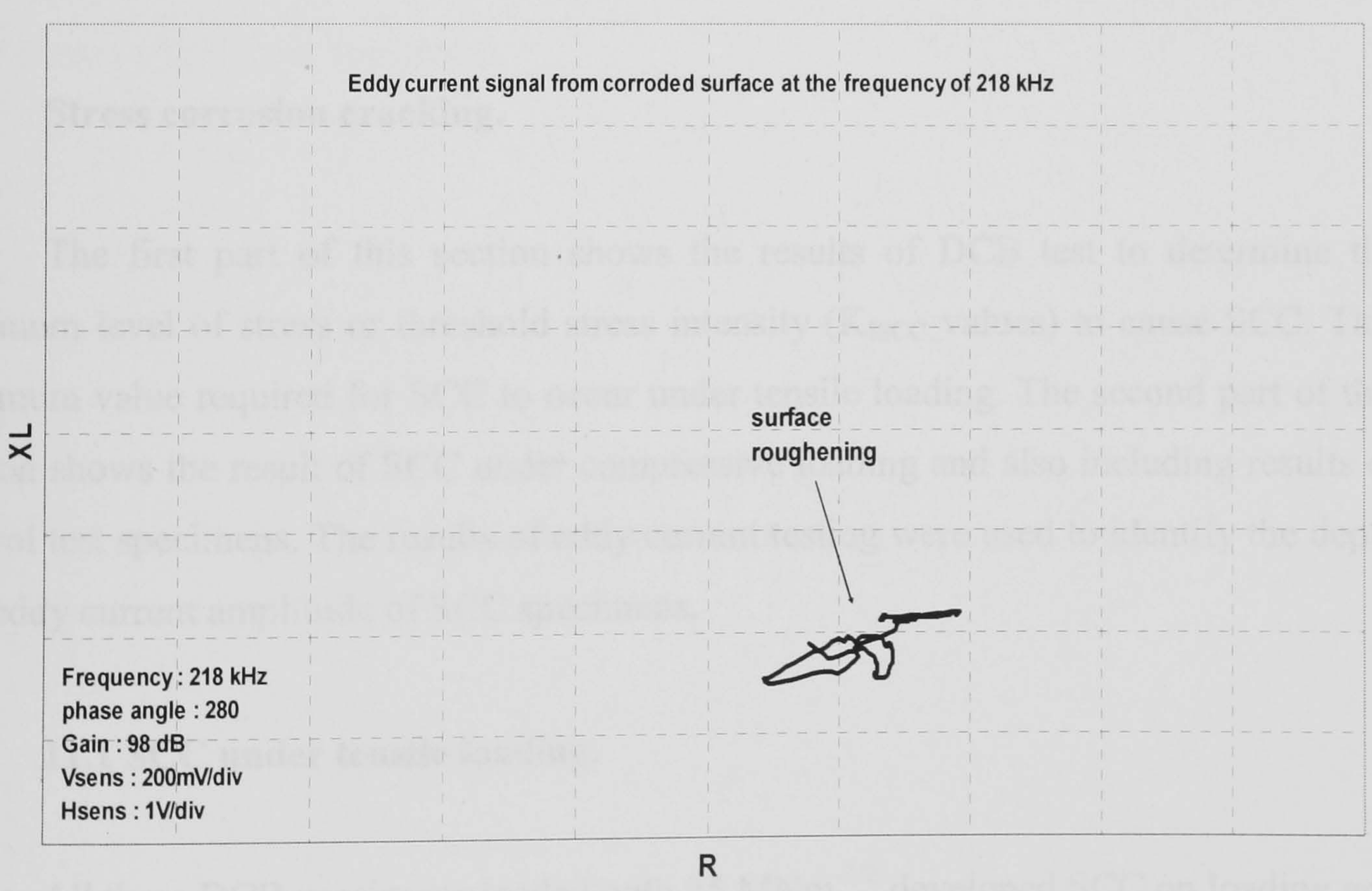


Figure 70 shows the result of eddy scan on corroded surface at frequency of 218 kHz.

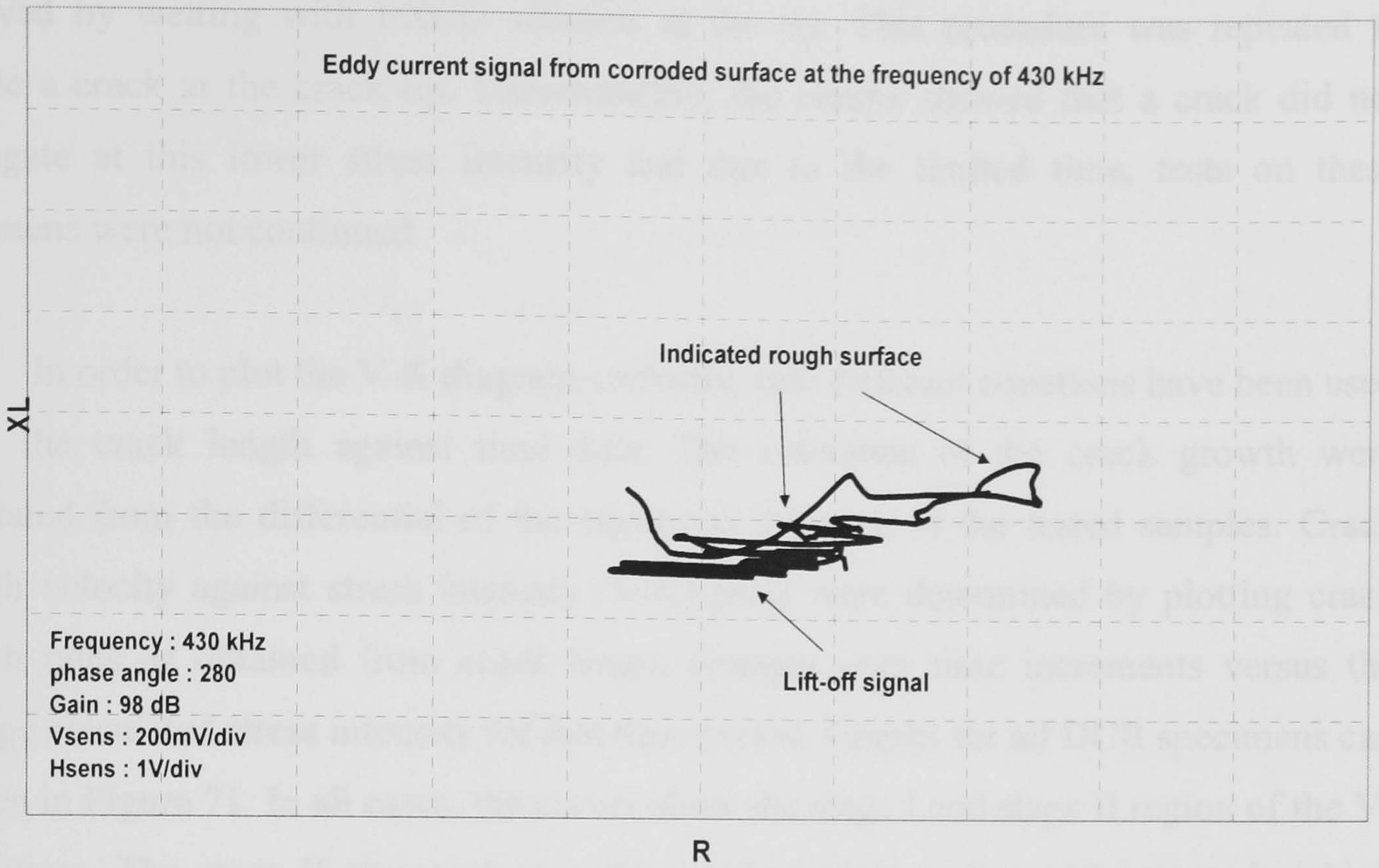


Figure 71 shows the result of eddy scan on corroded surface at frequency of 430 kHz.

## 11.0 Stress corrosion cracking.

The first part of this section shows the results of DCB test to determine the minimum level of stress or threshold stress intensity ($K_{ISCC}$ values) to cause SCC. This minimum value required for SCC to occur under tensile loading. The second part of this section shows the result of SCC under compressive loading and also including results of control test specimens. The results of eddy current testing were used to identify the depth and eddy current amplitude of SCC specimens.

### 11.1 SCC under tensile loading.

All three DCB specimens loaded with 25 $MNm^{-3/2}$ developed SCC on loading and the stress corrosion cracks continued to grow after being immersed in the test environment. However, only one DCB specimen loaded with 15 $MNm^{-3/2}$ initiated a stress corrosion crack. An effort was made to break down the film on the notch surface

for the other two specimens. A scalpel was used to very lightly score the surface and followed by wetting with EXCO solution at the tip. This procedure was repeated to initiate a crack at the crack tip. Unfortunately, the results showed that a crack did not propagate at this lower stress intensity and due to the limited time, tests on these specimens were not continued.

In order to plot the V-K diagram correctly, two different equations have been used to fit the crack length against time data. The velocities of the crack growth were calculated from the differential of the equations for each of the tested samples. Crack growth velocity against stress intensity (V-K) plots were determined by plotting crack growth rates as obtained from crack length changes over time increments versus the average calculated stress intensity for that time period. Graphs for all DCB specimens can be seen in Figure 71. In all cases, the curves show the stage I and stage II region of the V-K diagram. The stage II appeared as a stress-independent region and occurred at high stress intensities [82]. The stage III region was not observed due to the rapid initial crack growth rates of all three specimens.

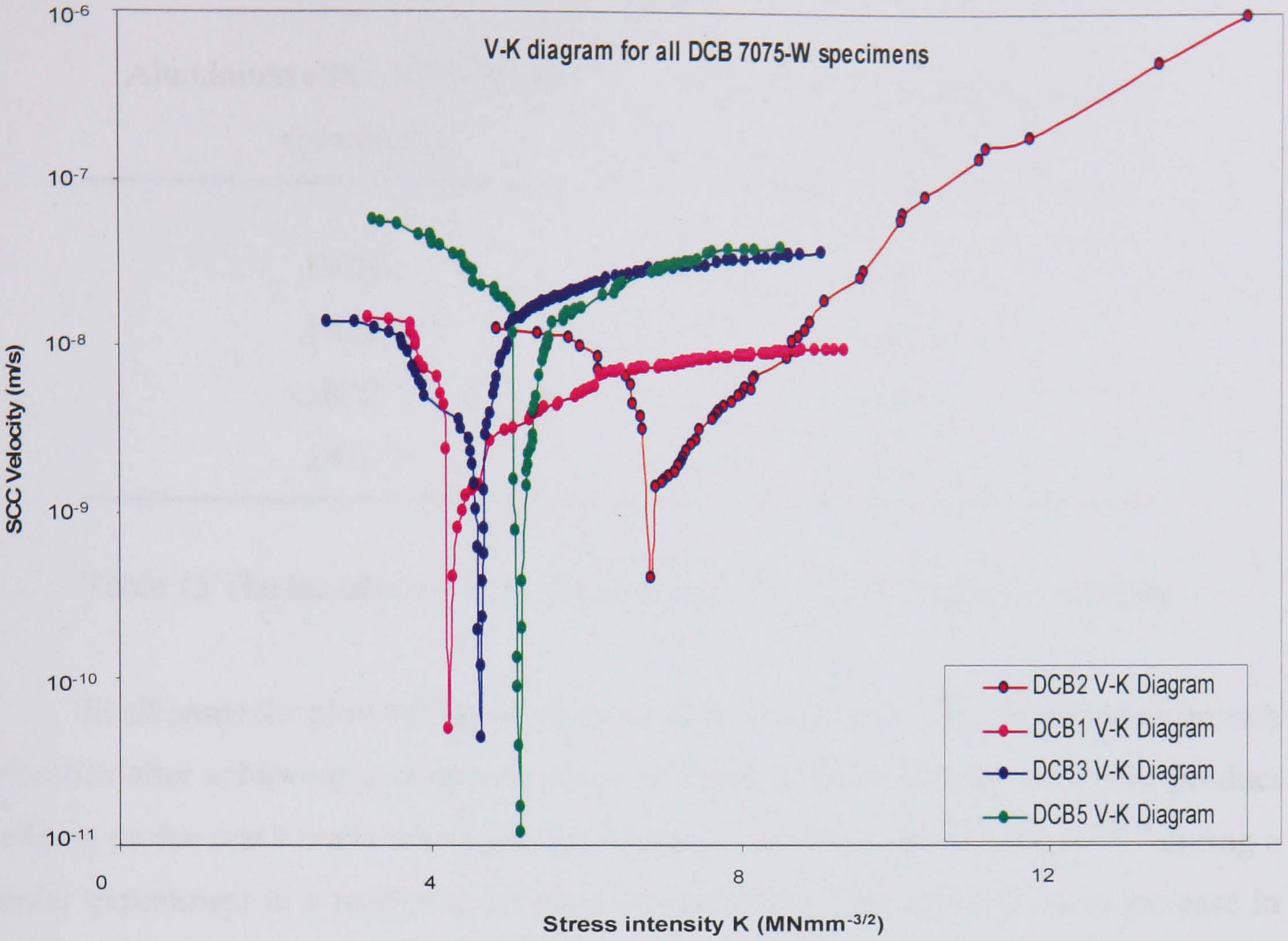


Figure 72 V-K diagram for bolt loaded DCB specimens from 7075 W material.

In general, crack growth in the DCB specimens causes reducing values of stress intensity at the crack tip. It can be seen that the crack velocity was significantly higher at the beginning of the test and then decreased as the stress intensity decreased. This continued until the stress intensity reached a certain point where the crack stopped growing. This situation only occurred in the stage I where threshold stress intensity for stress corrosion was reached minimum value. The $K_{ISCC}$ values were obtained by extending the point in the V-K diagram [82]. The calculated values of $K_{ISCC}$ were shown in Table 15. Table 15 shows the $K_{ISCC}$ value for each specimen. The material had a lowest $K_{ISCC}$ value of 4.2 $MNm^{-3/2}$. These values are lower than measured in most high strength aluminium alloys, indicating that the sample of 7075 W is particularly susceptible to stress corrosion crack and has a low resistance to stress corrosion cracking.

| Aluminium alloy 7075-W DCB specimens | Threshold stress intensity $K_{ISCC}$ ($MNm^{-3/2}$) |
|---|---|
| DCB 1 | 4.2 |
| DCB 2 | 6.8 |
| DCB 3 | 4.6 |
| DCB 5 | 5.1 |

Table 15 The threshold stress intensity ($K_{ISCC}$) of 7075-W aluminium alloy.

In all cases the plots in Figure 72 showed an apparent increase in the crack growth velocities after achieving a minimum value of stress intensity, due to corrosion product wedging on the crack walls which has been reported by Dorward and Hasse [137] during a similar experiment in a marine atmosphere environment. This resulted in an increase in crack velocity, as shown in figure 72, until the stiffness of the material overcame the effects of corrosion product wedging and no further crack growth occurred. There was evidence that the build up of corrosion product within the crack has then effectively generated stress intensity at the crack tip, as can seen in figure 72, where there are an increase in crack velocity on the left hand side of the graph after the minimum value of $K_{ISCC}$ has been obtained. Thus crack velocity increased and effectively retracing the V-K diagram.

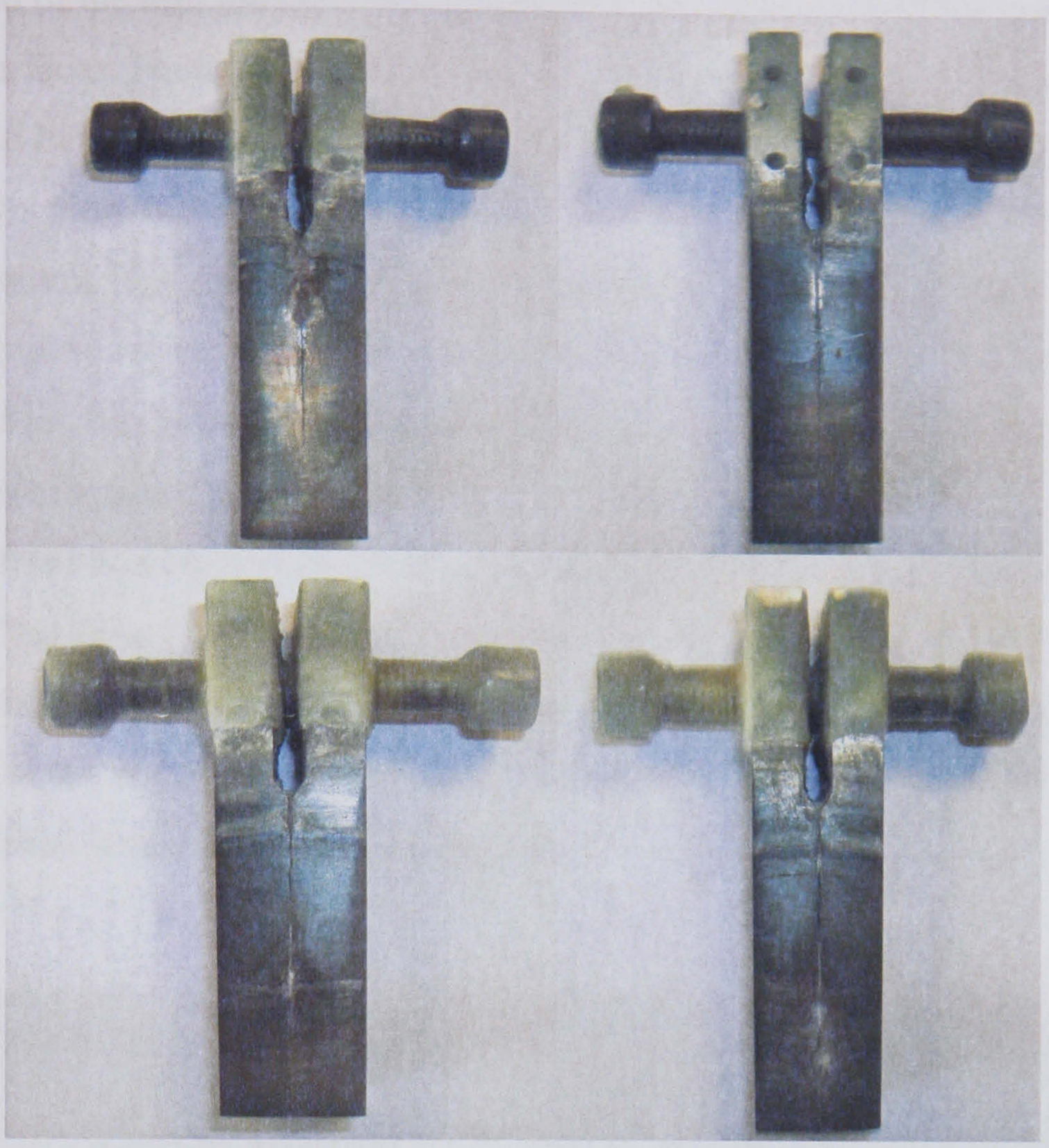

Figure 73 Photographs of DCB specimens showing the stress corrosion cracking under tensile loading.

Figure 73 shows photographs of the DCB specimens after 3 months immersed in 3.5% NaCl. As can be seen, constant immersion caused corrosion product build up around the surface of the DCB specimens. Therefore, the surfaces of specimens were polished with a 1 μm grit paper at 45° angle to the SCC direction. This highlights the crack path, making it easier to see the crack tip. It is also became evident that the stress corrosion cracking in the 7075-W material, propagated in a straight line along the centre of the specimen indicating that stress corrosion cracking follows the elongated grain boundaries.

At the end of the test, the DCB specimens were broken open to allow examination of the fracture surfaces. Photographs of the surface are shown in figure 74. The crack can clearly be seen to have propagated in the longitudinal direction through the materials. It was clear from the examination of the fracture surface that corrosion product build up had occurred in the crack. The corrosion product of aluminium is a white to grey powdery material which can be removed by mechanical polishing or brushing as it is softer than the metal. Therefore, this is supporting the corrosion product wedging effect of the stress corrosion crack mechanism, as expected from the V-K diagrams. In addition, it appeared that some crack front bowing had occurred at the crack tip. If crack bowing had occurred, it could be an effect from the thickness of the specimen. The thickness of specimen used for this work was 22 mm. therefore the plane strain condition could be the best reason for possible leading at the crack front in the centre, whereas the plane stress condition at the edge of the specimen would have retarded (lag behind) crack growth.

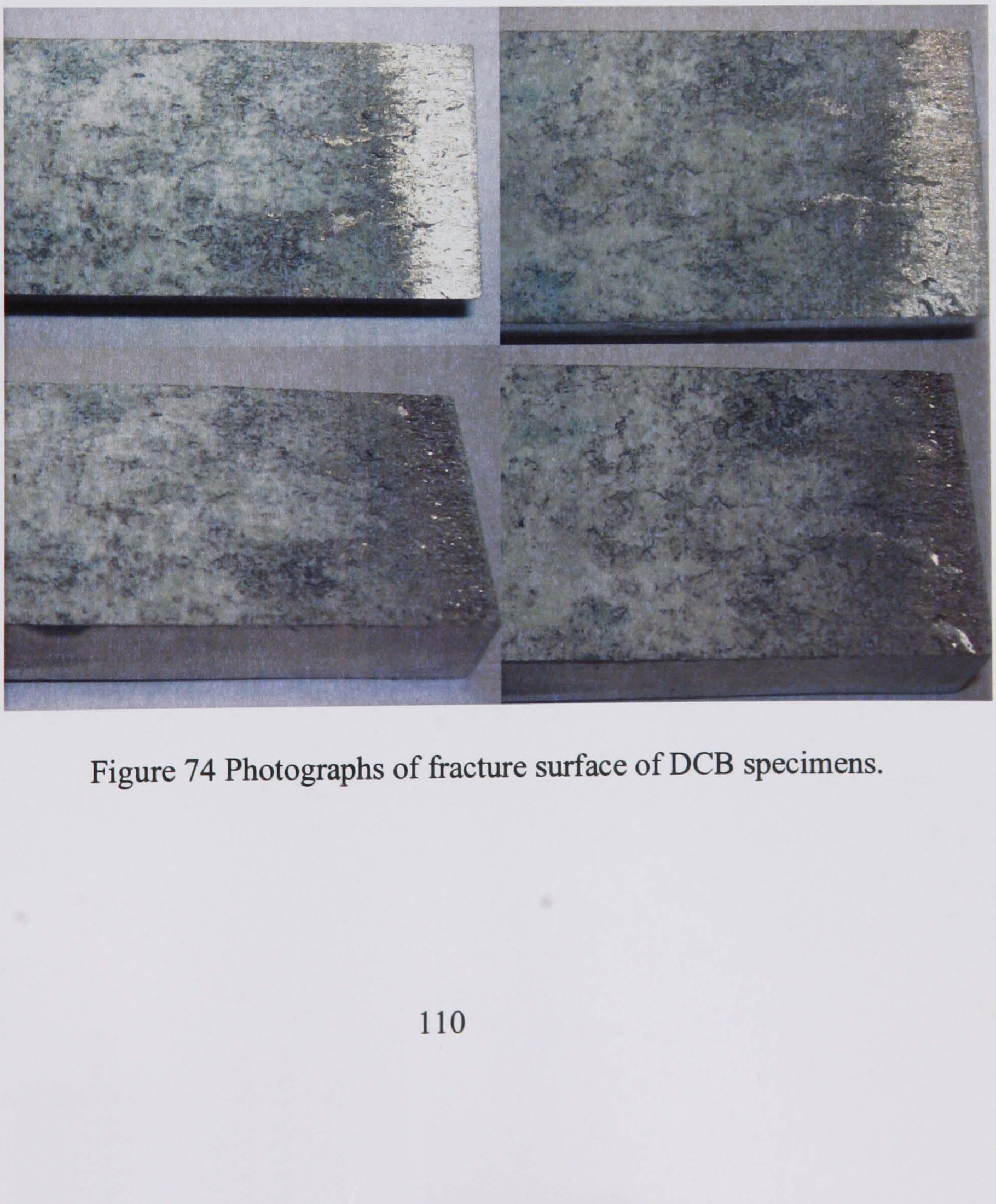

Figure 74 Photographs of fracture surface of DCB specimens.

## 11.2 The pH measurement at the crack tip.

The pH of the solution at the crack tip was close to pH 4 for all specimens tested throughout about the two months of duration of the experiment. The measurements of production of an acid solution in the advancing crack of stress corrosion cracked specimens were close to these previously reported by Shastry et al [99] and Sotoudeh et al [138]. They reported that the pH of solution at the crack tip on a stress cracking specimen of aluminium alloy was approximately 3.5. The work carried out by Foley and Le [139] also showed that acidic conditions exist within stress corrosion cracks. They reported the pHs along the crack increasing from 3.0 to 4.5 as they moved away from the crack tip. It is suspected that the acidic environment is one of the important factors causing stress corrosion crack in high strength aluminium alloys.

## 11.3 Eddy current measurement of SCC under tensile loading.

Figures 75 - 77 show the ultrasonic C-scan images from DCB4, DCB5, and DCB6 respectively. As can be seen, these tests demonstrated that the crack front bowed from one side to the other. The crack position along the left and right sides of the specimen in the C-scan were not exactly the same as expected from the optical traveling microscope measurement. The scans also showed that the internal crack shape was not always in the same line but bowed out at several positions.

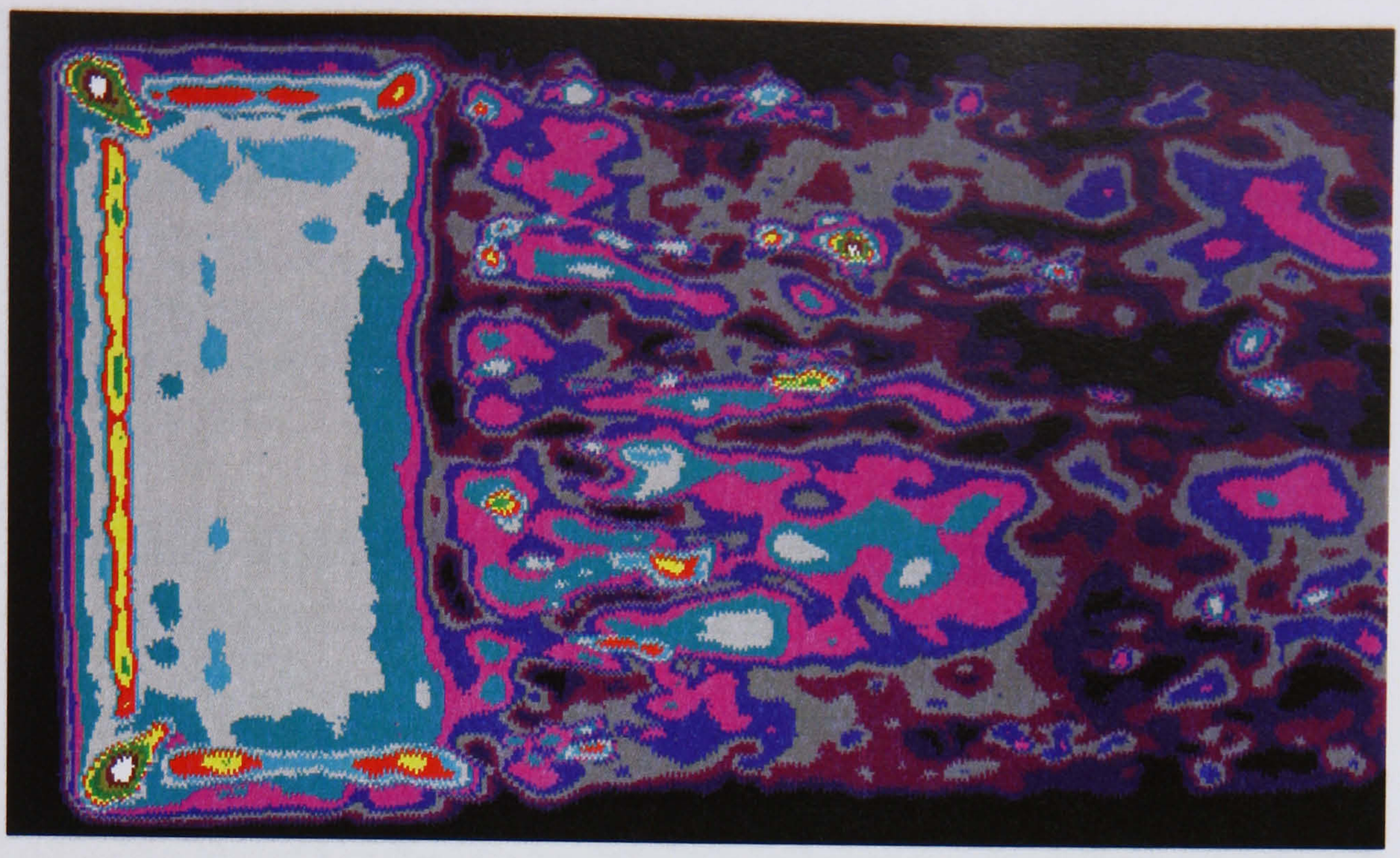

Figure 75 shows the image of ultrasonic C-scan obtained from DCB 4.

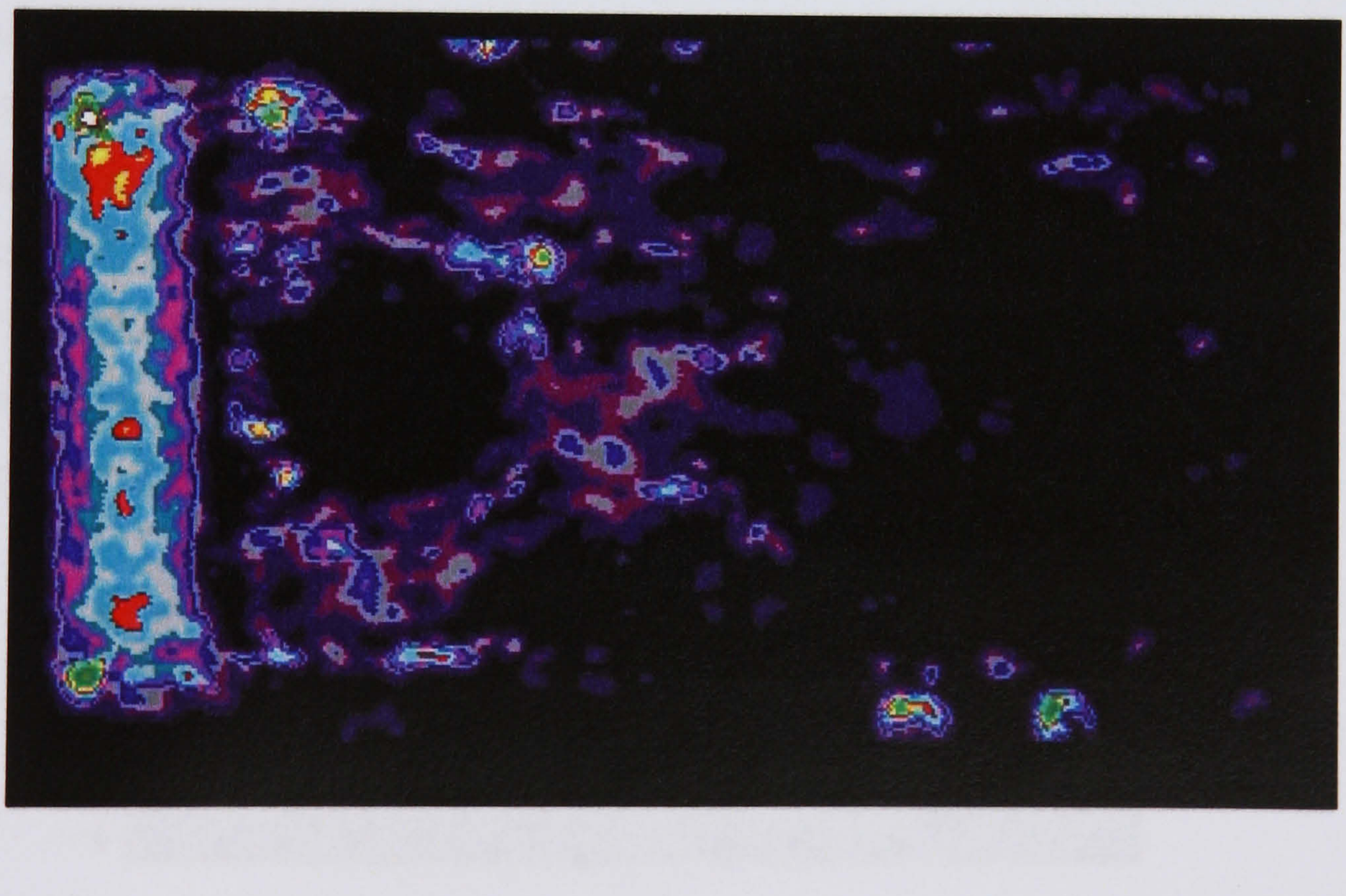

Figure 76 shows the image of ultrasonic C-scan obtained from DCB 5.

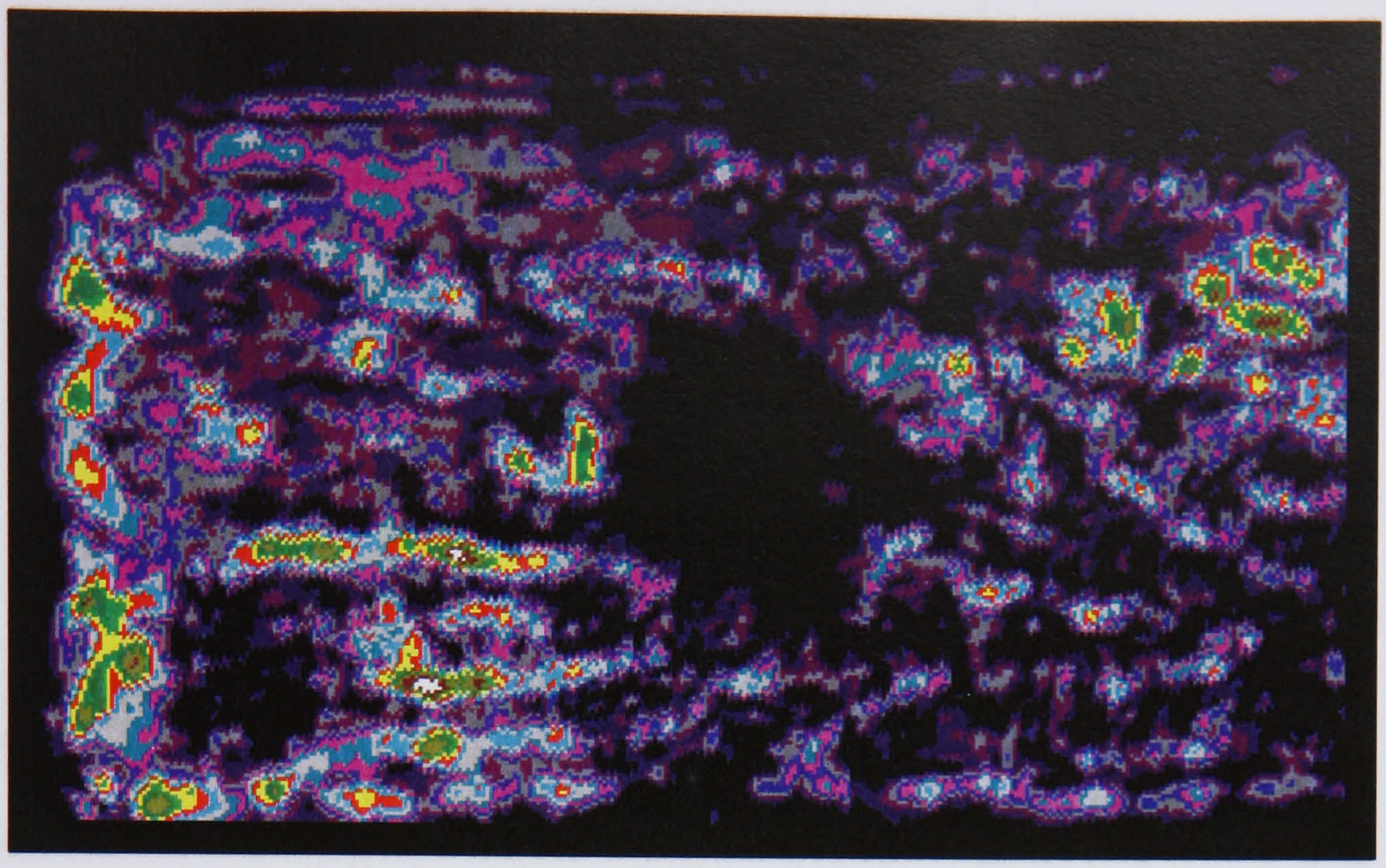

Figure 77 shows the image of ultrasonic C-scan obtained from DCB 6.

Figures 78 and 79 show schematic diagrams of the crack at side A and side B in the ultrasonic C-scan image and actual DCB specimen respectively. These figures were used to determine the length involved in the extra crack length measurement. By using the magnification ratio between the images from the ultrasonic C-scan compared to the actual specimens, the actual crack length of the DCB specimens was measured. As a check, the extra length due to crack bowing at the centre was measured by determining the difference between the average crack length measured on both sides from end of specimen compared to the crack length at centre obtained from ultrasonic C-scan.

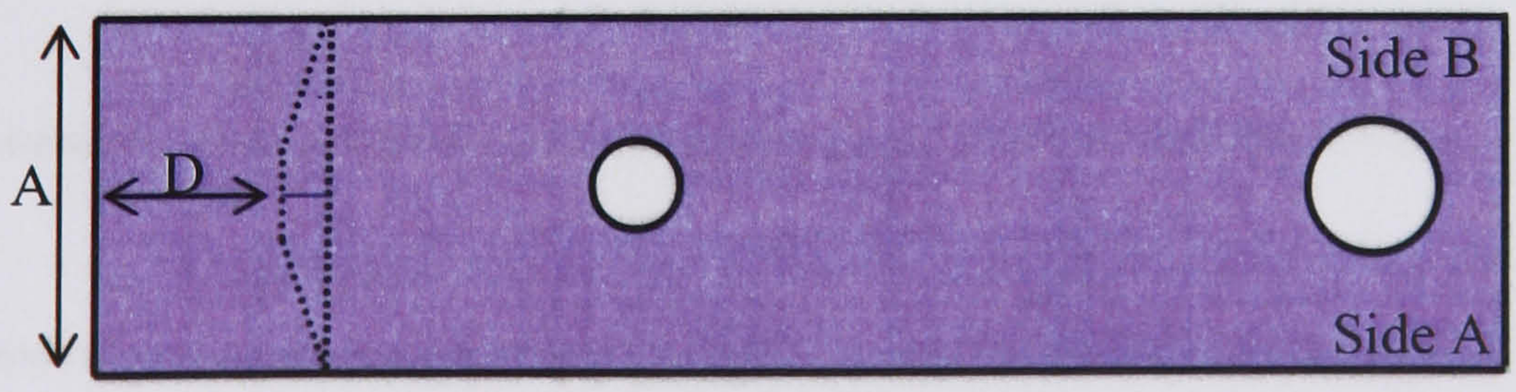


Figure 78 Schematic diagram of ultrasonic C-scan image for DCB specimen.

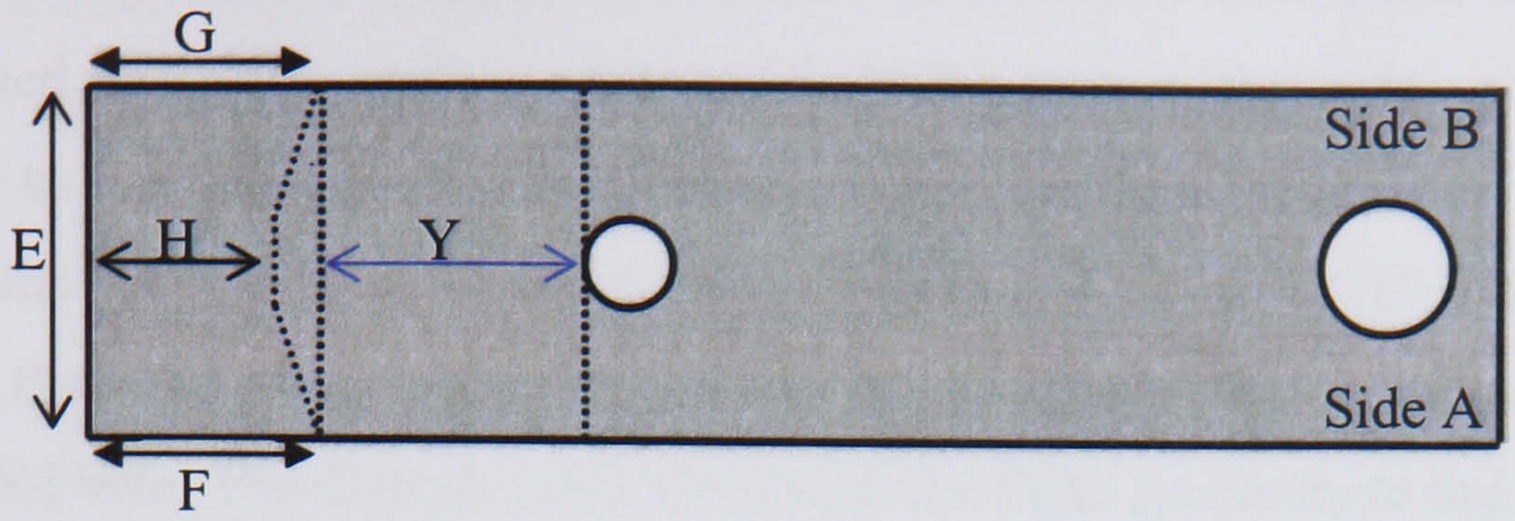


Figure 79 Schematic diagram of crack for actual DCB specimen.

In order to do that, the lengths from the C-scan image were compared to the actual lengths of the cracked DCB specimen. It should be noted that the dimensions from the actual DCB specimen and C-scan images such as A, D, E, F and G were measured with a traveling microscope. By using the magnification and substituting the appropriate length, the true crack length was scaled from the C-scan image. This procedure was made to determine the remaining uncracked material, which is the length of H in each DCB specimens. The extra length can be measured by determining the difference between the average crack length F and G compared to the crack length H in the DCB specimen. The estimated extra crack length of each DCB specimens was shown in table 16.

| DCB Specimen | The estimated extra crack length due to bowed crack (mm) |
|---|---|
| DCB 4 | 1.79 |
| DCB 5 | 1.46 |
| DCB 6 | 2.02 |

Table 16 shows estimated extra crack length due to crack bowed for each DCB specimen.

By assuming that the crack always has the same shape then the true crack length can be obtained from the surface measurements by adding the extra crack length corresponding to each specimen. Therefore the corrected crack length can be directly compared to the amplitude of the eddy current response. Each DCB specimen was scanned using the eddy current probe to measure the amplitude of eddy current response inside the drilled hole. The distance from the end of the DCB specimen to the edge of the drilled hole were 17mm, 9.5mm and 17mm for DCB 4, DCB 5 and DCB 6 respectively. It also should be noted that all the results from eddy current testing were taken with the same eddy current parameters set up. Tables 17 – 19 show corrected crack lengths and the amplitude of the eddy current response for each scan.

| Average crack length from the end of specimen X = (F+G)/2 (mm) | Crack length from the drilled hole Y = 17-X (mm) | Corrected crack length due to crack front bowing (mm) | Amplitude of eddy current crack length (mV) |
|---|---|---|---|
| 18.35 | -1.35 | 0.44 | 604.49 |
| 18.10 | -1.10 | 0.69 | 760.17 |
| 17.98 | -0.93 | 0.86 | 788.99 |
| 17.73 | -0.73 | 1.06 | 876.94 |
| 17.70 | -0.70 | 1.10 | 887.19 |
| 17.35 | -0.35 | 1.44 | 916.82 |
| 16.95 | 0.05 | 1.84 | 996.16 |
| 14.80 | 2.20 | 3.99 | 1183.65 |
| 14.00 | 3.00 | 4.79 | 1563.46 |
| 13.50 | 3.50 | 5.29 | 1675.05 |
| 13.20 | 3.80 | 5.59 | 1784.70 |
| 12.90 | 4.10 | 5.89 | 1792.87 |
| 12.35 | 4.65 | 6.44 | 1916.82 |
| 11.50 | 5.50 | 7.29 | 2000.33 |
| 10.85 | 6.15 | 7.94 | 2057.43 |
| 8.47 | 8.53 | 10.32 | 2203.19 |
| 8.00 | 9.00 | 10.79 | 2228.07 |
| 7.50 | 9.50 | 11.29 | 2304.02 |
| 6.55 | 10.45 | 12.24 | 2281.49 |
| 4.55 | 12.45 | 14.24 | 2304.66 |
| 1.35 | 15.65 | 17.44 | 2493.23 |

Table 17 shows corrected crack lengths and the amplitude of the eddy current response for DCB 4.

| Average crack length from the end of specimen X = (F+G)/2 (mm) | Crack length from the drilled hole Y = 9.5-X (mm) | Corrected crack length due to crack front bowing (mm) | Amplitude of eddy current crack length (mV) |
|---|---|---|---|
| 8.82 | 0.68 | 2.14 | 720.00 |
| 8.07 | 1.43 | 2.89 | 890.00 |
| 6.12 | 3.38 | 4.84 | 1676.18 |
| 5.32 | 4.18 | 5.64 | 1736.31 |
| 5.10 | 4.40 | 5.86 | 1797.99 |
| 4.70 | 4.80 | 6.26 | 1925.61 |
| 4.33 | 5.17 | 6.63 | 1978.22 |
| 3.77 | 5.75 | 7.19 | 1980.20 |
| 2.07 | 7.43 | 8.89 | 2329.66 |
| 2.00 | 7.50 | 8.96 | 2265.85 |
| 1.30 | 8.20 | 9.66 | 2332.66 |
| 0.87 | 8.63 | 10.09 | 2526.42 |

Table 18 shows corrected crack lengths and the amplitude of the eddy current response for DCB 5.

| Average crack length from the end of specimen X = (F+G)/2 (mm) | Crack length from the drilled hole Y = 17-X (mm) | Corrected crack length due to crack front bowing (mm) | Amplitude of eddy current crack length (mV) |
|---|---|---|---|
| 18.18 | -1.18 | 0.84 | 69.24 |
| 17.62 | -0.62 | 1.40 | 258.62 |
| 16.40 | 0.60 | 2.62 | 878.70 |
| 15.90 | 1.10 | 3.12 | 966.61 |
| 14.50 | 2.50 | 4.52 | 1228.08 |
| 13.20 | 3.80 | 5.82 | 1463.22 |
| 12.60 | 4.40 | 6.42 | 1768.84 |
| 11.80 | 5.20 | 7.22 | 1991.58 |
| 11.60 | 5.40 | 7.42 | 2023.91 |
| 11.05 | 5.59 | 7.97 | 2097.75 |
| 10.75 | 6.25 | 8.27 | 2146.94 |
| 10.20 | 6.80 | 8.82 | 2147.17 |
| 9.65 | 7.35 | 9.37 | 2250.00 |
| 9.10 | 7.90 | 9.92 | 2314.99 |
| 2.15 | 14.85 | 16.87 | 2569.06 |
| 1.20 | 15.80 | 17.82 | 2677.32 |

Table 19 shows corrected crack lengths and the amplitude of the eddy current response for DCB 6.

The depth of an unknown stress corrosion crack in a fastener hole can now be analyzed by using the amplitude of its eddy current response. For this purpose, all the results from the three DCB specimens were combined together to produce a calibration graph. This graph represents stress corrosion cracks directly as a function of crack length and the amplitude response. A corrected crack length has been made by adding an extra

length to the original crack length. A graph of corrected crack length (crack depth) against amplitude of the signal was plotted. Figure 80 shows the graph of eddy current amplitude as a function of crack length.

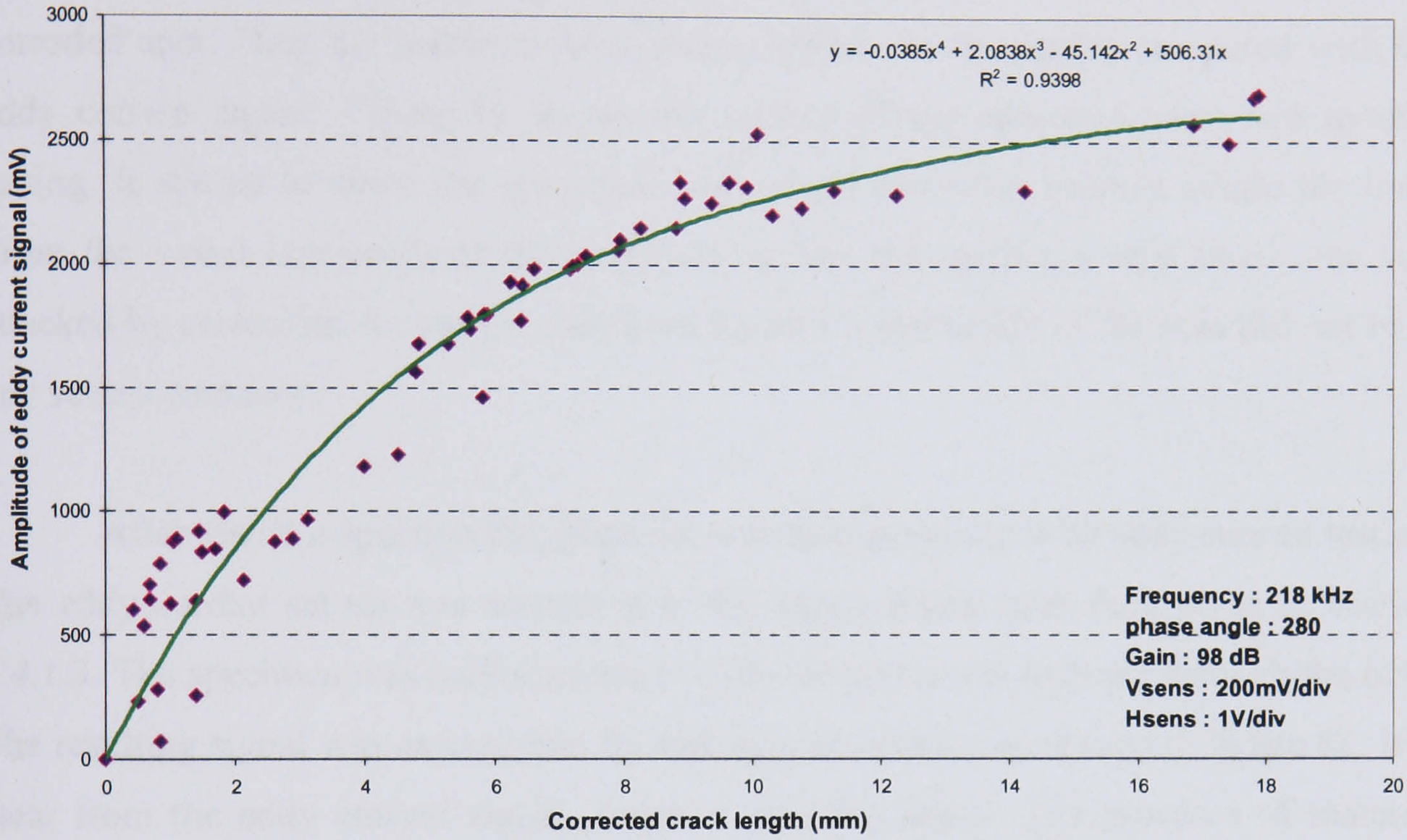


Figure 80 Calibration of eddy current amplitude as a function of crack length.

It appears from this graph that for crack lengths between 0 and 2mm. the amplitude of the eddy current response rapidly increased with crack length. The eddy current was very sensitive to change in crack length in this region and this would be the best crack length range with this probe and this operating frequency. While it was possible to detect cracks up to 18mm. in length, the measurements had poor resolution with long cracks and in for such cases a lower test frequency would be recommended.

**11.4 SCC under compressive loading.**

In this section the experiment result has been split into three parts; SCC under compressive loading with a 3.5% NaCl solution, SCC under compressive loading with EXCO solution and finally SCC without compressive loading.

### 11.4.1 SCC under compressive loading with 3.5% NaCl solution.

After two months of wetting and drying with a 3.5% NaCl corrosive solution, the specimen was removed from the test. It was cleaned with propanol and washed in running water. The specimen was inspected with a low powered microscope to locate the corroded area. Then the specimen was photographed and the results compared with the eddy current signal. Figure 81 shows the surface of the specimen after two months testing. It started to show the appearance of a light corrosion product inside the hole. From the visual inspection of the specimen, it was shown that a very small area was attacked by corrosion. As can be seen from figure 81, the inside of the hole did not have any severe corrosion.

After visual inspection the specimen was then inspected with eddy current testing. The eddy current set up was according to the experimental procedure given in section 8.4.1.3. The specimen was held stationary while the probe was scanned through the hole. The resulting signal was as expected for uncorroded material as shown in figure 82. It is clear from the eddy current signal shown a very flat signal. The presence of material degradation was very small and it would not expect to show any indication of the crack in the hole specimen. The small displacement of the signal indicates the different in light of corroded and uncorroded areas.

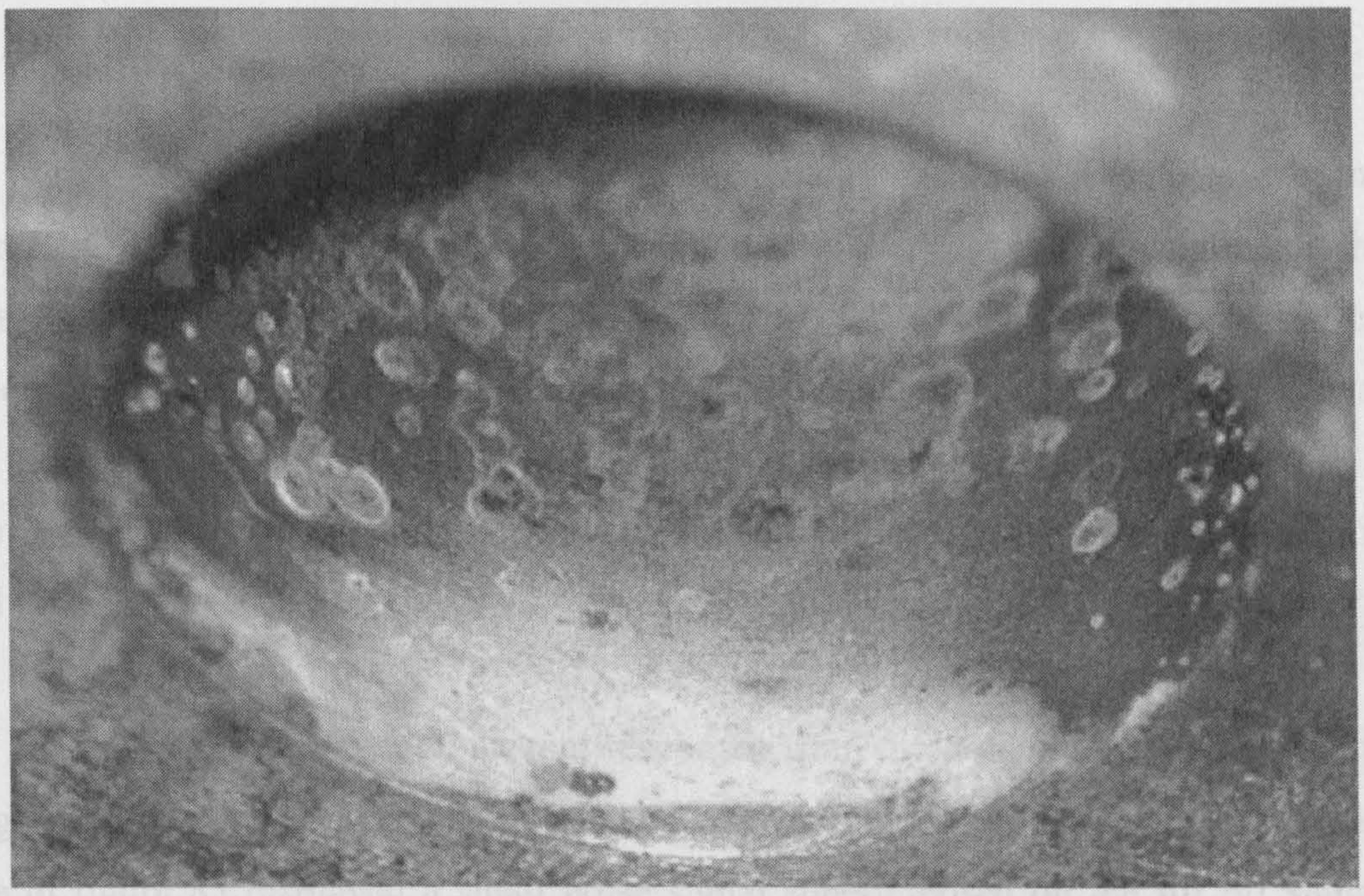


Figure 81 shows the surface of the specimen after two months wetting and drying with a 3.5 % NaCl.

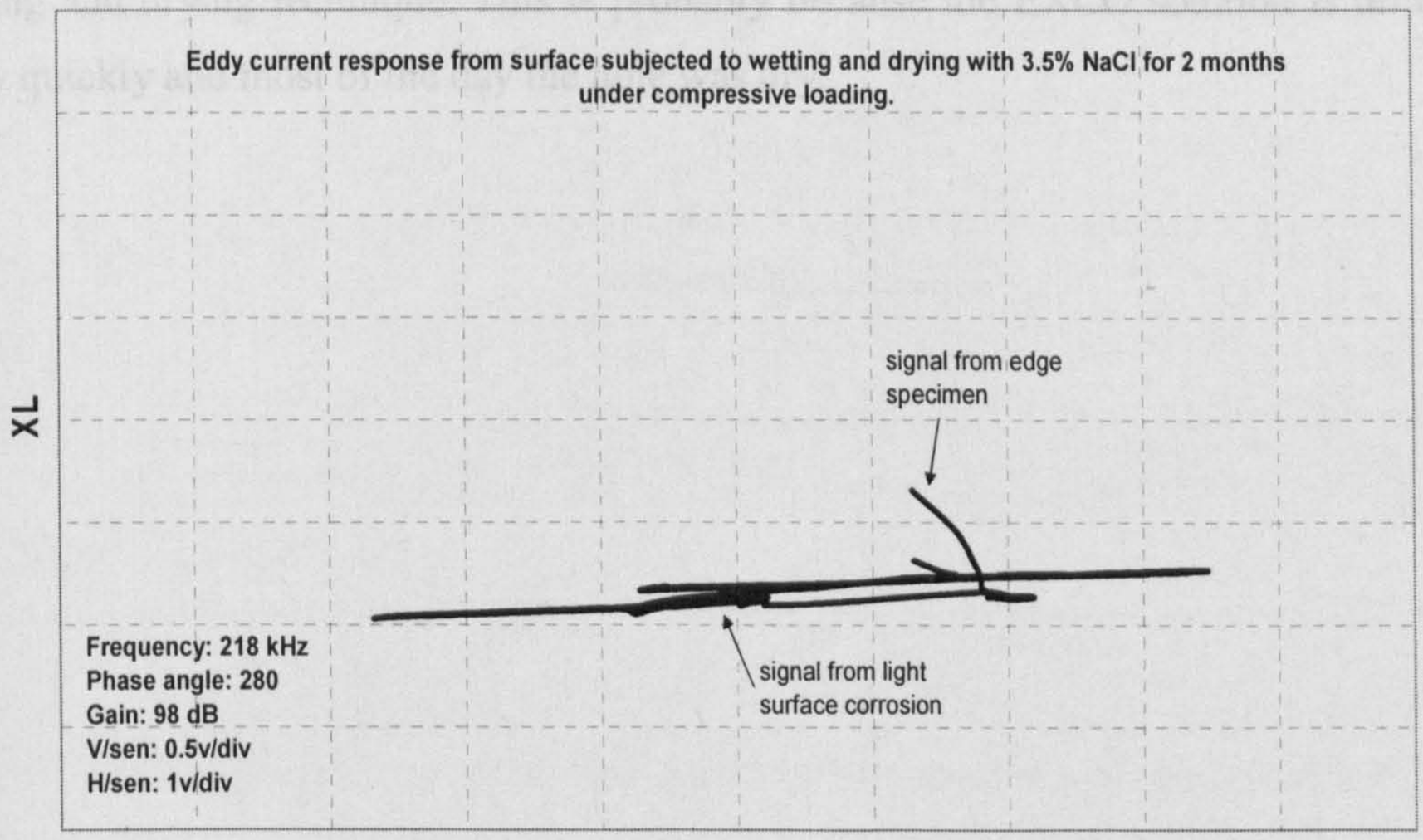


Figure 82 Eddy current responses after 2 months subjected to wetting and drying with a 3.5 % NaCl solution under compressive loading.

### 11.4.2 SCC under compressive loading with EXCO solution.

Figure 83 shows the surface of the specimen after two months wetting and drying with an EXCO solution. It can be seen that more corrosion product built up inside the hole than with the 3.5% NaCl solution. The surface of the specimen was covered by corrosion product over all the area. From the visual inspection of the specimen, it was shown that more area was attacked by corrosion compared to the previous experiment. It can be noticed from figure 83 that the inside of the hole had more severe corrosion around the hole.

Figure 84 shows the eddy current responses from the hole which is subjected to wetting and drying with EXCO solution. The eddy current signal corresponding to the surface in figure 83 displayed a small noise signal superimposed on the lift off signal. This was due to a small amount of metal loss at the surface specimen. The signal suggests that the depth of corrosion has increased compare with figure 82. However, there was no indication of a crack in the hole. There was no amplitude in the y-direction which is the usual indication of a crack. Therefore, it seems very difficult to produce a crack with wetting and drying technique. This is probably because the EXCO solution is dries out fairly quickly and most of the day the hole was dry.

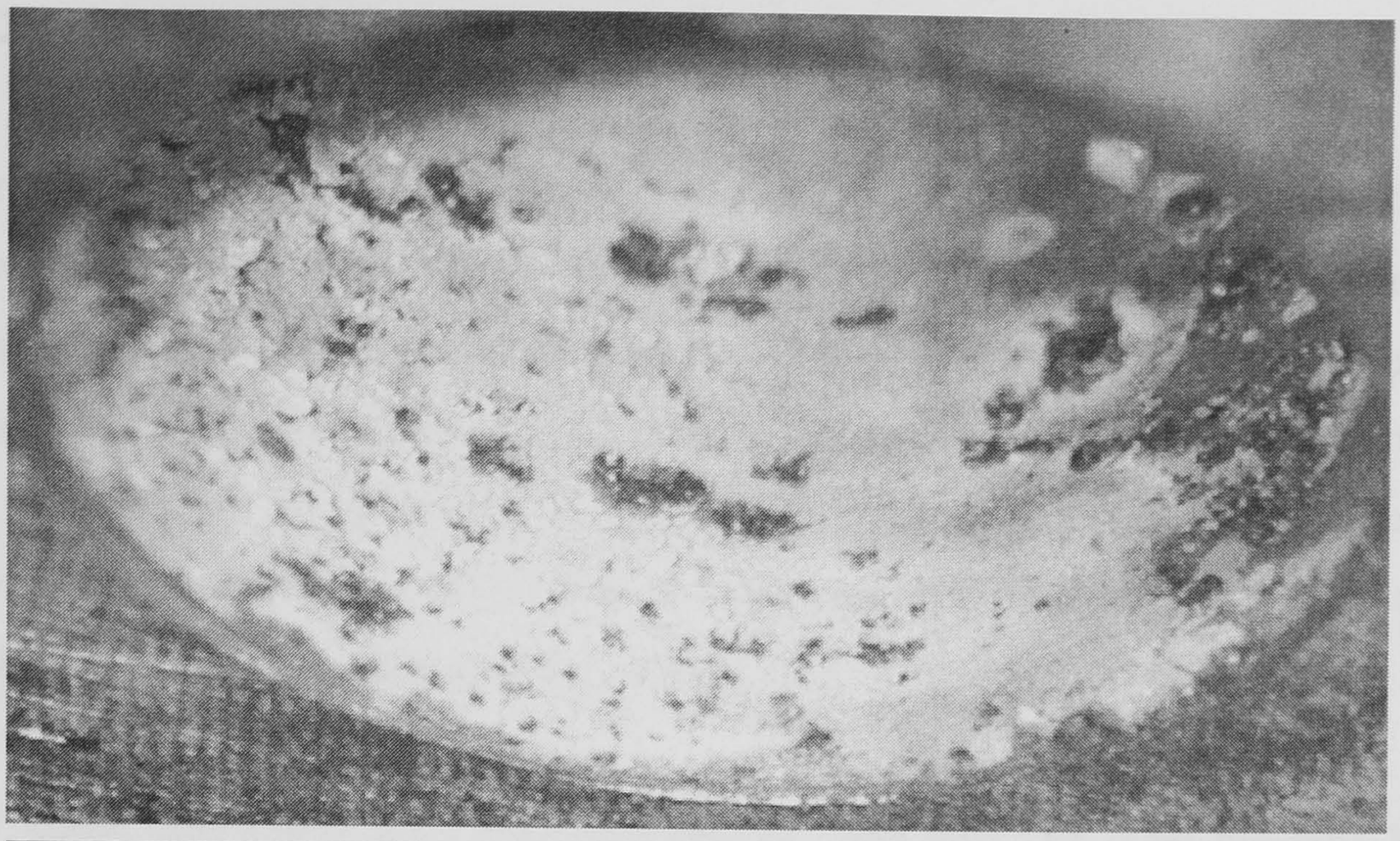


Figure 83 shows the surface of the specimen after two months wetting and drying with EXCO solution

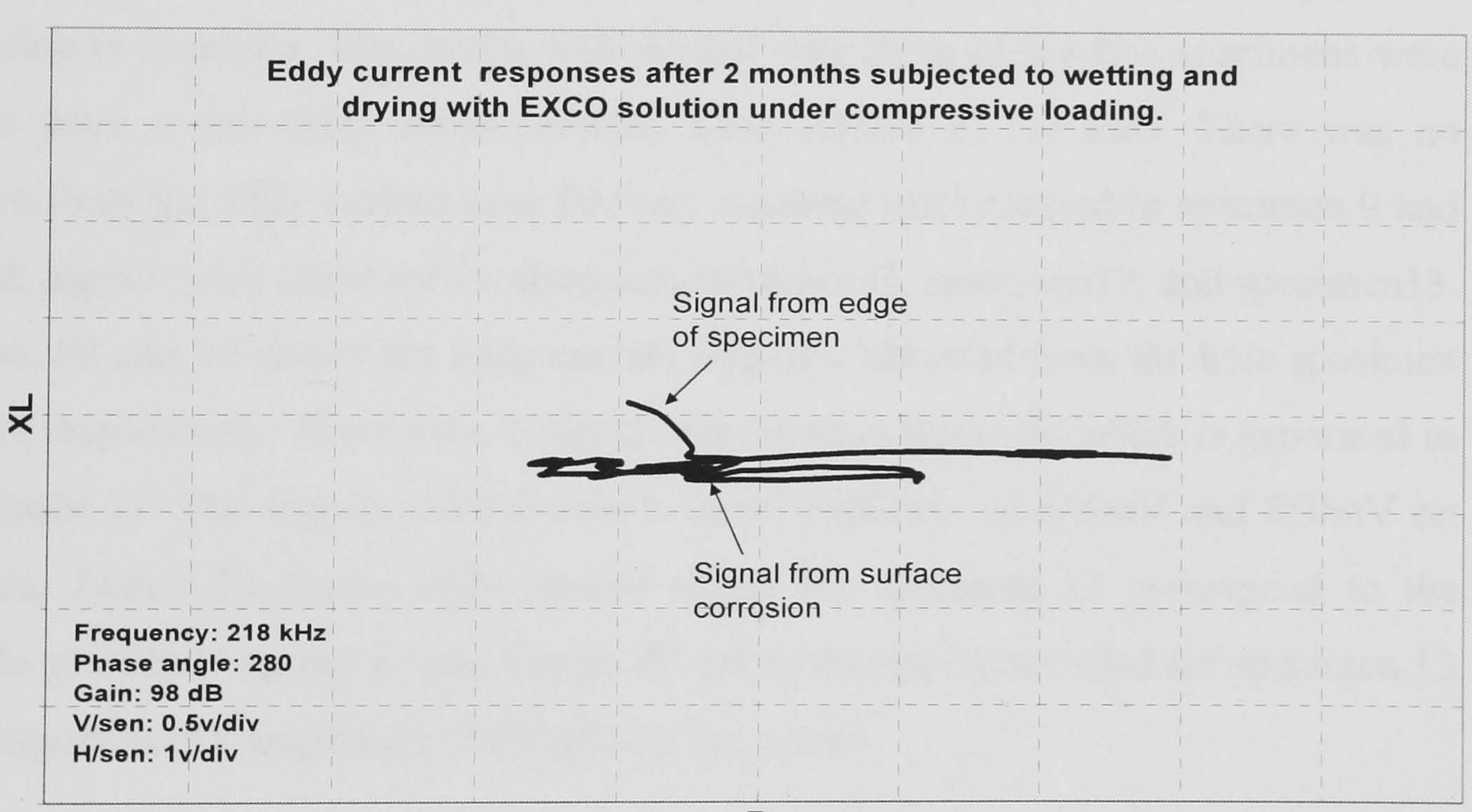


Figure 84 Eddy current responses after 2 months subjected to wet and dry with EXCO solution under compressive loading.

### 11.4.3 SCC under compressive loading with immersion technique.

After 2 weeks exposure to EXCO solution the specimen was removed from the test. It was washed in running water and dried with a stream of warm air. The specimen was inspected with a low magnification microscope to show the corrosion damage around the hole. The photographs in figure 85, 87, 89 are for specimen11, specimen12 and specimen13 respectively. All specimens showed very severe of corrosion attack which was quite uniform over the surface of the hole. In some cases, exfoliation had occurred at the edge of the hole resulting in lifting of the surface grain.

After visual inspection, light corrosion product was removed from the hole to allow the eddy current probe access into the hole. Each specimen was scanned with eddy current testing according to procedure given in the previous section. All specimens showed a lift-off signal and edge effect. There was also evidence of amplitude of the eddy current signal along the y-axis of the impedance plot which indicated the presence of corrosion or cracking. The results showed that only three of the five specimens were found to have a detectable crack initiated from surface of the hole. There was no indication from the eddy current scan that any cracking had occurred in specimen 9 and 10. Crack signals were observed for specimen specimen11, specimen12, and specimen13. Figure 86, 88 and 90 shows the eddy current response obtained from the hole specimen 11, 12, 13 respectively. There were 2 signals displayed in figure 86 which is generated in the specimen 11. The signals were shown to have amplitude of 645mV and 850mV on the screen. Figure 88 shows eddy current signal for specimen 12 correspond to the amplitude of 640mV on the screen. Figure 90 shows the signal recorded for specimen 13 and correspond to the amplitude of 283mV on the screen.

From the eddy current measurement, the cracked areas of the specimen were marked. Then the specimens were sectioned in the short transverse direction of the hole and polished to a 1 μm finish to examine the cracks by metallography. The sectioned specimens were re-examined and re-polished until the longest cracks were achieved. This process was completed for the other two specimens. The longest cracks were inspected

by high magnification optical microscopy. A comparison was made between crack lengths measured by metallography and those recorded from the amplitude eddy current signal.

As demonstrated in figures 91, 92, 93 and 94 for all cases the cracks were initiated from the surface of the hole and propagated into the material. In some but not all cases, the cracks had initiated from broad corrosion fissures at the surface. Two cracks were found in the specimen 11 as shown in figure 91 – 92. The measurement was made by using the eddy current and dial indicator to determine the separation between two those cracks. One side of the specimen was scanned to provide a first crack signal separate with horizontal signal of remaining thickness until the second crack signal detected on the screen again. By using this procedure with dial indicator, the distance between them can be assessed. The separation of those two cracks was 5.30mm and for this reason their eddy current signals were slightly overlapping. This resulted in the complex plot shown in figure 86, without clearly defined lift-off signal. There was also evidence of the end grain attack to be seen parallel to the rolling direction of the material and had for some distance spread out from the edge of the specimen. Moreover, large fissures developed at the edge of the hole specimen. Table 20 shows the voltage of the eddy current signals corresponding to cracks length in the specimen.

| The voltage of the Eddy signal (mV) | Crack length in specimen (mm) |
|---|---|
| 283 | 0.780 |
| 640 | 1.414 |
| 645 | 0.683 |
| 850 | 1.796 |

Table 20 shows the voltage of the eddy current signals corresponding to cracks length in the specimen.

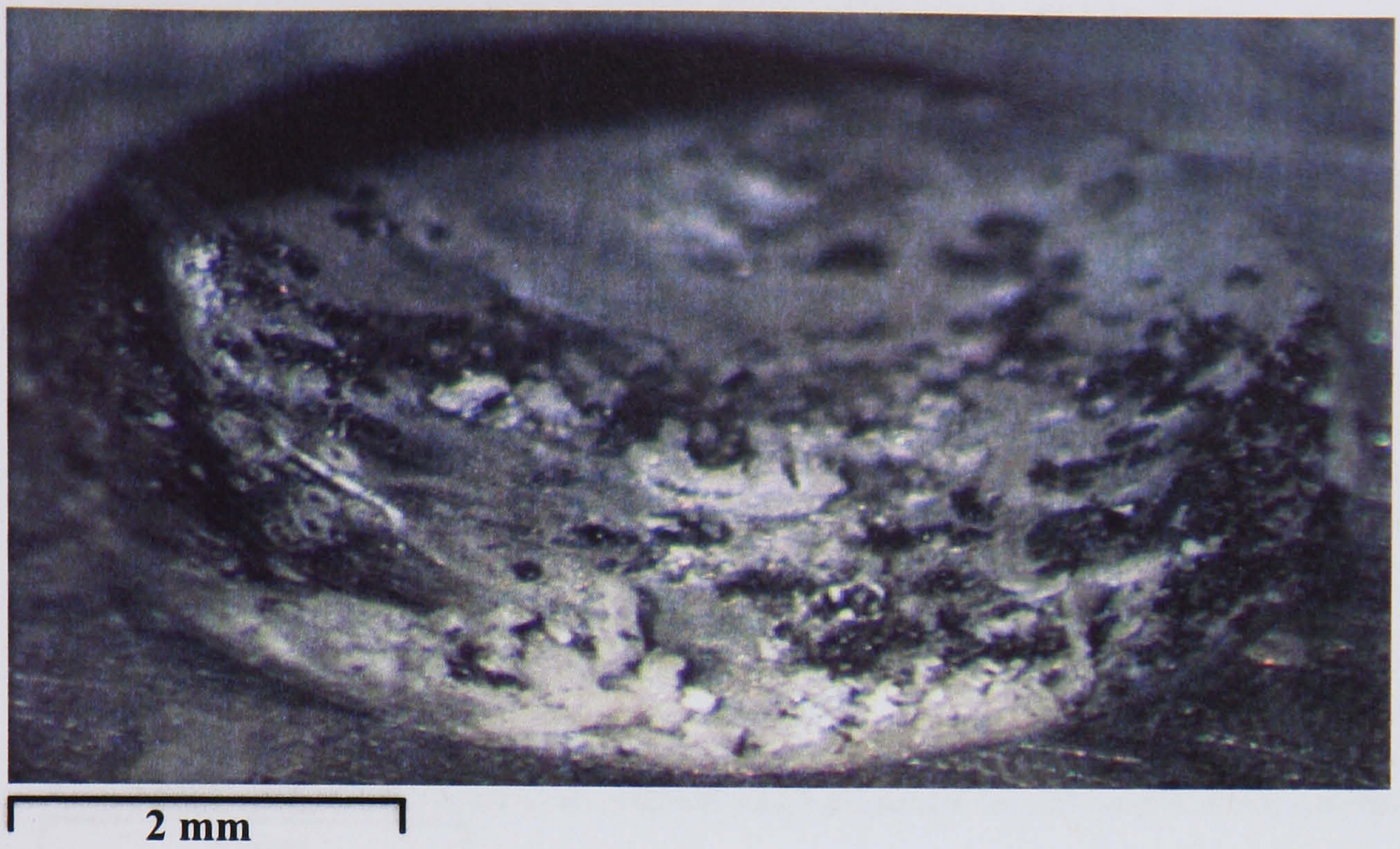


Figure 85 shows the corrosion product inside the hole surface for specimen 11.

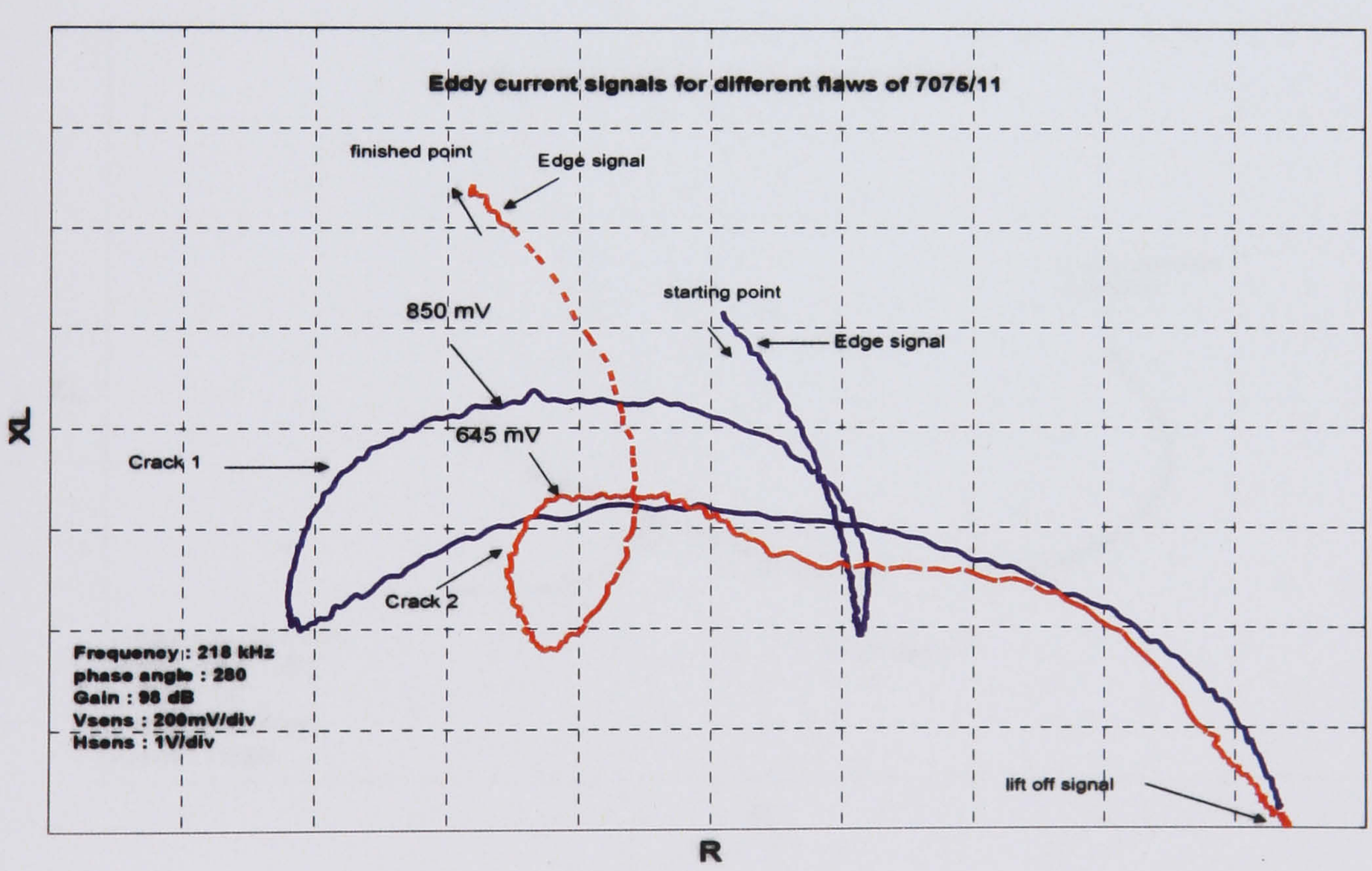


Figure 86 shows the typical response to a crack and the edge effect in the specimen 11.


Figure 87 shows the corrosion product inside the hole surface for specimen 12.

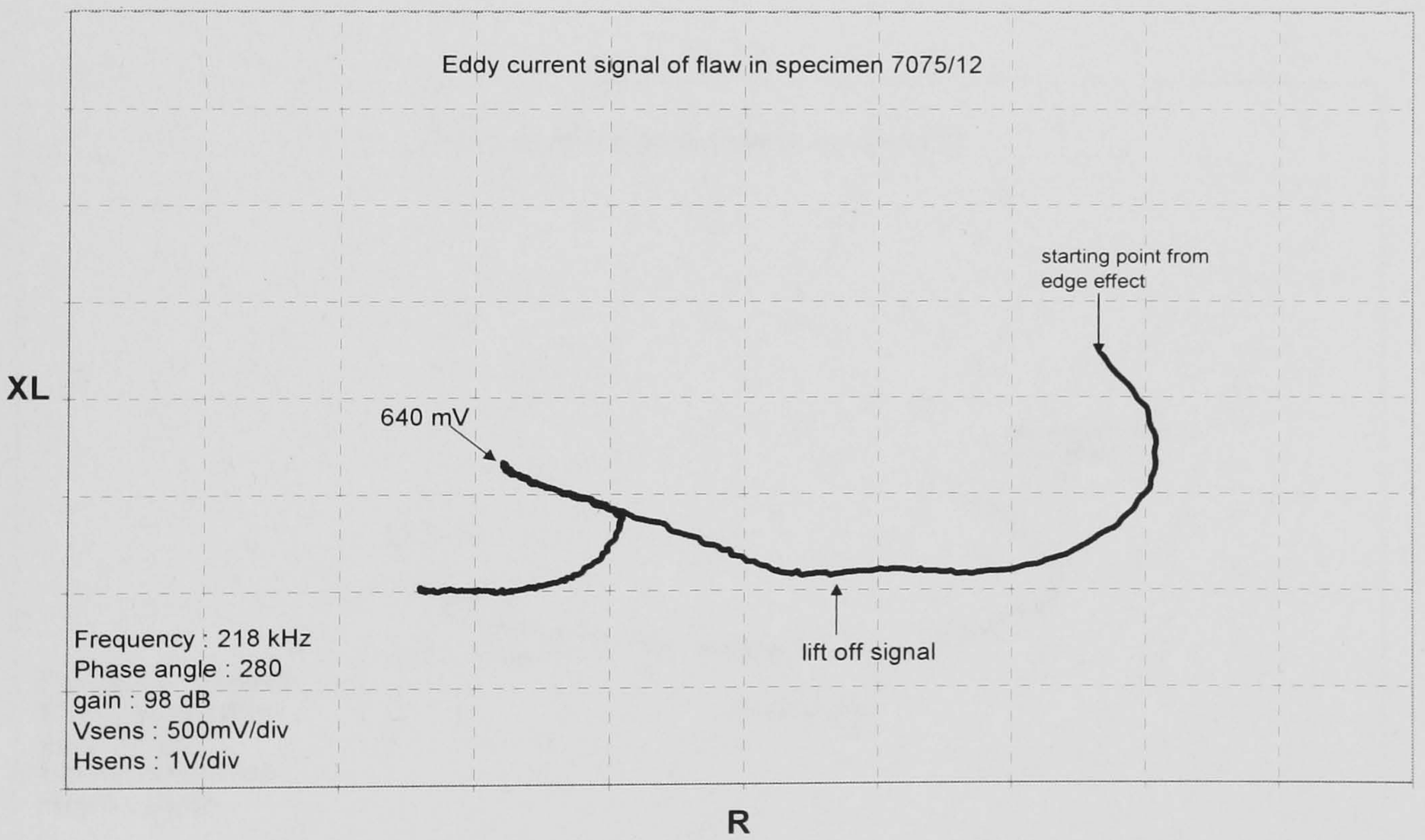


Figure 88 shows the typical response to a crack and the edge effect in the specimen 12.

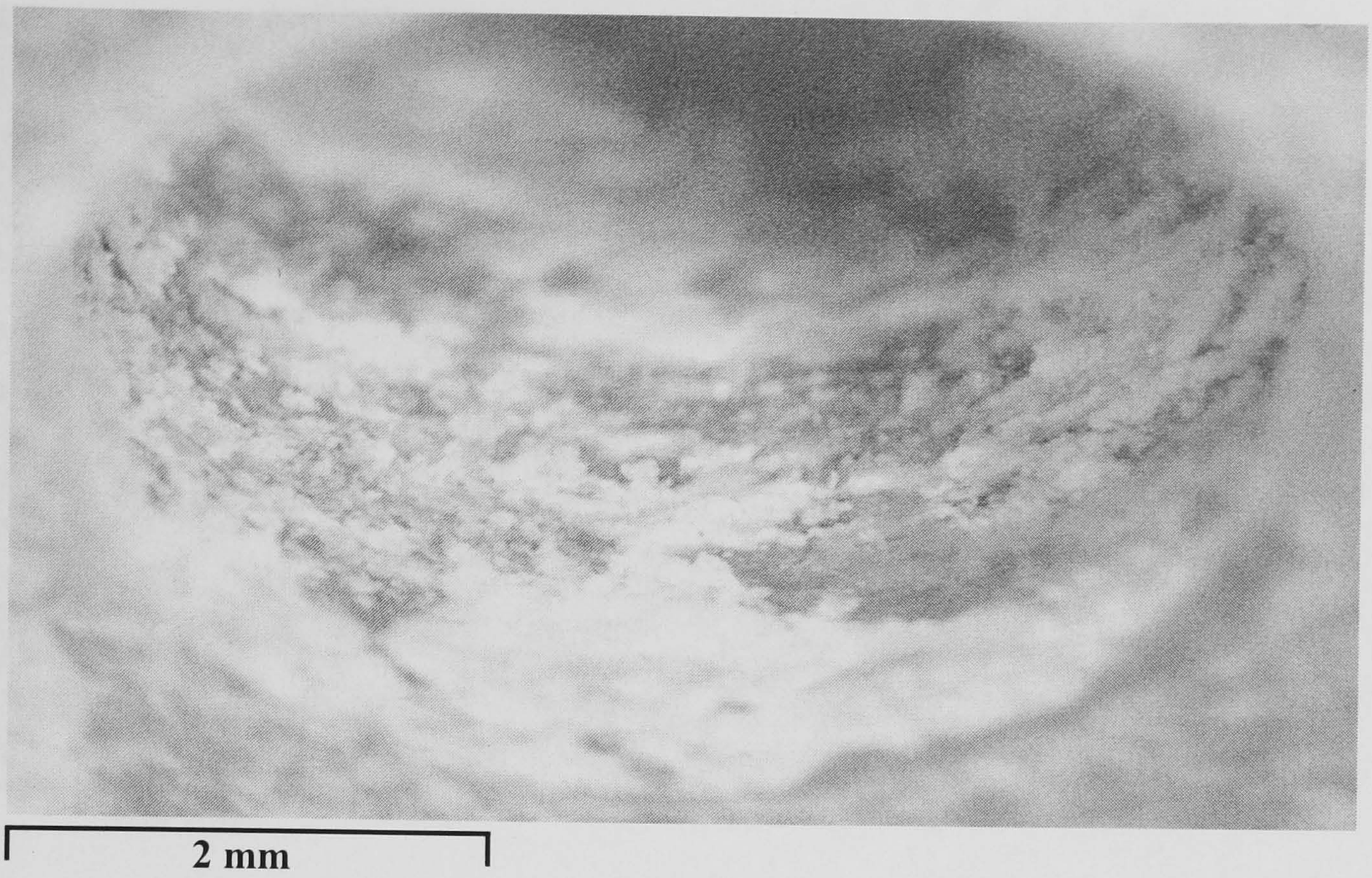


Figure 89 shows the corrosion product inside the hole surface for specimen 13.

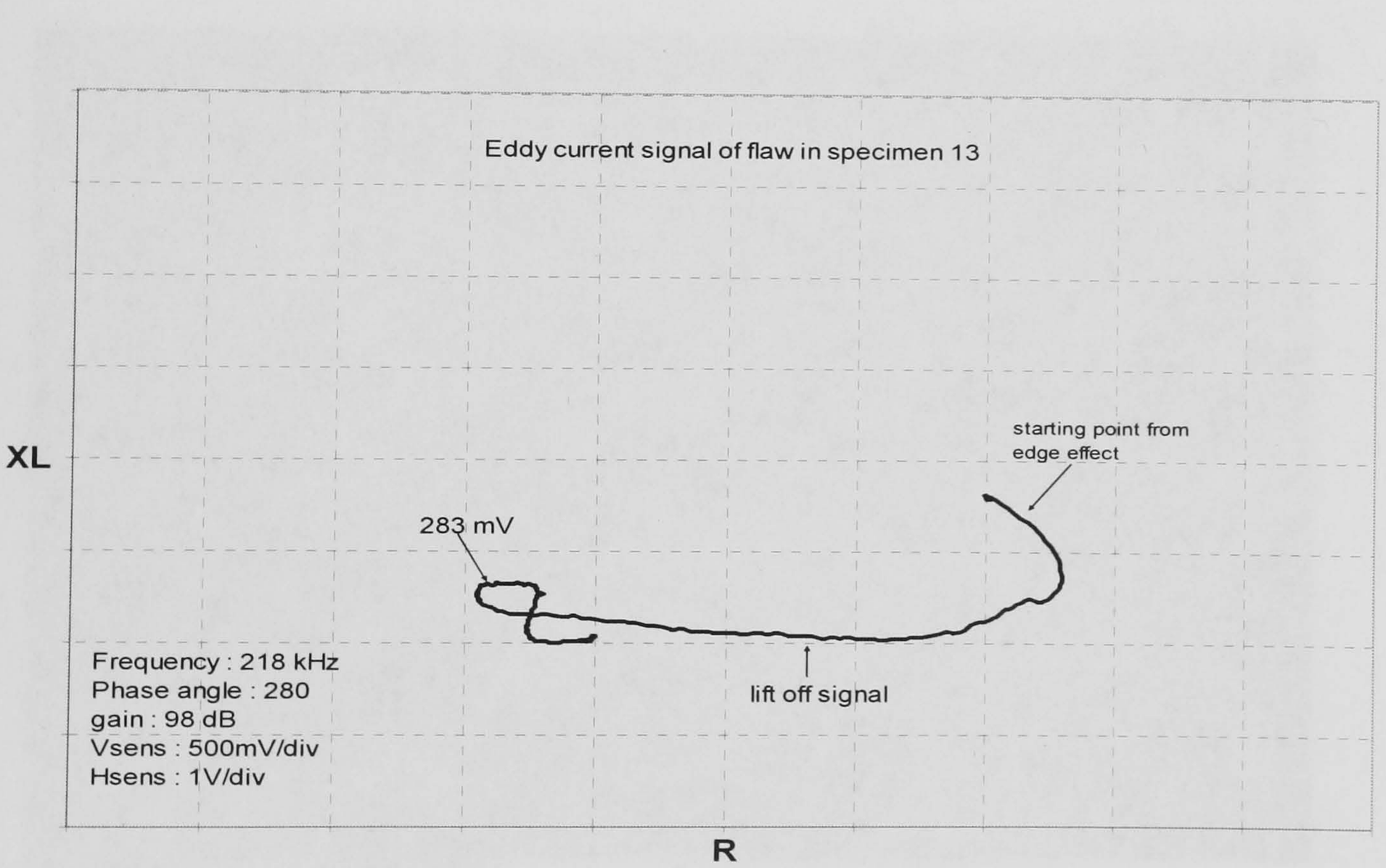


Figure 90 shows the typical response to a crack and the edge effect in the specimen 13

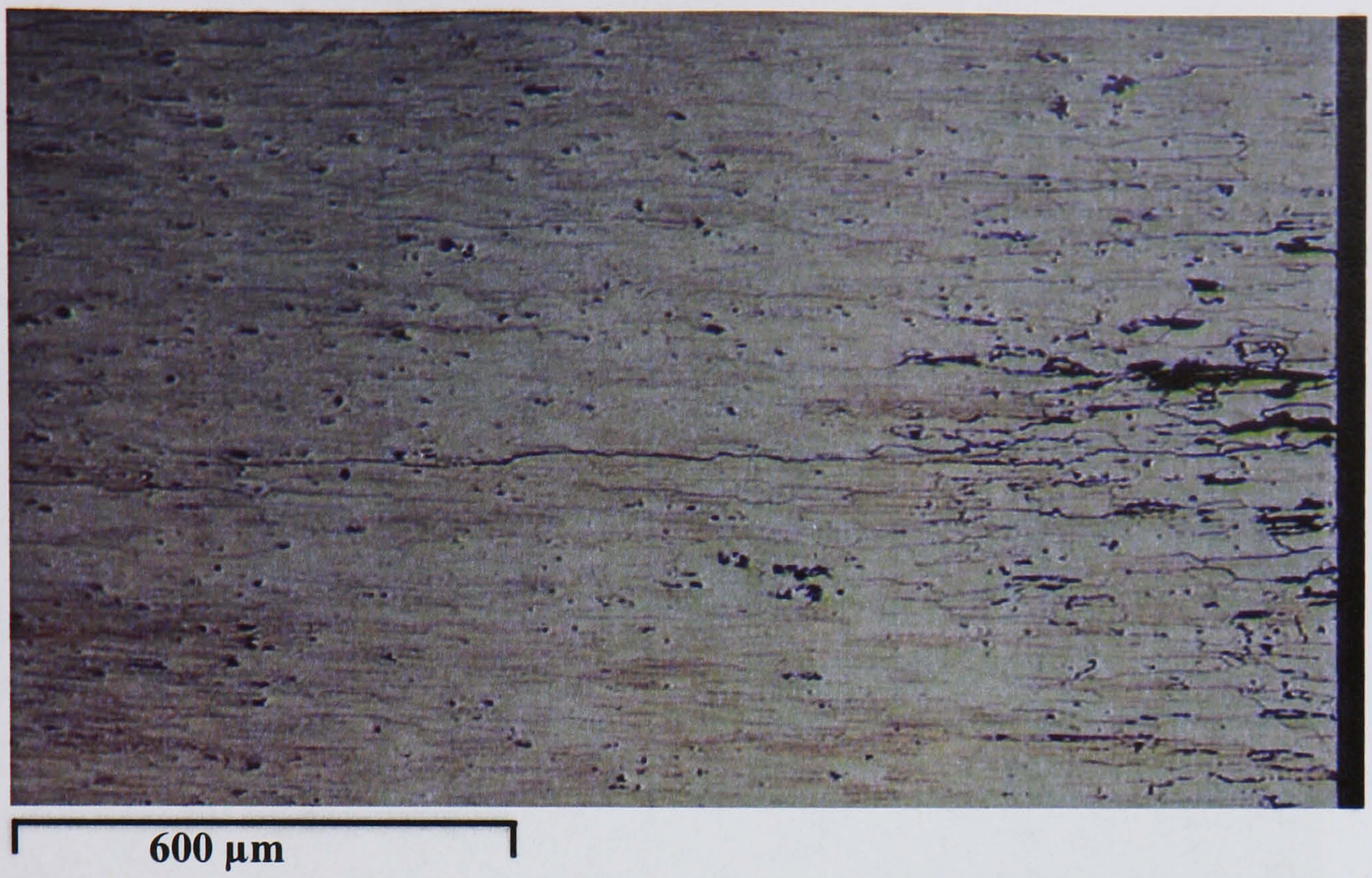


Figure 91 Optical micrograph shows the first crack in the specimen 11

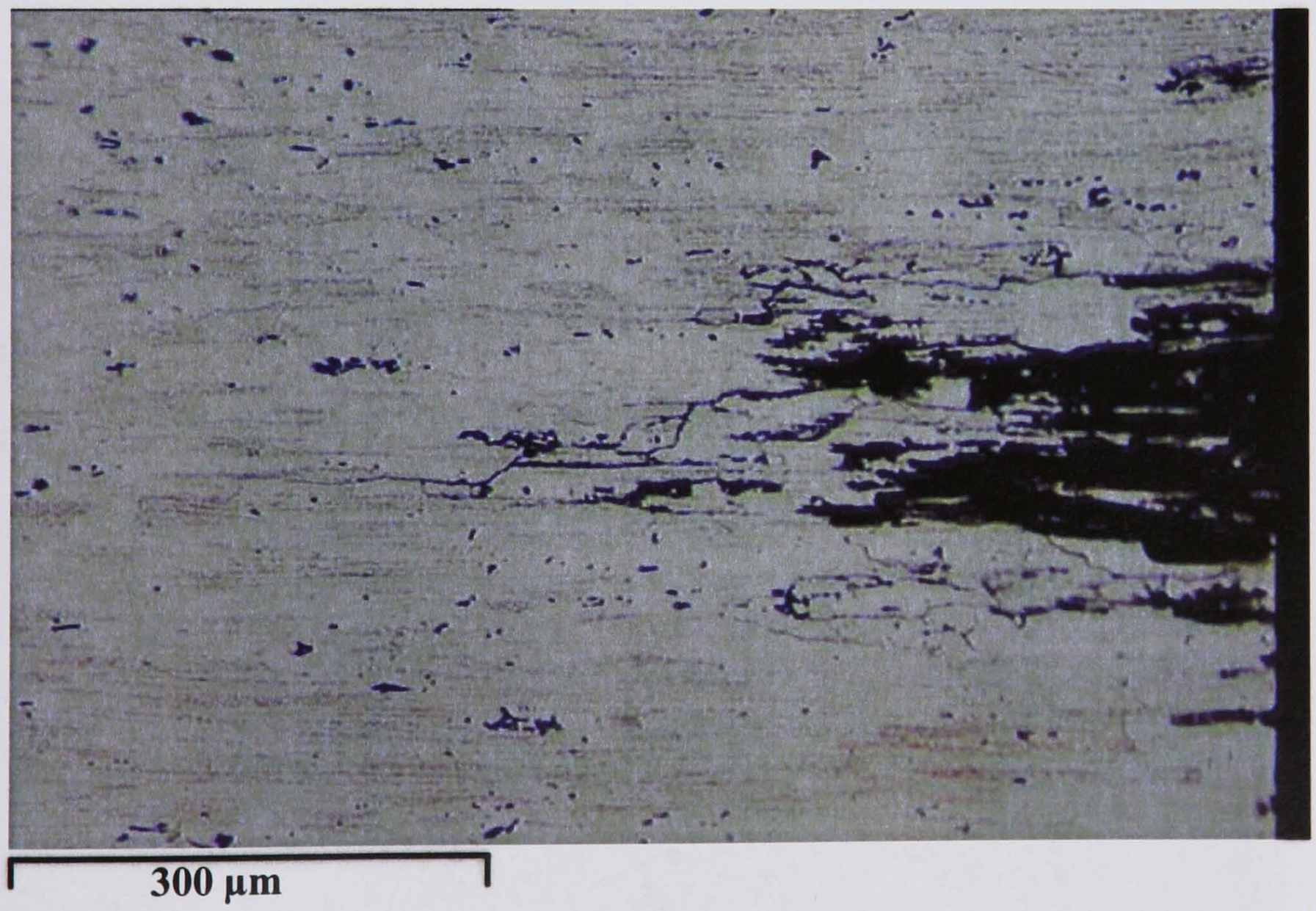


Figure 92 Optical micrograph shows the second crack in the specimen 11.

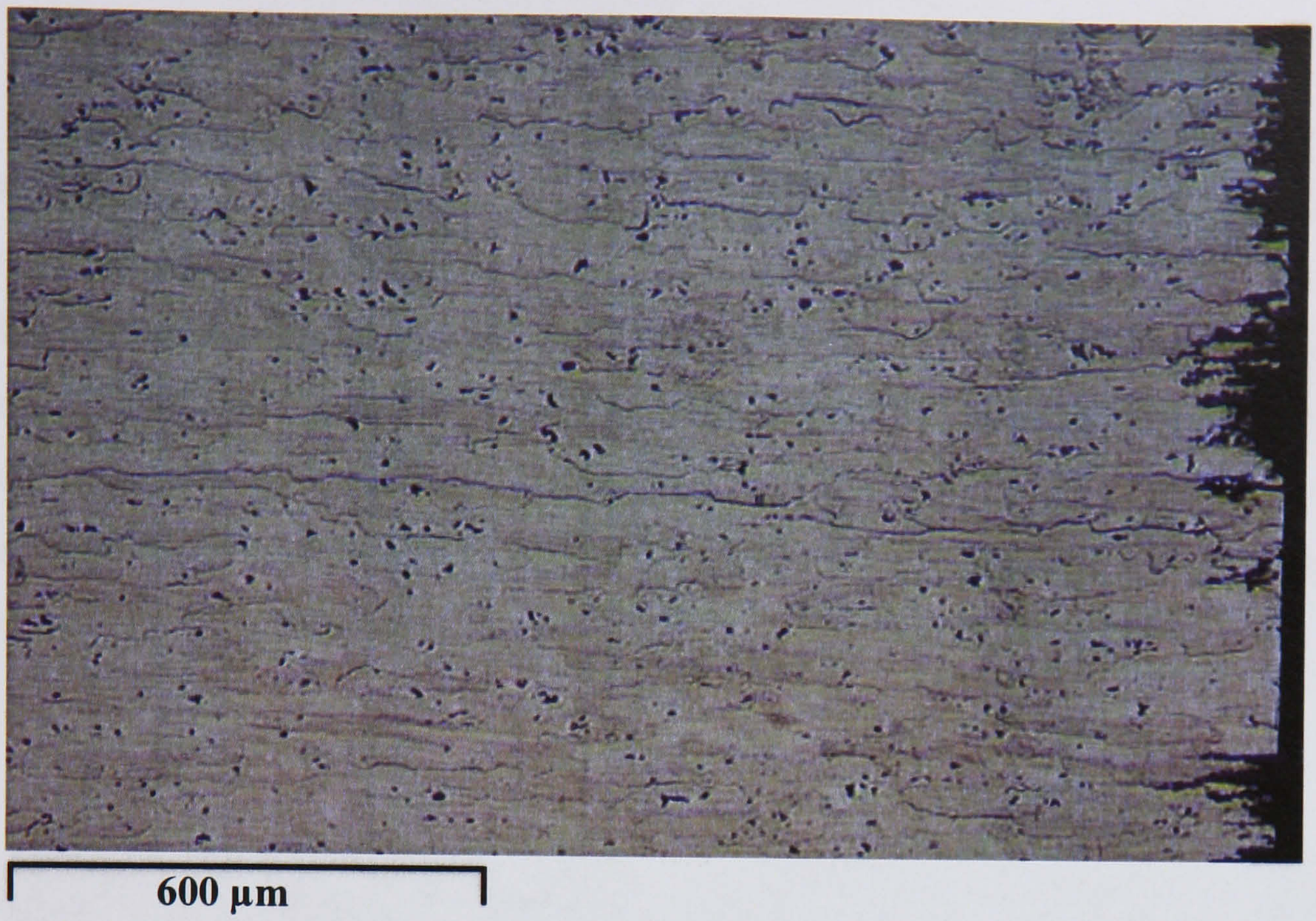


Figure 93 Optical micrograph shows the crack in the specimen 12.

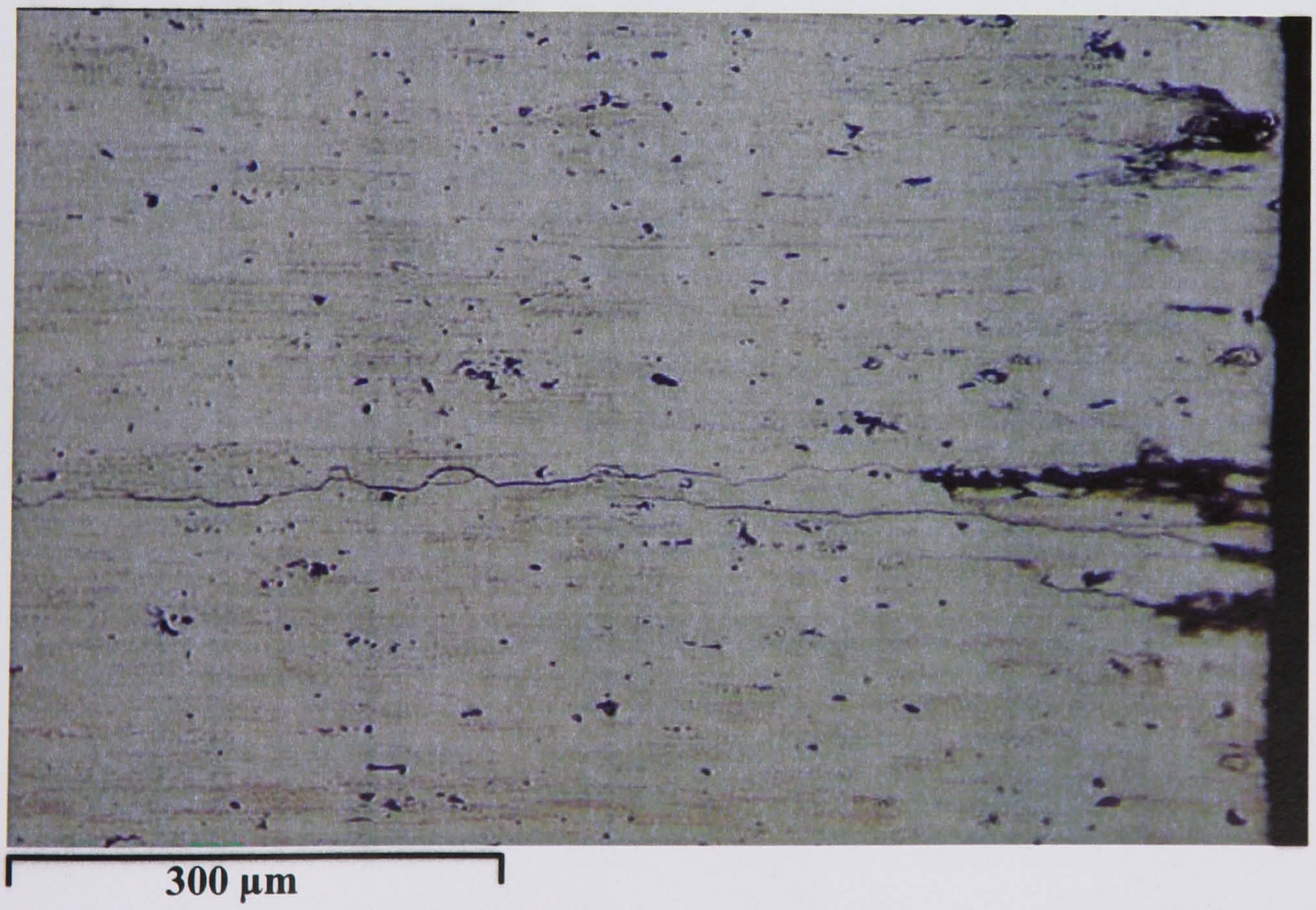


Figure 94 Optical micrograph shows the crack in the specimen 13.

### 11.4.4 Control tests without compressive loading.

This set of experiments looked at the effect on the hole surface after it was allowed to corrode for different exposure times without compressive loading. Exposure times of 2, 4, 6, 8 weeks were chosen. The specimens were re-tested and re-examined with eddy current testing after every each of the exposure time for a total of 8 weeks. On completion of the eddy current testing, the specimen was then sectioned so that the extent of corrosion damage around the hole surface could be examined. Figures 95 – 98 are the optical images inside the hole. It can be seen that the corrosion product built up progressively between 2 and 8 weeks.

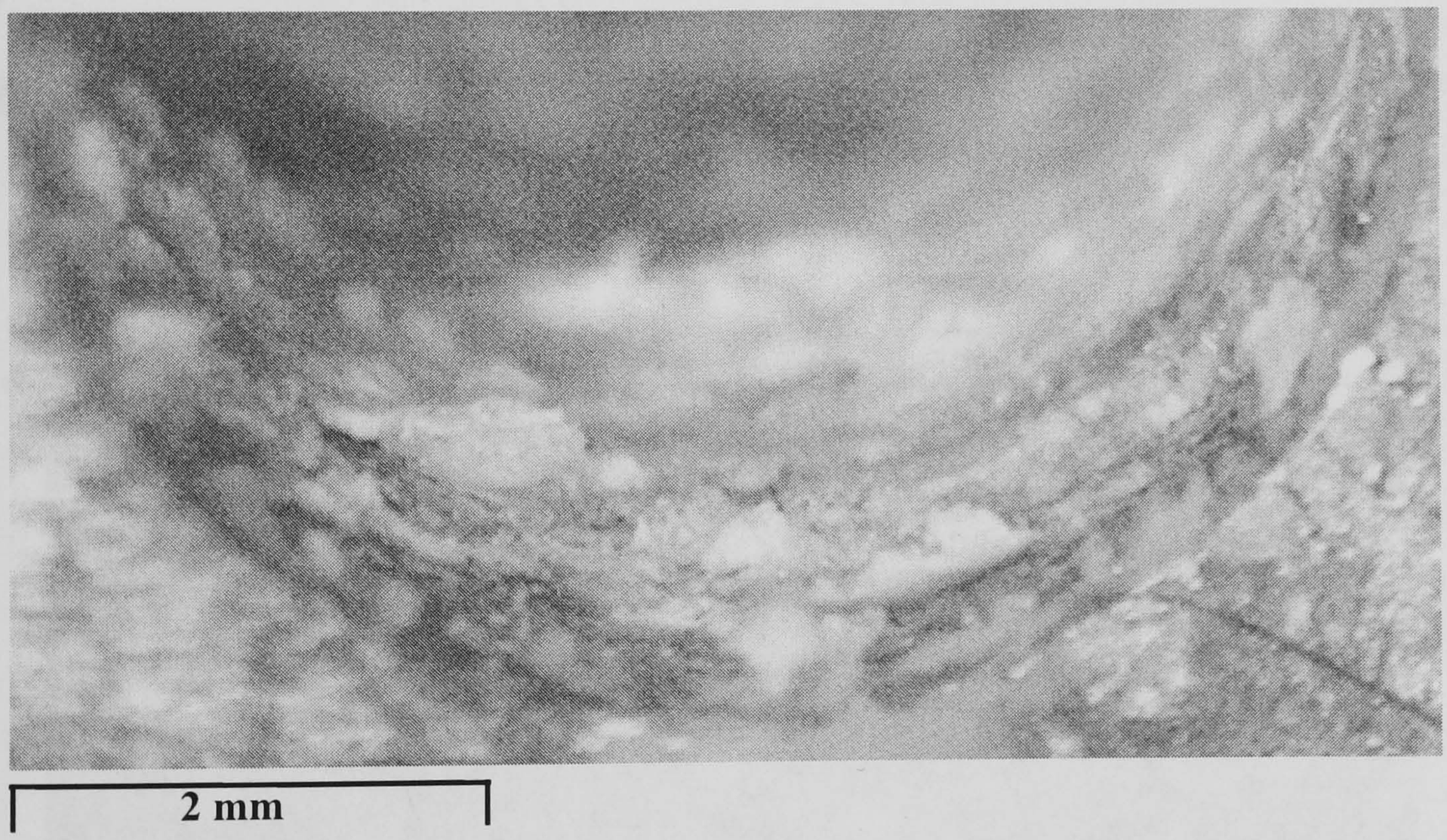


Figure 95 Optical micrograph showing the corrosion product inside the hole surface after 2 weeks.

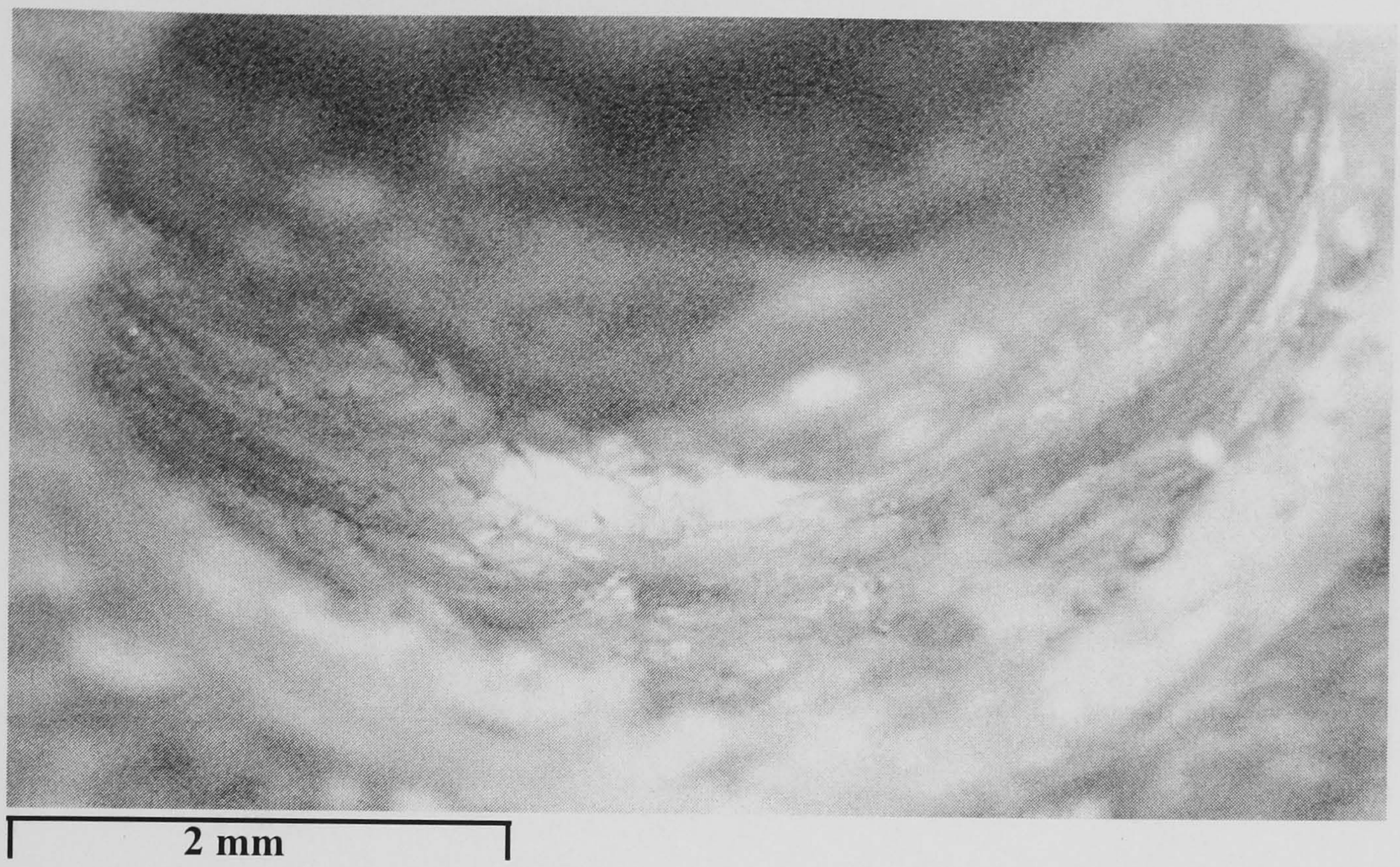


Figure 96 Optical micrograph showing the corrosion product inside the hole surface after 4 weeks.


Figure 97 Optical micrograph showing the corrosion product inside the hole surface after 6 weeks.


Figure 98 Optical micrograph showing the corrosion product inside the hole surface after 8 weeks.

The corresponding eddy current signals from 2, 4, 6 and 8 weeks are shown in figures 99 –102. In each case of eddy current however there was no evidence of crack signal at the hole surface. They just show a lift off signal which may indicate increased roughening of the surface with corrosion over the 8 weeks period. Figure 103 shows the optical micrograph of the specimen that exposed to EXCO solution for 8 weeks without compressive loading.

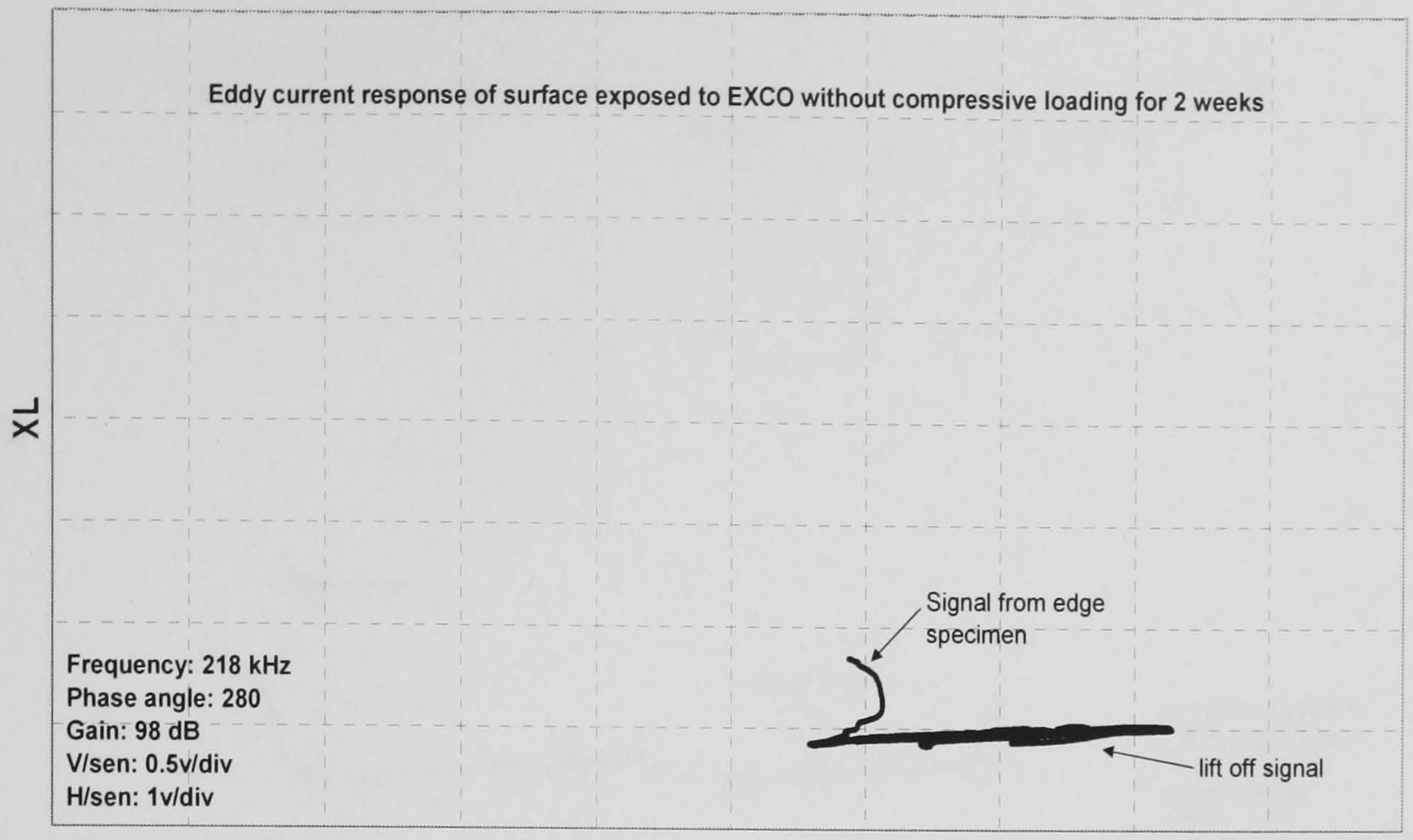


Figure 99 Eddy current responses from surface exposed to EXCO solution without compressive loading for 2 weeks.

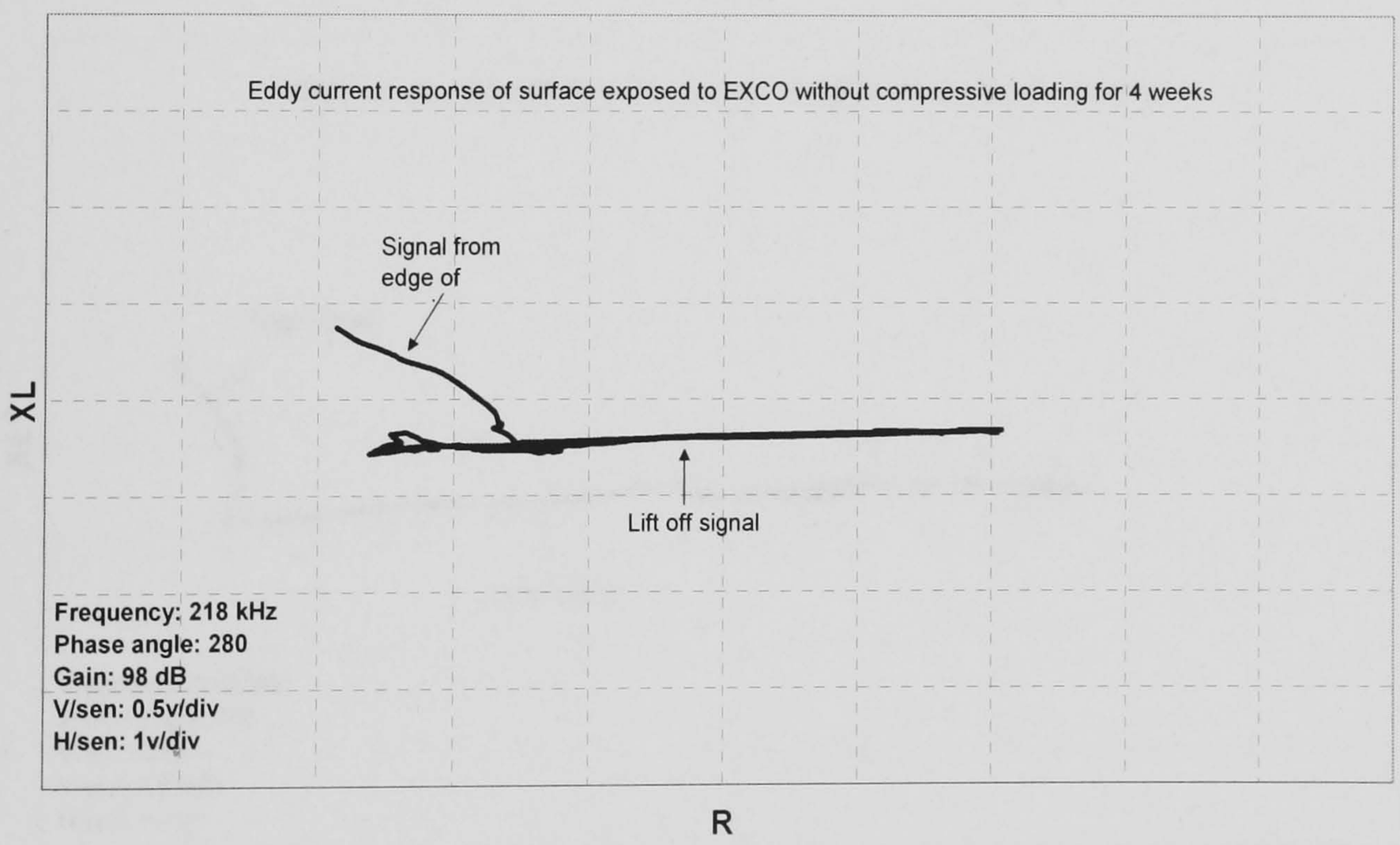


Figure 100 Eddy current responses from surface exposed to EXCO solution without compressive loading for 4 weeks.

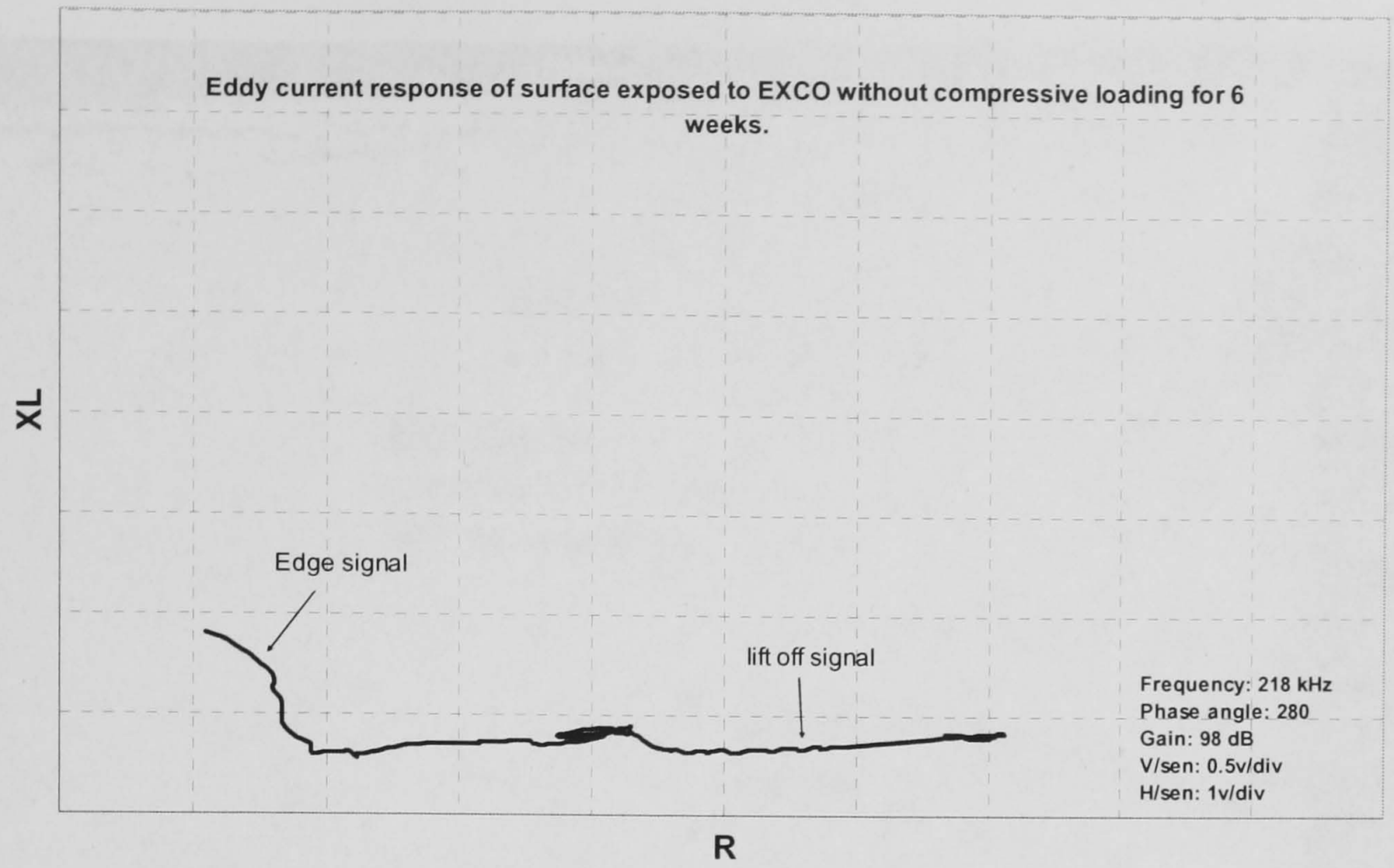


Figure 101 Eddy current responses from surface exposed to EXCO solution without compressive loading for 6 weeks.

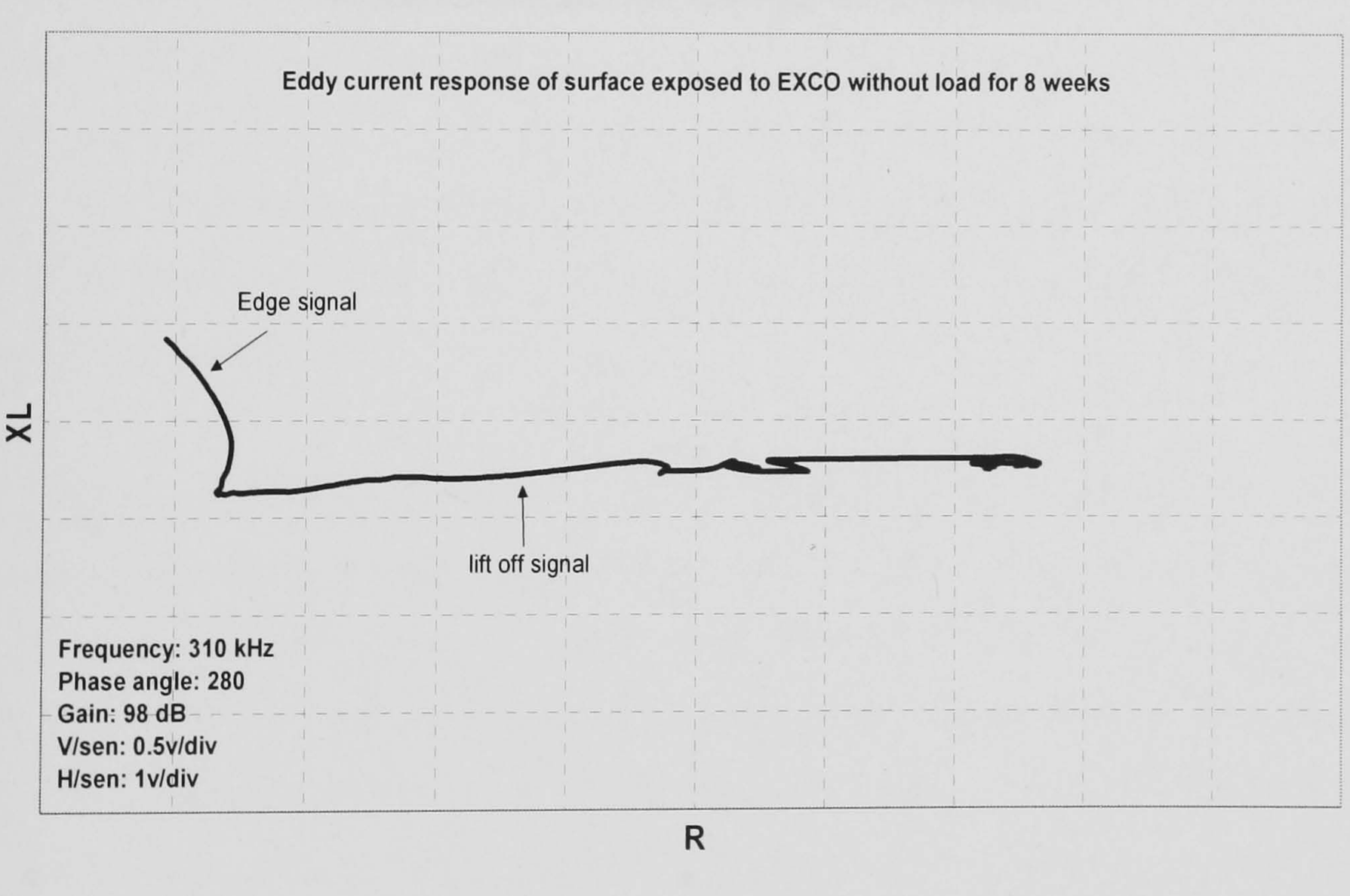


Figure 102 Eddy current responses from surface exposed to EXCO solution without compressive loading for 8 weeks.

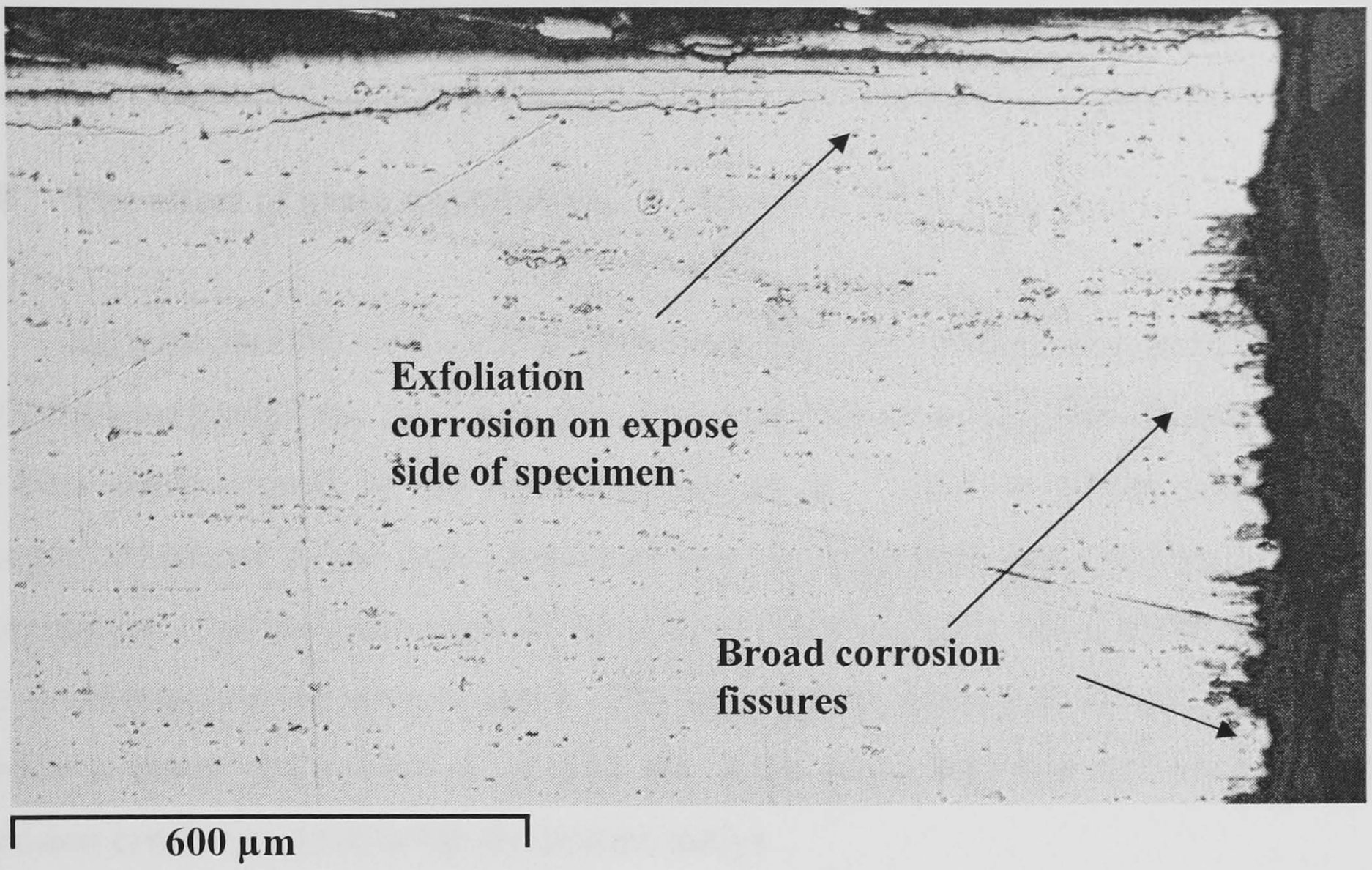


Figure 103 Optical micrograph shows surface of the hole exposed to EXCO solution without compressive loading for 8 weeks.

# Discussion

## 12.0 The effect of grain aspect ratio.

Extreme statistic value analysis has been used for intergranular corrosion studies, particularly to predict the most probable maximum value for the grain dimensions [140]. It has been demonstrated by the work of Kelly et al [70] that the intergranular attack is strongly influenced by the grain shape and size. As stress corrosion cracking is a form of intergranular corrosion, the grain orientation of the aluminium alloy plays an important role in determining the path of attack. The aim of using grain size measurements was to provide a better understanding of how the grain shape and size influence the stress corrosion cracking attack in the aluminium alloys.

The method assumed that all the grains were spherical and the same size and is based on the probability of sectioning on a plane through the diameter of the grain. The greatest length and width were therefore observed the grain was sectioned across its diameter through the centre of the grain and this will represent the true grain length and width [114]. In practice it was found that the grains become more elongated toward the centre of the plate due to the rolling process and developed a higher grain aspect ratio at the middle section (T/2) [68].

The grain aspect ratio for the 7075-W aluminium alloy was found to be highest in the longitudinal orientation due to the rolling process. There was a significant difference in the grain aspect ratio in the transverse orientation and it was low compared to the longitudinal case. This suggested that the material had a microstructure that would be susceptible to stress corrosion cracking, with the longitudinal orientation being the most susceptible. This statement is supported by the work of Robinson et al [68] who demonstrated that the grain shape of aluminium alloys determines the length of the intergranular path whereas the heat treatment influences the corrosion rate at grain boundary. They found that a high grain aspect ratio resulted in larger blister formation giving rise to a more severe visual rating of exfoliation corrosion. Kelly et al [70] showed

a similar trend where a higher grain aspect ratio produced greater corrosion product wedging forces generated in Al-Li alloys as well as increased intergranular corrosion rate.

This type of statistical approach was shown to be the best method for calculating grain aspect ratios. However, there were a number of errors that occurred during the measurements, due to the optical resolution and poor sample preparation, which may have influenced these measurements. Steps were taken carefully to minimise the errors. Automatic polishing equipment was used to obtain an optimum polish of the materials while retaining a uniform flat surface. The use of Keller's etch also highlighted a clear grain boundary for more accurate measurement. The use of an image analyser made it easier to measure the large number of grains to be inspected [113]. In each case, 200 grains were used in this analysis to reduce the statistical error.

## 13.0 Eddy current testing.

The present work was carried out to develop an eddy current technique to detect stress corrosion cracks inside a fastener hole. It was thought that this technique could provide a sensitive method to provide an early detection of stress corrosion cracking. The difficulty of the test was to detect a stress corrosion crack inside the hole, particularly for a crack propagating parallel to the direction of the grains and lying in a plane parallel to the surface. Previously this technique has not been used for such stress corrosion cracks but has been used successfully for the detection of a fatigue crack which is a crack open to the surface. There are many examples of eddy current testing used to detect fatigue cracks [16,30,35,36] outside the holes. This method offered a great potential for detection of small cracks. Therefore the technique for detecting stress corrosion cracks inside the hole was important and lead to this present work.

The stress corrosion cracks studied in this work lie in the plane of the material and do not extend onto the external surface. They were difficult to detect by the other NDT methods such as radiography or ultrasonic techniques. This is because of the geometry of

the specimen and the small crack size. The fact that the eddy current technique provided a wide range of frequencies made the measurements possible.

It was because of the difficult geometry that several depths of spark machined defect were selected to produce very narrow slots inside the hole to simulate [141] stress corrosion cracks in the calibration standard specimen. Calibration signals could be obtained from this calibration specimen and allowed the signal to be compared with the signal from test specimens. This geometry means that the eddy current probe must be moved in and out of the hole so that the flux intersects the crack, rather than being rotated, as is normally the case. Detecting and sizing cracks in this way forms an important part of the project.

Several tests were carried out to establish the optimum eddy current technique on stress corrosion crack. For the analysis of the signal it was assumed that the material parameters such as conductivity and permeability were constant. Also, variations in test system such as lift off, probe orientation, temperature, scan speed and probe wear were minimised.

### 13.1 Effect of eddy current frequency.

The general objective of frequency selection is to obtain frequencies which have a good phase separation between defect and lift-off signals. The most accurate results can be obtained by selecting the correct operational frequency using a calibration sample with the same conductivity as the material to be tested as was done in this project. The frequency for a particular metal can also be obtained by calculation of the depth of penetration, as discussed in the literature. However, the best method is considered to be to show the eddy current response on the CRT instrument.

Several frequencies have been tested in this work. At the frequency of 100 kHz, the phase angle between eddy current response and the lift off is almost zero. When the testing frequency changed to 180 kHz, the phase angle between eddy current responses

and the lift off signal was increased, compared to phase angle at 100 kHz. However, it was difficult to discriminate between defect signals in the calibration specimen. As the frequency increased to 218 kHz, a better separation was obtained for all defect signals in the calibration specimen. As frequency increased further to 700 kHz, the eddy current response changed the shape of the original loop, which was deflected to one side. Figure 104 shows eddy current responses from the different operating frequencies. While the 700 kHz signals had greater amplitudes, there was pronounced distortion and the optimum frequency was considered 218 kHz. The same effect has been shown in figure 105. Hallett et al [142] have shown the effect on eddy current signal appearance of changes in test frequency.

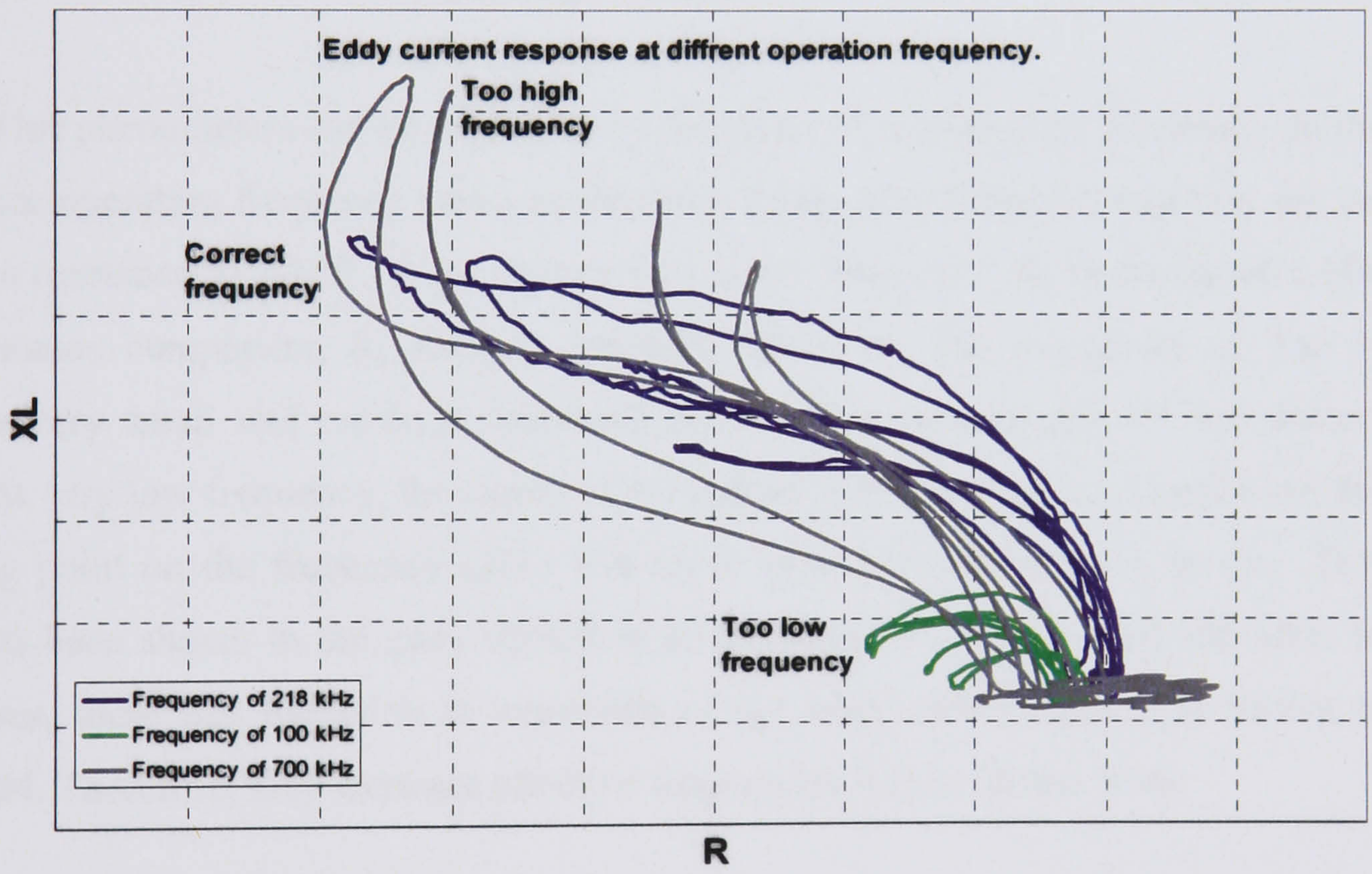


Figure 104 shows eddy response at the operating frequencies of 100, 218 and 700 kHz and same gain setting.

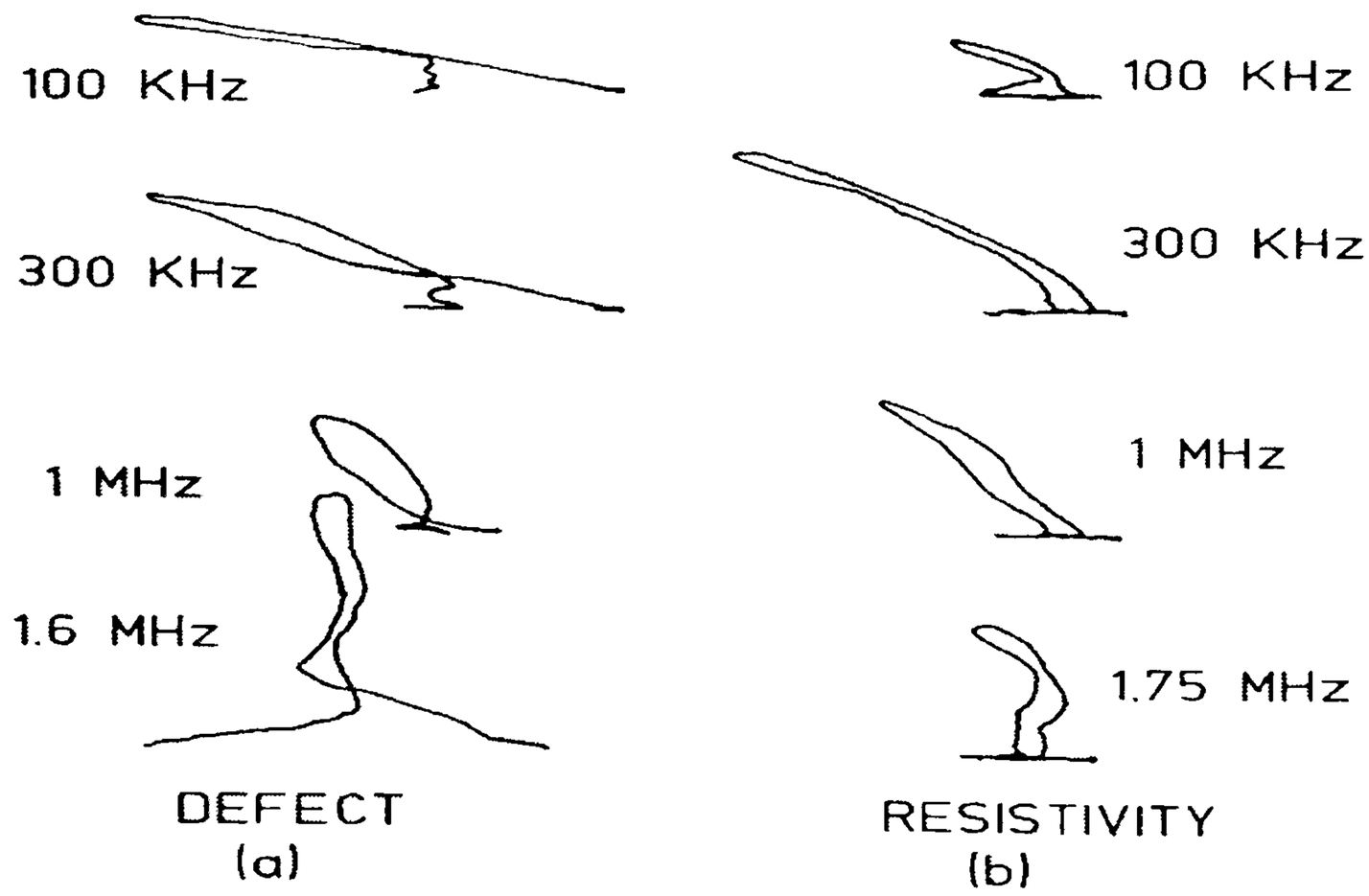


Figure 105 shows the effect of eddy current signal appearance with changing in operating frequency [142].

This phenomenon can be explained by the effect of changing the frequency on the impedance operating frequency curve as shown in figure 106. From the equation for the inductive reactance $X_L = 2\pi fL$, it can be seen that at low frequency, $X_L$ is decreased while the resistance component, R, remains constant. Therefore, the magnitude of Tan Θ becomes very small and result in decreased phase angle between lift off and defects signal. At very low frequency, the signal of the defects will rotate anti-clockwise and the operating point on the frequency curve will move upward to the point A or air. This effect has been shown in the eddy current at a frequency of 100 kHz, and 180 kHz. In both cases, there was reduction in amplitude of the eddy current signal, as shown in figure 104. Therefore, they were not effective frequencies for use in this work.

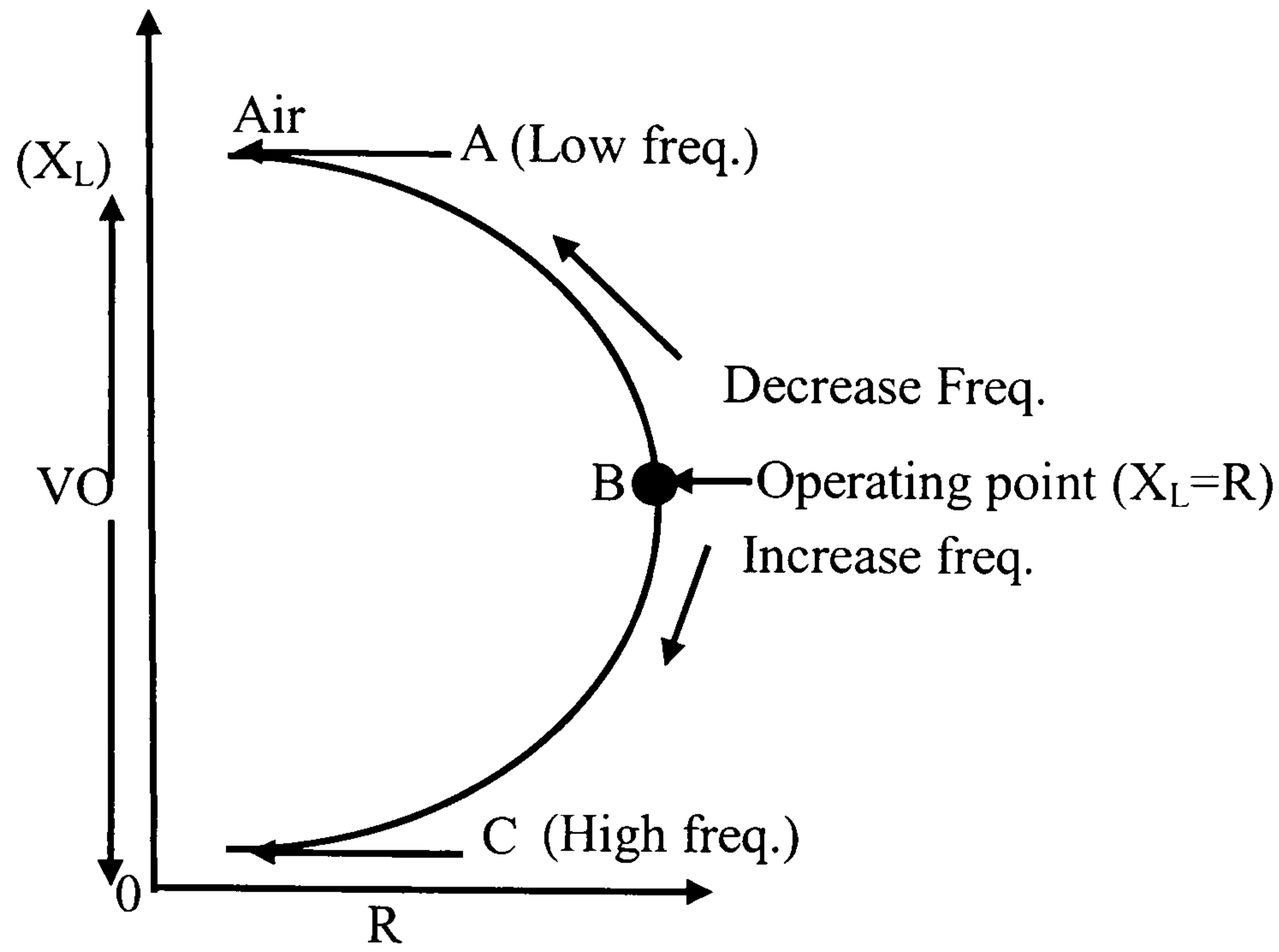


Figure 106 shows the eddy current impedance operating frequency curve.

As the frequency was increased to 218 kHz, the inductive reactance, $X_L$, started to increase in magnitude. On the other hand, the resistance component, R, remained the same value. Therefore the magnitude of Tan Θ also increased. With this change, the increased phase angle between lift off and defect signal gave better sensitivity. At the point, where $X_L$=R, the operating frequency provided the best separation angle without affecting the eddy current loop. In this situation the impedance of the test coil is balanced as showed at point B. This phenomenon was also illustrated by the work of Hagemaier [20] who showed the effect of changing operating frequency on the impedance plane diagram.

In the present work, as the frequency increased from 280 kHz to 450 kHz and 700 kHz, and $X_L$>R, the magnitude of the impedance increased rapidly with increasing the frequency. This range of frequency was giving a wide range of the phase angle which shifts the phase angle up to $90^0$ as shown in figure 105. As a result, the eddy current loop started to change in appearance making it very difficult to interpret. Therefore, it was concluded that an optimum test frequency for the material involved in this study was 218 kHz.

### 13.2 Effect of surface finish.

Another important parameter in eddy current testing is the lift-off signal. This is related to the separation between the eddy current probe and the test specimen. All measurements were made at a constant lift off so that the results can be compared directly. In each case, the lift-off response was rotated to the horizontal direction with the defect response giving a signal in the vertical direction. When the specimen surface suffered from corrosion attack, the original surface become rougher and the effect of changing the operating frequency was investigated.

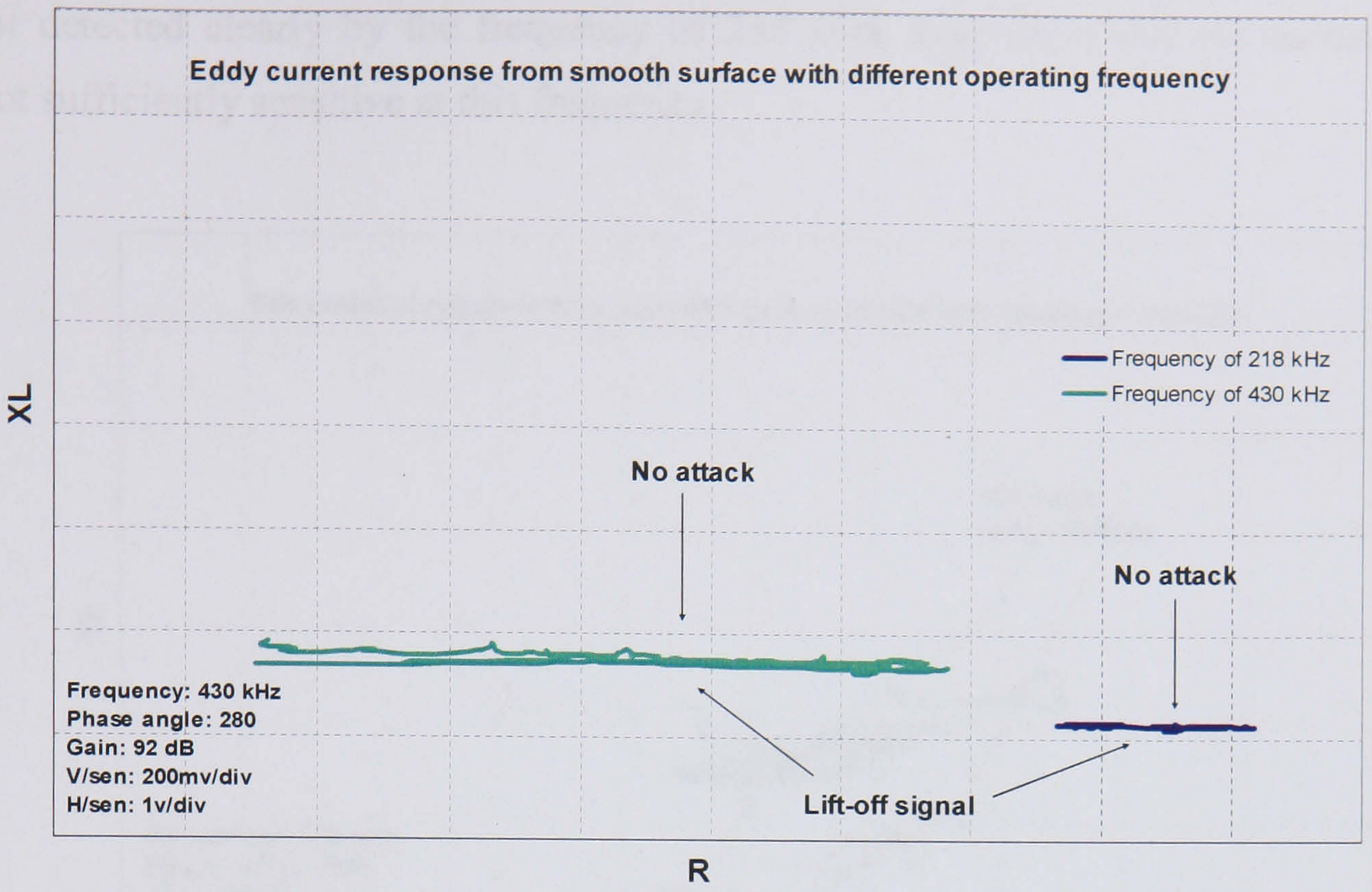


Figure 108 shows eddy current response from smooth surface at the operating frequencies of 218 and 430 kHz.

Figure 108 shows a comparison of the eddy current responses at 218 kHz and 430 kHz for a smooth surface. It is important to note that these scans were taken with the same parameters setup but a different in the operating frequency. It can be seen that the eddy current response at 218 kHz was much smaller compared to the eddy current response produced at 430 kHz. In addition there was a small increase in the vertical component at the frequency of 430 kHz. It is thought that any small defect in the surface would be more likely to be picked up in that frequency. This means that an increase in frequency also increases the eddy current response.

As frequency increases, the magnitude of the eddy current signal also increases, particularly in the vertical direction. This can be seen in figure 109, which shows a comparison of the eddy current response at 218 kHz and 430 kHz for a corroded surface. In both cases, the eddy current signal indicated the existence of surface roughness. It could be seen visually that corrosion attack extended some distance below the surface. At the higher frequency 430 kHz, the vertical component was approximately twice in magnitude compared to that at a frequency of 218 kHz. The presence of surface damage

was not detected clearly by the frequency of 218 kHz, suggesting that measurements were not sufficiently sensitive at this frequency.

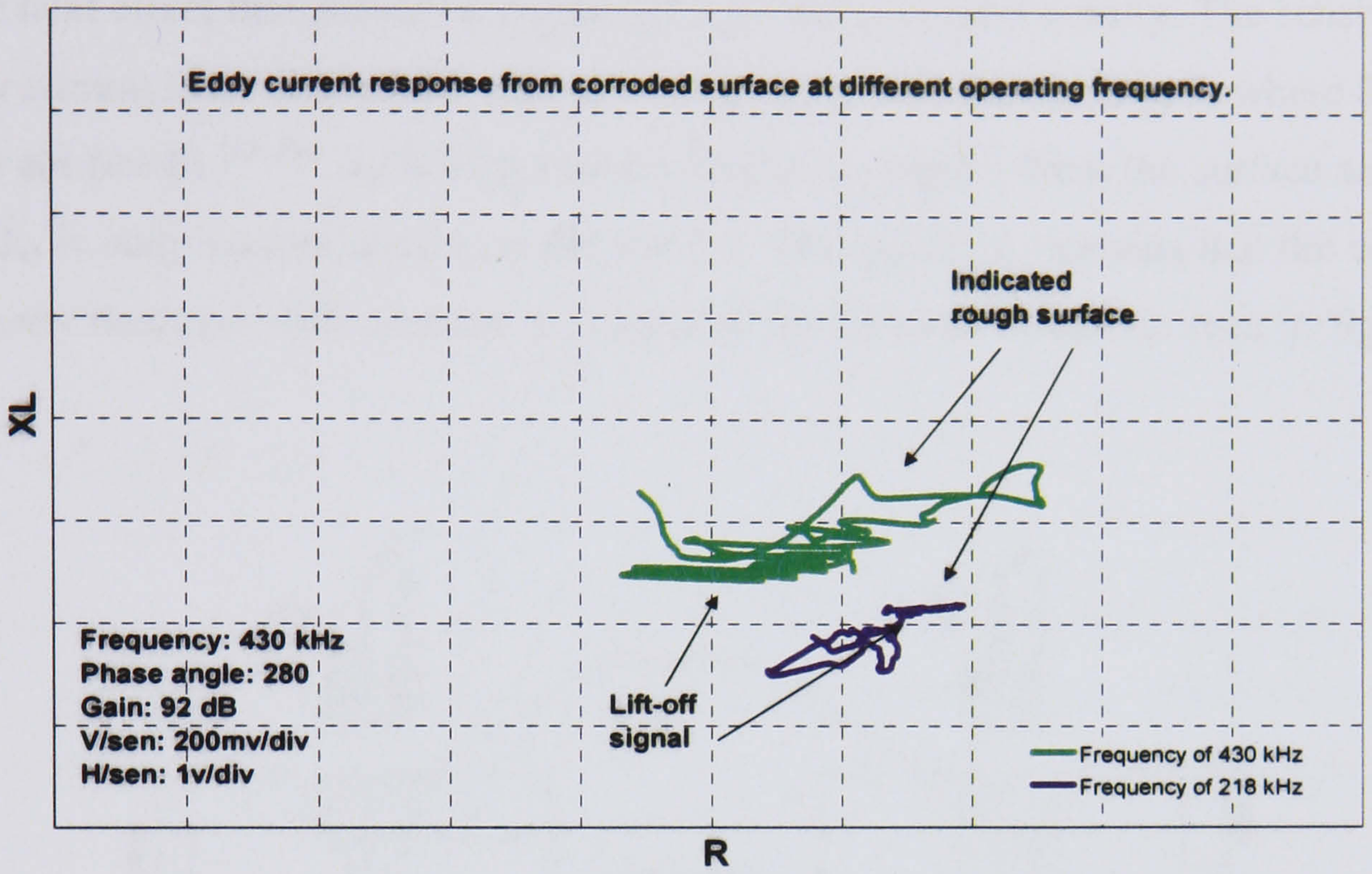


Figure 109 shows eddy current response from corroded surface at the operating frequency of 218 and 430 kHz.

It is clear from figure 109 that there was an effect on the eddy current response of the test frequency. This is thought to be related to the depth of penetration. The eddy currents induced in material are not distributed all through the thickness. Rather, they are concentrated near to the surface of the material and decrease with increasing depth. This is thought to be the cause of limitation of the defect detection at different depth in the material. The distance that eddy currents penetrate into the material is called the Standard Depth of Penetration, $\delta$. The Standard Depth of Penetration is defined as the depth at which the eddy current decrease to 1/e (36.8%) of its surface value. It is a function of electrical conductivity, $\sigma$, and magnetic permeability, $\mu$, of the material. It can be explained by the equation $\delta = 26/ (f\sigma\mu)^{1/2}$. This effect has been explained by many researchers [16,29,36]. At high frequency, there is a low depth of penetration into the specimen and the eddy current is very sensitive to the surface of the material. On the

other hand, at low frequency there is a greater depth of penetration and the sensitivity to surface defects is reduced.

The next effect that should be explained is the eddy current density. The sensivity of the eddy current near the surface depends on the eddy currents density, $J_x$ where $\mathbf{J_X = J_O \exp(-\beta) \sin(\omega t-\beta)}$ [15, 26]. $\mathbf{J_X}$ is eddy current density at depth x from the surface and $\beta$ is $x/\delta$ and $\mathbf{J_O}$ is eddy current density at the surface. This equation explains that the eddy current density decrease with increase the depth of the material as can be seen in figure 110.

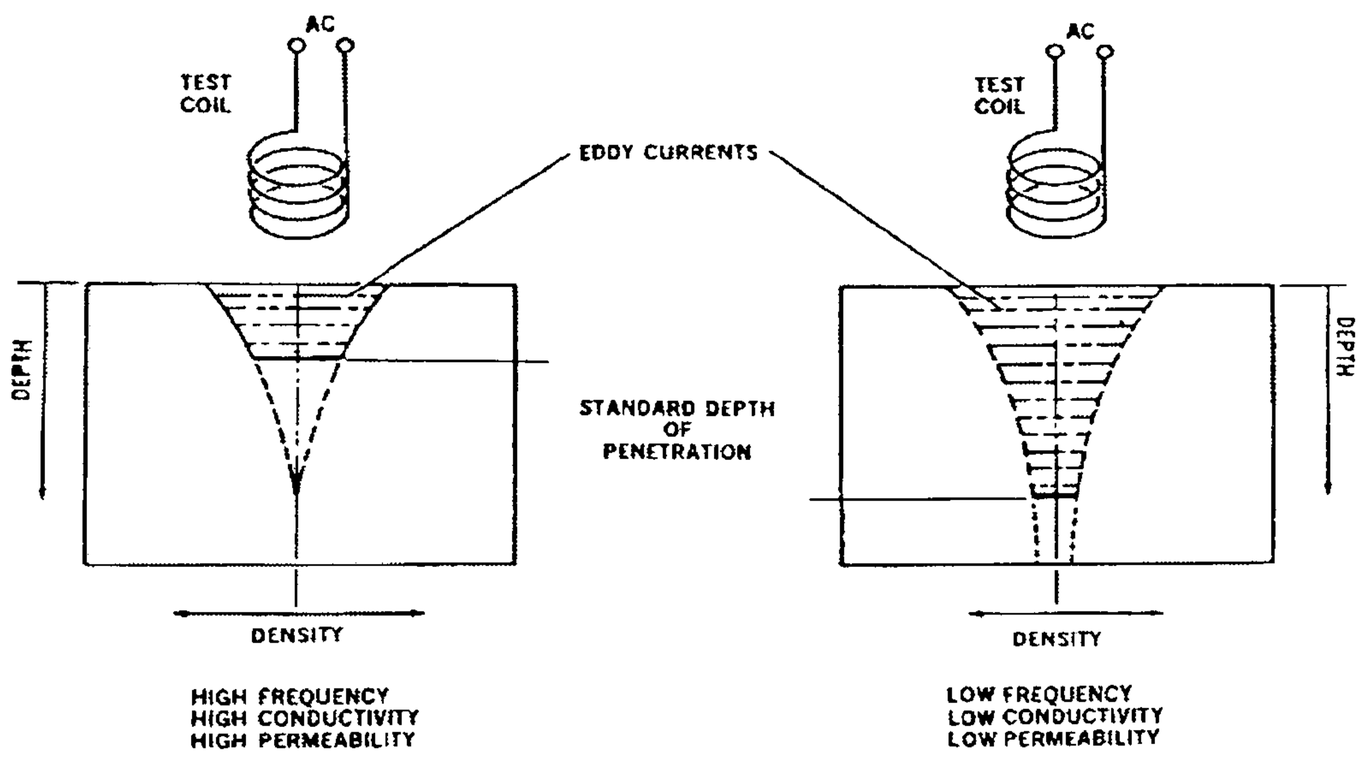


Figure 110 shows effect of frequency, conductivity and permeability on standard of the penetration [26].

Figure 110 shows the depth of penetration of eddy current is controlled the skin depth which is depend on operating frequency, material conductivity and the magnetic permeability. By considering all these effects, it shows that an increase in frequency of the test coil will decrease in depth of penetration but increase the eddy currents density at the surface. The eddy current testing therefore becomes more sensitive at surface of the material. On the other hand, a greater depth of the penetration is produced as frequency decreases. The eddy current density becomes less at the surface but the greater depth of penetration is useful for detecting flaws remote from the surface.

### 13.3 Effect of a crack on the eddy current signal.

One aim of this work was to establish whether the technique could detect a stress corrosion crack under compressive loading. This crack was inside the hole and propagated into the material parallel to the rolled microstructure. After the specimen had been immersed in EXCO solution under compressive loading for 2 weeks, pitting started to form at the beginning of the test followed by attack along the grain boundaries. This situation then leads to cracking. The work has shown that stress corrosion cracking in high aluminium alloy 7075-W is detectable by the technique used in this work and the crack can be distinguished from exfoliation corrosion at the edge of the specimen.

It has been stated earlier in the Literature Review that if the eddy current probe is moved from the air and placed on the specimen, the resistance component is increased and the inductive reactance of the coil decreases, as shown in figure 111. The impedance point is moved from $P_0$ to $P_1$. The magnetic field in the test coil is modified by the magnetic field produced by the eddy currents in the test specimen [20]. As a result, the overall effect resulted in a weaker magnetic field and produced a change in inductance of the test coil. Figure 111 shows the test coil characteristics on the impedance plane diagram.

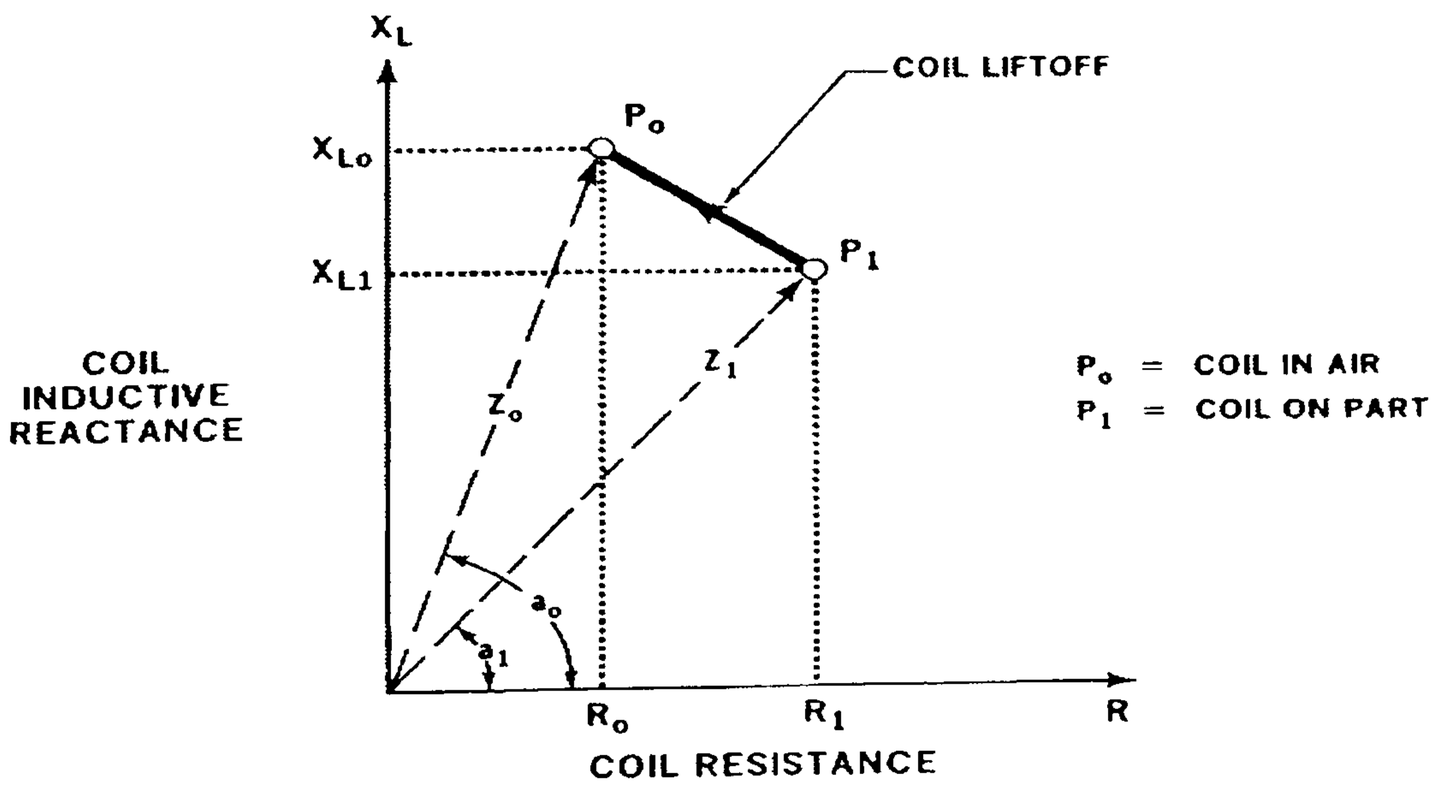


Figure 111 shows the test coil characteristics on the impedance plane diagram [20].

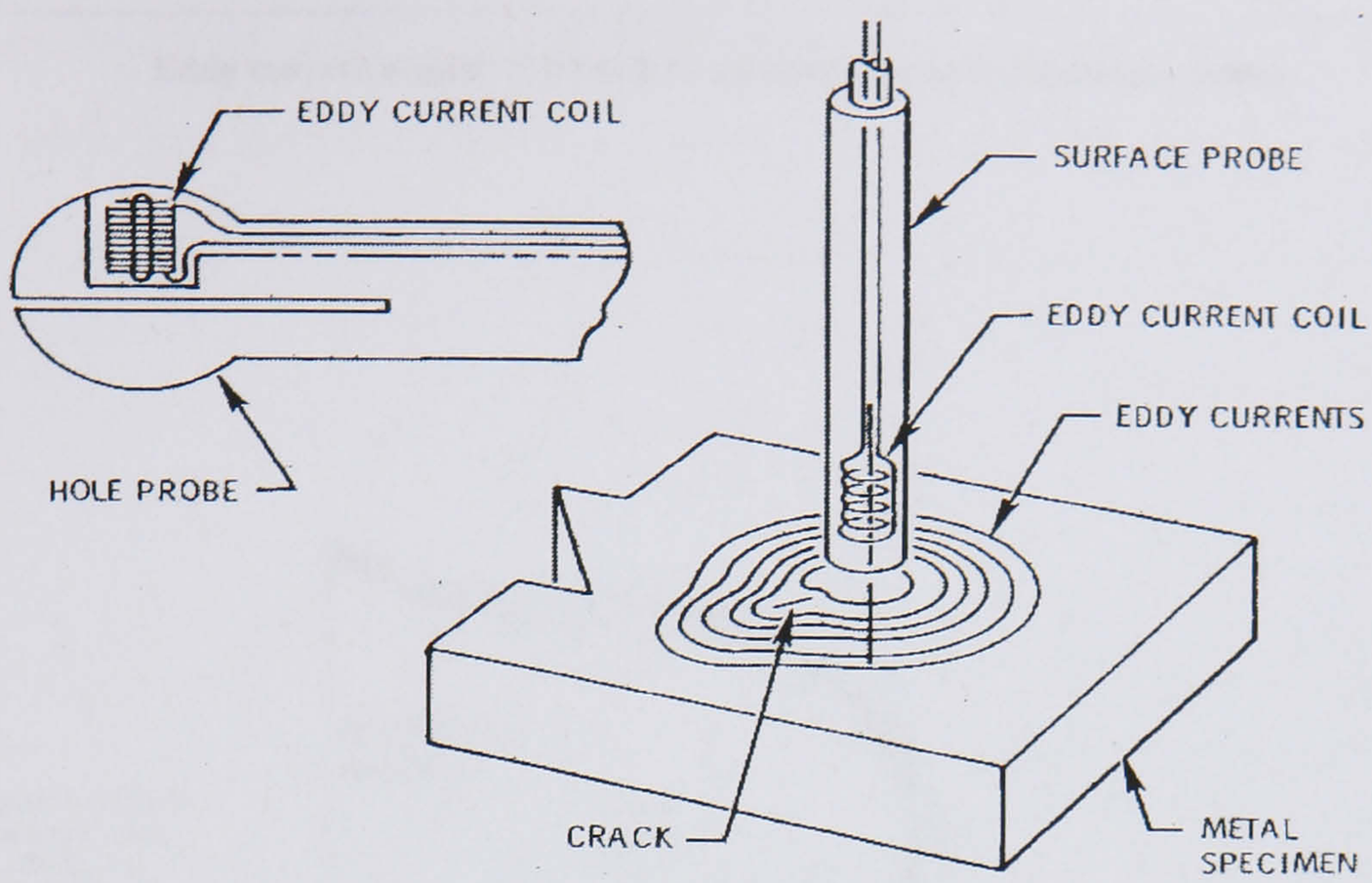


Figure 112 shows the eddy current flow in the presence of crack [30].

When a crack was present in the material, which disturbed the eddy current flow, changes occurred in the test coil impedance as the test coil was passed over the crack. This condition can be seen in Figure 112[30]. Figure 112 shows the eddy currents produced by a test coil in the specimen. When the crack disturbs the eddy current flow, the eddy current is forced to flow around the crack. The resistance component is decreased and the inductive reactance component is increased. In this situation, the impedance point is moved upward to the height determined by the depth of the crack and then comes back to the balance point. This produces a signal indicating a crack, as shown in Figure 113. Figure 113 shows the eddy current response from a 0.6 mm deep spark machined defect.

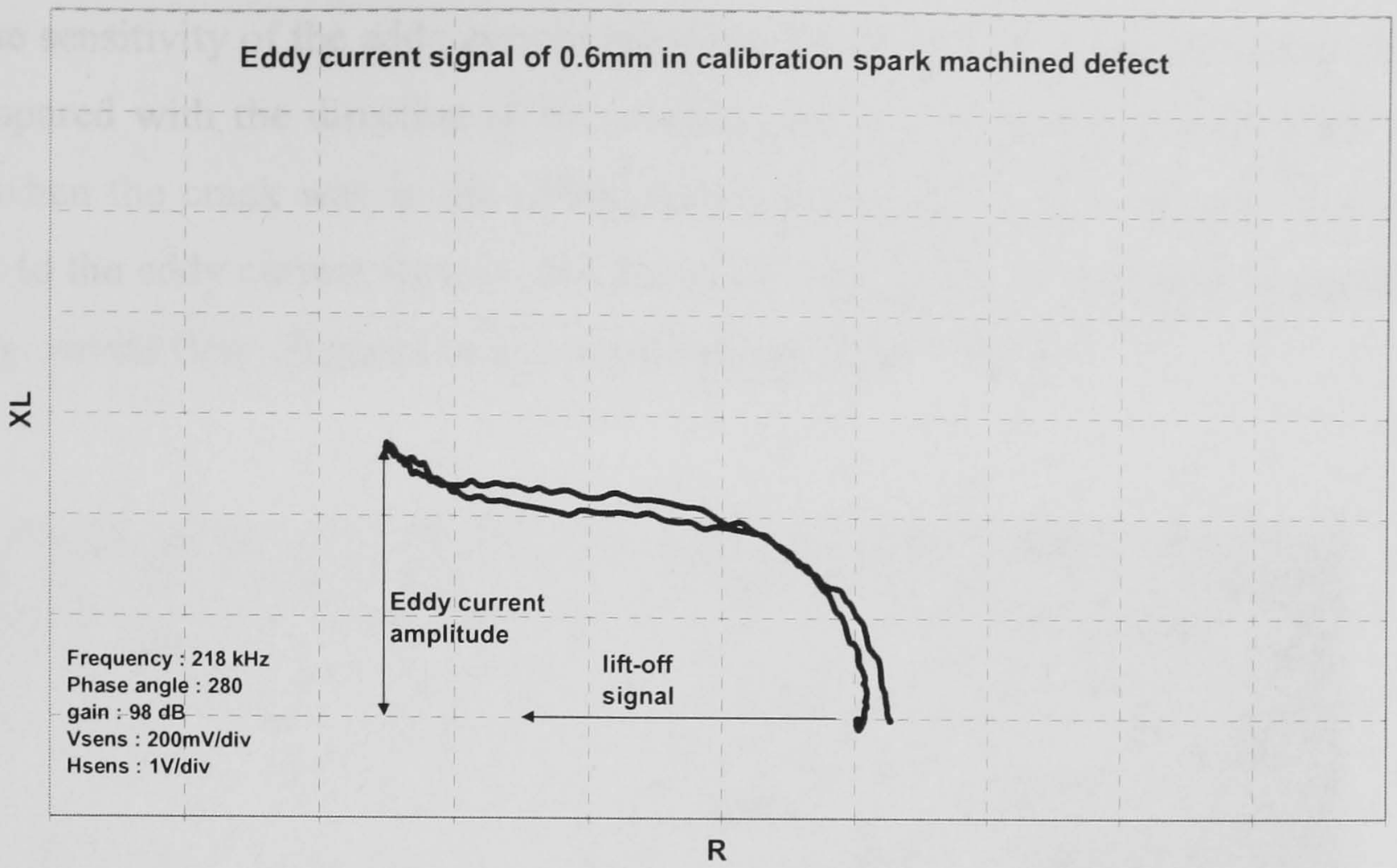


Figure 113 shows the eddy current response from a 0.6 mm crack depth.

The vertical amplitude of the signal depends on the crack depth, with deeper cracks giving large signals. Hallett et al [142] has shown the eddy current response from various depths of cracks in a zirconium alloy calibration standard with the operating frequency of 300 kHz. Figure 114 demonstrates the eddy current response at 300 kHz for cracks of a range of depths.

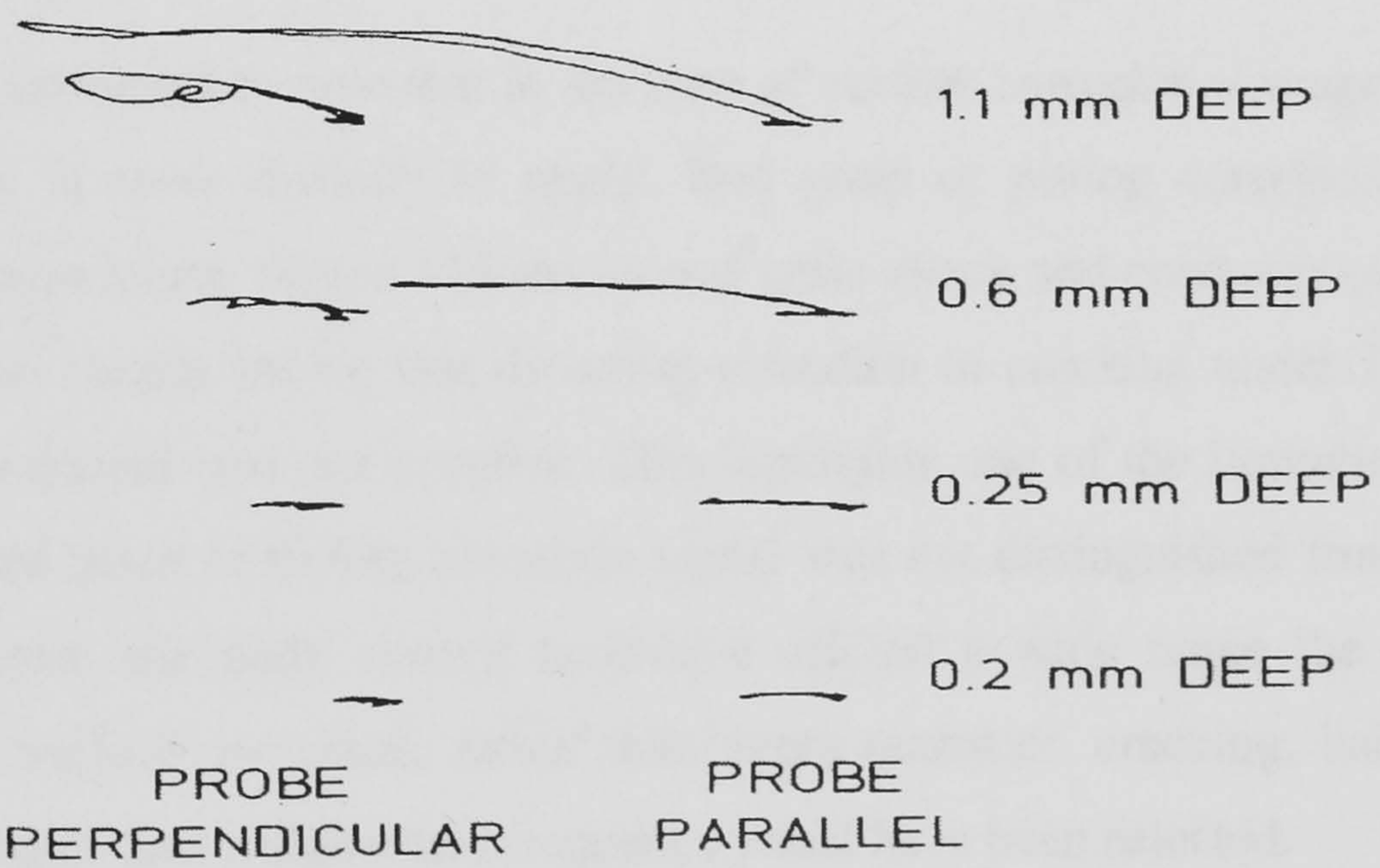


Figure 114 shows eddy current response at 300 kHz from various crack depths [142].

The sensitivity of the eddy current response also depended on the direction of the crack compared with the direction of the magnetic field. The optimum amplitude was obtained when the crack was in the rolling direction parallel to the magnetic field and transverse to the eddy current flow so that the crack was giving a maximum interruption to the eddy current flow. Figure 114 also demonstrates these effects.

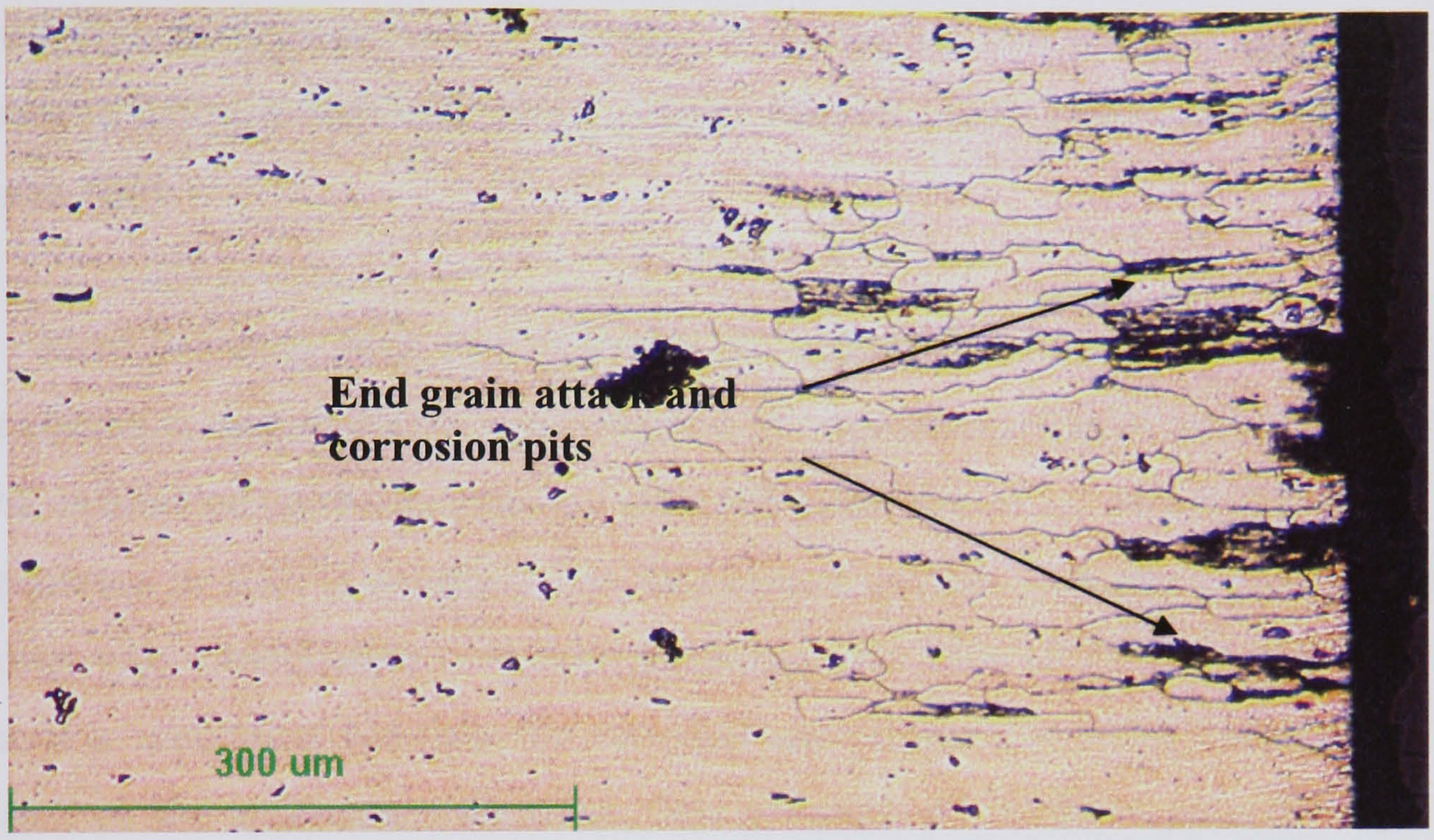


Figure 115 shows end grain attack and corrosion pits near to the surface.

It is also important to note that in the case of surface corrosion damage the eddy current technique is more difficult to apply. End grain or pitting corrosion was not detected in this experiment. Figure 115 shows end grain attack and corrosion pits near to the surface. It was clearly shown that detecting corrosion or cracking under 300 μm in depth in this experiment was not possible. This highlights one of the limitations of the technique. The end grain or pitting corrosion signal was not distinguished from the lift-off signal. However, the eddy current technique offered a wide range the operating frequency and if surface corrosion, rather than stress corrosion cracking, had been of interest in this project then a higher test frequency could have been selected.

### 13.4 Effect of exfoliation near the edge.

One of the difficult problems in eddy current testing is an edge effect. This phenomenon occurs as the eddy current probe moves near to the edge of the specimen. This situation happens because the magnetic field produced by the probe is outside the edge of the specimen. Therefore, it is thought to be difficult to detect any crack or corrosion that has occurred at the edge of the specimen. This information is supported by the work done by Elsberry et al [143]. In their work, the high frequency of a shielded probe was used to detect defects near to the edge of fastener hole by limiting the extent of the magnetic field.

Most structures built from high strength aluminium alloys have serious problems with exfoliation corrosion after many years after exposure to marine atmospheres. In this project, exfoliation corrosion also was achieved in the laboratory with total immersion of the specimen in EXCO solution. This test caused another problem to the edge of the specimen where exfoliation corrosion occurred at the edge of the hole. This corrosion produced a separation between the corroded and uncorroded metal surface causing a reduction of the specimen's thickness. The presence of exfoliation corrosion was not detected using the eddy current technique, due to the location of the corrosion at the edge of the specimen. This is one of the limitations of the technique. The exfoliation corrosion was found to be very severe around the edge of the specimen. Figure 116 shows an optical micrograph which confirms that the edge 7075-W was affected by exfoliation corrosion. As can be seen the attack was mainly on the grain boundaries and parallel to the rolling direction.

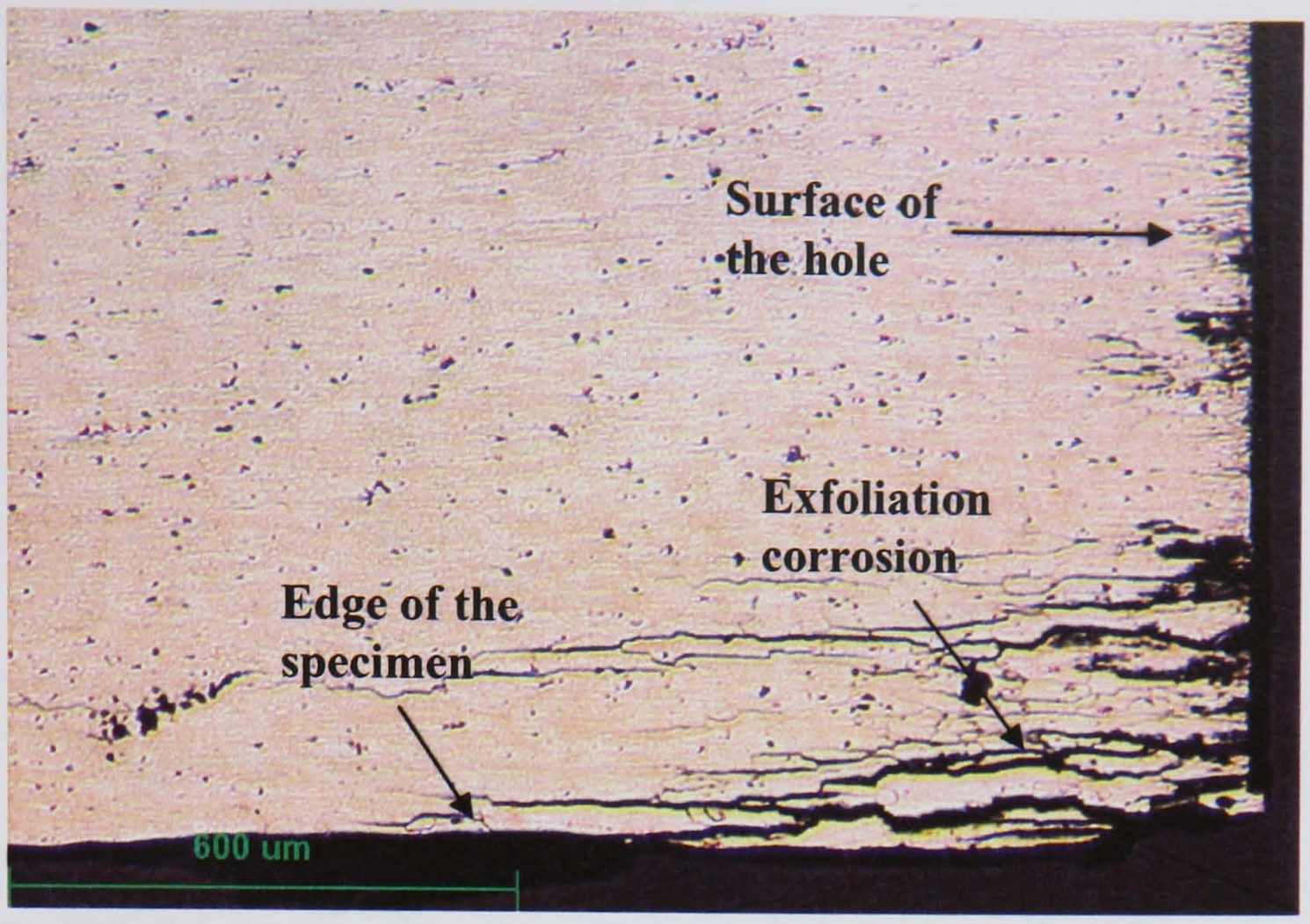


Figure 116 Optical micrograph showing section of a 7075-W specimen with exfoliation corrosion at the edge.

## 13.5 Eddy current measurement on stress corrosion cracking.

It was observed that the stress corrosion cracks were bowed, giving a longer crack length in the centre of the specimen. It was important to measure the extent of this bowing as it would otherwise affect the accuracy of the eddy current measurements. The causes of crack bowing were also considered.

### 13.5.1 Effect of thickness.

There are two factors affecting the bowing of the crack tip in the DCB specimen. The most important is the stress distribution near the crack tip [144] which is related to the plane stress and plane strain conditions. The stress condition near the crack tip is different from edge to middle of the specimen. The DCB used in these test had a thickness of 18mm. therefore, the effect of thickness on the plane strain and plane stress could lead to crack bowed at the centre [28,97,144].

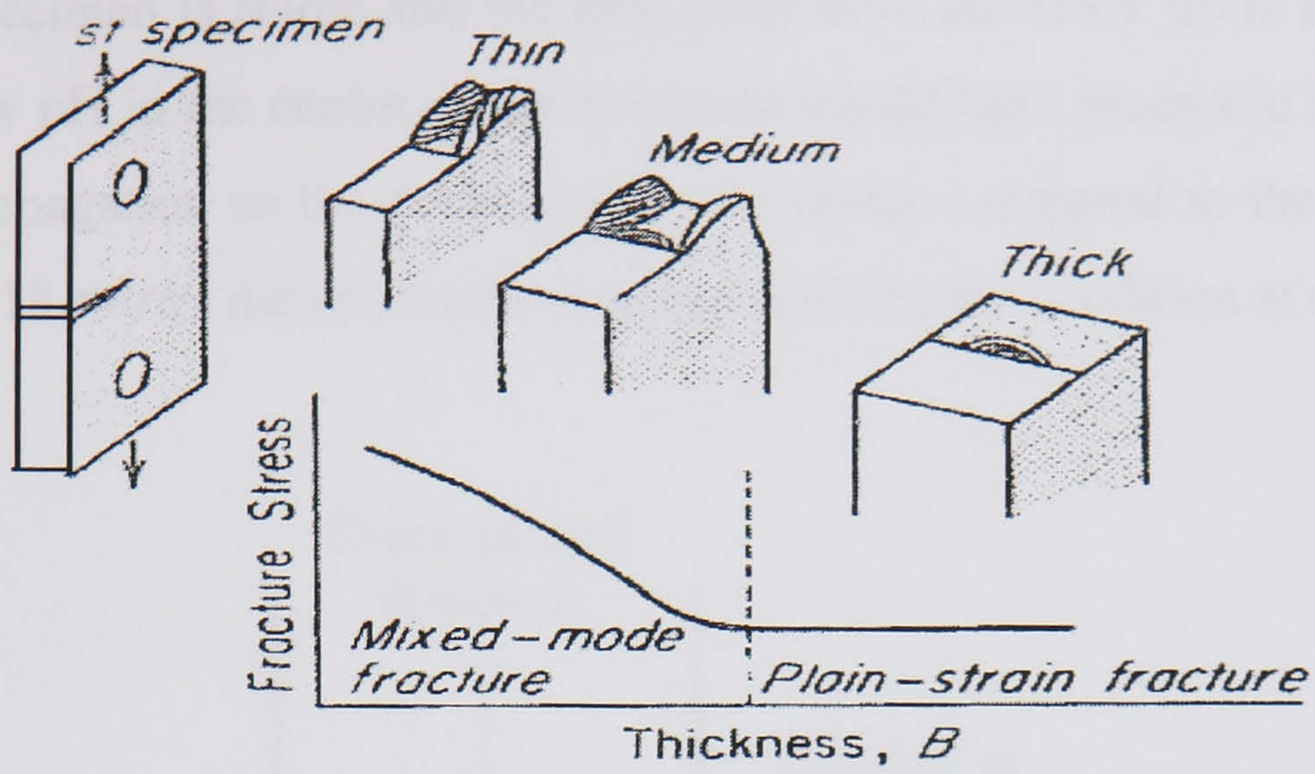


Figure 117 shows the effect of specimen thickness on stress [97].

Figure 117 shows the effect of specimen thickness on fracture stress. As can be seen, the curve is divided into two important regions. The first region applied to thin specimens in the plane stress condition. The second region is for thicker specimens in which the centre of the notch is in plane strain. Due to the higher constraint of this condition, the crack grows at a lower fracture stress and the crack front is therefore expected to be bowed.

### 13.5.2 Effect of environment.

Another explanation for crack bowing may be the effect of pH in the crack. The test solution used was 3.5% NaCl solution with pH of 7.0. However, hydrolysis of aluminium ions [139] produced hydrogen ions which decreased the pH, giving acid solution within the crack of DCB specimen. The reaction equation can be explained as follows $Al^{3+} + 3H_2O \rightarrow Al(OH)_3 + 3H^+$ (acid). The pH value inside specimen decreased. Note that the result shows pH inside the DCB specimens was acidic, which was low at 3.5 pH [94,138]. However, dilution processes may have occurred at the edge due to mixing with bulk solution (pH 7) and could result in a higher pH value at the edge. Similar results were report by Foley et al [139], measuring the pH value at the crack tip and bulk solution. He reported that the pH value was 3.0-3.2 at the crack tip and the pH of 7.0-7.2 at the bulk solution. It was thought that the best explanation for the pH at the crack tip

within the DCB specimen is acidic and the area away from the crack tip is alkaline. The development of low pH in the centre of the specimen would have promoted higher stress corrosion crack propagation so the crack lead at the centre compared to the edge of the specimen. Figure 118 shows the schematic diagram explains the condition at crack tip.

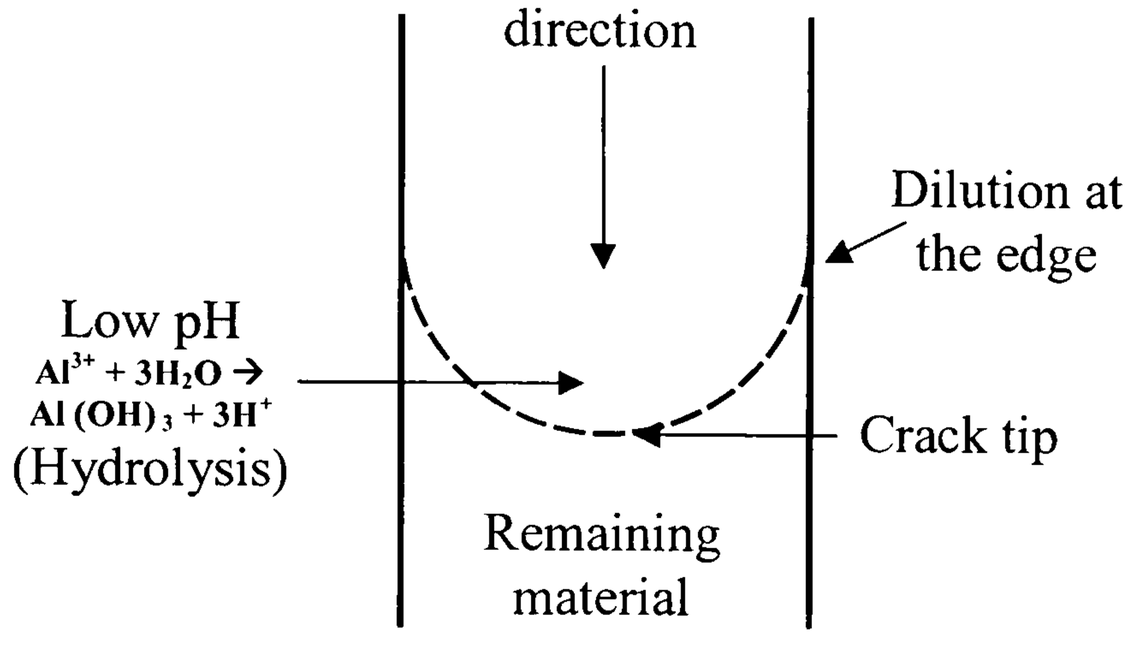


Figure 118 schematic diagram show the pH conditions at the crack tip.

### 13.5.3 Effect of frequency on eddy current measurements.

The eddy current technique is considered the most suitable NDT method for crack detection inside the hole [145]. For that reason the crack length measurement was used to plot a graph the amplitude eddy current response of the crack against crack length. The graph provided important information for detection of stress corrosion crack length inside the holes, as a function of amplitude of eddy current response.

Figure 119 shows the graph of amplitude of eddy current signal against stress corrosion crack length. This graph provided the means to estimate crack depth within the fastener holes. At first, it was thought that the graph could be used to detect all depths of the stress corrosion crack inside the hole. However, it can be noticed that the amplitude of eddy current response approached a maximum value on the graph. Near that point, it is clear from the graph increase in crack length no longer increases the eddy current amplitude. An explanation of this observation is required.

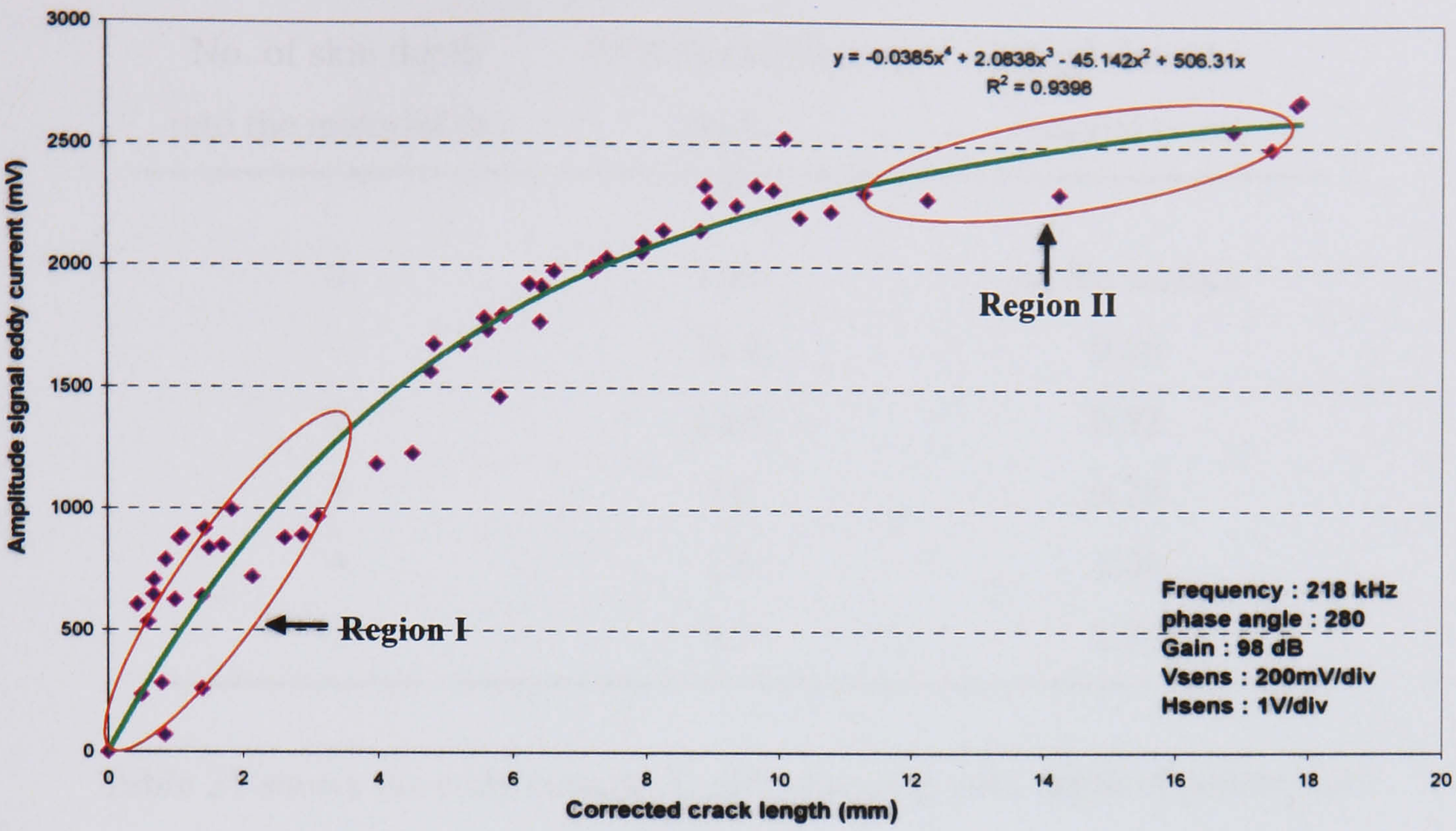


Figure 119 shows the graph of amplitude of eddy current signal against stress corrosion crack length.

There is a factor affecting the amplitude of eddy current response on the graph shown in the figure 119. Region I showed that a small increase in crack length produced a large increase in amplitude of eddy current response compared to region II. It is indicating that in region I the amplitude of eddy current response is strongly affected by SCC crack length. The reason is due to the sensitivity of the parameters used. In this region the frequency of 218 kHz had shown the best amplitude separation for all defects in the calibration specimen. At this frequency the first, **δ**, and fifth, 5**δ**, skin depth are approximately 0.26mm and 1.30mm respectively. Cracks which are open to the surface can be detected more easily than those that are entirely sub-surface.

| No. of skin depth into the material ($\delta$) | % at the surface depth | Depth into the material (mm) |
|---|---|---|
| 0 | 100 | At the surface |
| 1 | 36.8 | 0.26 |
| 2 | 13.5 | 0.52 |
| 3 | 5.0 | 0.78 |
| 4 | 1.8 | 1.04 |
| 5 | 0.7 | 1.30 |

Table 21 shows the eddy current density changing with depth of penetration.

Table 21 shows the eddy current density is changing with depth of penetration. Note that the conductivity, $\mu$, and relative permeability, $\sigma$, for aluminium alloy 7075 used in the calculation are 30 percent IACS and 1 respectively [12]. Therefore any signals from a SCC defect within 0-4mm (short open crack) range could be easy detected and accurately estimated. It is thought that region I provided a high sensitivity of measurement. This region I can be used to determine and to detect early SCC crack length inside the hole.

In contrast, region II showed that a big increase in crack length produced only a small increase in amplitude of eddy current response. This indicated that the strength of the eddy current signal will reduce with increased attenuation of the eddy current field with depth into the material [7-10]. Nevertheless, the graph showed the presence of SCC length up to 17mm can be detected. However the amplitude signal cannot be interpreted further. This is due to the amplitude of the eddy current signals being too difficult to distinguish clearly and they tend to merge at long crack lengths. This phenomenon can be explained by considering the operating frequency used in the test.

It has already been stated in the Literature Review that high frequency reduced the depth of penetration and at low frequency gives a high depth of penetration. This means that an eddy current signal is not penetrated all through the thickness of the test specimen. The operation frequency of the test probe influenced the depth of penetration of the eddy current into the material. As the SCC length increased from 12mm up to 18mm (long crack), the increment of the amplitude of eddy current signal becomes small compared to region I. In region II, with the operation frequency of 218 kHz there is a reduction in depth of penetration and amplitude of the eddy current signal at the position of a deep crack. If there is a SCC crack that needs to be measured in region II, then adjustment has to be made to the operation frequency. It is necessary to decrease the operating frequency to produce a greater depth of penetration. At low frequency range, would provided a better separation angle and allow better increment of the amplitude of eddy current signal for all defects in region II.

In both cases, this graph should be used as a guideline to detect SCC defects inside the hole since defect signal and phase angle can change with defect and probe geometry.

### 13.5.4 Improving the test calibration.

It has already been stated in the literature review that eddy current testing is a comparative method and only used for electrically conductive materials. A calibration graph is necessary to compare the amplitude and phase of the known defects signal to an unknown (real) defect signal to estimate the size of a defect in the test specimen. Thus, the calibration specimen should have the same material properties, such as electrical conductivity and magnetic permeability, as the specimen under test. They cannot be used to examine another material with different electrical properties. For instance, the existing calibration graph for aluminium alloy 7000 series in figure 119 can not be used as a calibration graph to conduct examination and evaluation for aluminium alloy 2000 series.

The ASME national Code and Standard [146] is provided as a basic guideline for selecting test parameters for eddy current set up. There is no code or standard that identifies test parameters for a specific test. Therefore, defects in a calibration specimen should be manufactured to represent as nearly as possible actual defects in the test specimen. However, since a stress corrosion crack was a combination of cracking and corrosion damage inside the hole, it is always difficult to produce similar defects in the calibration specimen. Therefore, simulated spark machined defects were thought to be the best method to represent cracks inside hole. During the examination, if a defect signal is detected it is a good idea to repeat the scan at another frequency. This approach is taken to make sure that a defect exists and to improve the estimate of the crack length. It is also good practice to have more than one calibration specimen to cover a complete range of defects, thicknesses, frequencies and materials.

The calibration test can be improved by controlling the vertical and horizontal gain in the impedance plane plot. Note that it has been shown in selecting frequency how the signal increases and decreases with changing the operating frequency. The vertical gain is increased to increase the crack response in the vertical component. Hagemaier [20] has reported that the maximum gain of the horizontal and vertical components can be set at 2 volts per division, unwanted offset signal, and 0.5 volts per division, signal of interest, respectively. This approach would help in measuring the sensitivity of the measurement. Recent developments in eddy current testing equipment now offer a wide range of multifrequency or mixed frequency techniques [146,147] where an unwanted signal can be easily eliminated from the test system. A further discussion on this technique can be found in ASME code [146].

If the eddy current measurement needs to be used for detecting corrosion at the surface in the bore of a hole, then the calibration specimen should contain a circumferential groove [146] on the surface of the hole to simulate the corrosion damage. As corrosion damage is always at the surface there is a need for greater sensitivity at the surface and therefore the experiment must use higher operating frequency in the

measurements. Thus, the eddy currents penetrate less into the material but produce a high density of eddy current at the surface.

## 14.0 Stress Corrosion Cracking.

Stress corrosion cracking (SCC) is an interdisciplinary problem which involves corrosion, physical metallurgy and fracture mechanics. For stress corrosion cracking to occur three conditions need to be satisfied; first, there must be a susceptible alloy, second, there must be a corrosive environment and third there must be a component of stress. Normally, stress corrosion cracking requires a tensile component of stress at the developing corrosion tip. In this present work, however, it was demonstrated that a stress corrosion crack can occur with compressive loading.

The main purpose of the present study was to investigate how the grain structure, type of loading, environment and stress influenced the stress corrosion crack and to provide under standing of the failure mechanism in high strength aluminium alloy 7075-W. The approach was to compare the stress corrosion crack behaviour of 7075-W under tensile loading in mode I to the specimen under compressive loading. A second purpose of this work was to determine whether highly aggressive environments are useful to accelerated stress corrosion crack testing of high strength aluminium alloys.

### 14.1 Stress corrosion crack under tensile loading.

#### 14.1.1 Crack initiation at the crack tip.

The fracture mechanics [122,148,149] mode I experiment was performed in this study in the form of a DCB specimen. The crack tip wetting and drying technique has been reported by Stanley et al [91] and Blain et al [150] and found to be a suitable method for crack initiation. With this procedure, the crack tip was wetted with 3.5% NaCl solution and the specimen was allowed to dry before beginning another wetting procedure. This procedure was repeated for a few days to initiate a stress corrosion crack at the crack tip.

The specimen which was loaded with an initial stress intensity of 25 $MNm^{-3/2}$ developed stress corrosion cracks with the shortest incubation time, in comparison with the specimen with an initial stress intensity of 15 $MNm^{-3/2}$. The specimen with initial stress intensity of 15 $MNm^{-3/2}$ required approximately two weeks exposure to the solution before cracks were initiated at the crack tip. In this case, due to the low initial stress intensity, wetting and drying with EXCO of the notch tip was found to be necessary to initiate stress corrosion crack at the crack tip. The mechanism of crack initiation appears to be that corrosion pits develop in the material at the crack tip due to the concentration salt solution caused by the period of wetting and drying. Under the high stress concentration, the pits then transform to stress corrosion cracks [87].

### 14.1.2 The V-K diagram.

The construction of V-K diagram is very important since it could be one of the sources of error during the determination of the minimum threshold value ($K_{ISCC}$) which stress corrosion crack would not propagate. In order to reduce an error, the incremental order of polynomial [122] was used for curve fit on the graph of crack length against time data to calculate crack velocities rather than using only straight line fits. This method also has been used by Connolly et al [95] to construct a V-K curve defined by the ASTM E647 Standard test procedure [151]. There was a rapid crack growth curve at the beginning followed by a slow crack growth as the crack was approaching the threshold value as a result of the longer period of test. Therefore, two polynomial equations were used to cover different crack growth for each DCB specimen. A further reason for the error in measurement on DCB specimen is due to the fact that crack did not develop uniformly across the crack front. This can be attributed to the crack leading at one side to the other side and caught up each other as a stress distribution change. This will lead to error in crack measurement which was taken as an average from the both sides of the DCB specimen.

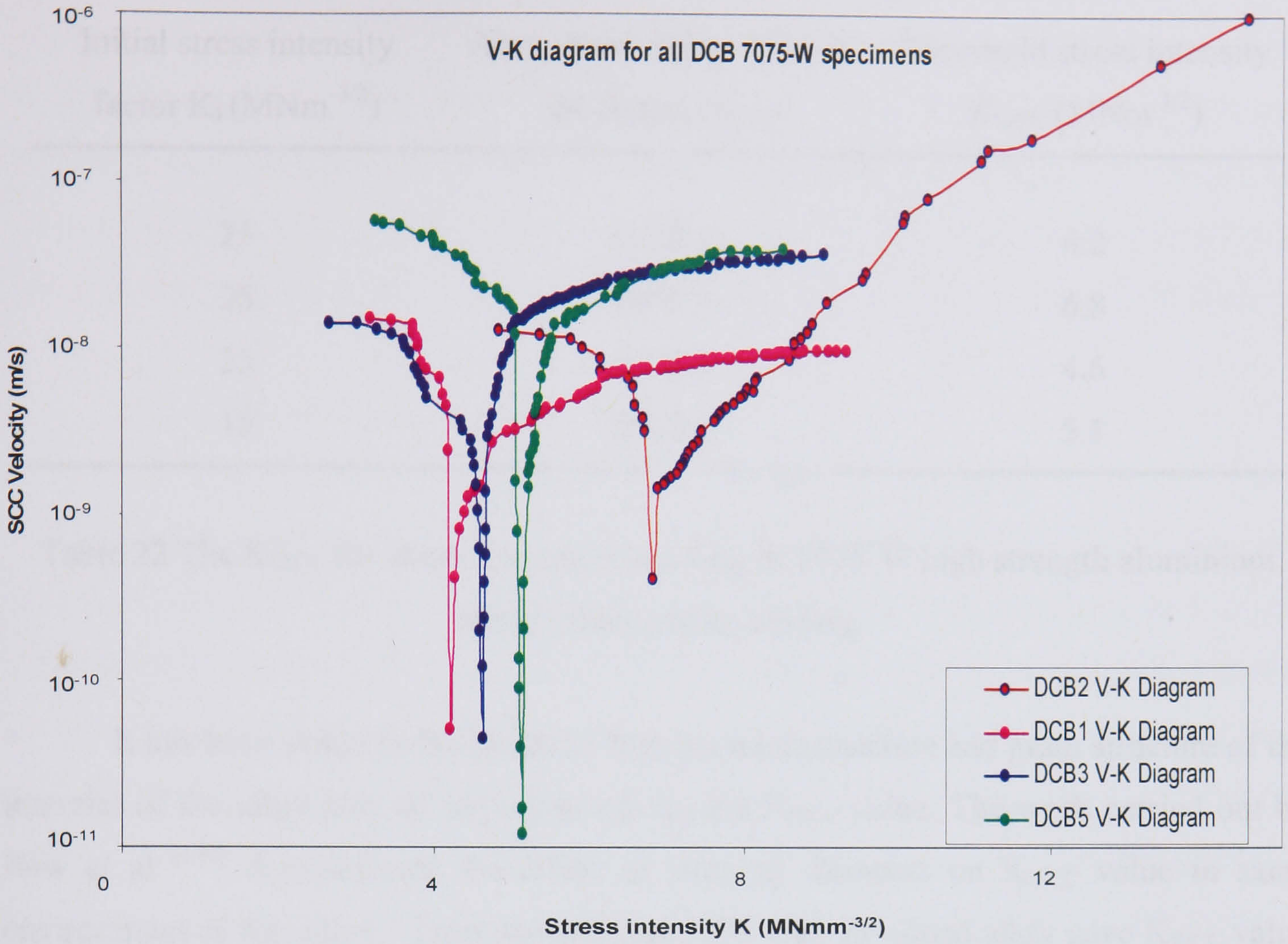


Figure 120 shows stress corrosion crack velocities against stress intensity factor in 3.5% NaCl for 7075-W material.

Figure 120 compares the curves of stress corrosion crack velocities against stress intensity factor in 3.5% NaCl for 7075-W material. The V-K diagrams obtained from all specimens show a range of $K_{ISCC}$ for the alloy in this environment. As the initial stress intensity $K_I$ exceeded the threshold stress intensity $K_{ISCC}$, the crack growth rate was high. In each case, there was a relatively constant crack velocity in region II, followed by a gradual decrease in crack velocity in region I, until $K_{ISCC}$ was reached, known as threshold stress intensity for stress corrosion cracking. Table 22 shows a summary of the $K_{ISCC}$ values measured in the work for stress corrosion cracking in 7075-W high strength aluminium alloys under tensile loading. As can be seen, although initial stress intensity values were different value, the $K_{ISCC}$ value as expected is consistent for the alloy. However, these results suggest that $K_{ISCC}$ has a low value in this alloy indicating its high susceptibility to stress corrosion cracking. Values of $K_{ISCC}$ for 7075 in the peak aged T6 condition are generally to be 8-10 $MNm^{-3/2}$ as described below.

| Initial stress intensity factor $K_I$ ($MNm^{-3/2}$) | Aluminium Alloy 7075-W DCB specimens | Threshold stress intensity $K_{ISCC}$ ($MNm^{-3/2}$) |
|---|---|---|
| 25 | DCB 1 | 4.2 |
| 25 | DCB 2 | 6.8 |
| 25 | DCB 3 | 4.6 |
| 15 | DCB 5 | 5.1 |

Table 22 The $K_{ISCC}$ for stress corrosion cracking in 7075-W high strength aluminium alloys under tensile loading.

It has been stated in the literature that the microstructure and grain structure of the material of the alloy play an important role in the $K_{ISCC}$ value. The work carried out by Pow et al [109] demonstrated the effect of alloying elements on $K_{ISCC}$ value in same environment as this alloy. They showed that 7075 with Zr-added alloy gave $K_{ISCC}$ value range from 7.1-8.9 $MNm^{-3/2}$ and 8.3-11.0 $MNm^{-3/2}$ for 7075 with Cr-added alloys. This would agree with the finding of Scamans [86] who proposed decreased susceptibility in 7017 alloy due to the addition of 0.5% Cu to the base alloy composition. He showed that 7017 with 0.5% Cu-added alloy increased $K_{ISCC}$ value of 5.4 $MNm^{-3/2}$ to 9.0 $MNm^{-3/2}$. Further, they suggested that a microstructure effect involving the precipitate formed due to magnesium segregation or metallurgical differences at the grain boundary produced hydrogen. As a result, a hydrogen embrittlement [91] mechanism occurred at the crack tip.

The test carried out by Stanley et al [91] on S-L direction on 7075-W gave generally similar $K_{ISCC}$ values to the result obtained from this work. However it appears that the present results have lower threshold values in terms of their susceptibility to stress corrosion crack. Blain et al [150] and Branco et al [152] observed the influence of specimen direction for crack propagation in the S-L and S-T orientation for 7XXX series. They found that an increase of SCC resistance in short transverse direction compared to longitudinal or rolling direction and suggested that this may be partially due to increased

in grain elongation as the crack propagated parallel to the grain boundary, in the nature of intergranular corrosion [99,153]. The S-L specimen orientation would therefore be expected to show lower $K_{ISCC}$ value. More recently Bayoumi [81] observed $K_{ISCC}$ value in short transverse on 7075 using sea water testing. He found that the critical stress intensity for stress corrosion cracking in this direction was 7.3 $MNm^{-3/2}$ (1/6 to fracture toughness $K_{IC}$) which is similar $K_{ISCC}$ value to the observation of Robinson [72] in 3.5% NaCl solution.

### 14.1.3 The Corrosion product wedging.

Stress corrosion cracking of DCB specimens produced evidence of corrosion product wedging for 7075-W aluminium alloys. This has had the effect of increasing the stress intensity at the crack tip and resulted in an increase in crack velocity. The effect of wedging became apparent after very low stress intensity had been reached, which is similar to observations of other authors [77,91] in 3.5% NaCl or sea water atmospheric testing. It has been proposed by Robinson [72] and Dorward et al [137] that the corrosion product within the crack tip has generated a sufficient stress to cause SCC to propagate in the DCB specimen. More recently work by McNaughtan et al [122] reported that the initial corrosion product, which is thought to be hydrated aluminium hydroxide transforms to $Al_2O_3.3H_2O$ and this increases the volumes to create forces at the crack tip. This would then relate to an increase in stress intensity at the crack tip and increase the crack velocity. They also reported that there was an inverse relationship between $K_{ISCC}$ value and corrosion product wedging, with an increase in corrosion product wedging with decreasing in $K_{ISCC}$ value. This is suggesting that increase in stress by corrosion product wedging can cause an increasing susceptibility to stress corrosion crack.

It is important to note that in the corrosion product region the stress intensity value is seen to decrease on V-K diagram as shown figure 120. However, in contrast the stress intensity value actually increases during corrosion product wedging. This explains the appearance of wedging after the $K_{ISCC}$ value had reached the lowest point. It has been reported [122] that stress generated internally by corrosion product increased the stress intensity at the crack tip after $K_{ISCC}$ had been reached. However, it is difficult to

determine where the corrosion products wedging is first taking place. Anderson [154] considered this corrosion product wedging action as corresponding to point loading. Jones [114] discovered that the corrosion product wedging caused crack growth but it was not known whether the wedging was at the initial corrosion site or at the crack tip. It is unlikely that this point will coincide with the load line of the bolts. This therefore makes the increased stress intensity applied by corrosion product wedging difficult to calculate and it can not be calculated in the normal way.

### 14.2 Stress corrosion crack under compressive loading.

In the previously described tests we have shown that stress corrosion cracking can occur under tensile loading. The outcome leads to the question of what would happen if the alloy was tested under compressive loading. Therefore, the compressive test specimen was designed from the same material and tested under compressive loading to see if stress corrosion cracks could be developed under these conditions. It was clear from the eddy current test that stress corrosion cracking also occurred under compressive loading. It is thought that the results of this experiment would be benefit from extension of this work in the future. In order to try to understand the conditions that may lead to stress corrosion cracking under compressive loading. The tests on the 7075-W high strength aluminium alloy were summarized, as shown in the table 23.

| Specimens | Solution | Method | Time |
|---|---|---|---|
| 7075/7 | - | Uncorroded reference surface | - |
| 7075/8 | 3.5%NaCl | Wet & dry, Under load | 2 months |
| 7075/9 | 3.5%NaCl | Wet & dry, Under load | 2 months |
| 7075/10 | EXCO | Wet & dry, Under load | 2 weeks |
| 7075/11 | EXCO | Immersion, Under load | 2 weeks |
| 7075/12 | EXCO | Immersion, Under load | 2 weeks |
| 7075/13 | EXCO | Immersion, Under load | 2 weeks |
| 7075/14 | EXCO | Immersion without load | 4 weeks |
| 7075/15 | EXCO | Immersion without load | 8 weeks |

Table 23 Summary of the complete testing programme for stress corrosion cracking in 7075-W high strength aluminium alloys under compressive loading.

### 14.2.1 Effect of environment.

#### 14.2.1.1 3.5% NaCl.

It has been stated in the literature that in order for stress corrosion cracking to occur, there are three requirements; a susceptible material, a specific environment and high load/stress or stress intensity factor where the stress has generally been thought to be tensile. The corrosive environment plays an important role as one of the factors in the stress corrosion cracking process. It was shown that the 7075-W did not initiate stress corrosion cracking under compressive loading by wetting and drying with a 3.5% NaCl solution within the two months test period. There was no evidence of stress corrosion cracking, either visually or by the eddy current testing. As a result, it was assumed that the material susceptibility was relatively low, with no failure on the eddy current signal recorded in two months. This may have been due to the solution drying out during the course of experiment so that for much of the test little corrosion was occurring. A light

corrosion product was seen to develop around the hole of the compressive specimen after 2 months. However, it may not have been severe enough to cause stress corrosion cracking. This information for the 7075-W Al alloy would suggest that stress corrosion cracking under compressive loading can not be occur in the 3.5% NaCl by wetting and drying environment.

There was either relatively low susceptibility of the 7075-W in 3.5% NaCl solution or the incubation was very long in this environment. This result suggested that for stress corrosion to occur the test solution should be more aggressive than 3.5% NaCl solution. It has been shown that increasing the aggressiveness of the solution can promote stress corrosion cracking failure. Work done by De Jong et al[155] showed that reducing the pH of the solution did promote stress corrosion cracking failure in aluminium alloys and this was associated with increased general corrosion, pitting and exfoliation in the material.

#### 14.2.1.2 EXCO solution.

As 3.5% NaCl solution did not initiate stress corrosion cracking by wetting and drying, it was decided to use EXCO solution as the corrosive environment to promote the more corrosion attack. The environmental conditions are different in this solution, which results in large volumes of corrosion product being formed. A decrease in pH value (to become more acidic) has been shown to cause pitting, end grain attack and exfoliation corrosion on the surface of the hole. This indicated that this is a more aggressive environment to 7075-W than the 3.5% NaCl solution. The time to initiate corrosion attack was significantly reduced in the aggressive environment of the EXCO solution. DuQuesnay et al [156] stated that aluminium 7075 produced more pitting corrosion damage by exposing it to EXCO solution for a short period of time. A comparison of the degree of the surface damage shows that in general the damage in EXCO condition is much more than in 3.5% NaCl condition. This explains the fact that the EXCO environment produces a greater susceptibility to corrosion. As pH of solution decreases, the time to attack also decreases. In wetting and drying with EXCO, the corrosion products build up

rapidly due to the aggressive nature of the solution, which produces corrosion wedging inside the specimen hole. However, there was no indication from the eddy scan that any cracking had occurred in the specimen after two weeks wetting and drying in EXCO solution, under load. This is probably because the exposure time was not long enough and corrosion stops when the EXCO solution dries out. It is likely that the hole was dry for most of the day.

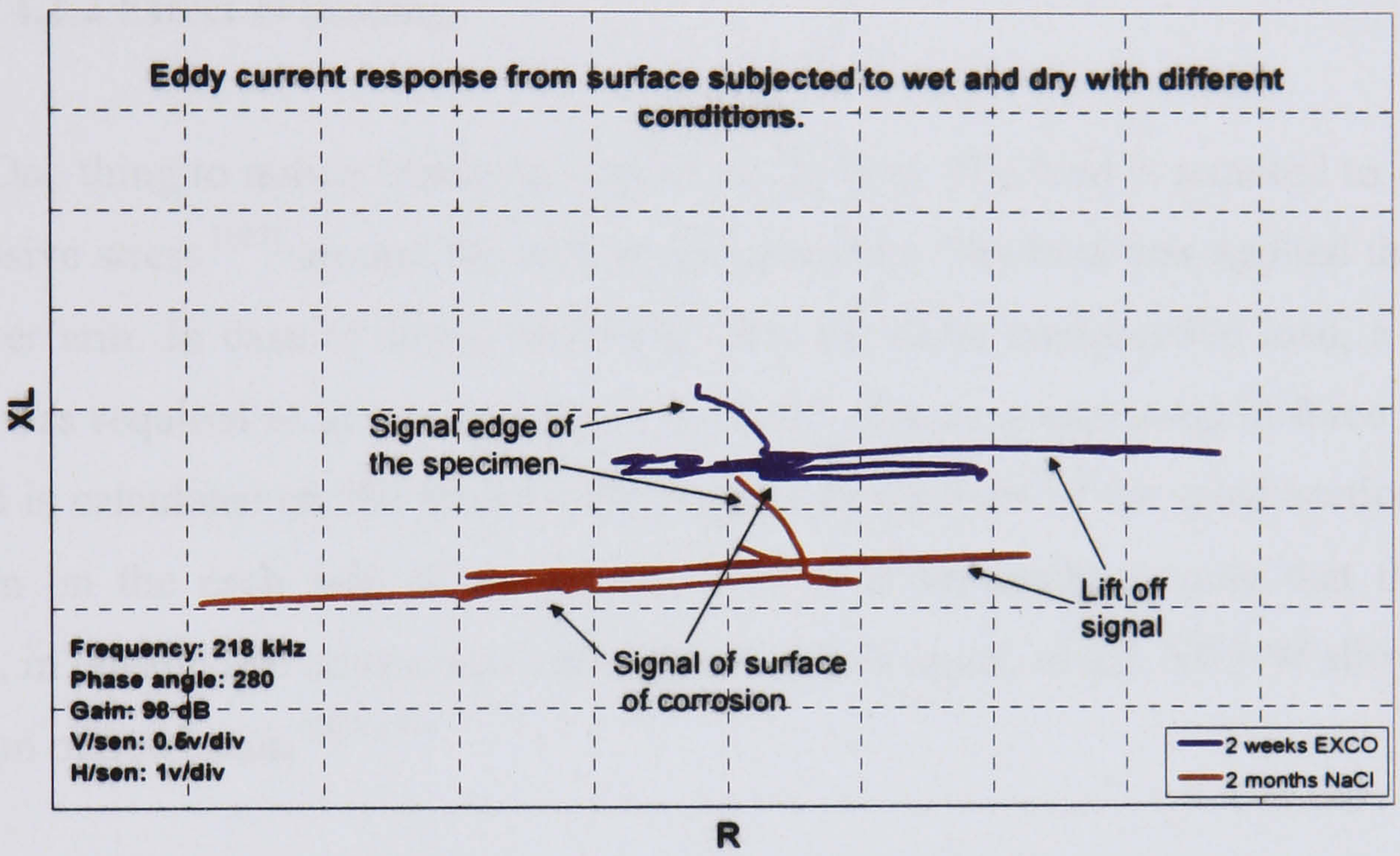


Figure 121 shows eddy current responses from specimen subjected to wet and dry with different condition.

Figure 121 shows the signals obtained for corroded surfaces caused by the different types of exposure conditions. Both of the eddy current scans have a similar trend. They were very flat signals with little evidence of a vertical component. The eddy current signal displayed a small noise signal superimposed on the lift off signal. This was due to a small amount of metal loss at the surface specimen. The signal suggests that the depth of corrosion has increased to be less than 0.30 mm. into the material.

Immersing the hole in the EXCO solution for the test period allowed the hole surface to react continuously with the fresh solution. With constant compressive loading for two weeks, pitting corrosion was evident in the region where the corrosion attack

transforms to a stress corrosion crack. The stress corrosion crack was running from surface of the hole into the material. It is assumed that stress corrosion cracks propagate from the base of a corrosion pit or the from end-grain attack mainly along the grain boundary to be intergranular corrosion. A similar result has been reported by Robinson [157] where 7000 series stress corrosion specimens were submerged in the 3.5% NaCl solution under constant tensile load.

### 14.2.2 Effect of loading.

One thing to notice here is the effect of the load. The load is required to give the compressive stress [127] around the hole in the specimen. The load was applied through a 10:1 lever arm. In case of stress corrosion cracking under compressive load, a load of 3750 N was required to give a stress of 375 $Nmm^{-2}$. Stress is expressed in force per unit area and is calculated on the basis of the original dimensions of the cross section of the specimen on the each side of the central hole. It is important to note that the yield strength, in tension and compressive are approximately equal, of the 7075-W alloy was in the region of 500 $Nmm^{-2}$ [28,45].

## 14.3 Control experiment.

Control experiments, without compressive loading, were carried out to confirm that the load was essential to the occurrence of stress corrosion cracking. Figure 122 shows the eddy current response of the control specimen holes after 2, 4, 6 and 8 weeks exposed to the EXCO solution. The eddy current responses indicated there was no existence of SCC in this observation. It would be expected that corrosion pits existed at the surface and the degree of damage increased with exposure time. However, the presence of surface damage was not clearly detected by the eddy current probe due to the limitation of the operating frequency, as has been explained in the eddy current discussion. There is a limitation of the eddy current technique to clearly distinguish corrosion pits or small end-grain attack, while at the same time detecting cracks that may be several millimeter in length.

In the case of immersion without load, after 8 weeks, the control specimen showed some corrosion damage at the surface of the hole. The specimen was also inspected with a high magnification microscope to locate and make comparisons with the results of eddy current testing. In figure 123, the optical micrograph confirmed that the only corrosion damage was occurred due to corrosion pits and small amount of end-grain attack around the surface of the hole. As can be seen, the attack was mainly on grain boundaries. This confirmed that although the material is susceptible to end grain attack. There was no evidence from metallography or eddy current measurements of stress corrosion cracking in the unloaded control specimens, even after four times the exposure period used on compressively loaded specimens.

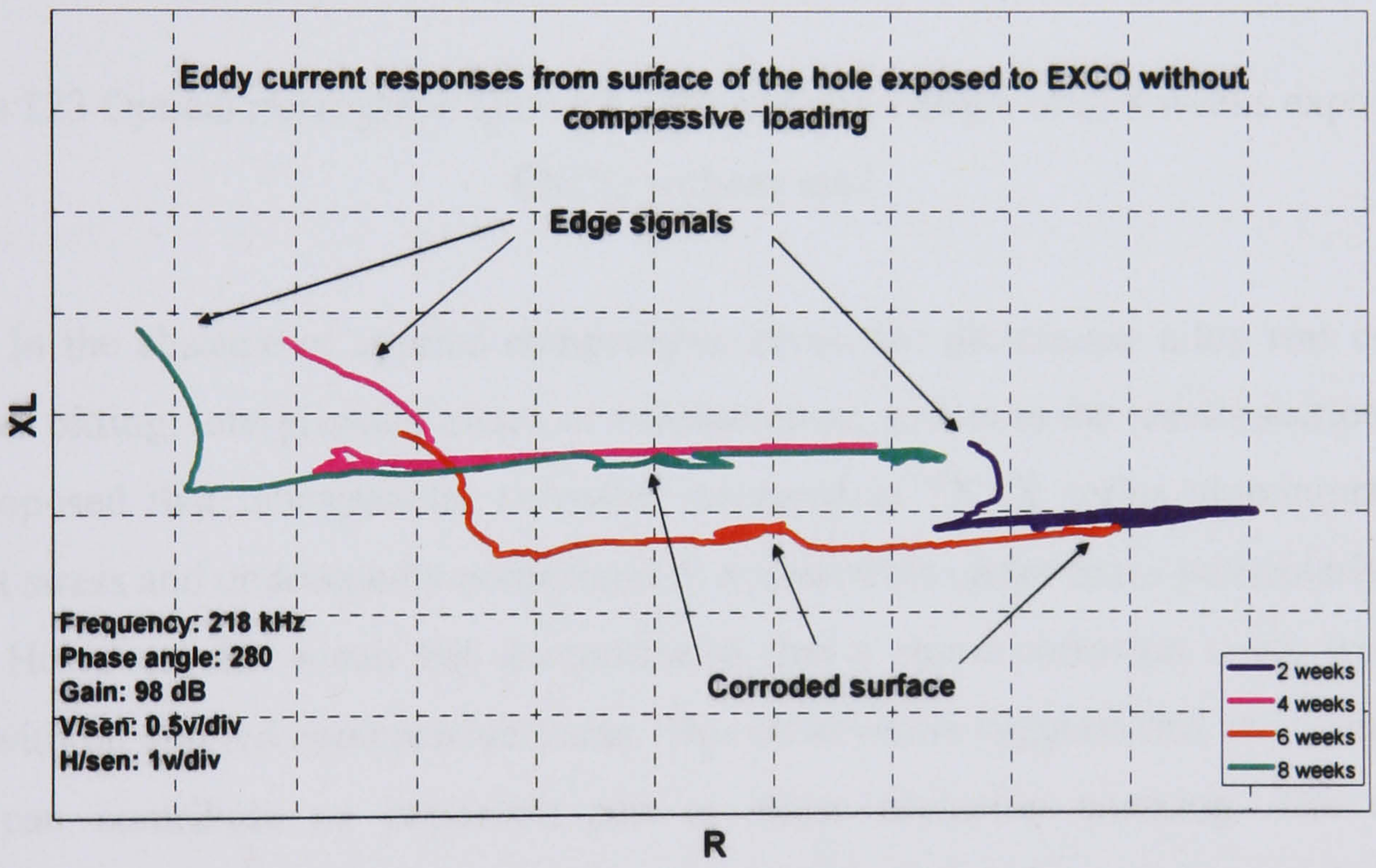


Figure 122 shows the eddy current responses of the hole after 2, 4, 6 and 8 weeks exposed to the EXCO solution.

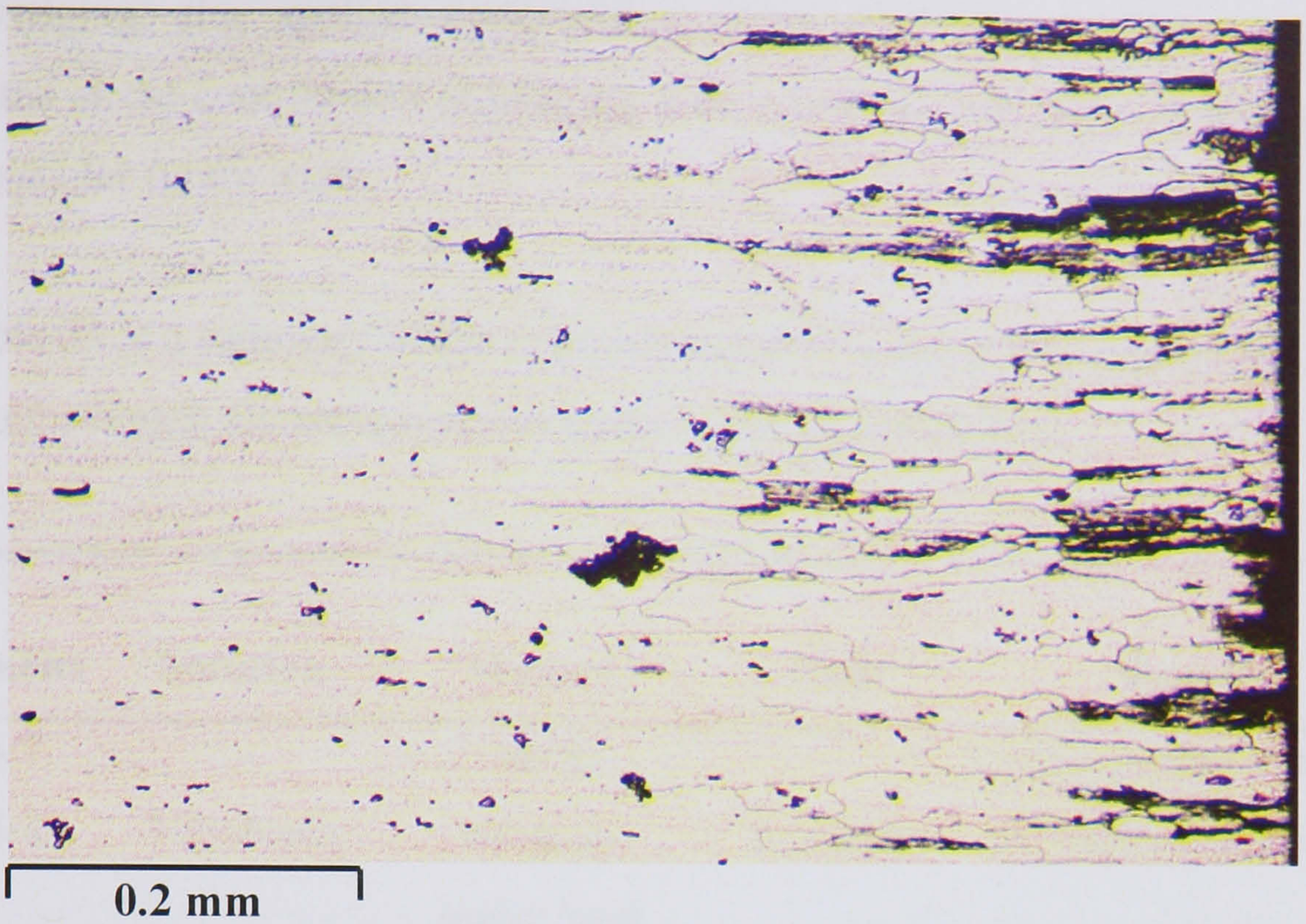


Figure 123 Optical micrograph showing only end grain attack after 8 weeks exposure to EXCO without load.

In the absence of applied compressive stress, the aluminium alloy was corroded by either pitting, intergranular attack or exfoliation as, shown in the results section. Gruhl [158] proposed that intergranular corrosion occurred in 7XXX series aluminium alloys without stress and undoubtedly contributes to acceleration under stress particularly tensile stress. However, this result has demonstrated that a stress corrosion crack would not occur without applied compressive stress. This observation suggests that the compressive stress can contribute an important part to stress corrosion cracking. The exposed specimens developed stress corrosion cracking after 2 week's exposure to the EXCO solution with the application of a compressive stress. The control specimens were only exposed to EXCO solution which produced voluminous corrosion product inside the hole. The corrosion product also should be considered as a possible cause of tensile stress on the surface of the hole. However, the corrosion product alone appears not to be sufficient enough to cause stress corrosion cracking in the material. There was no evidence of cracking on the eddy current scans shown in figure 122. The stress corrosion crack only occurred when the compression load was involved. From this result, it would

suggest that the stress corrosion cracking occurred due to combination of corrosion product wedging, the applied compressive stress and the material susceptibility. However, the stress contribution around the hole is still unclear and would need further stress analysis for future work.

Table 24 is a summary of the complete results for stress corrosion crack testing in 7075-W high strength aluminium alloys under compressive loading.

| Specimens | Solution | Method | Time | Results |
|---|---|---|---|---|
| 7075/7 | - | control | - | Uncorroded surface |
| 7075/8 | 3.5%NaCl | wet&dry under load | 2 months | No indication of crack |
| 7075/9 | 3.5%NaCl | wet&dry under load | 2 months | No indication of crack |
| 7075/10 | EXCO | wet&dry under load | 2 weeks | No indication of crack |
| 7075/11 | EXCO | immersion under load | 2 weeks | detected cracks |
| 7075/12 | EXCO | immersion under load | 2 weeks | detected crack |
| 7075/13 | EXCO | immersion under load | 2 weeks | detected crack |
| 7075/14 | EXCO | immersion without load | 4 weeks | No indication of crack |
| 7075/15 | EXCO | immersion without load | 8 weeks | No indication of crack |

Table 24 Summary of the complete testing results for stress corrosion cracking in 7075-W high strength aluminium alloys under compressive loading.

### 14.4 Mechanism of stress corrosion crack in aluminium alloys.

All the testing and discussion so far is convincing that aluminium alloys especially 7XXX series, are susceptible to stress corrosion cracking. It is an intergranular type of corrosion and strongly influenced by the grain structure [72,122]. During the heat treatment of aluminium alloys 7XXX series, the grain matrix and grain boundary differ due to the formation of precipitates [63,92,159]. The resulting corrosion process has occurred due to the grain boundary precipitates having a different galvanic potential from the grain matrix [82,87,93,94].

#### 14.4.1 Reaction at the crack tip.

The possible mechanism for the attack involves the evolution of hydrogen from the stress corrosion crack [160]. The process is controlled by the extent of the anodic or cathodic reactions at the crack tip. In the anode reaction, metal loss occurred in order to produce hydrogen ions at the adjacent cathodic sites on the walls. This suggests that there always has to be an anodic dissolution process with metal dissolved, at the grain boundary for the generated of hydrogen at the same time. Foley [61] and Speidel [82] have proposed similar model involved in this process. They can be divided into 3 main steps; anodic dissolution, hydrogen embrittlement and repeated rupture of a protective surface film.

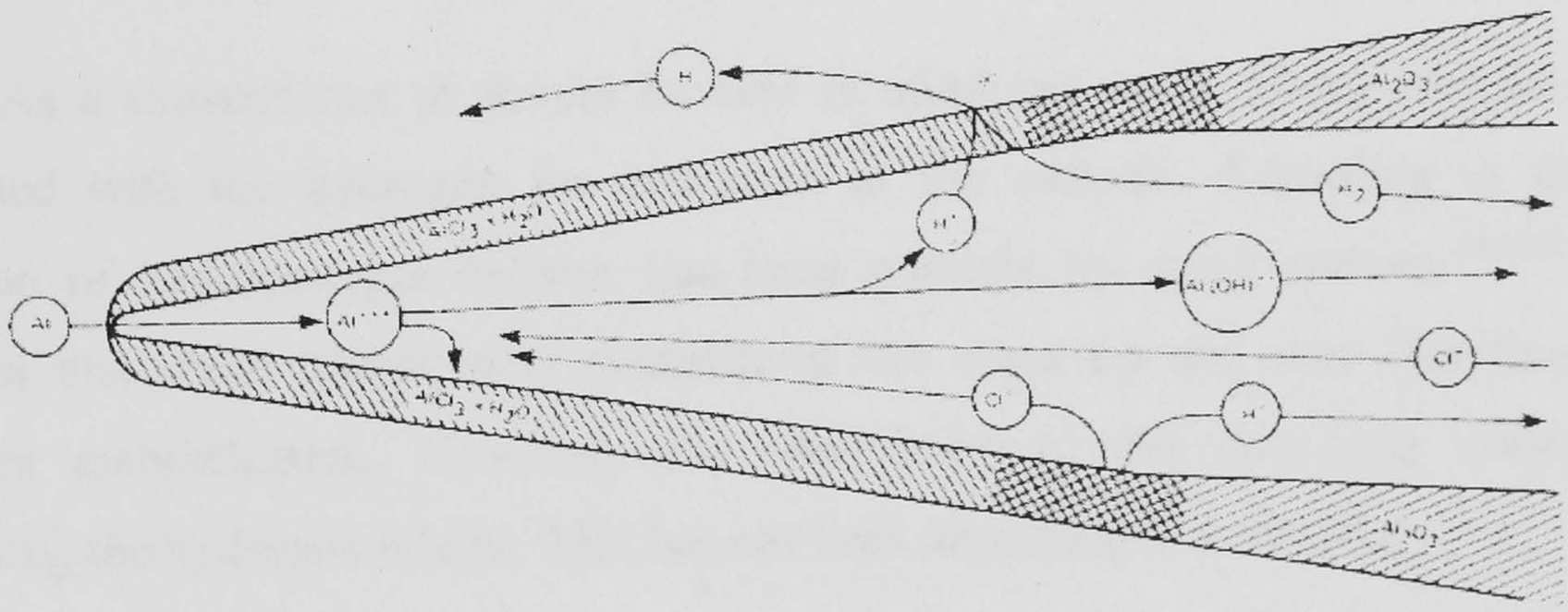

Figure 124 shows the reaction at the crack tip of a stress corrosion crack for aluminium alloys in 3.5% NaCl solution [82].

As can be seen in figure 124, in the first stages, anodic reaction that occurrs at the crack tip during the corrosion process is $Al \rightarrow Al^{3+} + 3e$. During this process, the $Al^{3+}$ ions diffuse away from the anodic site to the bulk solution due to the potential difference between these regions [160]. The $Al^{3+}$ ions, from metal corroded, is reacted with bulk solution to perform hydrated aluminium oxide for example $Al(OH)_2Cl$ [61,138] and remains at the crack tip as corrosion product. It was proposed that the thicker corrosion product away from the crack tip will result in more attack at the crack tip. Hydrolysis of $Al^{3+}$ leads to reduced pH values and acidic solution [67,161]. On the other hand, the free electron will flow in the metal to the region along the surface of the crack tip to a site described as a cathode. Note that when the bulk solution becomes more acidic, pH 3.5 [161], the hydrogen ions will be reduced to form hydrogen as the cathodic process [162]. It might be molecules of hydrogen gas which escape from the system as hydrogen bubbles. In contrast, if hydrogen does not collect and form molecules of gas then it can diffuse to the crack tip where it causes a hydrogen embrittlement process. However, it is still not clear that the reaction at the crack tip will produce enough hydrogen ions to develop hydrogen embrittlement process and embrittle the material. This is due to most of the hydrogen escaping from the system as hydrogen bubbles. It seems to suggest that the anodic dissolution process has to occur as the major process for cracking along the grain boundary and secondary effect of this process is the generation of hydrogen. In another words, if the corrosion reaction had not occurred at the grain boundary and then the hydrogen would not have been generated.

As a consequence, it should be kept in mind that anodic dissolution is always associated with the hydrogen ion reduction at the cathode. According to that, the evolution of hydrogen gas bubbles has been reported by many authors [94-96] which indicates that some hydrogen is available at the crack tip and may therefore cause hydrogen embrittlement. However, this observation is still remaining questionable concerning the hydrogen effects. This has not been investigated in this study.

### 14.4.2 Role of stress in stress corrosion cracking.

Up to this point in the discussion the mechanism of stress corrosion cracking in high strength aluminium alloys has been described an occurring due to an anodic reaction at the crack tip. The corrosion occurred because of the galvanic effect at the grain boundary with the grain boundary precipitates having a different galvanic potential from the grain matrix. This gives the crack an intergranular path along the grain boundary. It has also been shown by the work of Speidel [87] that at very low crack tip stresses the material failed by intergranular corrosion at slow rate. Figure 125 shows a schematic diagram, with intergranular corrosion occurring at low stress. The stress corrosion cracking of zinc containing high strength aluminium alloys is thought to be due to hydrogen embattlement, but in this case the main effect is the galvanic potential. However, the role of stress also plays a very important part in mechanism for stress corrosion cracking to occur.

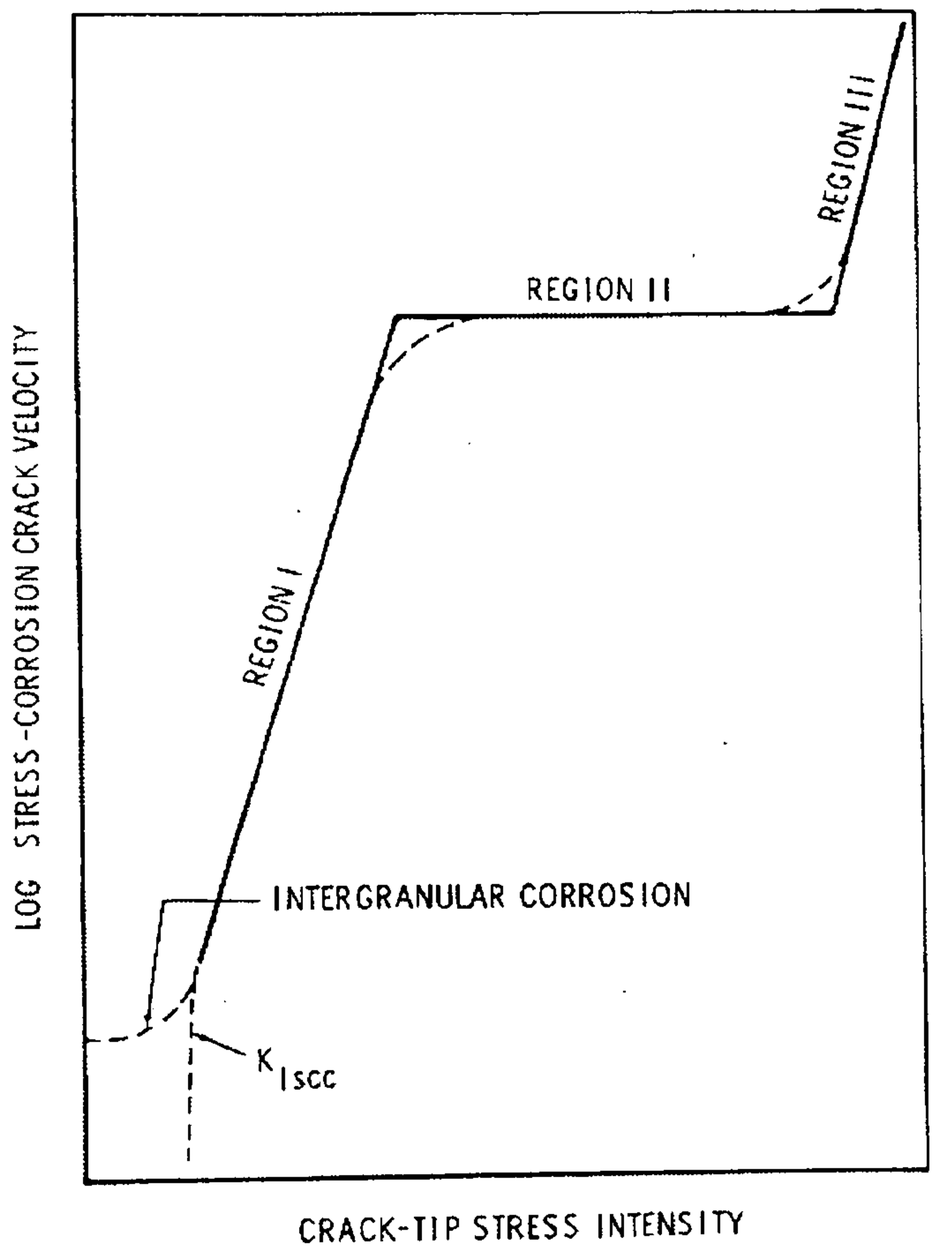


Figure 125 Schematic diagram showing intergranular corrosion occurring at very low applied stresses [87].

### 14.4.2.1 Tensile stress.

The effect of applied stress has also been examined by Robinson et al [68] who showed that stress corrosion cracking in high strength aluminium alloys is propagating by a stress-assisted intergranular corrosion mechanism. They measured intergranular corrosion rate in stress corrosion cracking and compared them to the rates during exfoliation corrosion. They showed that the greatest velocities were found in stress corrosion cracking due to the stress being applied externally by load rather than internally produced by corrosion product. The same view about stress also has been proposed by Gruhl [158] and Tanguy et al [161] that stress accelerated intergranular stress corrosion cracking caused by the anodic and cathodic reactions in the corrosive environment.

The component of tensile stress is creating high stress concentration at the crack tip. The plastic deformation [127,150] zone will occur more easily in the region at the crack tip when the specimen is under high stress. During plastic deformation, the specimen develops a high density of dislocation which move to the grain boundary [28,55,97,163]. Note that the movement of dislocations occurs on the slip plane and disrupts the protective corrosion product film to expose the fresh metal which is more prone to corrosion attack. Therefore, the corrosion process is accelerated and prevented from forming a new protective layer at the crack tip. These processes happened at the same time to produce crack growth, as shown in figure 126 and 127.

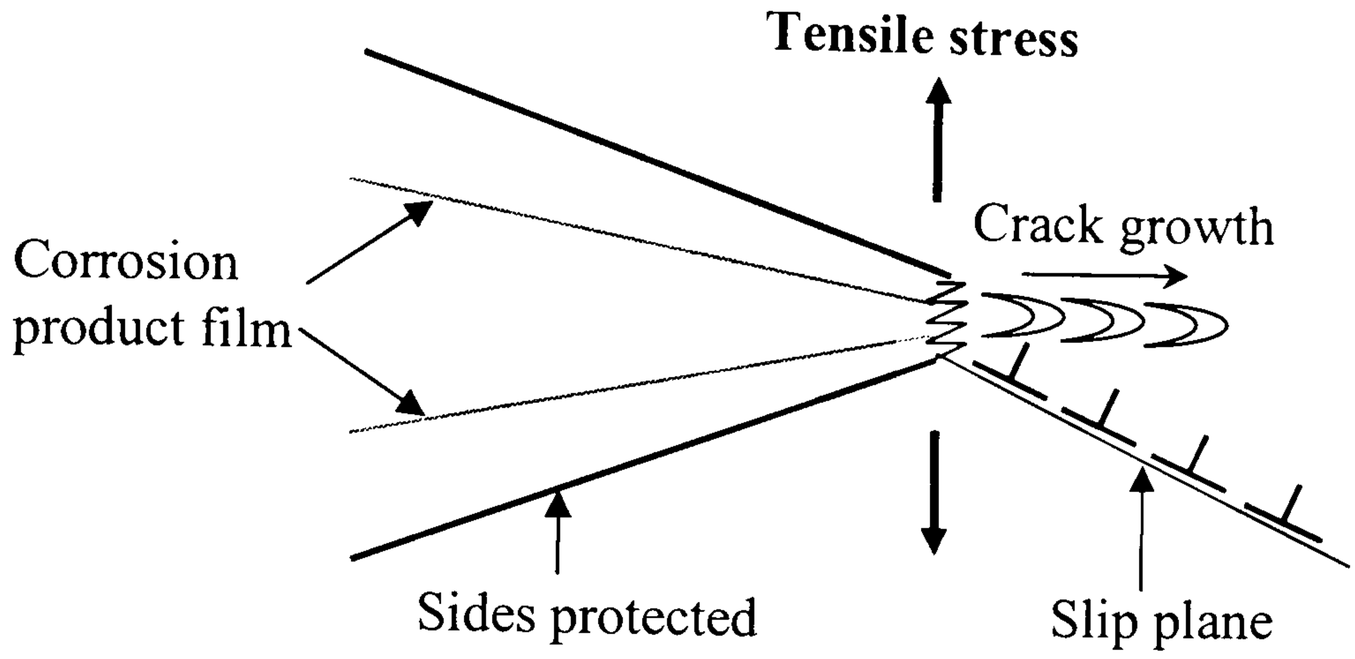


Figure 126 Schematic illustration of at the crack tip under stress and exposed to corrosive environment.

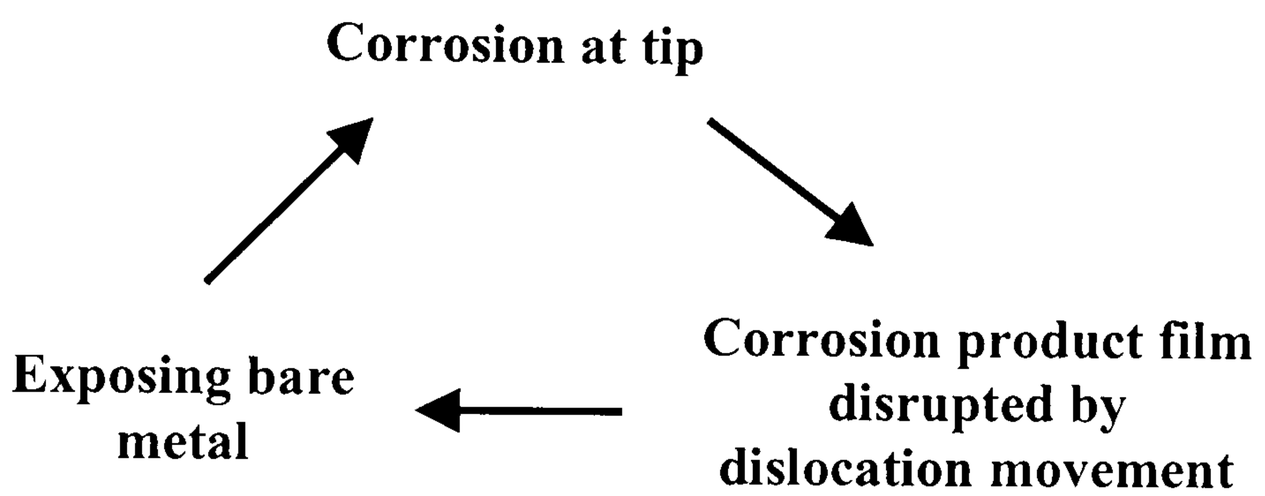


Figure 127 Steps in the cracking process to produce an extension at the tip.

The role of stress in opening the crack tip and exposing the metal surface to the solution [97,164] have been described by many authors. Recently, the importance of stress has been studied by the work of Bayoumi [81] who stated that stress concentration at the crack tip helped to open up the crack to propagate further and also prevent formation of a new film. Speidel [87] has considered the influence of stress on stress corrosion crack propagation in aluminium alloys with various papers that have attempted to predict the role of stress. He concluded that the role of stress in stress corrosion is to open the crack tip and exposing the more anodic fresh metal to the corrosion attack along the grain boundary.

Other work has been done by Logan [165], who measured electrochemical potentials of a notched specimen under stress. He found that the greatest change in

potential was recorded in the plastic deformation zone of the stress-strain curve, which was attributed to the repair mechanism of the protective film. It was concluded that higher stress leads to an increase in dislocation movement and crack growth rate.

#### 14.4.2.2 Compressive stress.

Stress corrosion cracking refers to crack propagation that is a result of combination of susceptible alloys, corrosive environment and stress events at the crack tip. Stress is the major variable to help the stress corrosion cracking process take place. It was generally thought that stress corrosion cracking requires tensile loading. In contrast, this particular work investigated the different situation where the direction of stress was in compression. In these experiments stress corrosion cracking has been shown to occur under compressive stress, as shown in table 24.

The results seemed to suggest that, under compressive stress, the mechanism of dislocation movement is still responsible for stress corrosion cracking in the compression test. In support of this statement, Hsiao et al [6] described the mechanism of stress corrosion cracking under compressive stress. They concluded that the compressive stresses help to produce dislocation movement, induce slip steps and also the film rupture process at the crack tip. As a result, the corrosion reaction can take place and the cracking process continues through anodic dissolution.

This is an accepted mechanism for stress corrosion cracking in aluminium alloys under tensile stress. However, dislocation movement will also occur under compressive stress. This clearly implies that the same mechanism can cause stress corrosion cracking in both cases. The tensile stress was thought to open the crack tip and expose the fresh metal to the corrosive environment. Conversely, crack closing was produced by the compressive stress. In this case, only a limited area of protective film was disrupted by the movement of dislocations. Therefore, it would be more difficult to expose fresh metal to the corrosive environment. Both phenomenon can be explained by the schematic diagram in figure 128.

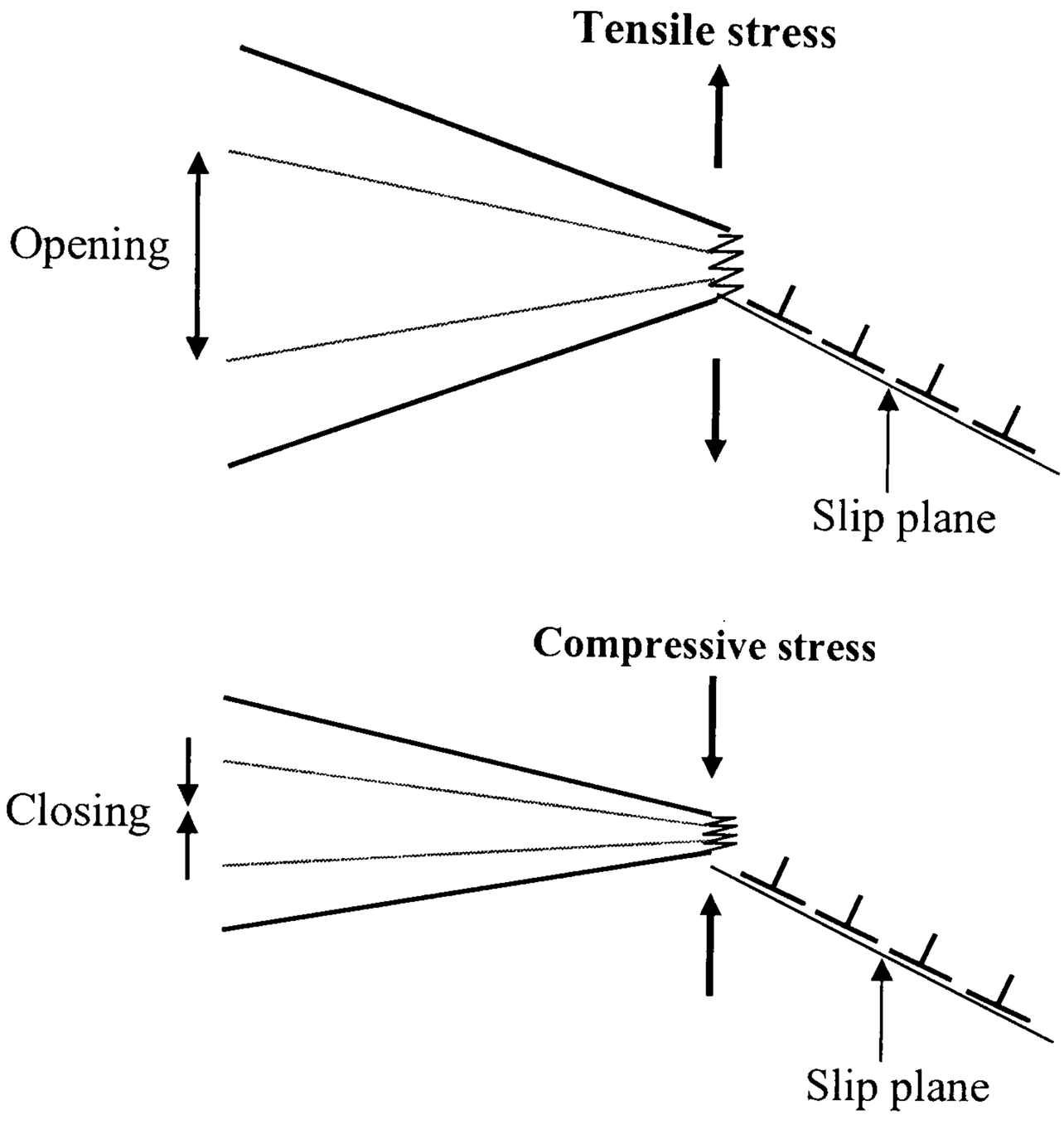


Figure 128 Schematic diagram showing the conditions of the crack tip subjected to different stresses.

The other important point that should be noted is the plane of the crack that developed in the test specimens. Hsiao et al [6] has demonstrated that the plane of the crack is in the same direction in the DCB specimen whether applied with tensile stress or compressive stress. However, in this particular work, the plane of crack was perpendicular to the crack produced by Hsiao et al's tests. Figure 129 shows the plane of crack in the specimens under compressive stress.

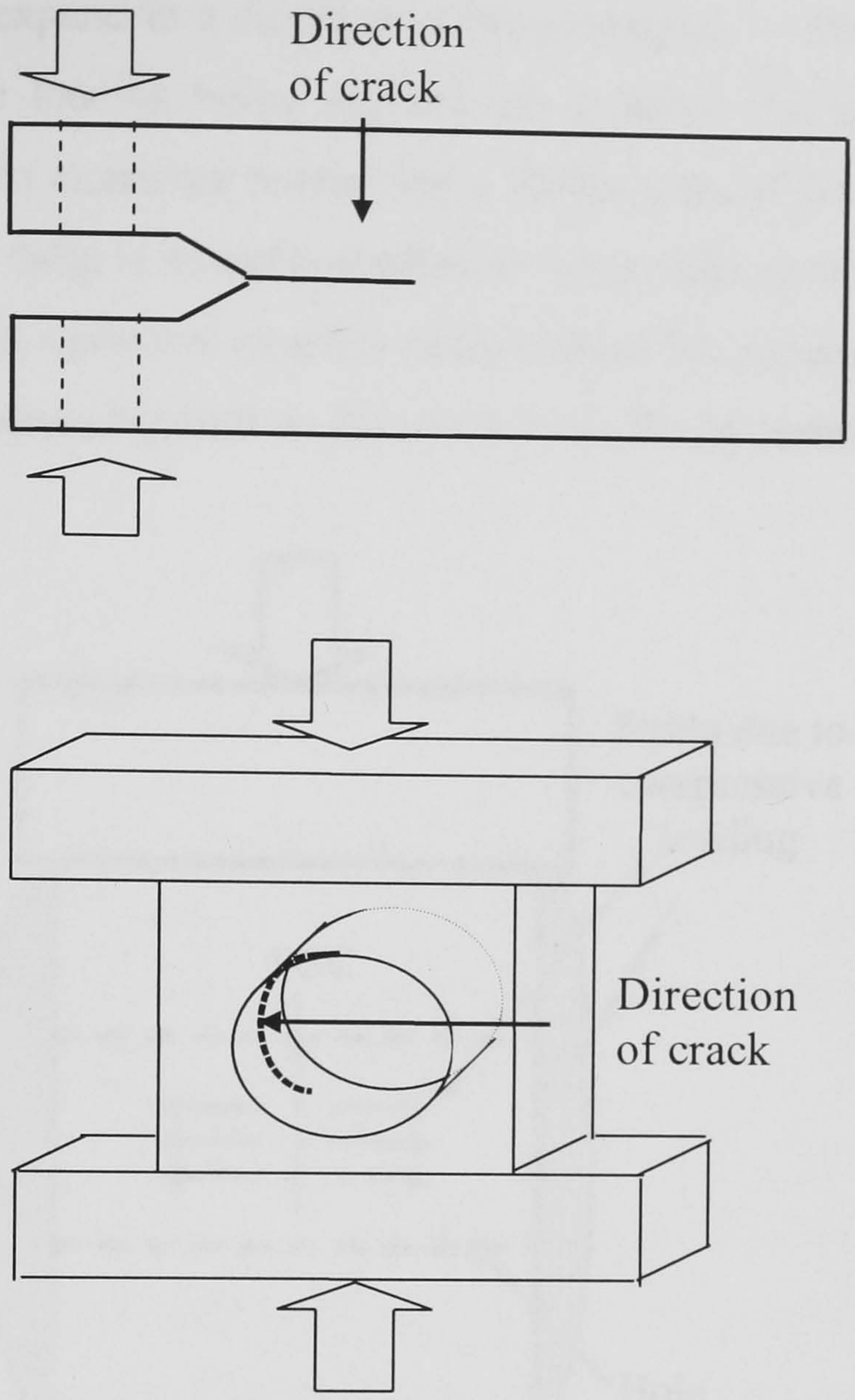


Figure 129 Schematic diagram shows the plane of crack in the specimens under compressive stress.

The experiment for investigating stress corrosion cracking in the compressive specimen has proved that to be an effective method as a result of the particular stress conditions and exposure to a corrosive environment. The original thought was that in some way the compressive stress caused the stress corrosion crack to occur in the compressive specimen. However, the results from the compressive tests have shown that the stress corrosion cracking was caused not by stress but by strain due to compressive loading.

Consider the case that when the specimen is stressed under compressive loading. The material deformed along the axis of loading to produce a strain [55,97,166]. The strain

will cause a material to expand in a direction at ninety degrees to this loading axis as a response to compressive loading being applied. As a result, the atomic structure of material is strained and the atoms are moved apart. As the sides of the specimen is a free surface. In this direction, there is no stress applied to move atom apart as shown in figure 130. That is to say there is a positive (tensile) strain without the application of stress. The magnitude of the tensile stress depends on Poisson's Ratio for the material.

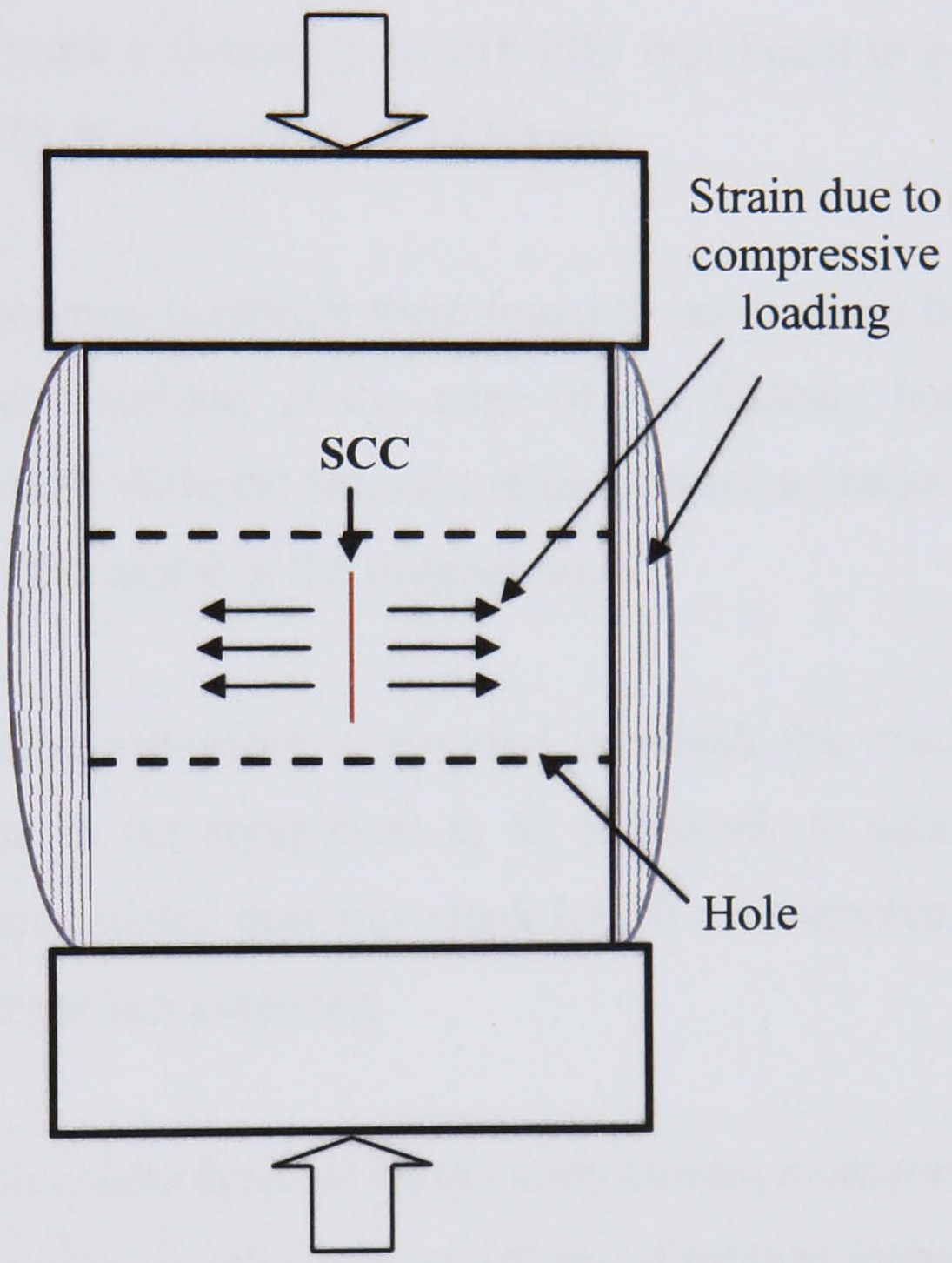


Figure 130 Schematic diagram shows the specimens under compressive loading.

In conclusion, it appeared that stress corrosion cracking is caused by the strain rather than tensile stress as there is no stress present in that direction. Nevertheless, strain is moving the material outward as a tensile strain. This indicates that the tensile strain could be the required parameter to produce stress corrosion cracking under compressive loading.

# Conclusions.

1. The eddy current technique is a sensitive non-destructive test method for detecting stress corrosion cracks around fastener holes in high strength aluminium alloys.

2. The eddy current frequency is an important parameter affecting the sensitivity of crack length measurements and should be determined for the particular material under test. In this work a frequency of 218 kHz was found to be most suitable to detect cracks in 7075-W up to depth of 18.00mm.

3. Exfoliation and end-grain corrosion were found to occur along the grain boundary, parallel to the metal surface, at the edge of the fastener holes. This form of corrosion was distinctly different from the stress corrosion cracks that were detected by eddy currents in the centre of the fastener holes.

4. A suitable calibration test piece is required in which the cracks have the same orientation as those in the component to be examined. In addition, a calibration graph based on accumulated previous crack length measurements can be used for calibration and comparison purposes.

5. The stress corrosion cracks detected by the eddy current measurements in this study were measured in a plane parallel to the surface, rather than intersecting the surface, as is usually the case for fatigue cracks around fastener holes.

6. Eddy current measurements had the advantage that they could detect crack bowing in the centre of the DCB specimens, which was not possible by optical observation of the surface. Good agreement between eddy current and ultrasonic measurement was obtained.

7. The used of extreme value statistic to measure the grain shape of the material was found to be very important in determining the susceptibility to corrosion. It was

found that alloys with a high aspect ratio in the longitudinal direction were more susceptible to intergranular corrosion.

8. Aluminium 7075-W alloy was found to be particularly susceptible to stress corrosion crack under tensile loading with a threshold $K_{ISCC}$ value of only 4.2 $MNm^{-3/2}$. This low value was attributed to the grain boundary precipitates resulting from this heat treatment condition.

9. There was evidence of self-loading of the stress corrosion crack due to corrosion product wedging. The stresses generated were sufficient to raise the crack tip stress above $K_{ISCC}$ so that further crack growth occurred. After long exposure, more stress corrosion crack growth could occur as a result of corrosion product wedging, although the applied stress intensity had reduced to $K_{ISCC}$.

10. While stress corrosion cracking under tensile loading is the common form of cracking in high strength aluminium alloys. It was found that stress corrosion cracking under compressive loading could also occur. Relatively high compressive stresses were found to be necessary and the cracks were again intergranular and oriented in the longitudinal direction.

11. The stress corrosion cracking mechanism was found to be an anodic reaction at the crack tip. The corrosion reaction occurred because of the galvanic effect at the grain boundary where the grain boundary precipitate has a different galvanic potential from the grain matrix. This mechanism should be applicable to all precipitation strengthened aluminium alloys, whether or not there is also damage caused by hydrogen generated in the corrosion reaction.

12. In control tests conducted without compressive loading, surface corrosion occurred in the fastener holes but stress corrosion was not detected in test times up to four times that of the compressive load tests.

13. It appears that stress corrosion cracks under compressive loading developed as a result of the tensile strain that occurred in the specimen, as no applied tensile stresses were present.

# Future Work

From the present study the following subjects are suggested for future work

1. There are preferred frequency ranges for eddy current testing depending on the form of corrosion to be detected. The early detection of pitting and end-grain corrosion could be considered very important in predicting the onset of stress corrosion cracking and higher operating frequency testing should be considered.

2. Carry out more detailed stress analysis of the compression test specimen to investigate the distribution of stress and strain and determine the effects on crack initiation and propagation.

3. Stress corrosion cracking was found to be strongly related to the value of $K_{ISCC}$. Similar testing should be carried out to establish $K_{ISCC}$ in the other high strength aluminium alloys.

4. Futher testing of 7XXX series aluminium alloys would be useful to establish the relationship between cracking under compressive loading and the dilation of the material. Electrical resistance strain gauge devices could be used to measure deformation of the material as shown in figure 131. As the specimen is deformed it would cause the electrical resistance of the gauge to change. The resistance change is usually measured using a Wheatstone bridge.

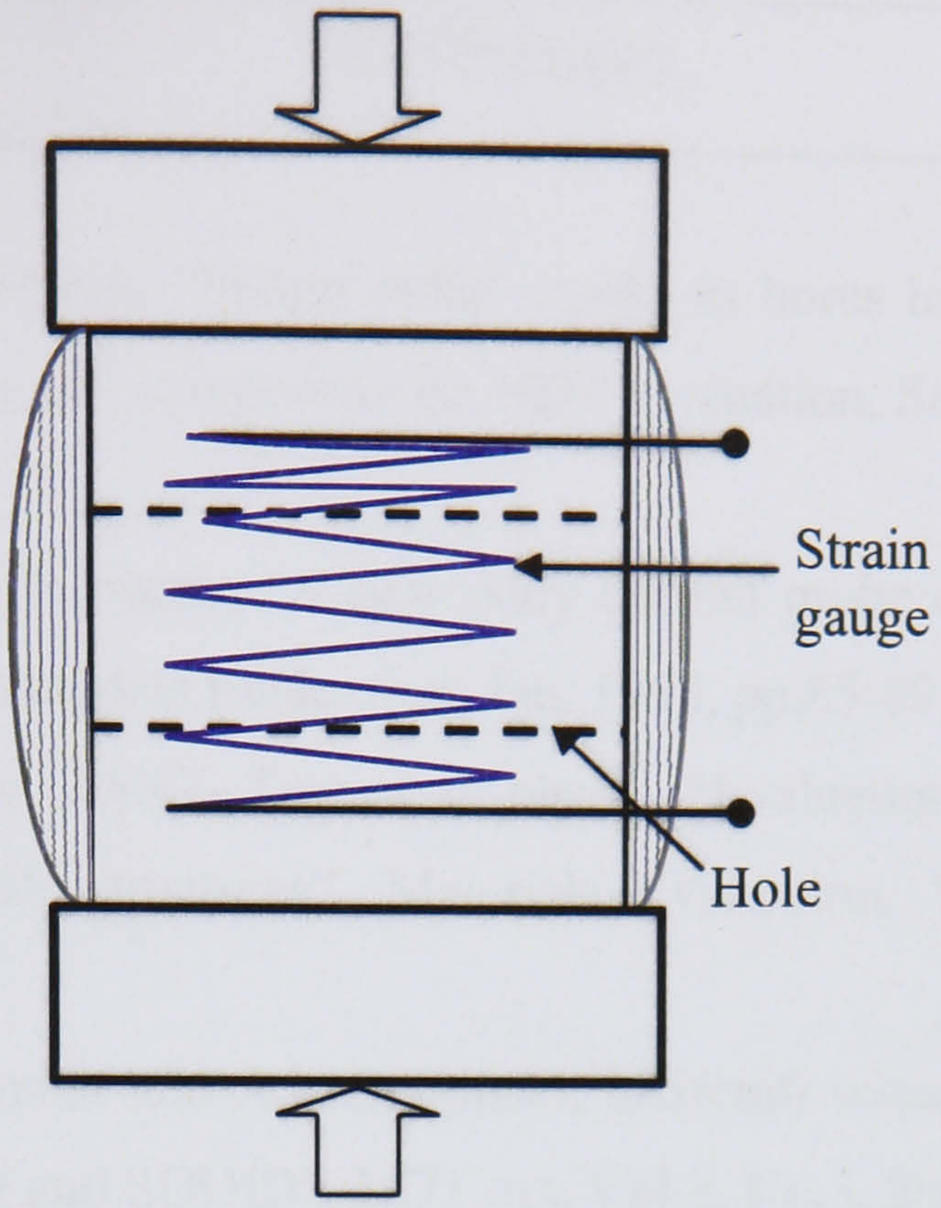


Figure 131 Schematic diagram shows strain gauge device on the specimen under compressive loading.

# References.


[1]. J. Bernardi and A. Serentti, "Sizing radial cracks in bores holes by eddy current", Proceeding of the 16th symposium on NDT evaluation, San Antonio, Apr. 1987, pp.194-202.

[2]. H. Hoshikawa and K. Koyama, "A new eddy current probe using uniform rotating eddy currents", Materials Evaluation, Jan. 1998, pp.85-89.

[3]. D.J. Hagemaier, The ASNT Technical paper, "Evaluation of heat damage to aluminium aircraft structures", Materials Evaluation, Vol.40, August 1982, pp.962-969.

[4]. H.J. Krause, R. Hohmann and A.I. Braginski, "Aircraft wheel and fuselage testing with eddy current and SQUID", NDT.net, Vol.3, No.3, September 1998.

[5]. D.J. Hagemaire, A.H. Wendelbo Jr. and Y. Bar-Cohen, "Aircraft Corrosion and Detection Methods", Materials Evaluation, Vol.34, March 1985, pp.426-437.

[6]. W.Y. Chu, C.M. Hsiao and J.W. Wang, "Stress Corrosion Cracking of an Aluminium Alloy under Compressive Stress", Metallurgical Transaction A, Vol.16A, Sept.1985, pp.1663-1670.

[7]. L. Cartz, "Nondestructive testing", ASM International the materials information society, 1995.

[8]. D.E. Bray and R.K. Stanley, "Nondestructive Evaluation – A tool for design, Manufacturing and Service, McGraw-Hill Book Company, 1989.

[9]. B. Hull and V. John, "Non-Destructive Testing", Basingstoke, MacMillan Education Limited, 1988.

[10]. R. Halmshaw, "Non-destructive Testing", 2nd Edition, Edward Arnold LTD., Metallurgy and Materials Science Series 1987.

[11]. D.E. Bray and D. McBride, "Nondestructive Testing Techniques", John Wiley & Sons Inc., 1992.

[12]. Convair Division of General Dynamics, "Nondestructive testing-Eddy current", Classroom training handbook, 2nd edition, 1979.

[13]. R.C. McMaster, "Nondestructive testing Handbook", The Ronald Press Company, Vol. 2, 1963.

[14]. H.L. Libby, "Introduction to Electromagnetic Nondestructive Test Methods". Robert E. Krieger Pub. Company, 1979.

[15]. R.C. McMaster, "The American Society for Nondestructive testing - NDT Handbook", Vol. 4, 2nd edition, Electromagnetic Testing Methods", 1986.

[16]. R.C. McMaster, "The Present and Future of Eddy Current Testing", Materials Evaluation, vol.43, November, 1985, pp1512-1521.

[17]. W.J. McGonnagle, "Nondestructive testing", 2nd edition, Gordon and breach science Publishers, 1961. [1]. W.E Quist & G.H. Narayanan, "Treatise on materials Science and technology", Vol. 31, No.8, 1989, pp.219-254.

[18]. http://www2.tech.purdue.edu/at/courses/at308/Technical_Links 02/07/2006.

[19]. D. Dugdale, "Essentials of Electromagnetism", MacMillan Physics Science Series, American institute of Physics, New York, 1993.

[20]. D.J. Hagemaier, The ASNT Technical paper, "Eddy Current Impedance Plane Analysis", Materials Evaluation, Vol.41, February, 1983, pp.211-218.

[21]. V.B. Rojansky, "Electromagnetic Fields and Waves", Dover Publications, 1979.

[22]. R.G. Powell, "Electromagnetism", MacMillan Education Limited, 1990.

[23]. J. Blitz, "Electrical, Magnetic and visual methods of testing materials", Brunel University, London, Butterworth & Co., 1969.

[24]. http://www.hocking.com/theory_testing.htm 04/06/2006.

[25]. I.J. Polmear, "Light alloys, Metallurgy of the light metals" Metallurgy and materials Science series, third edition, British library cataloguing in publication data, 1995, pp. 49-53.

[26]. D.J. Hagemaier, The ASNT Technical paper, "Eddy Current Standard Depth of penetration", Materials Evaluation, vol.43, October, 1985, pp.1438-1441.

[27]. D.J. Hagemaier, "Application of Eddy Current Impedance Plane Testing", Materials Evaluation, Vol. 42, July 1984, pp.1035-1040.

[28]. G.E. Dieter, "Mechanical Metallurgy", SI Metric Edition, McGraw-Hill Book Company, 1988, Chapter 12, pp.375-400.

[29]. T.D Cooper, D.M. Forney, "Detection of Cracks under installed fastener in aircraft structures", Materials Evaluation, vol. 41, September 1983. pp.1178-1185.

[30]. A.P. Rogel, J.J. Scalese, "Automatic eddy current bolt-hole scanning system", Materials evaluation, Vol.41, June 1983, pp.839-843.

[31]. D. Hagemaier, G. Kark, The ASNT Technical paper, "Eddy Current detection of short cracks under installed fasteners", Materials Evaluation, vol.42, January 1997, pp.25-30.

[32]. C.E. Chapman, A. Fahr, A. Pelletier and D.R. Hay, "Artificial Intelligence in the eddy current inspection of aircraft engine components", Materials evaluation, September, 1991, pp.1090-1094.

[33]. N.C. Haywood, "An Advanced Eddy Current bore-hole inspection system", British Journal of NDT, Vol. 35, No.3, March 1993, pp.119-123.

[34]. D.J. Hagemaier, "Nondestructive detection of exfoliation corrosion around fastener holes in aluminium wing-skins", Materials evaluation, Vol.40, No.6, May 1982, pp.682-685.

[35]. D.J. Hagemaier and A.P. Steinberg, ASNT conference, "Low-Frequency Eddy Current Inspection of Aircraft Structure", Materials Evaluation, Vol.40, February 1982, pp.206-210.

[36]. D. Hagemaier, B. Bates, and A Steinberg, "On-Aircraft Eddy Current subsurface crack inspection", Materials Evaluation, Vol.42, January, 1988, pp.518-522.

[37]. D.J. Hagemaire, A.H. Wendelbo Jr. and Y. Bar-Cohen, "Aircraft Corrosion and Detection Methods", Materials Evaluation, Vol.34, March 1985, pp.426-437.

[38]. T.D. Burleigh, "Corrosion of Aluminium and its Alloy", Handbook of Aluminum, Edited by G.E. Totten and D.S. Mackenzie, 2003, pp.421-464.

[39]. J. Brockington, "Combined Chemistry", Harlow Longman, 1981.

[40]. I.J. Polmear, "Light Alloys – From Traditional Alloy to Nanocrystals", 4th edition, Butterworth-Heinemann Press, 2006.

[41]. World Aluminium http://www.world-aluminium.org/history/index.html.01/4/2007.

[42]. World Aluminium http://www.world-aluminium.org/production/index.html.04/4/07.

[43]. M.F. Ashby and D.R.H. Jones, "Engineering Materials 2 – An Introduction to Microstructure, Processing and Design", Pergamon Press, 2nd edition, 1988.

[44]. Metals Handbook, ASM International, Vol. 8, 8th edition, 1985.

[45]. J.B. Kaufman, "Introduction to Aluminium Alloys and Tempers", ASM International, 2000.

[46]. F. King, "Aluminium and its alloys", Ellis Horwood Limited, John Wiley & Sons, 1987.

[47]. G.E. Totten and D.S. Mackenzie, "Corrosion of Aluminium and its Alloy", Handbook of Aluminum, Marcel Dekker Inc., 2003.

[48]. V. Gondhalekar and K. Patni, "New 2XXX Aluminium Aircraft Alloys", Advanced Materials & Processes, Vol.149, No.3, Nov. 1996, pp.24-25.

[49]. J.T. Staley, "Aluminium Alloy and Process Developments", Metals Engineering Quarterly, May 1976, pp.52-57.

[50]. W.H. Hunt Jr. and J.T. Staley, "High Strength Aluminum Alloys for Aerospace application", Light-Weight Alloys for Aerospace Applications, Conference paper 28/02-02/03 1989, Nevada USA, pp.111-120.

[51]. J.T. Staley, J. Liu and W.H. Hunt Jr, "Aluminium Alloys For Aerostructures", Advanced Materials & Processes, Vol.152, No.10, Oct. 1997, pp.17-20.

[52]. J.J. Thompson, E.S. Tankins and V.S. Agarwala, "A Heat Treatment for reducing Corrosion and Stress Corrosion Cracking Susceptibility in 7XXX Aluminium Alloys", Materials Performance, Vol.26, No.6, 1987, pp.45-52.

[53]. J.T. Staley, "Research on High-Strength Aerospace Aluminium Alloys", Canadian Aeronautics and Space Journal, Vol.31, No.1, March 1985, pp.15-29.

[54]. T. Gladman, "Precipitation hardening in Metals", Materials Science and Technology, Vol.15, 1999, pp.30-36.

[55]. W.D. Callister, "Materials Science and Engineering An Introduction", Chapter 11, 4th Edition, John Wiley & Sons Inc., 1997.

[56]. P. Auger, C. Schmuck, F. Danoix and D. Blavette, "Quantitative Analysis of GP zones Formed at room Temperature in a 7150 Al based alloy", Applied Surface Science, Vol. 87/88, March1995, pp.228-233.

[57]. M.O. Speidel, M.V. Hyatt, "Advances in Corrosion Science and Technology, Vol.2, Edited by M.G. Fontana & R.W. Staehle, Plenum Press, New York-London 1972.

[58]. J.E. Hatch, "Aluminum – Properties and Physical Metallurgy", American Society for Metals, Chapter 5, May 1984.

[59]. R.W. Revie, "Stress Corrosion of Aluminium Alloys - A review", Australian Corrosion Association, 15th Annual Conference, 11-15 Nov. 1974, Hobart Tasmanian Branch, pp.01-21.

[60]. H.P. Godard, W.B. Jepson, M.R. Bothwell and R.L. Kane, "The Corrosion of Light Metals", John Wiley & Son Inc., New York-London-Sydney, 1967.

[61]. R.T Foley, "Localized Corrosion of Aluminum Alloys-A review", Corrosion-NACE, Vol.42, No.5, May 1986, pp.277-286.

[62]. E. Mattsson, "Basic Corrosion Technology for Scientists and Engineers", Ellis Horwood Limited, John Wiley & sons, 1989.

[63]. M.G. Fontana, "Corrosion Engineering", 3rd edition, McGraw-hill Book Company, 1987.

[64]. V.J. Colangelo and F.A. Heiser, "Analysis of Metallurgical Failures", John Wiley & Sons Inc, 1987.

[65]. R. Baboian, "Corrosion Tests and Standards: Application and Interpretation", ASTM, June 1995.

[66]. Z.A. Foroulis and M.J. Thubrikar, "On the Kinetics of the Breakdown of Passivity of Preanodized Aluminum by Chloride Ions", Journal of Electrochemical Society, Electrochemical Science and Technology, Vol.12, No.10, Oct. 1975, pp.1296-1301.

[67]. R.T Foley and T.H. Nguyen, "The Chemical Nature of Aluminium Corrosion", Journal of Electrochemical Society, Electrochemical Science and technology, Vol.129, No.3, March1982, pp.464-467.

[68]. M.J. Robinson, N.C. Jackson, "The influence of grain structure and intergranular corrosion rate on exfoliation and stress corrosion cracking of high strength Al-Cu-Mg alloys", Corrosion Science, Vol.41, 1999, pp.1013-1028.

[69]. M. Posada, L.E. Murr, C.S. Niou, D. Roberson, D. Little, R. Arrowood and G. Debra, "Exfoliation and related microstructure in 2024 Aluminium body skins on Aging Aircraft", Materials Characterization, Vol.38, 1997, pp.259-272.

[70]. D.J. Kelly, M.J. Robinson, "Influence of Heat Treatment and grain shape on Exfoliation corrosion of Al-Li Alloy 8090, Corrosion, Vol.49, No.10, 1993, pp.787-795.

[71]. J.P. Chubb, T.A. Morad, B.S. Hockenhull and J.W. Bristow, "The effect of Exfoliation corrosion on the fracture and fatigue behaviour of 7178-T6 aluminium", International Journal of Fatigue, Vol.17, No.1, 1995, pp.49-54.

[72]. M.J. Robinson, "The Role of Wedging Stresses in the Exfoliation Corrosion of High Strength Aluminium Alloys, Corrosion Science, Vol.23, No.8, 1983, pp.887-899.

[73]. F. Bellenger, H. Mazeille, H. Idrissi, "Use of acoustic emission technique for the early detection of aluminium", NDT & E International, Vol.35, 2002, pp.385-392.

[74]. S. Ketcham, I.S. Shaffer, "Exfoliation Corrosion of Aluminium Alloys – Localized Corrosion", Cause of metal failures, ASTM STP 516, 1972, pp.3-16.

[75]. B.W. Lifka, D.O. Sprowls, "An Improved Exfoliation test for Aluminium Alloys", Corrosion, Vol.22, No.1, Jan. 1966, pp.7-15.

[76]. V.J. Colangelo, F.A. Heiser, "Analysis of Metallurgical Failures", 2nd edition, John Wiley & Sons, 1987, pp.184.

[77]. L.S. Anwar, "Exfoliation Corrosion of Al-Cu-Mg alloys", PhD thesis Cranfield Library, Cranfield University, England, 1982.

[78]. M. Keddam, C. Kuntz, H. Takenouti, D. Schuster and D. Zuili, "Exfoliation of Aluminium Alloys examined by electrode impedance", Electrochimica Acta, Vol.42, No.1, 1997, pp.87-97.

[79]. "The Standard Test Method for Exfoliation Corrosion Susceptibility in 2XXX and 7XXX series Aluminium Alloys (EXCO Test)", ASTM Standard G34-90, American Society for Testing and Materials, 1990.

[80]. D.O. Sprowls, "Corrosion Tests and Standard – Exfoliation", Application and Interpretation, American Society for Testing and Materials, June 1995.

[81]. M.R. Bayoumi, "The Mechanics and Mechanism of Fracture in Stress Corrosion Cracking of Aluminium Alloys", Engineering Fracture Mechanics, Vol. 54, No 6, 1996, pp.879-889.

[82]. M.O. Speidel, "Stress Corrosion Crack of Aluminium Alloys", Metallurgical Transactions A, Vol. 6A, April 1975, pp.631-649.

[83]. E.H. Hollingsworth, H.Y. Hunsicker, "Stress Corrosion Cracking of Aluminium Alloys, Corrosion of Aluminium and Aluminium Alloys", Corrosion, ASM Handbook, Vol.13, chapter 8, 9th edition, 1987.

[84]. J. Onoro and C. Ranninger, "Stress corrosion crack behavior of heat-treated Al-Zn-Mg-Cu Alloy with temperature", Materials Science, Vol. 35, No. 4, 1999, pp.509-514.

[85]. H.J. Kolkman, G.A. Kool and R.J.H. Wanhill, "Aircraft Crash Caused by Stress Corrosion Cracking", International Gas Turbine Congress and Exposition, The Hugue, Netherlands, June 13-16, 1994, pp.1-5.

[86]. G.M. Scamans, "Discontinuous Propagation of Stress Corrosion Crack in Al-Zn-Mg Alloys", Scripta Metallurgica, Vol.13, Pergamon Press Ltd., 1979, pp.245-250.

[87]. M.O. Speidel, "Theory of Stress Corrosion Cracking in Alloys", NATO, Edited Scully, Brussels Belgium, 1971, pp.288-353.

[88]. H.F. De Jong, "Influence of Environment and Temperature on the Stress Corrosion Crack Growth rate of Aluminium 7075", Aluminium Jahrg, Vol.58, No.9, 1982, pp.526-531.

[89]. A.H. Le, B.F. Brown and R.T. Foley, "The Chemical Nature of Aluminium Corrosion: IV. Some anion effects on SCC of AA7075-T651", Corrosion, Vol.36, No.12, 1980, pp.673-679.

[90]. N.J.H. Holroyd, "Environment-Induced Cracking of High-Strength Aluminium Alloys", EICM Proceedings, NACE, Houston, Texas, 1989, pp.311-345.

[91]. J.T. Stanley, S.C. Byre, E.L. Colvin and K.P. Kinnear, "Corrosion and Stress-Corrosion of 7XXX-W products", Transtec Publications, Materials Science Forum, Vol.217-222, Switzerland, 1996, pp.1587-1592.

[92]. G. Deshais, S.B. Newcomb, "Anodic Dissolution: Its characterization and Relevance to Corrosion and Stress Corrosion Cracking in 7XXX alloys", Second International Symposium on Aluminium Surface Science and Technology; Manchester; UK, 21-25 May 2000, pp.277-282.

[93]. S.M. Lee, S.I. Pyun and Y.G. Chun, "A Critical Evaluation of the Stress Corrosion Cracking Mechanism in High Strength Aluminum Alloys", Metallurgical Transactions A, Vol.22A, Oct. 1991, pp.2407-2413.

[94]. M. Landkof and L. Gal-or, "Stress Corrosion Cracking of Al-Zn-Mg alloy AA-7039", Corrosion-NACE, Vol. 36, No. 5, May 1980, pp241-245.

[95]. B.J. Connolly, M.G. Koul and A.L. Moran, "A comparison study of Stress Corrosion Crack growth rates for AA7XXX alloys as a function of bulk aqueous chloride concentrations and simulate crack tip chemistries", Department of Mechanical Engineering, United State Naval Academy, NACE International Corrosion 2003.

[96]. D. Najjar, T. Magnin, T.J. Warner, "Influence of Critical surface defects and localized competition between anodic dissolution and hygrogen effects during stress corrosion cracking of a 7075 aluminium alloy", Materials Science and Engineering, No.A238, 1997, pp.293-302.

[97]. T.L. Anderson, "Fracture Mechanics – Fundamentals and Applications", Third Edition, CRC Press, Taylor & Francis Group, 2005.

[98]. T. Pardoen, D. Dumont, A. Deschamps, Y. Brechet, "Grain boundary versus transgranular ductile", Journal of the Mechanicacs and Physics of Solids, Vol.51, 2003, pp.637-665.

[99]. C.R. Shastry, M. Levy and A. Joshi, "The effect of solution treatment temperature on stress corrosion susceptibility of 7075 aluminium alloy", Corrosion Science, Vol.21, No.9-10, 1981, pp.673-688.

[100]. N.J.H. Holroyd and D. Hardie, "Factors controlling crack velocity in 7000 series Aluminium Alloys during fatigue in an aggressive environment", Corrosion Science, Vol.23, No.6, 1983, pp.527-546.

[101]. F. Andreatta, H. Terryn and J.H.W. de Wit, "Corrosion behaviour of different tempers of AA7075 Aluminium Alloy", Electrochemica Acta, Vol.49, 2004, pp.2851-2862.

[102]. T.C Tsai, T.H. Chuang, "Role of grain size on the stress corrosion cracking of 7475 aluminium alloy", Materials Science and Engineering : A, Vol.225, No.1, 1997, pp.135-144.

[103]. I.J. Polmear, "Light Alloys Metallurgy of the Light Metals", Second Edition. Metallurgy and Materials Science Series, 1989.

[104]. M. Puiggali, A. Zielinski, J.M. Olive, E. Renauld, D. Desjardins and M. Cid, "Effect of microstructure on Stress Corrosion Cracking of Al-Zn-Mg-Cu alloy", Corrosion Science, Vol.40, No.4/5, 1998, pp.805-819.

[105]. B. Sarkar, M. Marek, and E.A. Starke Jr, "The Effect Of Copper Content and Heat Treatment on the Stress Corrosion Characteristics of Al-6Zn-2Mg-XCu Alloys", Metallurgical Transactions A, Vol.12A, Nov.1981, pp.1939-1943.

[106]. M. Talianker, B. Cina, "Retrogression and Reaging and the role of dislocations in the stress corrosion crack of 7000-type Aluminium alloys", Metallurgical Transactions A, Vol.20A, Oct.1989, pp.2087-2092.

[107]. D.A. Hardwick, A.W. Thompson and I.M. Berstein, "The Effect of Copper Content and Microstructure on the hydrogen embrittlement of Al-6Zn-2Mg Alloys" Metallurgical Transactions A, Vol. 14A, no.12, Dec.1983, pp.2517-2526.

[108]. J.K. Park, "Influence of Retrogression and Reaging Treatments on the Strength and Stress Corrosion Resistance of aluminium alloys", Materials Science and Engineering, Vol. A103, 1988, pp223-231.

[109]. E.C. Pow, W.W. Gerberich and L.E. Toth, "Analysis of Stress Corrosion Crack-Tip surface chemistries in 7075 type Aluminium Alloys", Scripta Metallurgica, Vol.15, 1981, pp.55-60.

[110]. R.G. Song, M.K Tseng, B.J Zhang, J. Liu, Z.H Jin and K.H Shin, "Grain Boundary Segregation and Hydrogen-Induce Fracture in 7050 Aluminium Alloy" ,Pegamon, Vol. 44, No. 8, 1996, pp.3241-3248.

[111]. J.C. Scully, "The Fundamentals of Corrosion", 2nd edition, Pergamon International Library Company, Vol.17, 1975.

[112]. D.J. Kelly, "The Exfoliation and Stress Corrosion Cracking of Aluminium alloy 8090", PhD thesis Cranfield Library, Cranfield University, England, 1981.

[113]. D. McNaughtan, "Investigation into Sub-surface Corrosion of High Strength 7XXX series Aluminium alloys", PhD thesis Cranfield Library, Cranfield University, England, 2001.

[114]. S.P. Jones, "Stress Corrosion and Exfoliation of High Strength Aluminium alloys", PhD thesis Cranfield Library, Cranfield University, England, 1989.

[115]. W.Y. Chu, J. Yao and C.M. Hsiao, "Stress Corrosion Cracking of Austenitic Stainless Steel under Compressive loading", Corrosion, Vol.40, No.6, June 1984, pp.302-306.

[116]. W.Y. Chu, R.T. Ma and C.M. Hsiao, "Stress Corrosion Cracking of Mild Steel under Compressive stress", Corrosion, Vol.43, No.4, Apr.1987, pp.251-254.

[117]. National Standard of Canada, "Advanced Manual for Eddy Current Test Method", May 1997, pp.175.

[118]. W.F. Kehler, "Handbook of international alloy compositions and designations" volume 3 aluminium, October 1980, Published by Metal and ceramics information center, Battelle, Columbus laboratories, 505 king avenue, Ohio, pp.1-130.

[119]. P.M. Unterweiser, Marilyn Penzenik, "Worldwide Guide to equivalent Nonferrous Metals and Alloys", 1980, Published by American Society for Metals, Ohio, USA.

[120]. H.E. Boyer, "Hardness Testing", 1987, Published by ASM International, Metals Parks, OH 44073.

[121]. T.S. Srivatsan, S. Anand, S. Sriram, V.K Vasudevan, "The high-cycle fatigue and fracture behavior of aluminium alloy 7055" Materials Science and Engineering, A281, 2000, pp 292-304.

[122]. M.J. Robinson, D. McNaughtan, M. Worsfold, "Corrosion product force measurements in the study of exfoliation and stress corrosion cracking in high strength aluminium alloys" Corrosion science 45, 2003, pp2377-2389.

[123]. T. Shibata, "Application of Extreme Value Statistics to Corrosion, Journal of Research of the National Institute of Standards and Technology, Vol.99, No.4, pp.327-336, 1994.

[124]. R.W. Randle and B.D. Woody, "Caution about Simulated Cracks in Steel for Eddy Current Testing", Materials Evaluation, Vol. 43, January 1991, pp 44-48.

[125]. J. Pelicer, "General Application of Eddy Current Instruments to detect and measure Corrosion in Aircraft Skins", Materials Evaluation, Vol.43, November 1985, pp.1543-1545.

[126]. X.E. Gros, "NDT Data fusion, Chapter 3, 1st edition John Wiley & Sons Inc, 1997.

[127]. J.C. Scully, "The Theory of Stress Corrosion Cracking in Alloys", Anti-Corrosion Methods Material, Vol.19, No.9, Sept 1972, pp.5-10.

[128]. M.G. Fontana and N.D. Greene, "Corrosion Engineering", 2nd edition, McGraw-hill Book Company, 1978.

[129]. J.I. Dickson, P. Martin and J.P. Bailon, "The study of variations in Stress Corrosion Crack velocities in aluminium alloy 7075-T651 by acoustic emission", Materials Science and Engineering, Vol.58, 1983, pp.L5-L8.

[130]. C.J. Peel, B. Evans and D.S. Mcdarmaid, "Development of aluminium alloys in the UK", Metals and Materials, Vol.3, No.8, Aug. 1987, pp.449-455.

[131]. C.J. Peel, P. Poole, "The Application of Double Cantilever Beam (DCB) Testing To Stress Corrosion Cracking Of Aluminium Alloys", Technical Report 80046, April 1980, pp1-14.

[132]. P.J. Blau and W.M. Griffith, "Measurement of Stress Corrosion Cracks in Aluminum Alloys DCB Specimens using an Ultrasonic Pulse-Echo technique", Air Force Material Laboratory, Wright-Patterson Ohio, January 1975, pp.1-33.

[133]. P. Renaud, P. Violan, J. Petit and D. Ferton, "Microstructure Influence on fatigue crack growth near threshold in 7075 Al Alloy", Scripta Metallurgica, Pergamon Press Ltd, Vol.16, 1982, pp.1311-1316.

[134]. P.J. Blau, "Observations of Stress Corrosion Crack-Front Bowing in High-Strength Aluminum Alloy Double Cantilever Beam Specimen", Metallurgical Transactions A, Vol.7A, March 1975, pp.463-465.

[135]. W.J. Helfrich, "Fractography of Stress Corrosion Cracks in Aluminium Alloy 7075", Corrosion, Vol.29, No.8, August 1973, pp.316-318.

[136]. C.T. Sun and S. Zheng "Delamination Characteristics of Double Cantilever Beam and End-Notched Flexure Composite specimens", Composite science and Technology, Vol.56, 1996, pp.451-459.

[137]. R.C. Doward, K.R Hasse, "Flaw Growth in High Strength Al-Zn-Mg-Cu alloys exposed to stress corrosion environment", Corrosion, Vol.34, No.11, 1978, pp.386-395.

[138]. K. Sotoudeh, T.H. Nguyen, R.T. Foley and B.F. Brown "The Chemical Nature Of Aluminium Corrosion: I Corrosion of Aluminium Surfaces by Aluminium Salts" Corrosion, Vol. 37, No 6, June 1981, pp.358-362.

[139]. R.T. Foley and A.H. Le, "On the Nature of the Occluded Cell in the stress corrosion cracking of AA7075-T651- Analysis of the solution inside the crack" Corrosion, Vol.40, No.4, April 1984, pp.195-197.

[140]. J.J. Vajo, R. Wei, A.C. Phelps, L. Reiner, G.A. Herera, O. Cervantes, D. Gidanian, B. Bavarian and C.M. Kappes, "Application of extreme value analysis to crevice corrosion", Corrosion Science, Vol.45, 2003, pp.497-509.

[141]. J. Blitz, V.J. Willistatter, S.R. Oaten and N.T Hajian, "Eddy Current surface crack sizing in steel with high lift off", NDT International, Vol. 20, No. 2, April 1987, pp.105-109.

[142]. J.B. Hellett, G. Van Drunen and V.S.Cecco, The ASNT Technical paper, "An Eddy Current Probe for Separating Defects from Resistivity Variations in Zirconium alloy tubes", Materials Evaluation, vol.42, Sept. 1984, pp.1276-1280.

[143]. R.T. Elsberry and D.M. Bailey, "Characterization of Shielded Eddy Current Probes", Materials Evaluation, Vol. 44, July 1986, pp 984-988.

[144]. M.A. Meggiolaro, J.T.P. Castro, "On the dominant role of crack closure on fatigue crack growth modelling", International Journal of fatigue, Vol. 25, 2003, pp.843-854.

[145]. J. H. Heida and W. G. J. Hart, "Eddy current detection of pitting corrosion around the fastener holes", paper presented at 79th meeting of the AGARD structure and materials panel, Seville Spain, 5-6 Oct 1994.

[146]. ASME Boiler and Pressure Vessel Code An American National Standard, Section V, Article 8, Non-destructive Examination, 1986 edition, pp.97-103.

[147]. P. Neumaier, Institute Dr Forster, "Testing heat exchanger tubes using eddy current techniques with computerised signal analysis", British Journal of NDT, September 1983, pp. 233-237.

[148]. D. Rhodest and J.C. Radon, "Fracture Analysis of Exfoliation in an Aluminium Alloy", Engineering Fracture Mechanics, Vol.10, 1978, pp.843-853.

[149]. M. Yoda, "Stress Corrosion Cracking under Modes I, II, III Loadings", Engineering Fracture Mechanics, Vol.30, No.4, 1988, pp.461-467.

[150]. J. Blain, J. Masounave and J. I Dickson, "A Comparison of SCC Velocity Measurement under Conditions of Constant Load and Constant Displacement" Corrosion Science, Vol. 24, No. 1, 1984, pp.1-12.

[151]. Standard test method for measurement of fatigue crack growth rates, ASTM E-647, 2003, pp.615-657.

[152]. C.M. Branco, J.C. Radon and L.E. Culver, "Influence of specimen orientation and loading history on S.C.C in an Aluminium Alloys.", Corrosion Science, Vol. 17, No. 2, February 1977, pp.125-141.

[153]. K.R. Hasse and R.C. Dorward, "Long-term Marine Atmospheric Stress Corrosion Tests on High Strength Al-Zn-Mg-Cu Alloys", Corrosion Science, Vol.42, No.11, Nov 1986, pp.663-669.

[154]. W.E. Anderson, "Proceeding Conference-Physical Metallurgy of Stress Corrosion Fracture", Interscience, 1959, pp.147-148.

[155]. H.F Dejong & J.W.G.A Berkelaar, "Influence of Pretreatmnet, Environment and Strain rate on Stress Corrosion Cracking of the Aluminium Alloy 7075-T6", Technische Hogeschool, Netherlands, Apr. 1984, pp.1-11.

[156]. D.L. DuQuesnay, P.R. Underhill and H.J. Britt, "Fatigue crack growth from corrosion damage in 7075-T6511 Aluminium Alloy under aircraft loading", International Journal of fatigue, Vol.25, 2003, pp.371-377.

[157]. J.S. Robinson, "Improving the properties of Aluminium alloys by retrogression and reageing", Material Wissenschaft Und Werkstofftechnik, Vol.34, 2003, pp.385-390.

[158]. W. Gruhl, "Stress Corrosion Crack of High Strength Aluminium Alloys", Zeitschrift Fur Metallkunde, Vol.75, No.11, Nov.1984, pp.819-826.

[159]. R.P. Wei, M. Gao and P.S. Pao, "The Role of Magnesium in CF and SCC of 7000 series aluminium alloys", Scripta Metallurgica, Vol.18, 1984, pp.1195-1198.

[160]. R.F. Hehemann, "Stress Corrosion Cracking of Stainless Steels", Metallurgical Transactions A, Vol.16A, Nov. 1985, pp.1909-1921.

[161]. D. Tanguy, B. Bayle, R. Dif and Th. Magnin, "Hydrogen effects during IGSCC of pure Al-5Mg alloy in NaCl media", Corrosion Science, Vol.44, 2002, pp.1163-1175.

[162]. C.F. Barth, A.R. Troiano, "Cathodic Protection and H in Stress Corrosion Cracking", Corrosion, Vol.28, No.7, July 1972, pp.259-263.

[163]. D.A. Jones, "A Unified Mechanism of Stress Corrosion and Corrosion Fatigue Cracking, Metallurgical Transactions A, Vol.16A, June 1985, pp.1133-1141.

[164]. P. Greenfield, "Stress Corrosion Failure", Mills & Boon Limited, 1971.

[165]. H.L. Logan, "Film-Rupture Mechanism of Stress Corrosion", Journal of Research of the National Bureau of Standards, Vol.48, No.2, Feb. 1952, pp.99-105.

[166]. http://www.engineersedge.com/material_science/stress_definition.htm. 01/05/07